Ollscoil na Gaillimhe
University of Galway

Provided by the author(s) and University of Galway in accordance with publisher policies. Please cite the published version when available.

Title	Experimental characterisation, computational modelling and design tool development for fretting fatigue and wear in flexible marine risers
Author(s)	O'Halloran, Sinéad
Publication Date	2017-09-25
Item record	http://hdl.handle.net/10379/6828

Downloaded 2024-04-26T15:26:35Z

Some rights reserved. For more information, please see the item record link above.

OÉ Gaillimh
NUI Galway

Experimental Characterisation, Computational Modelling and Design Tool Development for Fretting Fatigue and Wear in Flexible Marine Risers

Sinéad O'Halloran B.E. (2013)

Supervisors: Prof. Sean Leen & Dr. Annette Harte

Thesis submitted to the National University of Ireland Galway as fulfilment for the requirements for the Degree of Doctor of Philosophy

Mechanical Engineering, National University of Ireland Galway

September 2017

Abstract

Fretting is a key concern in the fatigue design of the pressure armour layer of flexible marine risers, due to the combination of extreme global dynamic loading conditions and the local geometrical-tribological conditions in the nub-groove contact regions. This thesis presents experimental characterisation, global-local computational modelling and the development of a stand-alone analytical design tool for fretting fatigue and wear in the pressure armour layer of flexible marine risers. Extensive experimental testing is carried out to identify tribological and mechanical properties of pressure armour material. The effects of grease-lubricant, contact conformity and loading conditions on fretting behaviour are investigated on cylinder-on-flat specimen configurations. A newly-designed fretting rig provides testing under partial and gross-slip conditions with high contact pressure, low slip conditions, representative of riser nub-groove contact loading conditions. A pre-service flexible marine riser is dissected to extract pressure armour material for monotonic tensile and fatigue testing.

A global-local computational methodology for analysis of the pressure armour layer in flexible risers is presented. The methodology consists of a hierarchy of models, including a global riser dynamics model, a three-dimensional riser sub-model, an axisymmetric nub-groove local contact model and cylinder-on-flat fretting contact models of test geometries. This allows, for the first time, quantification of key fretting variables, such as contact pressure, relative slip and sub-surface stresses in this complex geometry, under representative loading conditions. Fatigue lives are calculated using the three-dimensional critical plane Smith-Watson-Topper (SWT) multiaxial fatigue

indicator parameter. It is shown that operating pressure and bending-induced axial displacement significantly affects predicted crack initiation. It is also shown that friction coefficient has a significant effect on predicted trailing-edge tensile stresses in the pressure armour layer and, hence on fretting crack initiation in risers. A combined fretting wear-fatigue finite element model has been developed using an adaptive meshing technique and the effect of bending-induced slip is characterised. It is shown that a surface damage parameter combined with a multiaxial fatigue parameter can accurately predict the beneficial effect of fretting wear on fatigue predictions.

A design study is conducted using the framework outlined in this thesis. The key functional relationships between global riser variables (running conditions) and local nub-groove fretting variables are identified. This facilitates identification of the critical riser curvatures for minimum predicted numbers of cycles to crack initiation for different riser design geometries. Furthermore, a weight function method for crack propagation is implemented for various riser geometries, to allow prediction of total fretting fatigue life. Running condition fretting maps for different riser geometries are thus developed. Interestingly, the resulting predicted fretting fatigue lives are found to be in the same range as tensile armour layer plain fatigue lives.

A stand-alone, computationally efficient, analytical fretting wear-fatigue model is developed. The model solves for frictional contact surface and sub-surface tractions and stresses using quadratic programming and theory of elasticity; fretting fatigue predictions are calculated using the SWT multi-axial fatigue indicator parameter and transient wear is modelled using the Archard wear equation. The analytical solution is validated against finite element incremental wear and crack initiation predictions for fretting in the nub-groove region. This provides a computationally efficient design tool for fretting in the pressure armour layer of flexible marine risers.

List of publications

Journal papers:

O'Halloran, S.M., Harte, A.M., Connaire, A.D., Leen, S.B., 2016a. Modelling of fretting in the pressure armour layer of flexible marine risers. Tribol. Int. 100, 306–316. doi:10.1016/j.triboint.2016.02.040

O'Halloran, S.M., Shipway, P.H., Connaire, A.D., Leen, S.B., Harte, A.M., 2017. A combined wear-fatigue design methodology for fretting in the pressure armour layer of flexible marine risers. Tribol. Int. 108, 7-15, doi: 10.1016/j.triboint.2016.10.020

O'Halloran, S.M., Shipway, P.H., Harte, A.M., Connaire, A.D., Leen, S.B., 2017. An experimental study on key fretting variables for flexible marine riser nub-groove contact doi. 10.1016/j.triboint.2017.07.032 (In Press)

O'Halloran, S.M., Harte, A.M., Leen, S.B., Development of a piezoelectrically-actuated fretting wear test rig for pressure armour layer nub-groove contact (In preparation)

O'Halloran, S.M., Harte, A.M., Connaire, A.D., Leen, S.B., Implementation of fretting wear-fatigue predictions for a flexible marine riser system (In preparation)

O'Halloran, S.M., Harte, A.M., Connaire, A.D., Leen, S.B., Development of an analytical fretting model with application to nub-groove contacts in flexible marine risers (In preparation)

Conference proceedings:

O'Halloran, S., Harte, A., Connaire, A. and Leen, S., 2016b. The prediction of fretting fatigue in the pressure armours of dynamic flexible pipes. Offshore Technology Conference, Huston, Texas, USA, May 2nd - 5th 2016 doi: 10.4043/26985-MS

Acknowledgements

I wish to thank my supervisors, Prof. Sean Leen, Dr. Annette Harte and Dr. Adrian Connaire, for their support and guidance during this research, without which this would not have been possible. I would like to thank Prof. Phil Shipway for inviting me to carry out testing at the University of Nottingham and his guidance during my visit and subsequently. I wish to acknowledge the Irish Research Council, Wood Group and the National University of Ireland for the financial support to undertake this research.

I would also like to take this opportunity to thank the Faculty of Engineering at the University of Nottingham and the NUI Galway Engineering Building technical staff; particularly Mr. Bonaventure Kennedy, Mr. Patrick Kelly and Mr. William Kelly for their technical support in experimental testing and manufacture of the fretting rig. Thanks to all the postgrads in the Engineering Building who have helped me out along the way, especially, Caoimhe, Richard, Conor, Eimear and Patrick. I also want to thank the staff of Wood Group, Galway, in particular Mr. Kieran Kavanagh and Mr. Brian O'Keefe as well as Mr. Ray Burke of BP Global for their helpful and precious information on flexible marine risers, and also Mr. Wim Van Haver and Mr. Michael Roughton (NV Bekaert SA), for their insight into the material manufacturing process and for providing material for testing.

I wish to thank my parents, T.J. and Bríd, and sisters Aoife and Eilís for their support throughout my education. Finally, thank you to Eoin for being there for me and for his continuous encouragement and support.

Table of contents

Abstract ..... **i**

List of publications ..... **iii**

Acknowledgements ..... **iv**

Nomenclature ..... **xi**

Acronyms ..... **xvi**

Chapter 1: Introduction **1**

1.1. Background 1
1.2. Framework for design tool for fretting in flexible marine risers 6
1.3. Aims and objectives 6
1.4. Layout of thesis 8

Chapter 2: Literature review **12**

2.1. Introduction 12
2.2. Friction 13
2.3. Contact mechanics 16
2.3.1. Introduction 16
2.3.2. Sliding cylinder-on-flat 17
2.3.3. Partial slip cylinder-on-flat 19
2.3.4. Punch-on-flat 21
2.3.5. Crossed-cylinders 22
2.3.6. General solution 23
2.4. Wear 25
2.4.1. Introduction 25
2.4.2. Archard wear equation 26
2.4.3. Energy wear method 28

2.5. Fatigue of metals 29
2.5.1. Introduction 29
2.5.2. Fatigue mechanisms 30
2.5.3. Stress-strain based approaches 31
2.5.4. Fatigue crack growth 35
2.5.5. Short crack growth 37
2.5.6. Fracture mechanics-contact mechanics analogy 39
2.6. Fretting 41
2.6.1. General 41
2.6.2. Fretting fatigue 46
2.6.3. Fretting wear 48
2.6.4. Surface damage parameter for fretting 50
2.6.5. Role of lubrication in fretting 52
2.7. Experimental characterisation of fretting behaviour 54
2.7.1. Introduction 54
2.7.2. Fretting fatigue rigs 54
2.7.3. Fretting wear rigs 58
2.8. Flexible marine riser technology 61
2.8.1. Modelling of flexible marine risers 61
2.8.2. Experimental testing of risers 65
2.8.3. Fretting in flexible marine risers 68
2.9. Summary and conclusions 68

Chapter 3: Design of fretting test rig 72

3.1. Introduction 72
3.2. Review of fretting wear rig designs 73
3.2.1. Specimen geometry and alignment 73
3.2.2. Drive line and reciprocating displacement 75
3.2.3. Applying normal loading 78
3.3. Requirements for new fretting test rig 79
3.4. Development of new fretting rig 81
3.4.1. Design 81
3.4.2. Drive line and actuator 82
3.4.3. Specimen and normal load application 84
3.4.4. Displacement measurement 85
3.4.5. Tangential force measurement 86
3.4.6. Control 88
3.4.7. Data acquisition and post-processing 90
3.5. Summary and conclusions 93

Chapter 4: Fretting and fatigue experimental characterisation of pressure armour material 94

4.1. Introduction 94
4.2. Material and specimen manufacture 95
4.2.1. University of Nottingham test specimen 95
4.2.2. Newly designed fretting rig test specimen 96
4.2.3. Tensile and low-cycle fatigue test specimen 97
4.2.4. Test material and specimen summary 99
4.3. Effect of grease-lubrication on fretting variables 100
4.3.1. Introduction 100
4.3.2. Test conditions and procedures 101
4.3.3. Estimation of wear volume and surface topography 103
4.3.4. Characterisation of wear scars and debris 107
4.3.5. Effect of lubrication 108
4.3.6. Effect of loading conditions 115
4.3.7. Durability of the low friction conditions 118
4.4. Discussion 121
4.5. Fretting wear tests using piezoelectric fretting rig 125
4.5.1. Introduction 125
4.5.2. Test conditions and procedures 126
4.5.3. Characterisation of wear scars and debris 128
4.5.4. Results 129
4.5.5. Discussion 132
4.6. Comparison of fretting tests 135
4.6.1. Comparison of rigs 135
4.6.2. Comparison of dry fretting results 136
4.7. Tensile and low-cycle fatigue tests 139
4.7.1. Test conditions and procedures 139
4.7.2. Results 139
4.8. Summary and conclusions 145

Chapter 5: Modelling of fretting in pressure armour layer 147

5.1. Introduction 147
5.2. Modelling of fretting contact 148
5.2.1. Analytical model 148
5.2.2. Cylinder-on-flat finite element model 148
5.2.3. Comparison between finite element and analytical models 151
5.3. Local pressure armour layer fretting FE model 153
5.3.1. Axisymmetric riser model 153
5.3.2. Pressure armour material model 155
5.3.3. Local nub-groove contact results 157
5.4. Fatigue model 160
5.4.1. Fatigue indicator parameter 160
5.4.2. Critical plane approach 161

5.4.3. Fatigue constants for pressure armour material 164
5.4.4. Crack initiation lives for pressure armour layer 167
5.5. 3D riser modelling 169
5.5.1. Sub-modelling approach 169
5.5.2. Global model details 170
5.5.3. Sub model details 172
5.5.4. Validation of 3D modelling technique 174
5.5.5. Effect of bending moment on nub-groove contact conditions 175
5.6. Summary and conclusions 180

Chapter 6: Combined fretting wear and fatigue model for pressure armour wire contacts 182

6.1. Introduction 182
6.2. Modelling fretting wear 182
6.2.1. Adaptive meshing techniques 182
6.2.2. Effect of wear on fretting variables 187
6.3. Combined wear-fatigue model 189
6.3.1. Wear-fatigue damage accumulation 189
6.3.2. Wear-fatigue life predictions 190
6.4. Fretting wear-fatigue design parameter 192
6.5. Summary and conclusions 196

Chapter 7: Global-local fretting analysis of flexible risers 197

7.1. Introduction 197
7.2. Methodology 197
7.3. Global riser analysis 199
7.3.1. General 199
7.3.2. Riser configuration and geometrical properties 200
7.3.3. Vessel and environmental loading 202
7.4. Global-local loading conditions 204
7.4.1. General 204
7.4.2. Global riser axial tension 205
7.4.3. Global riser curvature 206
7.5. Local nub-groove analysis 209
7.5.1. Finite element analysis 209
7.5.2. Crack initiation 210
7.5.3. Crack propagation 210
7.6. Results 213
7.6.1. Global analysis 213
7.6.2. Global-local loading conditions 216

7.6.3. Predicted life to crack initiation 222
7.6.4. Crack propagation 225
7.7. Summary and conclusions 228

Chapter 8: EASY-FRET: An analytical fretting wear-fatigue design tool 230

8.1. Introduction 230
8.2. Analytic model 231
8.3. Model validation 235
8.3.1. Contact pressure distributions 235
8.3.2. Stress distributions 236
8.3.3. Wear simulation 239
8.3.4. Multi-axial fatigue 241
8.4. Discussion 243
8.4.1. Computational efficiency 243
8.4.2. Further development 243
8.5. Summary and conclusions 244

Chapter 9: Conclusions and recommendations 245

9.1. Conclusions 245
9.2. Recommendations for future work 250

Appendix A: New fretting rig documents 253

A.1. Overview 253
A.2. Calibration certification for piezoelectric actuator 254
A.3. Calibration certificate for DVRT 257
A.4. Calibration certificate for force sensor 261
A.5. Operational procedure 263

Appendix B: Riser dissection procedure 266

B.1. Overview 266
B.1. Health and Safety 266
B.2. Procedure 267
B.2.1. General 267
B.2.2. External Sheath 268
B.2.3. High Strength Tape 268
B.2.4. Second Armour Layer 269
B.2.5. Anti-Wear Tape 271
B.2.6. First Armour Layer 272
B.2.7. Anti-Wear Tape 273

B.2.8. Pressure Armour Zeta Wire 274

Appendix C: Global riser analysis results 278

C.1. Overview 278
C.2. Global riser curvature envelopes 278
C.3. Local nub-groove contact displacements 278
C.2. Global riser axial force envelopes 283

APPENDIX D: Estimation of stress gradient redistribution due to wear 287

D.1. Overview 287
D.2. Wear simulation results 287
D.3. Estimation of stress distributions 289

Bibliography 291

Nomenclature

α	Energy wear coefficient (MPa^{-1})
α_{FS}	Normal stress sensitivity
γ	Shear strain
γ_c	Fatemi-Socie parameter
δ	Maximum observed slip across a contact over one fretting cycle (finite element) (μm)
δ^*	Measured (experimental) contact displacement amplitude (μm)
δ_{th}	Threshold limit beyond which wear becomes dominant (μm)
δP	Normal load supported by a single asperity contact (N)
δQ	Average asperity wear volume per unit sliding distance (mm^3/mm)
δV	Volume of material removed by wear of an asperity (mm^3)
Δ	DVRT displacement measurement (μm)
Δ^*	Experimental applied displacement amplitude (μm)
Δ_{app}	Finite element applied displacement amplitude (μm)
$\Delta\gamma_{max}$	Maximum shear strain range
$\Delta\varepsilon_e$	Elastic strain range over one fretting cycle
$\Delta\varepsilon_p$	Plastic strain range over one fretting cycle
$\Delta\varepsilon$	Strain range over one fretting cycle
$\Delta\sigma$	Stress range over one fretting cycle (MPa)
Δh	Finite element incremental wear depth (μm)
$\Delta\kappa$	Change riser in curvature with respect to time (1/m)
$\Delta\kappa_{crit}$	Critical change in riser curvature with respect to time (1/m)
$\Delta\kappa_{th}$	Threshold riser curvature when for nub-groove gross-partial-slip transition (1/m)
ΔK	Stress intensity factor
ΔK_{eff}	Effective stress intensity factor (MPa $mm^{0.5}$)
ΔK_{th}	Threshold stress intensity factor (MPa $mm^{0.5}$)
ΔK_I	Mode I stress intensity factor (MPa $mm^{0.5}$)
ΔK_{II}	Mode II stress intensity factor (MPa $mm^{0.5}$)
ΔN	Number of cycles for cycle jumping

Δn_i	Number of cycles experienced at loading cycle *i*
ε	Strain
ε'	Transformed strain
ε'_f	Coffin-Manson fatigue ductility exponent
ε_{eq}^{pl}	Equivalent plastic strain
γ	NLKH back-stress material parameter
κ	Proportion of asperity contact that give riser to wear particles
κ	Riser curvature (1/m)
λ	Eigenvalue
μ	Coefficient of friction
ν	Poisson's ratio
σ	Stress (MPa)
σ'	Transformed stress (MPa)
$\boldsymbol{\sigma'}$	Deviatoric stress tensor (MPa)
σ_a	Alternating stress (MPa)
σ_{app}	Alternating bulk stress (MPa)
σ'_e	Effective alternating stress at failure (MPa)
σ_e	Endurance limit for a given life (MPa)
σ'_f	Basquin fatigue strength exponent (MPa)
σ_f	True fracture stress (MPa)
σ_m	Mean stress (MPa)
σ_{max}	Maximum normal stress in a fatigue cycle (MPa)
$\sigma_{max,soft}$	Maximum peak tensile stress after initial cyclic softening task place in LCF test (MPa)
σ_y	Yield stress (MPa)
σ_{UTS}	Ultimate tensile stress (MPa)
τ	Shear stress (MPa)
τ_c	Fatemi-Socie parameter
$(\tau\delta)_{th}$	Threshold limit beyond which wear becomes more dominant over cracking (MPa μm)
θ	Angle of rotation of riser
θ_c	Critical plane angle
θ_i	Angle of plane *i*
υ	Poisson's ratio
ω_{crit}	Critical frequency at which DVRT lift-off occurs (Hz)

A	Curve fit constant
a	Contact semi-width (μm)
a	Radius of a single asperity contact
a	Initial crack length (m)
a	Acceleration (ms^{-2})
a	Compliance constant
a_{th}	Threshold crack length (m)
b	Basquin fatigue strength exponent (MPa)
b	Rate of decay towards saturation of isotropic parameter
b_c	Covered contact width (μm)
b_y	Fatemi-Socie parameter
B	Curve fit constant
c	Coffin-Manson fatigue ductility exponent
c	Contact semi-width of the stick region (μm)
c_y	Fatemi-Socie parameter
C	Paris law coefficient
C	D_{fret} material constant
C	Curve fit constant
C	System compliance
C	Hardening modules (Frederick-Armstrong)
C_{CoF}	Effect of coefficient on rig compliance
C_{rig}	Effect of rig compliance
D	Damage accumulation from Miner-Palmgren rule
D_c	Critical damage for crack initiation to occur
D	Damage accumulation for back-calculation to crack initiation
$D_{i,j}$	Influence function
d_c	Critical depth for averaging techniques (μm)
E	Young's modulus (GPa)
E^*	Combined Young's modulus (GPa)
E_d	Dissipated energy (J)
$E_{d,th}$	Threshold energy required for wear to take place (J)
$E_{overall}$	Overall error
f	Yield function
$f_{i,j}$	Eigenfunction
F	Riser axial force (kN)

F_I	Inertia force (N)
G	Shear modulus (GPa)
h_o	Gap function (μm)
h_n	Gap function after wear takes place (μm)
h_I	Weight function for mode I crack propagation
h_{II}	Weight function for mode II crack propagation
H	Hardness (MPa)
I	Object function
k	Initial cyclic yield stress (MPa)
k	Dimensional wear coefficient (K/H) (MPa^{-1})
k	Spring stiffness (Nm^{-1})
k	F_2 parameter
k_l	Local wear coefficient
K	Generalised stress intensity factor
K	Dimensionless wear coefficient
K	Wear coefficient
K_{IC}	Fracture toughness of the material (MPa $mm^{0.5}$)
m	D_{fret} material constant
m	Paris law exponent
m	Tribological constant
m	Mass (kg)
n	Number of cycles
n	Number of variables
n	Paris law exponent
$\boldsymbol{n}$	Unit normal to a plane
N	Fretting test duration (number of cycles)
N_f	Number of cycles to failure
N_i	Number of cycles to crack initiation
N_p	Number of crack propagation cycles (from initiation to failure)
P	Normal load (N)
P	Normal load per unit length (N/mm)
p	Contact pressure (MPa)
p_0	Maximum contact pressure (MPa)
p_d	Design internal fluid pressure for riser (MPa)
p_{int}	Riser internal fluid pressure (MPa)

p_l	Internal fluid pressure for riser (lower than operating pressure) (MPa)
p_e	Riser external fluid pressure (MPa)
p_o	Operating internal fluid pressure for riser (MPa)
p_{yield}	Yield pressure for a plastically deforming asperity
Q	Tangential load (N)
Q	Saturation value of the isotropic parameter
Q	Total wear volume per unit sliding distance (mm^3/mm)
Q^*	Maximum measured tangential (frictional) force (N)
q	Shear traction (MPa)
R	Radius of contact surface (mm)
R	Stress ratio
R	Bend radius of riser (m)
R^*	Combined radius of contact surface (mm)
R_c	Cyclic strain ratio
R_a	Surface roughness (μm)
r	Distance from center of crossed-cylinder contact (mm)
r	Isotropic hardening state variable variable
r	Tribological constants
S	Rig stiffness (MPa)
S	Cross-sectional area (mm^2)
T_s	Pre-load force in DVRT spring (N)
u_n	Variable n
v	Vertical displacement of node due to normal loading (μm)
V	Wear volume (mm^3)
V^-	Total experimental wear volume (mm^3)
V^+	Total experimental transfer volume (mm^3)
W	Width of flat specimen (mm)
x	Sensor output (V)
$\boldsymbol{x}$	Back-stress
$\boldsymbol{x}$'	Deviatoric back-stress tensor (MPa)
Y	Geometrical factor for Paris Law
z	Depth below the contact surface (mm)

Acronyms

2D	Two-dimensional
3D	Three-dimensional
BSE	Back-scatter electon
CoF	Coefficient of friction
CALM	Cantenary anchor leg mooring
CPU	Central processing unit
DAC	Digital to analog converter
DAQ	Data acquisition
D_{fret}	Fretting fatigue surface damage parameter
DVRT	Differential variable reluctance transducer
EASY-FRET	Engineering Analysis SYstem for FRETting
ECoF	Energy coefficient of friction
EDX	Energy-dispersive X-ray spectroscopy
eFFDP	Enhanced fretting fatigue damage parameter
EVM	Electromagnetic vibrator
FE	Finite element
FFDP	Fretting fatigue damage parameter
FIP	Fatigue indicator parameter
FLRF	Fretting life reduction factor
FPSO	Floating, production, storage and offloading
FS	Fatemi-Socie
GICoF	Geometry independent coefficient
GS	Gross slip
GSR	Gross slip regime
GUI	Graphical user interface
HCF	High-cycle fatigue
HDPM45	Highly dynamic precise motion 45
ID	Inner diameter (mm)
LCF	Low-cycle fatigue
LEFM	Linear elastic fracture mechanics

LSMB	Lower specimen mounting block
LVDT	Linear variable differential transformer
MDR	Method of dimensional reduction
MPM	Material point mesh
MRFM	Material response fretting map
MS	Mixed slip
MSL	Mean sea level
NI	National instruments
NLKH	Non-linear kinematic hardening
OD	Outer diameter (mm)
PID	Proportional - integral - derivative (controller)
PS	Partial slip
PSR	Partial slip regime
RCFM	Running condition fretting map
SEM	Scanning electron microscope
SCG	Short crack growth
SCR	Steel cantenary riser
SLHR	Single line hybrid riser
SWT	Smith-Watson-Topper
UoN	University of Nottingham
USMB	Upper specimen mounting block
VIV	Vortex-induced-vibration

Chapter 1: Introduction

1.1. Background

Flexible marine risers have transformed the oil and gas industry since their introduction in the 1970's by enabling the use of floating production units for oil extraction at deeper sea levels (up to 3,000 m) and at higher pressures (up to 140 MPa) in comparison to the conventional rigid structures. This has also allowed the oil and gas industry to maintain a supply of hydrocarbon to the global market despite global consumption increasing by over 50 % in the past 15 years (BP Global, 2017). Since the introduction of flexible marine risers, they have become widely used within the oil and gas industry; it is estimated that up to 99% of FPSO (floating, production, storage and offloading) vessels use flexible pipes to some extent. A schematic of flexible riser usage in an oil field is depicted in Figure 1.1.

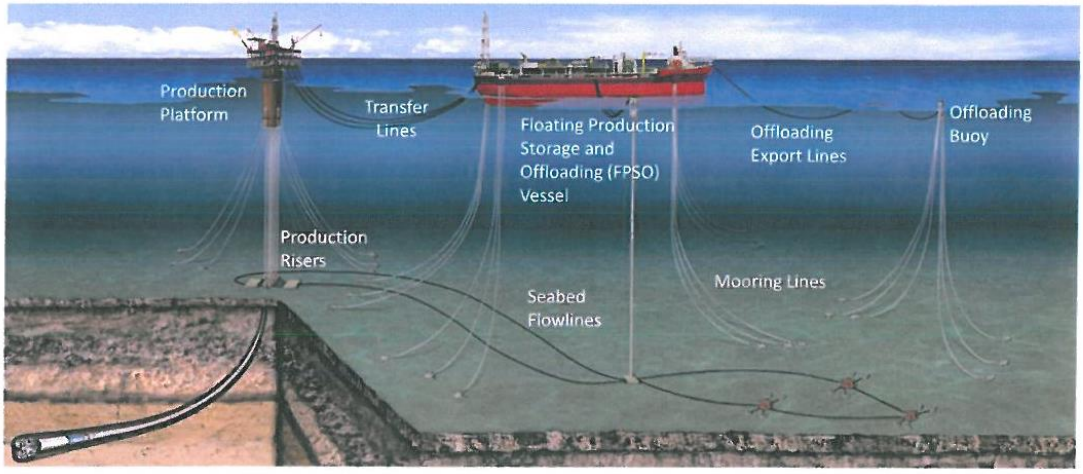

Figure 1.1. Deepwater production, storage and offloading system (MCS Kenny 2014).

Flexible marine risers are a key component in the delivery of offshore hydrocarbons from the seabed to seawater level, typically to a floating structure, such as a production platform or vessel. Flexible risers rely on a complex, composite cross-sectional architecture of helically-wound, interlocking steel wires and polymer layers to give a unique combination of high bending flexibility, axial and torsional stiffness and internal pressure resistance, as well as internal and external corrosion resistance (Sullivan, 2009) (see Figure 1.2). Failure of flexible risers due to fatigue is a major concern and better prediction of fatigue failure in the sub layers of flexible risers under service operating and extreme conditions is required, both in terms of (i) safety to the environment and personnel, and (ii) economic considerations. For example, the cost of a single flexible of 1000 m length is approximately €1.3 million. Failure of these sub layers due to fatigue is one of the main concerns during the service lifetime of the flexible riser. The effect of fretting wear (surface damage) and fretting fatigue (cracking) is a potential problem that is difficult to analyse and solve, so it is not presently considered during design of flexible risers. One of the layers, which is susceptible to fretting fatigue damage is the pressure armour (Burke and Witz, 1995). Fretting has a large potential to nucleate fatigue cracks in the pressure armour layer. For the inter-locking steel wires, micro-articulation of nub and groove mechanical contacts plays a key role in achieving this complex combination of exceptional mechanical and structural properties. Normal forces keep the nub and groove of the pressure armour in contact. The inner normal force is due to internal pressure in the flexible riser and the outer normal force is due to the tension of the tensile armour wire of the flexible riser (see Figure 1.3).

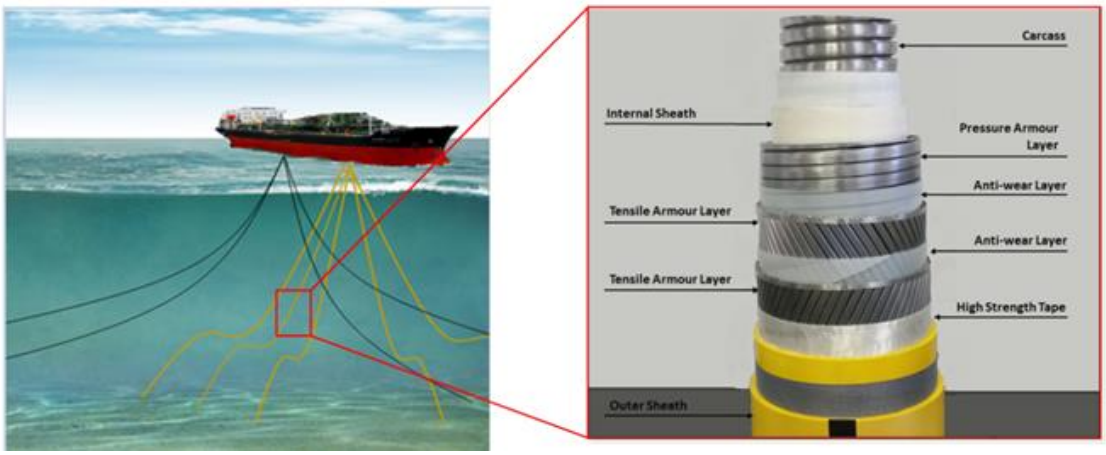

Figure 1.2. Schematic of flexible risers in an oil field and cross section of a flexible marine riser (courtesy of Wood Group Kenny).

Fretting action along the contact surfaces is produced by shearing loads due to bending of the riser. This gives rise to a micro-scale frictional contact phenomenon leading to micro-scale surface damage, typically, a combination of wear and fatigue micro-crack nucleation, ultimately leading to loss of function and fatigue cracking and failure. The predominance of wear or fatigue crack nucleation is dependent on a large number of mechanical and physical variables (Dobromirski, 1992) so that the development of a combined modelling and experimental capability is critical for a scientifically-based service life prediction (design) methodology. Fretting behaviour in the pressure armour layer of flexible marine risers has been recently identified as a critical aspect of riser design which requires further research (Lange and Berge, 2004). The American Petroleum Industry (API) design codes recommend a safety factor of 10 for fatigue design of pressure armour layers (API, 2009), to account for the uncertainties associated with fretting, among other factors. Løtveit and Bjaerum (1994) identified fretting of the pressure armour wire as a potential failure mode for flexible

marine risers. Since then little or no research has been published on this aspect of riser design despite significant advances in the understanding of fretting more generally, e.g. (Hills, 1994).

(a)

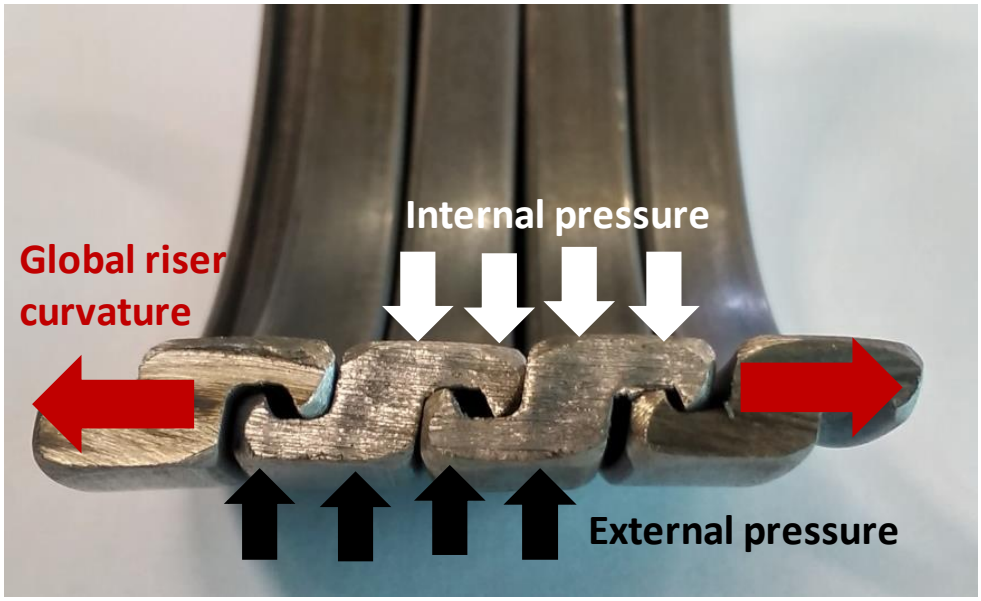

(b)

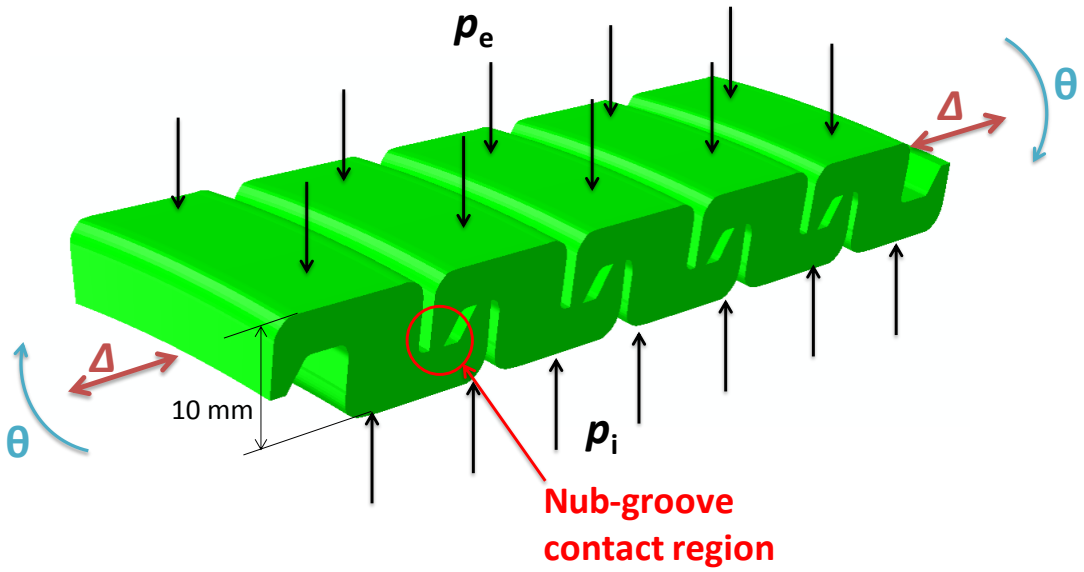

Figure 1.3. Schematics of loading conditions on the pressure armour layer; Δ - relative slip between wires; p_e - external pressure on the layer; p_i - internal pressure on the layer; θ – global riser bending.

Fretting contact conditions can be classified according to slip regime (Dobromirski, 1992), depending on the slip amplitude as follows: (i) gross slip (for limiting friction conditions), (ii) partial slip (below limiting friction) and (iii) stick regime. The slip regime depends specifically on the applied combination of normal (clamping) load and tangential load or displacement. In the case of pressure armour layers, the normal load is primarily due to internal and external fluid pressures (hydrocarbon and hydrostatic) and the tangential load (displacement) is due to bending moment, axial load, torque or a combination of all three, due to vessel motions, wave and current effects on the riser deformation.

Glaeser (1981) reported that billions of dollars could be saved if wear and fatigue life of engineering components could be improved. Since then great improvements have been made in the knowledge of fretting wear and fatigue performance of components, such as spline couplings, used in aerospace engineering (Ding et al., 2007a; Wavish et al., 2009), gas turbine dovetail joints (Ruiz et al., 1984), steel wire ropes (Cruzado et al., 2010) and other industrial applications. The problem of fretting fatigue in flexible marine risers has received relatively little attention. Féret and Bournazel (1987) presented a theoretical approach to calculate stresses, contact pressures and slip between tensile armour layers of flexible pipes under axisymmetric loading. However, the issue of fretting of the pressure armour wire is of concern to the oil and gas industry; Burke and Witz (1995) presented an excellent review of the problem at an industrial conference. More recently, Perera et al. (2007) presented an experimental method for fretting of the pressure armour layer of unbonded flexible pipes.

1.2. Framework for design tool for fretting in flexible marine risers

A key design challenge for pressure armour layers in flexible risers is the determination of the optimum nub-groove contact geometry and loading conditions for resistance to fretting crack nucleation. However, this requires the development of a combined experimental-computational methodology to establish the relevant material tribological characteristics (viz. coefficient of friction and wear coefficient evolutions and dependencies on stroke-load combinations), fatigue characteristics (low- and high-cycle fatigue), as well as an identification of the relevant local loading conditions (contact pressure or load, tangential stroke or slip, substrate stresses) for representative global (riser) loads, viz. bending moment, axial load and external and internal pressure conditions. A framework for the formulation of a fretting design tool for flexible marine risers developed in this work is represented in Figure 1.4; an additional key aspect here is a riser dissection process to establish the relevant contact geometry, which is of critical importance. Details on each aspect of this methodology will be outlined in subsequent chapters.

1.3. Aims and objectives

The primary aim of this research is to characterise and simulate fretting behaviour of pressure armour nub-groove contacts in flexible marine risers, in order to develop a framework for design of flexible marine risers against fretting. The key elements to this work are:

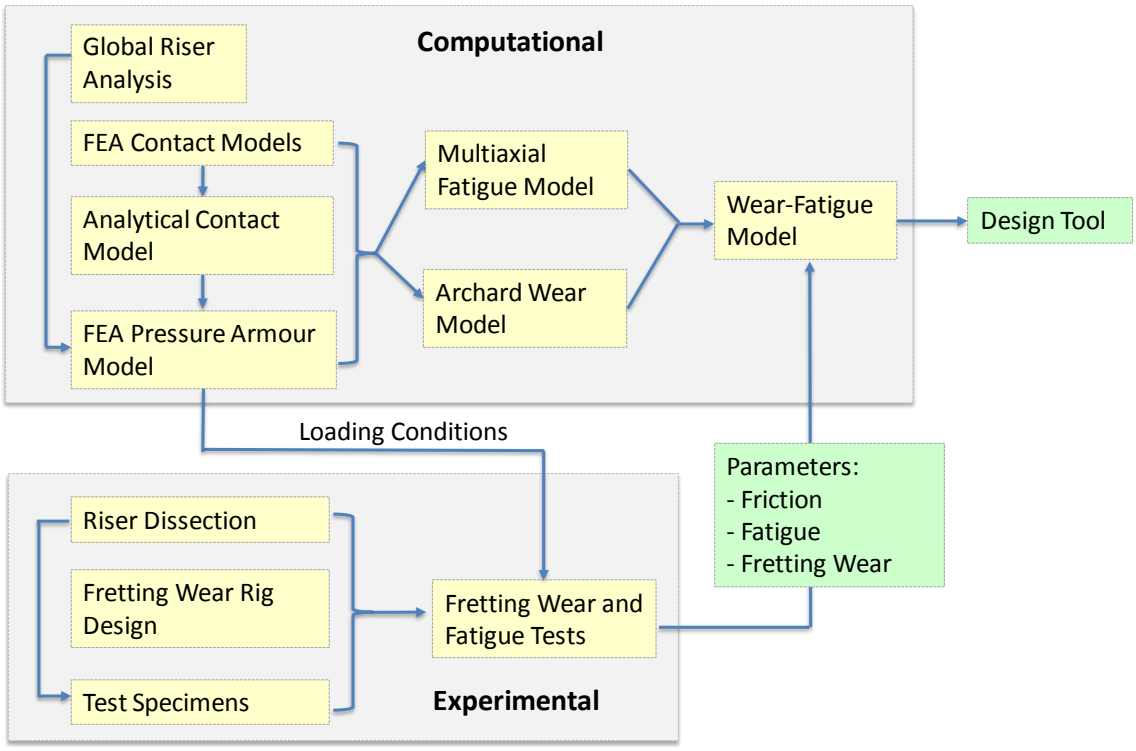

Figure 1.4. Flowchart representation of the framework for the development of a flexible riser design tool.

1. A key objective is to experimentally characterise the mechanical and tribological properties of pressure armour material under representative loading conditions. These tests will also seek to investigate the effects of contact conformity, contact pressure and stroke on the gross-slip fretting behaviour of dry and grease-lubricated cylinder-on-flat contacts.
2. Global dynamic analysis of flexible risers to identify local bending (curvature) and load time histories for typical design load risers.
3. The development of a frictional contact finite element model for the nub-groove contact including fretting fatigue crack initiation life prediction using a multiaxial fatigue model is also a key objective. The effect of fretting wear on calculated fretting fatigue crack initiation life will be investigated using

finite element adaptive meshing techniques. A surface damage parameter combined with a multiaxial fatigue parameter will be used to predict the effect of wear on fretting fatigue predictions.

4. Develop a fretting wear test rig at NUI Galway to allow measurement of coefficient of friction and wear coefficient under representative conditions for flexible risers.
5. Implementation of the framework outlined in Figure 1.4 in a realistic riser design case study. This will allow, for the first time, fretting wear and fatigue analysis to be conducted for a real-life riser application, including global-local dynamic riser analysis.
6. The development of a computationally efficient fretting fatigue life design tool to be used in the design of flexible marine risers against fretting is a key goal of this work. This design tool will need to simulate fretting wear and calculate the predicted fretting fatigue life for any geometry and loading conditions faster than the alternative, finite element method, while retaining the accuracy of a finite element model. This is achieved through optimisation techniques and cycle jumping for wear simulations. This will provide designers with a tool for detailed fretting analysis of frictional contacts and geometry and loading optimisation.

1.4. Layout of thesis

Chapter 2 contains a detailed background and review of the literature relevant to this research work, incorporating descriptions of frictional contact mechanics modelling, as well as wear, fatigue and fretting. Chapter 2 also discusses experimental

methodologies employed by other researchers to investigate the wear, fatigue and fretting performance of materials. Finally, a discussion on modelling of flexible marine risers and the key areas to be addressed in this thesis will be presented.

Chapter 3 discusses the design of a new fretting rig in NUI Galway, beginning with a review of methods employed by other researchers to experimentally investigate fretting behaviour. This review examines specimen geometry and alignment, methods of controlling and generating reciprocating (tangential) displacement and methods of applying normal loading. The requirements for the new test rig are outlined. Details of the development of the new test rig are given, including the design, drive line and actuator, specimen geometry and application of normal load, measurement of displacement and tangential force, control of the test rig, data acquisition and postprocessing.

The experimental characterisation of pressure armour material is outlined in Chapter 4. This includes the dissection of a riser to provide geometric and material details for computational models, as well as specimens for monotonic tensile and low-cycle fatigue tests. Experimental tests conducted on pressure armour raw material (before being drawn and cold formed into the pressure armour profile) on the new NUI Galway fretting test rig are discussed. The effect of grease lubricant on the fretting behaviour of a cylinder-on-flat fretting configuration is also discussed in Chapter 4. Dry and grease-lubricated fretting tests were conducted at the University of Nottingham. The effects of contact conformity (i.e. different possible riser nub-groove contact geometry designs), contact pressure, displacement amplitude and lubrication on the fretting behaviour of representative cylinder-on-flat contacts are investigated. Results from the NUI Galway fretting rig and fretting tests conducted at the University of Nottingham are compared.

A finite element modelling methodology for frictional contact is outlined in Chapter 5. This methodology is calibrated against analytical solutions for contact mechanics and implemented in an axisymmetric riser model. The axisymmetric riser model is designed to focus on the nub-groove frictional contact region in the pressure armour layer. A plasticity material model incorporating non-linear kinematic hardening (NLKH) based on experimental results from Chapter 4 is introduced. Fatigue crack initiation life predictions are made using the multi-axial critical plane Smith-Watson-Topper (SWT) parameter. A three-dimensional riser model is developed to investigate the effect of global riser bending, from global riser dynamic analysis, on local pressure armour nub-groove fretting conditions.

A combined fretting wear-fatigue model is described in Chapter 6. An adaptive meshing technique is implemented to explicitly model wear in a cylinder-on-flat finite element model. The effect of wear on substrate stresses and predicted life to crack initiation is examined. A surface damage parameter, D_{fret}, is combined with the SWT multiaxial fatigue parameter to accurately predict the beneficial effect of fretting wear on fatigue crack initiation predictions in the gross slip regime. This provides a computationally efficient design tool for fretting in the pressure armour layer of flexible marine risers.

Chapter 7 presents a case study of different flexible marine riser geometries in a hybrid riser configuration under various extreme sea-state loading conditions. A global-local modelling methodology is implemented to predict the critical locations for fretting damage in the risers. Number of cycles to crack initiation and total life predictions are calculated.

Chapter 8 presents an analytical design tool, EASY-FRET (Engineering Analysis SYstem for FRETting). This design tool can model frictional fretting contact for any contact geometry and loading conditions under partial or gross slip regimes. It also simulates wear and calculates fretting fatigue life using the critical plane approach of the multi-axial SWT fatigue parameter. Validation of EASY-FRET design tool results against finite element predicted pressure and stress distributions as well as predicted fatigue life to crack initiation are presented. This design tool provides a computationally efficient method of modelling fretting wear and fatigue and for geometry optimisation against fretting damage.

Chapter 9 outlines the conclusions of this work and overall discussions are provided. Recommendations for future work are also made.

Chapter 2: Literature review

2.1. Introduction

The design and characterisation of the fretting behaviour of a component require a combined experimental-computational approach. This will establish the relevant tribological (friction and fretting wear) and mechanical (fatigue) characteristics, as well as the identification of relevant local contact loading conditions (contact pressure and tangential stroke) for representative contact geometries. Such information is required to improve the current state of knowledge with regard to fretting in the pressure armour nub-groove contact of flexible marine risers and hence, to provide riser designers with a design framework for the accurate prediction of fretting fatigue service life of the nub-groove component of risers including the effects of wear.

The following review and discussion of the literature focus on the primary factors affecting fretting wear and fatigue performance of materials. In particular, this chapter presents the technical background of the experimental characterisation and computational models developed in this thesis and a review of the literature relevant to flexible marine riser modelling and characterisation. Firstly, friction is introduced and various methods of measuring coefficient of friction in fretting applications is reviewed. In Section 2.3, contact mechanics is reviewed, including known pressure distributions for three general contact mechanics cases, generalised solutions are also presented and the effect of stress gradient is discussed. Methods of simulating wear are reviewed in Section 2.4. Fatigue of metals will be discussed, including fatigue indicator

parameters, fatigue mechanisms and notch fatigue analogy for contact mechanics. A review of fretting is presented in Section 2.6, including numerical and analytical methods for modelling fretting fatigue and fretting wear. Section 2.7 reviews experimental characterisation of the fretting behaviour of materials, with a particular focus on rig development. The modelling and experimental techniques employed by other researchers and industry for flexible marine risers are reviewed in Section 2.8. The final section of this chapter highlights how this thesis will build upon the current literature to improve the understanding of fretting in the pressure armour nub-groove contact of flexible marine risers.

2.2. Friction

Friction is defined as the resistance encountered in one body when moving over another. Leonardo da Vinci was one of the first to study the tribology of sliding (dry) friction. However, the laws of sliding friction are named after Amontons, who described them in 1699. The laws of sliding friction are as follows:

- Tangential force (Q) is proportional to the normal load (P):

$$Q = \mu P \tag{2.1}$$

where μ is the frictional coefficient.

- Friction force is independent of the apparent area of contact.

Coulomb added a third law in 1785:

- Friction force is independent of sliding velocity.

It has been observed that the tangential force to initiate sliding is greater than the sliding tangential force. Therefore, the coefficient of static friction is greater than the coefficient of dynamic friction. Once steady-state sliding is achieved, it is found that the coefficient of friction is independent of the sliding velocity for most situations.

In fretting tests, the cyclical tangential behaviour is often plotted in the form of fretting loops i.e. graph of tangential force versus tangential displacement with respect to number of cycles. Examples of fretting loops are presented in Figure 2.1. The shape of the fretting loop depends on various parameters, such as the test rig stiffness, material elastic modulus and the geometry of the wear scar during testing.

Traditionally, the coefficient of friction (CoF) used by researchers was based on the Coulomb-Amontons' friction law. This method is applicable for an idealised experimental fretting loop, as indicated in Figure 2.1(a), with CoF given by:

$$CoF = \frac{Q^*}{P} \tag{2.2}$$

where Q^* is the measured tangential (frictional) force during sliding and P is the applied normal load.

Fouvry et al. (2004) observed that the tangential force does not remain constant through the sliding part of the fretting loop, as illustrated in Figure 2.1(b). It was suggested (Fouvry et al., 2004) that the peaks at the end of each sliding section of the fretting loops are caused by ploughing which occurs during fretting when material build-up occurs at the wear scar edges. To minimise the influence of the ploughing effect on calculation of CoF, Fouvry et al. (2004) proposed that the energy dissipated per cycle could be used to define a coefficient of friction which is more representative

of the overall behaviour of the contact. The energy coefficient of friction (ECoF) (Fouvry et al., 2004) is defined as follows:

$$ECoF = \frac{E_d}{4P\delta *} \tag{2.3}$$

where E_d is the dissipated energy per cycle (area of the fretting loop, see Figure 2.1(b)) and $4\delta *$ is the total sliding distance per cycle (Fouvry et al., 2004). The maximum contact slip, δ*, can be derived by measuring the displacement at zero force, as illustrated Figure 2.1.

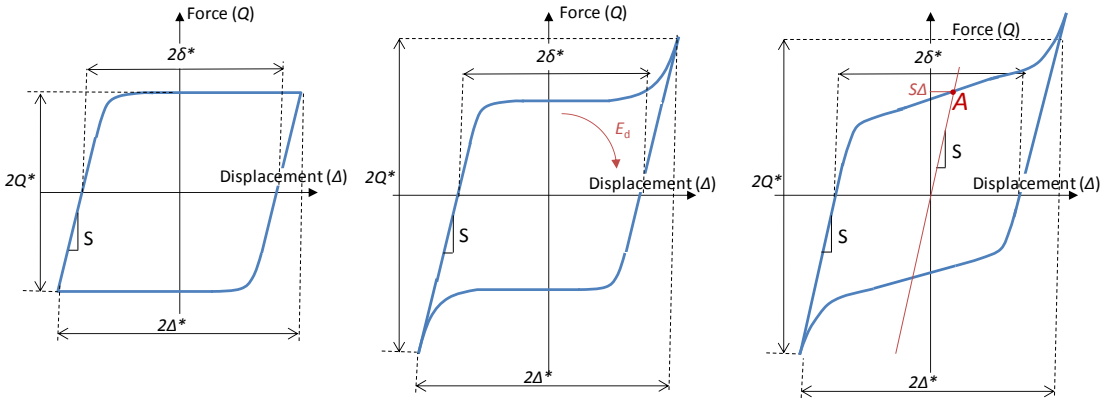

(a) (b) (c)

Figure 2.1. Schematic diagram of (a) an ideal fretting loop in the gross slip regime, (b) fretting loop with high tractional force peak at the ends of gross slip, and (c) fretting loop demonstrating the method of calculating GICoF, illustrating parameters defined in the text.

Jin et al. (2016) observed that the tangential force increases during the whole gross sliding stage and reaches a maximum at the ends of the stroke, which resembles a hook-like feature (see Figure 2.1(c)). A new method to determine a coefficient of friction, which is independent of system stiffness and geometry evolution of the wear

scars, was proposed (Jin et al., 2016). The geometrically independent coefficient of friction (GICoF) is defined as the CoF (Q^*/P) at the point where the slope of the wear scar is zero (marked *A* in Figure 2.1(c)); this point in the fretting loop is that which also lies on the line $Q = S\Delta$ (as illustrated in Figure 2.1(c)), where S is the stiffness of the fretting rig, as described by Jin et al. (2016).

2.3. Contact mechanics

2.3.1. Introduction

Contact mechanics is the study of the deformation of solids in contact. Hertz (1882) studied contact stresses of two normally-loaded, non-conforming, elastic solids, as described in Johnson (1985). The main assumptions of Hertzian contact are:

- Surfaces are continuous and non-conforming.
- The strains are small.
- Surfaces are frictionless so that only normal pressure is transmitted between them ($q = 0$, where q is the shear traction due to friction).
- The bodies are infinite elastic half-spaces ($a \ll l$). i.e. the dimension of the contact (a) is small in comparison to the dimensions of each body length, l, i.e. distance in the y-direction in Figure 2.2.
- The dimension of the contact (a) is small in comparison to the radii of the curvature of the surfaces i.e. $a \ll R_i$, ($i = 1, 2$).

Solutions for the two-dimensional (2D) elastic half-space case of cylinders in contact and the three-dimensional (3D) case for two contacting spheres are given by the

Hertzian theory. The flat punch with round edges on flat contact has been examined by Jäger (2002) and Ciavarella and co-workers (Ciavarella et al., 1998; Ciavarella and Macina, 2003).

2.3.2. Sliding cylinder-on-flat

When two parallel cylinders are in contact with each other, they deform elastically, producing a contact area. This deformation is shown in 2D schematically in Figure 2.2.

Hertz developed an analytical solution for the contact pressure and width for cylinder-on-cylinder contacts. These can also be used for cylinder-on-flat contacts, where the flat can be considered as a cylinder of infinite radius. Under normal loading the bodies deform, resulting in a contact width 2*a* (Figure 2.2), where *a* is given by:

$$a = \sqrt{\frac{4PR^*}{\pi E^*}} \tag{2.4}$$

R^* and E^* are the compound radius of curvature and modulus, respectively, given by:

$$R^* = \frac{1}{R_1} + \frac{1}{R_2} \tag{2.5}$$

$$\frac{1}{E^*} = \frac{1-\nu_1^2}{E_1} + \frac{1-\nu_2^2}{E_2} \tag{2.6}$$

where R_i, ν_i and E_i are the radius of curvature, Poisson's ratio and Young's modulus of body *i*, respectively, and i = 1, 2. The contact pressure distribution for two cylinders is given by:

$$p(x) = p_0\sqrt{1-\left(\frac{x}{a}\right)^2} \tag{2.7}$$

where x is the horizontal distance from the centre of contact (see Figure 2.2). The contact pressure has an elliptical distribution with a maximum at the centerline (x = 0) and reducing to 0 at the contact edges, given by $-a \geq x \leq a$. The maximum pressure is given by p_0:

$$p_0 = \frac{2P}{\pi a} \tag{2.8}$$

where P is the applied normal load per unit length, as illustrated in Figure 2.2.

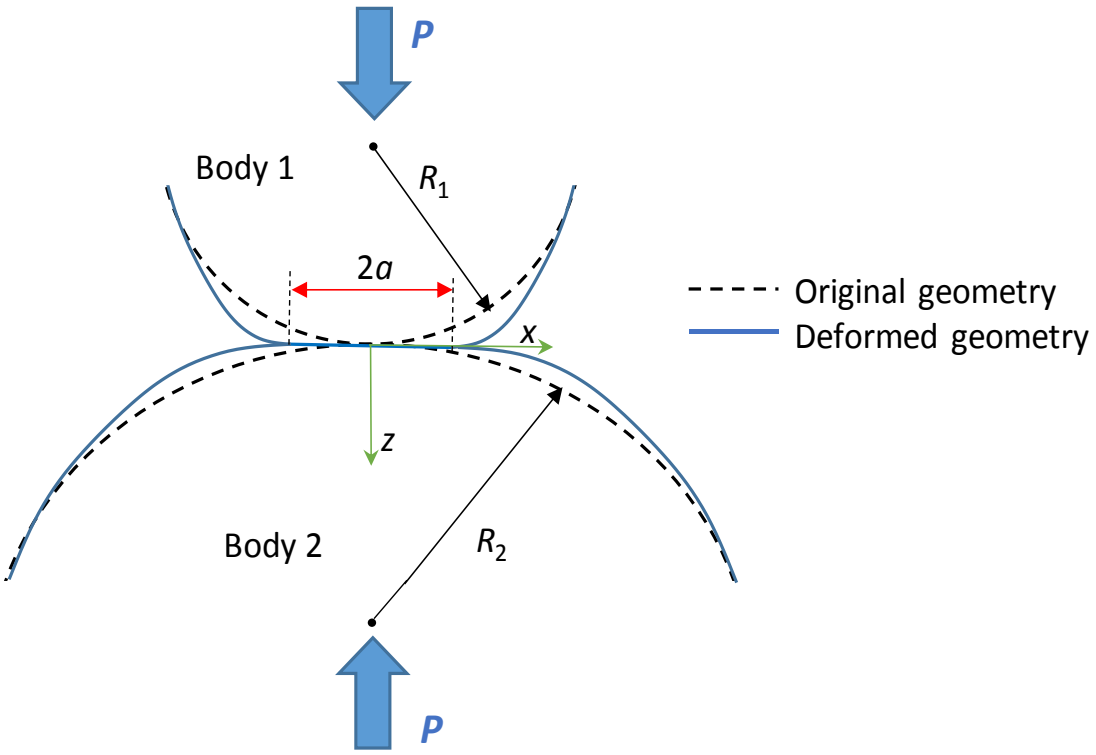

Figure 2.2. Schematic of two cylinders, of radii R_1 and R_2 in contact under normal load, P, giving a contact width of $2a$.

For a case of pure sliding, and assuming Coulomb-Amontons' Law (described above) for sliding friction, the tangential traction is given by:

$$q(x) = \mu p(x) \tag{2.9}$$

2.3.3. Partial slip cylinder-on-flat

When a tangential force, Q, with magnitude less than the limiting frictional force, μP, is applied to two bodies in contact under normal loading, no gross sliding motion takes place. A stick region occurs in the centre of the contact with slip regions on the edges of contact (as illustrated in Figure 2.3). For the stick region ($-c \leq x \leq c$), $q(x) < \mu p(x)$, resulting in no relative motion between the bodies within this region; in the slip zones $c \leq |x| \leq a$, $q(x) = \mu p(x)$. Separately, Cattaneo and Mindlin (1938, 1949) combined normal and tangential loading of a Hertzian contact, to derive an analytical solution for the partial-slip case.

The magnitude of the tangential force (Q) determines the size of the stick region. The stick region for partial-slip of contacting cylinders is given by:

$$\frac{c}{a} = \sqrt{1 - \frac{Q}{\mu P}} \tag{2.10}$$

where c is the contact semi-width of the stick region, Q is the tangential force applied (see Figure 2.3(a)) and a, P and μ are as described for the sliding cylinder-on-flat earlier (Section 2.3.2 and Figure 2.2).

The contact shear acting on the stick region ($-c \leq x \leq c$) is given by $q''(x)$:

$$q''(x) = -\frac{c}{a}\mu p_0 \sqrt{1-\frac{x^2}{c^2}} \tag{2.11}$$

The contact shear acting in the slip zones, ($c \le |x| \le a$) is given by $q'(x)$:

$$q'(x) = \mu p_0 \sqrt{1-\frac{x^2}{a^2}} \tag{2.12}$$

Equations (2.11) and (2.12) ensure that the stick-slip conditions for partial slip are satisfied. Contact shear using superposition of the load distributions for the stick and slip zones is given by:

$$q(x) = q'(x) + q''(x) \tag{2.13}$$

Contact pressure and shear traction distributions for a cylinder-on-flat gross and partial-slip cases are shown in Figure 2.3(b). The cylinder radius is 6 mm, with a CoF of 0.8, under 50 N/mm normal load (P) and a tangential force (Q) of 25 N (for the partial-slip case).

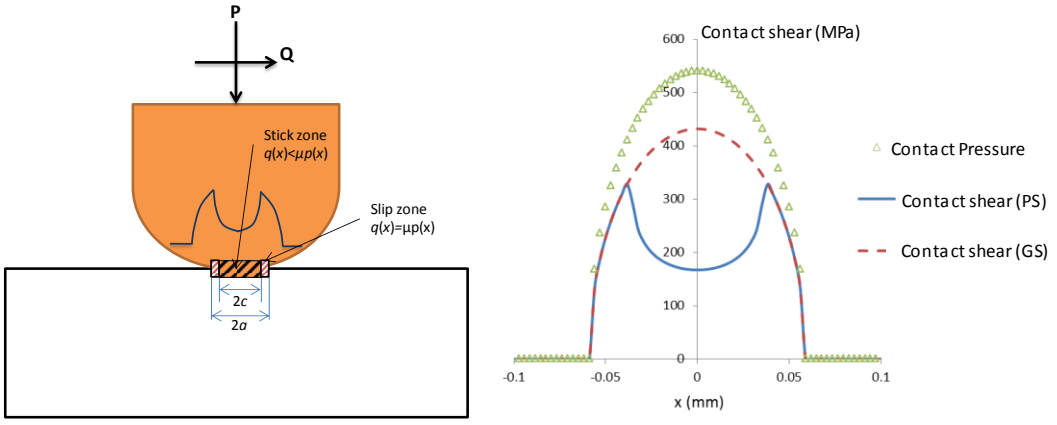

(a) (b)

Figure 2.3. (a) Schematic of the stick-slip zones for cylinder-on-flat partial slip regime and (b) contact pressure and shear distributions for a cylinder-on-flat gross- and partial-slip cases.

2.3.4. Punch-on-flat

The contact pressure distribution for a 2D case for a flat punch-on-flat contact, as shown in Figure 2.4(a), under normal loading conditions is given by (Johnson, 1985):

$$p(x) = \frac{P}{\pi\sqrt{a^2 - x^2}} \tag{2.14}$$

This pressure distribution has singularities at the contact edges i.e. $x = \pm a$ (see Figure 2.4(b)).

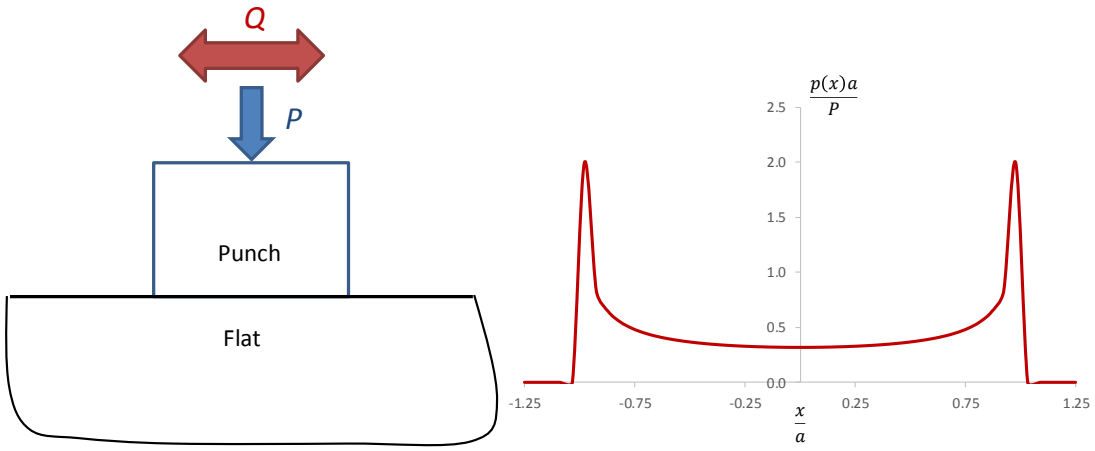

(a) (b)

Figure 2.4. (a) Schematic of a punch-on-flat contact, (b) normalised contact pressure distribution of punch on flat contact.

The pressure singularity at the contact edges leads to stress singularity also. For real materials, however, plasticity will occur at the contact edges due to these high localised stresses. Mugadu et al. (2002) presented a solution for the stress state at the contact edge for complete contacts, punch-on-flat, for example, using an asymptotic approach. The stress state at the apex is defined in the following:

$$\sigma_{ij}(r,\theta) = \frac{K}{r^{1-\lambda}} f_{ij}(\theta) \tag{2.15}$$

where K is a generalised stress intensity factor related to the overall geometry, $\lambda(f, \varphi)$ is the eigenvalue and $f_{ij}(\theta)$ is the eigenfunction; r, θ *and* φ are defined in Figure 2.5.

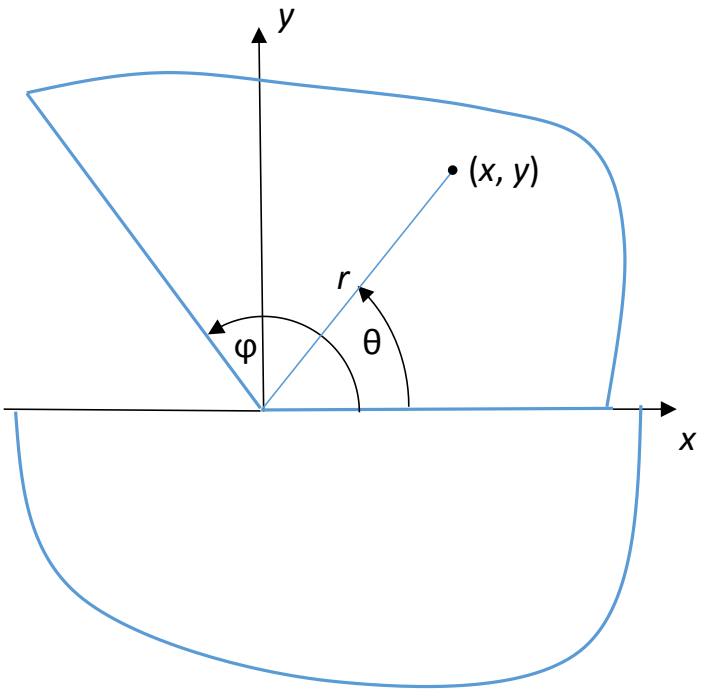

Figure 2.5. Apex of an angled flat-on-flat contact.

2.3.5. Crossed-cylinders

If two cylinders of equal radii, R, are in contact and lie on perpendicular axes (as shown in Figure 2.6(a)), the contact problem is equivalent to the contact between a sphere of radius, R and an elastic half-space (as shown in Figure 2.6(b)) (Johnson, 1985). The contact area will be circular, with a radius of a, given by:

$$a = \left(\frac{3PR}{4E^*}\right)^{\frac{1}{3}} \tag{2.16}$$

where E^* is given by Equation (2.6) and P is the normal load. The pressure distribution is given by:

$$p(r) = p_0 \sqrt{1 - \left(\frac{r}{a}\right)^2} \tag{2.17}$$

where r is the distance from the centre of contact and p_0 is the maximum pressure given by:

$$p_0 = \frac{3P}{2\pi a^2} \tag{2.18}$$

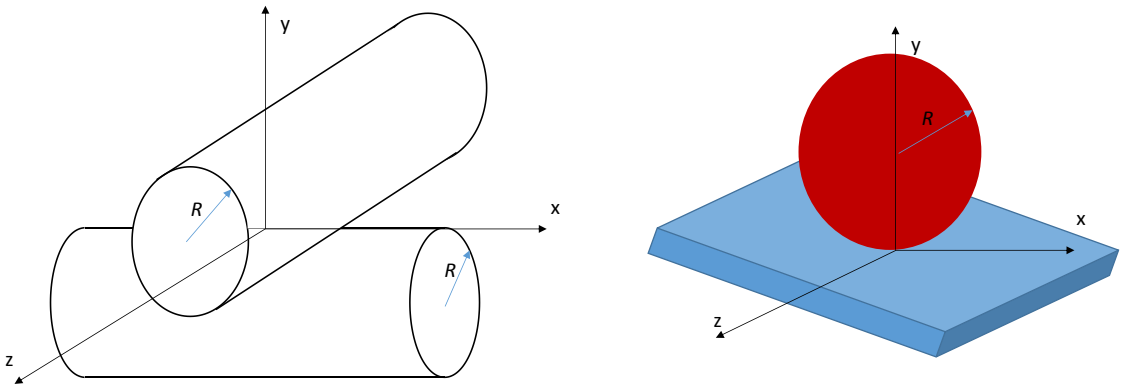

(a) (b)

Figure 2.6. Schematic of (a) crossed-cylinders and (b) sphere-on-flat contacts.

2.3.6. General solution

In general, contact stresses are transmitted through normal pressure and shear loading. A schematic of a generalised loading case is shown in Figure 2.7. For both normal pressure distribution ($p(s)$) and tangential load distribution ($q(s)$) the subsurface

stress components at a point (s, z) are given by integrating over the loaded region (see Figure 2.7).

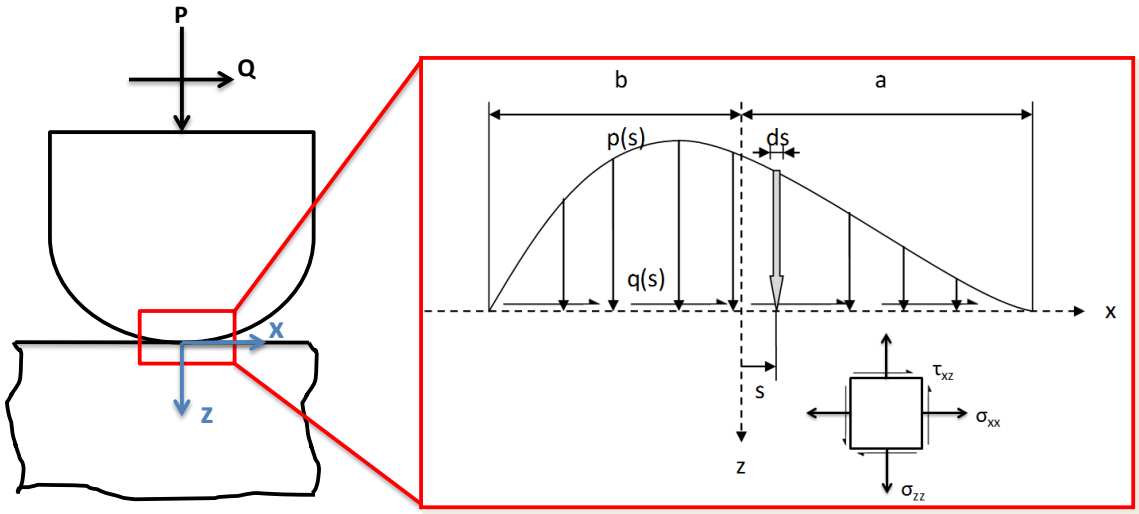

Figure 2.7. An elastic half plane loaded over a distance $-b < x < a$ by a normal pressure $p(s)$ and tangential traction $q(s)$ distributed in an arbitrary manner.

Substrate stresses are obtained through the application of elasticity theory (Mossakovski, 1954; Mossakovskii, 1963) for concentrated normal and tangential loads at distance s from the point $x = 0$ acting on an element of width ds and integration over the contact region for distribution of normal and shear traction. The two-dimensional Cartesian stress components are given by (Johnson, 1985; Switek, 1984):

$$(\sigma_{xx}) = -\frac{2z}{\pi}\int_{-b}^{a}\frac{p(s)(x-s)^2 ds}{\left\{(x-s)^2+z^2\right\}^2} - \frac{2}{\pi}\int_{-b}^{a}\frac{q(s)(x-s)^3 ds}{\left\{(x-s)^2+z^2\right\}^2} \tag{2.19}$$

$$(\sigma_{zz}) = -\frac{2z^3}{\pi}\int_{-b}^{a}\frac{p(s)ds}{\left\{(x-s)^2+z^2\right\}^2} - \frac{2z^2}{\pi}\int_{-b}^{a}\frac{q(s)(x-s)ds}{\left\{(x-s)^2+z^2\right\}^2} \tag{2.20}$$

$$(\tau_{xz}) = -\frac{2z^2}{\pi}\int_{-b}^{a}\frac{p(s)(x-s)ds}{\left\{(x-s)^2+z^2\right\}^2} - \frac{2z}{\pi}\int_{-b}^{a}\frac{q(s)(x-s)^2 ds}{\left\{(x-s)^2+z^2\right\}^2} \tag{2.21}$$

where *a*, *b*, *z*, *s*, *ds* and *x* are illustrated in Figure 2.7.

Figure 2.8 presents the effect of depth (*z*) below the contact surface on (a) tensile and (b) shear stress distributions for a punch-on-flat gross-slip contact (Switek, 1984) calculated using Equations (2.14) and (2.19) - (2.21). High values of trailing edge tensile stresses are observed close to the surface; similar results for trailing edge tensile stresses also occur in cylinder-on-flat contact. High stress gradients can also be seen, i.e. the stress decreases rapidly with depth (*z*). Figure 2.8 also shows that the stress gradient depends on the contact width, this is known as a contact size effect and will be discussed later.

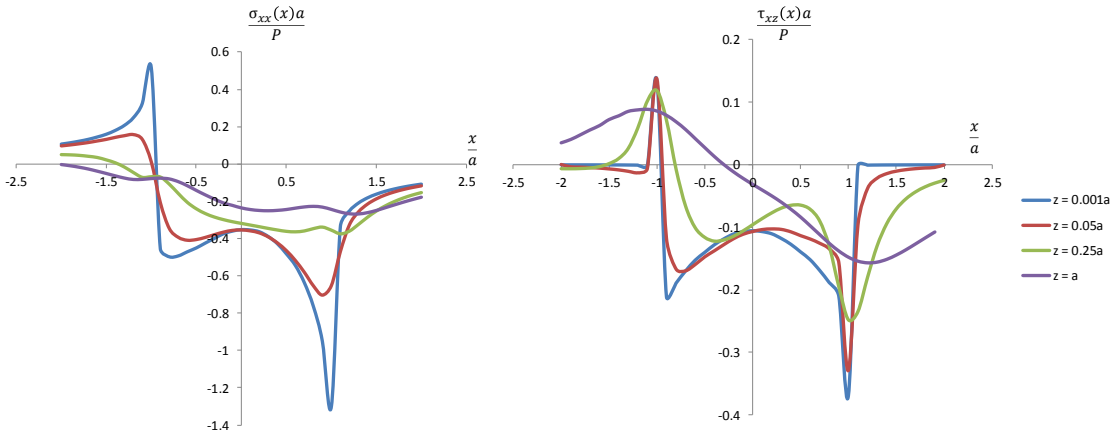

Figure 2.8. Normalised substrate stress distributions at depth z below the contact surface for punch-on-flat contact.

2.4. Wear

2.4.1. Introduction

Wear occurs when two contact surfaces moving over each other cause the progressive removal of particles from the surface. Bhushan and Gupta (1991) divided

wear into six main categories: adhesion, abrasion, fatigue, erosion, corrosion and electrical arc. Adhesive wear occurs when wear debris transfers from one surface to another. In many engineering applications, surfaces slide over each other and the resulting wear is associated with the presence of hard particles. This wear is called abrasive wear (Hutchings, 1992). It has been argued (Godet, 1984) that mechanisms such as adhesion and abrasion are only particle detachment mechanisms, whereas a real wear process should be governed by both particle detachment and elimination of wear particles. The concept of "third body flow" is described as the process where particles transport from inside the contact to outside; this takes into account the effect of the debris layer on wear.

2.4.2. Archard wear equation

The Archard wear law (Archard, 1953) is the most commonly used wear law and it has been shown to successfully predict sliding wear across a wide range of material (Archard and Hirst, 1956) and loading conditions. It is based on the assumptions that contact between two surfaces occurs where asperities touch and that the true area of contact is equal to the sum of all the individual asperity contact areas. This area is proportional to the normal load, and it is assumed that local deformations of asperities are plastic (Hutchings, 1992).

The normal load, δP, supported by a single asperity contact, which is assumed to be circular in plan view with radius, a, is given by:

$$\delta P = p_{yield} \pi a^2 \tag{2.22}$$

where p_{yield} is the yield pressure for the plastically deforming asperity. Continuous sliding leads to the individual asperities going in and out of contact continuously. Wear occurs when fragments of material from the asperities detach. The volume of material removed by wear, δV, is assumed to be proportional to the cube of the contact radius, a. This implies that the shape of the wear particle is independent of its size. However, for the formulation of the Archard wear equation, the volume can be taken as hemispherical, with a radius of a. Therefore, the volume of material removed is:

$$\delta V = \frac{2\pi a^3}{3} \tag{2.23}$$

The average volume of material worn away per unit sliding distance due to sliding one asperity pair through a distance of $2a$ (i.e. sliding the asperity pair in and out of contact), is given by:

$$\delta Q = \frac{\kappa(\delta V)}{2a} = \frac{\kappa \pi a^3}{3a} \tag{2.24}$$

where κ is the proportion of asperity contacts that give riser to wear particles. The overall wear volume per unit sliding distance (Q) and total normal load, P, are given by:

$$Q = \sum \delta Q = \frac{\kappa}{3} \sum \pi a^2 \tag{2.25}$$

$$P = p_{yield} \sum \pi a^2 \tag{2.26}$$

Hence:

$$Q = \frac{\kappa P}{3 p_{yield}} \tag{2.27}$$

The factor of 1/3 is combined with the proportionality constant, giving $K = \kappa/3$, and it is assumed that the yield pressure of the asperities is equal to the hardness of the material, H, giving:

$$Q = K\frac{P}{H} \tag{2.28}$$

In fretting, the wear volume per unit distance slid, Q, is given by:

$$Q = \frac{V}{4N\delta^*} = K\frac{P}{H} \tag{2.29}$$

where V is the wear volume, K is the dimensionless wear coefficient, N is the number of cycles and with a contact slip amplitude of δ^*, as shown in Figure 2.1. The term K/H is referred to as the dimensional (units: MPa^{-1}) wear coefficient (k).

One limitation of this equation is that it has been shown that the Archard wear equation is predicated on sliding conditions and therefore, is not strictly applicable to partial slip conditions (Fouvry et al., 2003).

2.4.3. Energy wear method

Fouvry et al. (2003) have proposed an alternative method of predicting wear using dissipated energy. In this method, the interfacial shear work is considered to be the controlling parameter in the calculation of wear volume. The advantage of this method over the Archard wear equation is that the energy wear method can be used across a range of fretting load-stroke combinations and slip regimes (especially partial slip, for example). The energy wear method is described by the following equation:

$$V = \alpha \sum E_d \tag{2.30}$$

where α is the dimensional (units: MPa^{-1}) wear coefficient, $\sum E_d$ is the accumulated dissipated frictional energy. It can be shown that, in the gross slip regime, the Archard equation and energy method are equivalent for an appropriate choice of Archard coefficient, i.e. $K = \frac{H\alpha}{\mu}$. However, the two methods do not give the same results in the partial slip regime unless K/H is modified to be a function of contact slip.

2.5. Fatigue of metals

2.5.1. Introduction

ASTM (2013) defines fatigue as "the progressive, localised permanent structural change occurring in a material subjected to conditions which produce fluctuating stresses and strains at some point or points which may culminate as cracks". Under fatigue loading, failure of materials can be observed at loads less than the monotonic yield strength of the material.

Fatigue can be categorised into either high-cycle fatigue (HCF) or low-cycle fatigue (LCF), depending on the number of cycles to failure, N_f. The total life, N_f, is represented as the sum of the number of cycles to crack initiation, N_i, and the number of cycles for the crack to propagate to a detectable or critical length, N_P, where $N_f = N_i + N_P$.

2.5.2. Fatigue mechanisms

Metals contain numerous grains, each with its own mechanical and directional properties. Slip in grains has been observed under both monotonic and cyclic loading, but with different slip profiles; it was shown (Forsyth, 1969; Stephens et al., 2000) that both slip band intrusions and extrusions occur on the metal surface when it experiences cyclic loading. These slip band intrusions cause micro-scale stress concentrations, which lead to the development of cracks. It has been shown (Kennedy, 1963) that more slip lines occur and thicken as the number of load cycles increases for a pure polycrystalline nickel. It has been found that fatigue cracks grow from persistent slip bands (Forsyth, 1969). Fatigue cracks initiate in local slip bands followed by the two stages of fatigue crack growth: Stage I and Stage II (Forsyth, 1969) (see Figure 2.9). In Stage I, the micro-fatigue cracks tend to grow in a plane of maximum shear stress. In Stage II, as the cycle number increases, the fatigue cracks tend to grown along planes of maximum tensile stress. Finally, fracture occurs.

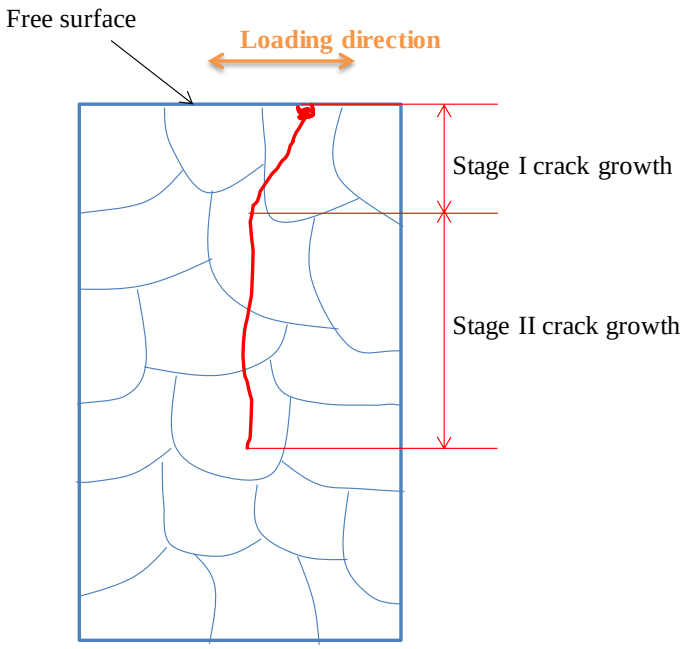

Figure 2.9. The two stages of crack growth.

2.5.3. Stress-strain based approaches

Wöhler (1858; 1860) was the first to carry out a systematic study on fatigue. A relationship between stress and fatigue life was observed; the stress range has a greater influence on fatigue life than the peak stress (Wöhler, 1870). From this work, S-N (stress Vs number of cycles to failure) curves were proposed to estimate fatigue lives; this S-N curve method is still used today. Goodman (1919, 1962) proposed a simplified theory relating the mean stress to fatigue life. Gerber (1984), Soderberg (1930) and Morrow (1930) proposed different relationships between the mean stress and alternating stress for a given fatigue failure lifetime (see Figure 2.10). The constant life line equations in the Haigh diagram (σ_a verses σ_m) proposed by Goodman, Gerber, Söderberg and Morrow are as follows:

Goodman: $$\frac{\sigma_a}{\sigma_e}+\frac{\sigma_m}{\sigma_{UTS}}=1 \quad (2.31)$$

Gerber: $$\frac{\sigma_a}{\sigma_e}+\left(\frac{\sigma_m}{\sigma_{UTS}}\right)^2=1 \quad (2.32)$$

Söderberg: $$\frac{\sigma_a}{\sigma_e}+\frac{\sigma_m}{\sigma_y}=1 \quad (2.33)$$

Morrow: $$\frac{\sigma_a}{\sigma_e}+\frac{\sigma_m}{\sigma_f}=1 \quad (2.34)$$

where σ_y is the yield stress, σ_{UTS} is the ultimate tensile stress, σ_f is the true fracture stress, σ_e is the endurance limit for a given life, typically infinite ($N_f = 10^6$ cycles), σ_a is the alternating stress and σ_m is the mean stress.

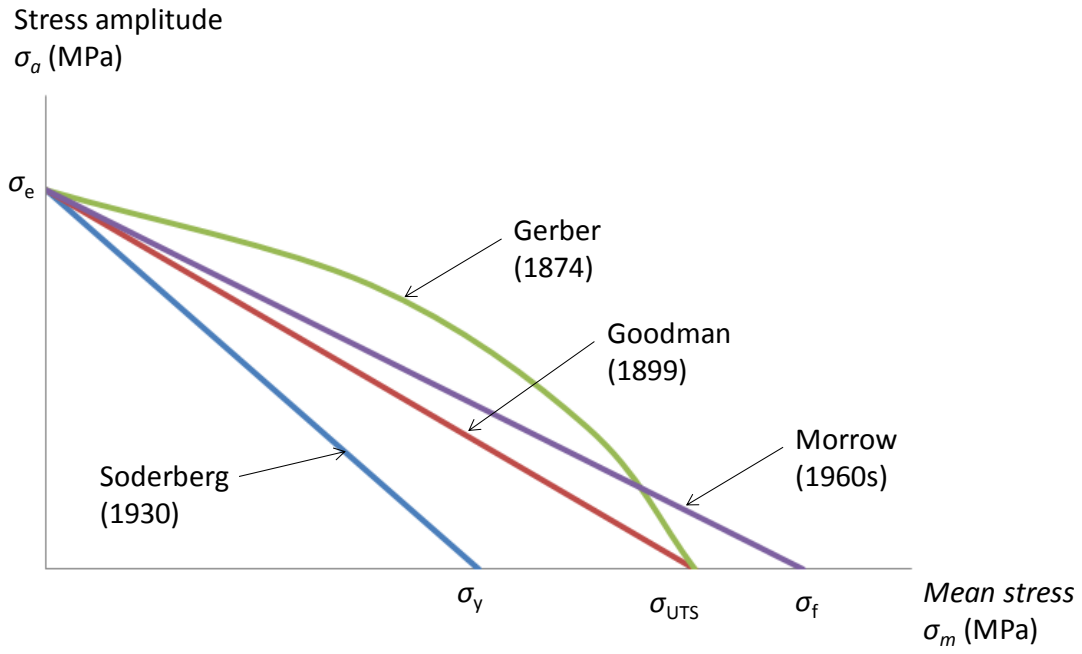

Figure 2.10. Constant life relationship between mean stress and alternating stress for a given fatigue failure lifetime by different researchers.

Basquin (1910) developed the stress-life approach, by observing a log-log relationship between stress amplitude and the fatigue life for high-cycle fatigue (HCF).

$$\frac{\Delta\sigma}{2} = \sigma'_f (2N_f)^b \tag{2.35}$$

where $\Delta\sigma$ is the stress range, σ'_f is the fatigue strength coefficient and b is the fatigue strength exponent.

At high amplitudes of cyclic stresses and strains, low-cycle fatigue (LCF) becomes the dominant fatigue regime. Due to the high strains in LCF, stress is no longer effective to characterise the material damage. Coffin (1954) and Manson (1954) formulated a relationship similar to Equation (2.35) between the plastic strain amplitude and the number of cycles to failure.

$$\frac{\Delta\varepsilon_p}{2} = \varepsilon'_f (2N_f)^c \tag{2.36}$$

where $\Delta\varepsilon$ is the plastic strain amplitude, ε'_f is the fatigue ductility coefficient and c is the fatigue ductility exponent.

By using Hooke's Law to express the stress range in terms of elastic strain range $\Delta\varepsilon_e$, the Basquin and Coffin-Manson relations were combined to provide a total strain-life approach. Thus, the total strain range can be related to the fatigue life as follows:

$$\frac{\Delta\varepsilon}{2} = \frac{\Delta\varepsilon_e}{2} + \frac{\Delta\varepsilon_p}{2} = \frac{\sigma'_f}{E}(2N_f)^b + \varepsilon'_f (2N_f)^c \tag{2.37}$$

where $\Delta\varepsilon$ is the total strain range.

Total fatigue damage is evaluated using different fatigue indicator parameters (FIPs). One such FIP, the Smith-Watson-Topper (SWT), was proposed by Smith et al. (1970) and can be derived from (Equation (2.37). SWT is given as:

$$SWT = \sigma_{\max}\frac{\Delta\varepsilon}{2} = \frac{(\sigma'_f)^2}{E}(2N_f)^{2b} + \sigma'_f\,\varepsilon'_f (2N_f)^{b+c} \tag{2.38}$$

where σ_{max} is the maximum normal stress in a fatigue cycle.

The above SWT approach was developed for uniaxial fatigue cases where the largest principal stress is much greater than the other principal stresses. However, fatigue is a multiaxial problem in most engineering applications. There have been many efforts to develop a scientific approach to multiaxial fatigue. Brown and Miller (1973) first suggested the combined use of maximum shear strain range and tensile strain normal to the plane of maximum shear. The use of shear stress could be justified due to

observations that crack initiation tends to be shear driven. The strain normal to the plane is used due to its effect on crack propagation.

Multiaxial fatigue is further complicated by the potential for non-proportional loading, such as in fretting. Under proportional loading conditions the principal stresses remain in constant proportion to each other, and hence the angle of the principal axes remains constant throughout the fatigue cycle. Non-proportional or out-of-phase loading results in extra cyclic hardening due to the rotation of principal axes. The critical plane approach was developed from the work of Brown and Miller (1973). It is based on the physical observation that fatigue cracks initiate and grow on certain planes within a material, where the crack growth and orientation depend on the normal stresses and/or shear stresses and strains on these planes (Shang et al., 2006). The planes on which most fatigue damage occurs are called critical planes. This approach overcame the limitations of the Brown and Miller (1973) approach with respect to the increased damage associated with out-of-plane loading.

Fatemi-Socie (FS) is an alternative FIP based on strain range (Fatemi and Socie, 1988), $\Delta\gamma$, and also includes mean stress effects, as follows:

$$FS = \frac{\Delta\gamma_{\max}}{2}\left(1+\alpha_{FS}\frac{\sigma_{\max}}{\sigma_y}\right) = \frac{\tau_c}{G}(2N_f)^{b_y} + \gamma_c(2N_f)^{c_y} \tag{2.39}$$

where $\Delta\gamma_{max}$ is the maximum shear strain range, α_{FS} is the normal stress sensitivity, σ_{max} is the maximum normal stress, σ_y is the material yield stress, G is the shear modulus and τ_c, b_y, γ_c and c_y are parameters similar to the ones used in the SWT equation, where:

$$\tau_c \cong \frac{\sigma'_f}{\sqrt{3}} \tag{2.40}$$

$$\gamma_c \cong \left(\varepsilon'_f\right)\sqrt{3} \tag{2.41}$$

$$b_y \cong b \tag{2.42}$$

$$c_y \cong c \tag{2.43}$$

Both SWT and FS parameters can take crack initiation and propagation into account. For tensile cracking the parameter should include maximum principal strain amplitude for crack initiation and maximum normal stress on the plane of maximum principal strain amplitude for propagation. For shear cracking failure modes, the parameter should include shear strain amplitude for crack initiation and maximum normal stress on the plane of maximum shear strain amplitude for crack propagation.

The advantage of SWT and FS as FIPs is their ability to consider the effect of mean stress on crack initiation and propagation. A negative or zero mean stress has a beneficial effect on crack growth, while a positive mean stress increases the fatigue damage per cycle. Another benefit of using SWT or FS is that they both include LCF and HCF, thus both elastic and plastic material responses are considered.

2.5.4. Fatigue crack growth

Linear elastic fracture mechanics (LEFM) focuses on the stress required for a crack to grow through a structure based on elastic isotropic assumptions. It is impossible for engineering components to be produced with perfectly smooth surfaces and free from defects. However, it is possible to detect cracks of a certain measurable crack length. From this initial crack length, growth equations can be used to estimate the fatigue life of the component. The Paris-Erdogan law (Paris and Erdogan, 1963)

describes the log-log property of the majority of the curve shown in Figure 2.11, known as 'Stage II' growth. It is proposed that the crack growth in this region is given as:

$$\frac{da}{dN} = C(\Delta K)^m \tag{2.44}$$

where C and m are material constants, $\frac{da}{dN}$ is the change in crack length per cycle (crack growth rate), a is the crack length and ΔK is the stress intensity factor, given by:

$$\Delta K = \Delta\sigma Y\sqrt{\pi a} \tag{2.45}$$

where $\Delta\sigma$ is the stress range equal to ($\sigma_{max} - \sigma_{min}$) and Y is a geometrical factor.

Plotted on a log-log plot, a linear relationship between crack growth rate, $\frac{da}{dN}$, and stress intensity factor, ΔK, can be seen. However, two additional non-linear regimes of crack growth exist above and below Stage II crack growth (see Figure 2.11) (Suresh, 1998).

Stage I crack growth represents short crack growth which occurs at a much faster rate than in the Paris regime (Stage II). ΔK_{th} is the threshold stress intensity factor below which crack arrest occurs. Once ΔK increases beyond this threshold value, the rate of crack propagation increases.

Stage II crack growth is linear and is described by the Paris-Erdogan law. It can be seen from Figure 2.11 that the Paris-Erdogan law cannot accurately predict the propagation rates for short cracks.

Stage III occurs as ΔK approaches the fracture toughness of the material K_{IC}, at which point unstable crack growth ensues, leading to sudden fracture.

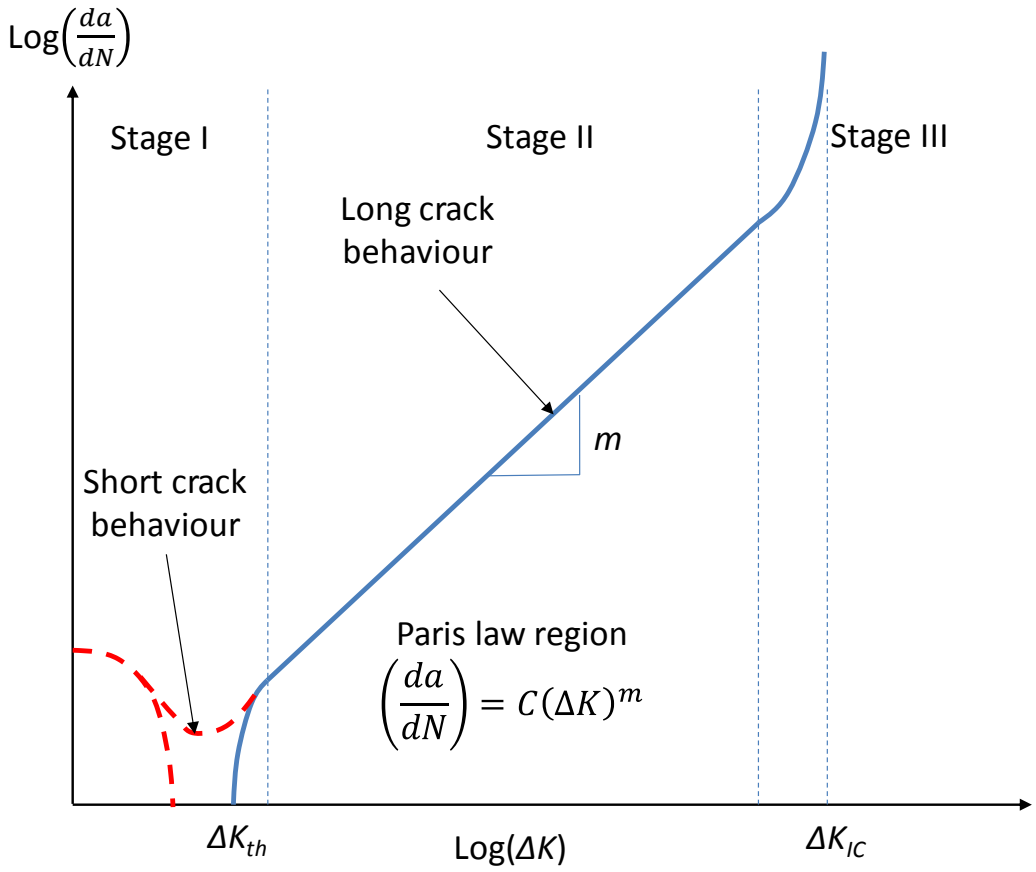

Figure 2.11. Schematic of typical crack growth behaviour.

2.5.5. Short crack growth

Short cracks were observed to propagate at a faster rate than long cracks (Suresh, 1998). The El-Haddad method (1979) of short crack growth incorporates a threshold crack length, a_{th}. This threshold crack length represents the transition from short crack growth (SCG) to long crack growth behaviour (LEFM can be used as described above), as shown in Figure 2.12 (Kitagawa and Takahashi, 1976). The threshold crack length is calculated as follows:

$$a_{th} = \frac{1}{\pi}\left(\frac{\Delta K_{th}}{\sigma_e}\right)^2 \tag{2.46}$$

where σ_e is the fatigue limit of the material and ΔK_{th} is the threshold stress intensity factor for $a > a_{th}$. The EL-Haddad approach is an empirical method that allows for SCG prediction by substituting for a in Equation (2.45) for $a < a_{th}$, as follows:

$$\Delta K = \Delta\sigma Y\sqrt{\pi(a + a_{th})} \tag{2.47}$$

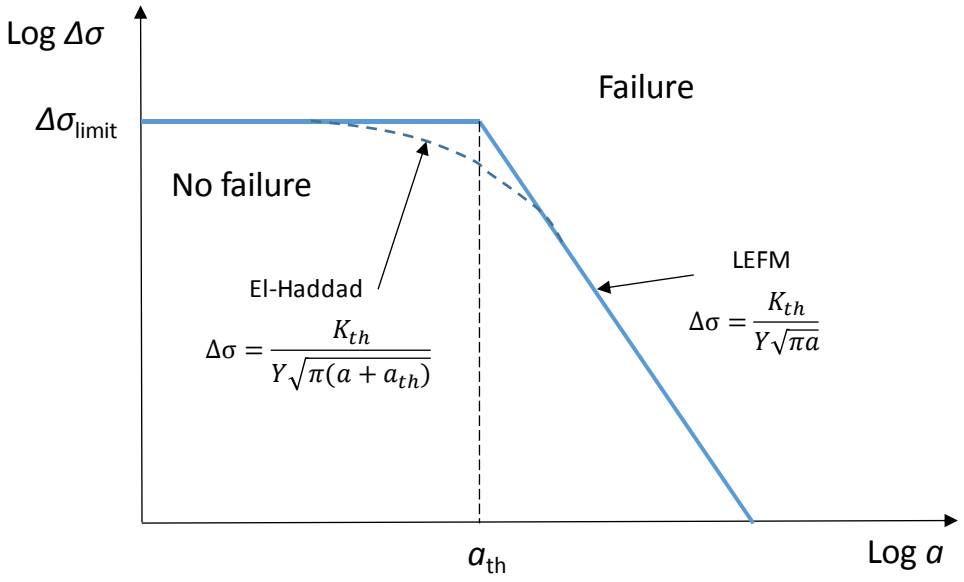

Figure 2.12. Schematic of the Kitagawa and Takahash diagram for SCG (Kitagawa and Takahashi, 1976).

This crack growth prediction methodology has also been implemented within a weight function method (Fett and Munz, 1997; Houghton et al., 2009) for mixed-mode cracking analysis. Researchers (Houghton et al., 2009; McCarthy et al., 2013) have implemented this technique in frictional contact FE models for crack growth prediction in fretting based on the work of Nicholas et al. (2003) who analysed crack growth for a rounded punch-on-flat fretting test rig.

2.5.6. Fracture mechanics-contact mechanics analogy

High stress gradients are observed in Figure 2.8, these stress gradients are also shown to be dependent on contact size. This section will review the analogy between fracture mechanics and contact mechanics studied by researchers; this, in turn, provides a method of investigating contact size effects in fatigue life prediction. It can be seen in Figure 2.8 that with most highly loaded point is at the contact edge; this is the case for many fretting geometries. If the contact is incomplete, such as in the case of rounded punch-on-flat, and the most highly stressed point is at this contact edge, the normal and shear tractions will be zero at this point, resulting in an almost uniaxial stress state, i.e. only stresses parallel to the surface exist at this point (Johnson, 1985). Giannakopoulos et al. (1998) investigated an analogy between the stress field at the corner of a rigid punch-on-flat and that at the tip of an elastic crack. It was shown (Giannakopoulos et al., 1998) that this crack analogy model gives good correlation between life prediction and fretting fatigue experiments. Researchers have also made the analogy between the stress state at the contact edge of a rounded punch-on-flat contact and that in a notch (Giannakopoulos et al., 2000) (see Figure 2.13). Nowell and Dini (2003) showed that the stress gradients at the trailing edge of a rounded punch-on-flat contact match closely with the notch stress gradients over the first 100 μm for stresses perpendicular to the crack. Nowell et al. (2006) used short crack growth theory to show that the analogy between a notch and fretting contact can be used to predict fretting fatigue strength for different contact configurations. The method was validated against experimental results (Dini et al., 2006). This method also predicted the contact size effect.

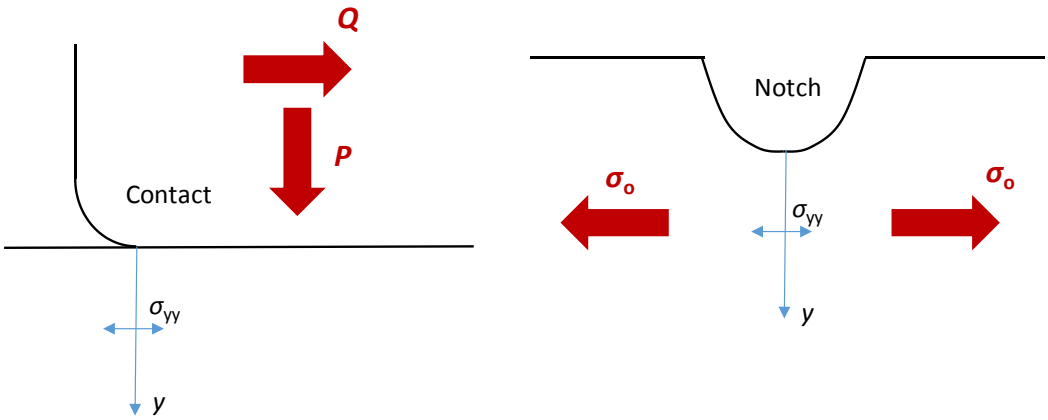

Figure 2.13. Analogy between stresses at a contact and at a notch.

The fracture mechanics-contact mechanics analogy has suggested that it is possible to apply traditional notch fatigue life prediction methods to fretting fatigue problems (Nowell et al., 2006). Three approaches suggested in the literature are (i) point, (ii) line and (iii) area methods (Taylor, 2001). The point method is used in fretting fatigue by calculating the chosen multiaxial FIP, SWT or FS, for example, at equally spaced points at a fixed depth below the contact surface, as shown in Figure 2.14(a). The line method averages the multiaxial FIP over a unidimensional critical depth, d_c, along the critical plane direction, as shown in Figure 2.14(b). The volume averaging method was developed by arguing that high stresses are sustained over a critical volume, such as a microstructure grain. In fretting, a square element (in 2D) at the crack initiation site has been used as the area (or volume in 3D) to average the multiaxial FIP, as shown in Figure 2.14(c). Araújo and Nowell (2002) compared two critical plane fatigue models (FS and SWT) to predict observed experimental results for various cylinder-on-flat radii and contact sizes. It was shown that multiaxial FIP such as SWT and FS can provide an over-conservative life prediction for tests that experience more rapidly varying contact stress fields, i.e. smaller contact size.

However, the use of a critical averaging dimension, d_c, of the order of grain size of the material can give more realistic estimates for the fatigue life across a range of contact sizes. This suggests that the averaging method can predict the contact size effect (Araújo et al., 2004; Araújo and Nowell, 2002). Sum et al. (2005) showed that mesh refinement (element size ≈ grain size) combined with the critical plane approach in a fretting finite element model can also capture stress gradient effects associated with different contact cylinder-on-flat sizes.

2.6. Fretting

2.6.1. General

Fretting occurs in a wide range of mechanical assemblies, such as osteosynthesis plates and screws (ASTM International, 2014), bolted and riveted joints (Szolwinski et al., 2000), steel wires (Cruzado et al., 2013, 2010), blade-disc dovetail connections in gas turbines (Ruiz et al., 1984), spline couplings in gas turbines used in aero-engines (Ding et al., 2007a; Leen et al., 2002) and in the pressure armour layer of flexible marine risers (Burke and Witz, 1995; Perera et al., 2007; Ye and Saevik, 2001). Examples of fretting damage are presented in Figure 2.15. A fretting fatigue crack in an experimental test specimen is illustrated in Figure 2.15(a), showing fretting direction, wear scar and debris, the crack nucleation site and the crack face (McCarthy et al., 2013). Figure 2.15(b) shows an example of a fretting fatigue crack between teeth in a spline coupling (Ding et al., 2007c).

(a)

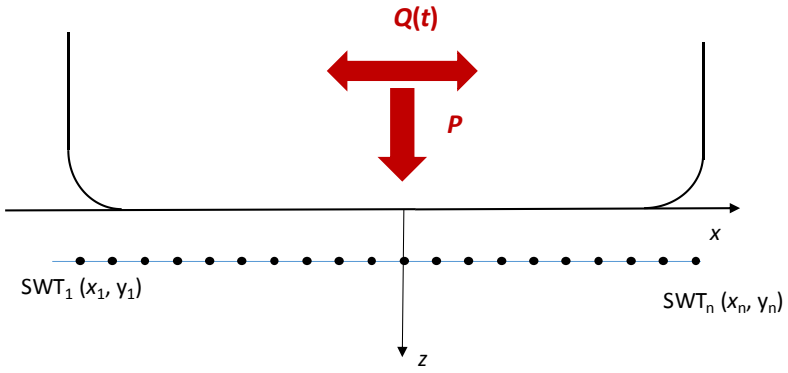

(b)

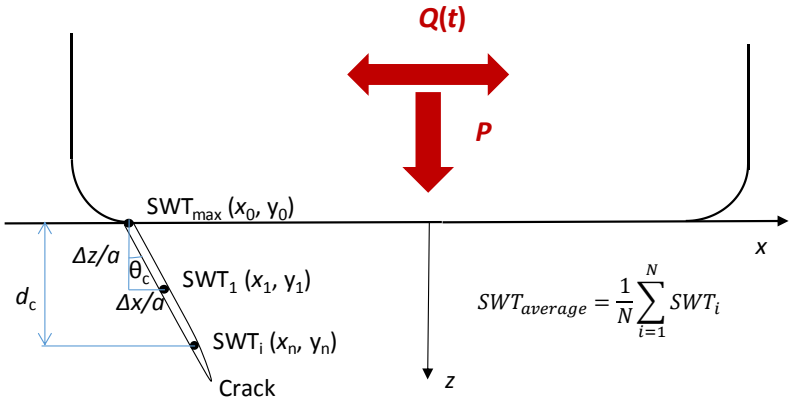

(c)

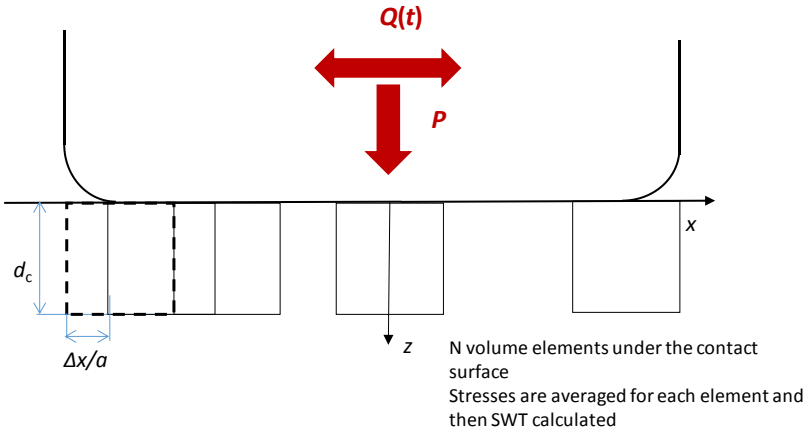

Figure 2.14. Schematic of (a) point, (b) line, and (c) volume averaging methods.

There are three main sliding regimes associated with fretting: partial slip (PSR), gross slip (GSR) and mixed slip (MSR) (Vingsbo and Söderberg, 1988). The sliding regime depends primarily on normal load, relative displacement amplitude and CoF (Dobromirski, 1992). Typical fretting maps are shown in Figure 2.16 and 2.17. Fretting generally occurs when relative motion is less than 300 μm; above this slip amplitude, it is categorised as reciprocating sliding. In general, fretting fatigue (cracking) occurs in MSR and PSR, and fretting wear is predominant in GSR. Fretting maps (see Figure 2.16 and 2.17) proposed by Vingsbo and Söderberg (1988) show that fretting damage evolution strongly depends on slip amplitude and normal load.

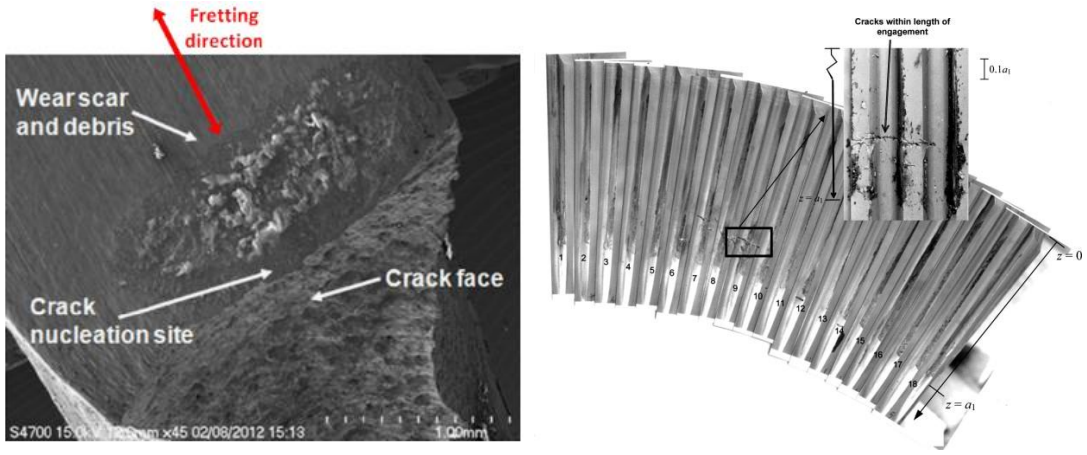

(a) (b)

Figure 2.15. Examples of fretting damage in (a) a fretting fatigue specimen (image from McCarthy et al. (2013)), and (b) a spline coupling teeth (image from Ding et al. (2007b)).

Figure 2.16 illustrates that there is little effect of wear in the stick region and since there is no relative motion, high fatigue life can be observed. Partial slip occurs as the slip amplitude increases. Wear remains low in this slip regime, but fatigue life decreases significantly due to increasing shear-traction and associated trailing-edge

tensile stresses, as well as surface damage. Also, low slip means that damage tends to be localised e.g. at the stick-slip interface or contact edges and slip zones. Material removal is low so that contact stresses remain high and little or no stress relief occurs. In gross-slip, wear becomes the predominant damage mechanism and fatigue life increases; this has been attributed to embryonic cracks being "worn away" before they nucleate to a significant length (Jin and Mall, 2004) and also due to wear-induced redistribution of contact stresses (e.g. Madge et al., 2008). This increase in fatigue life has also been shown experimentally (Magaziner et al., 2004).

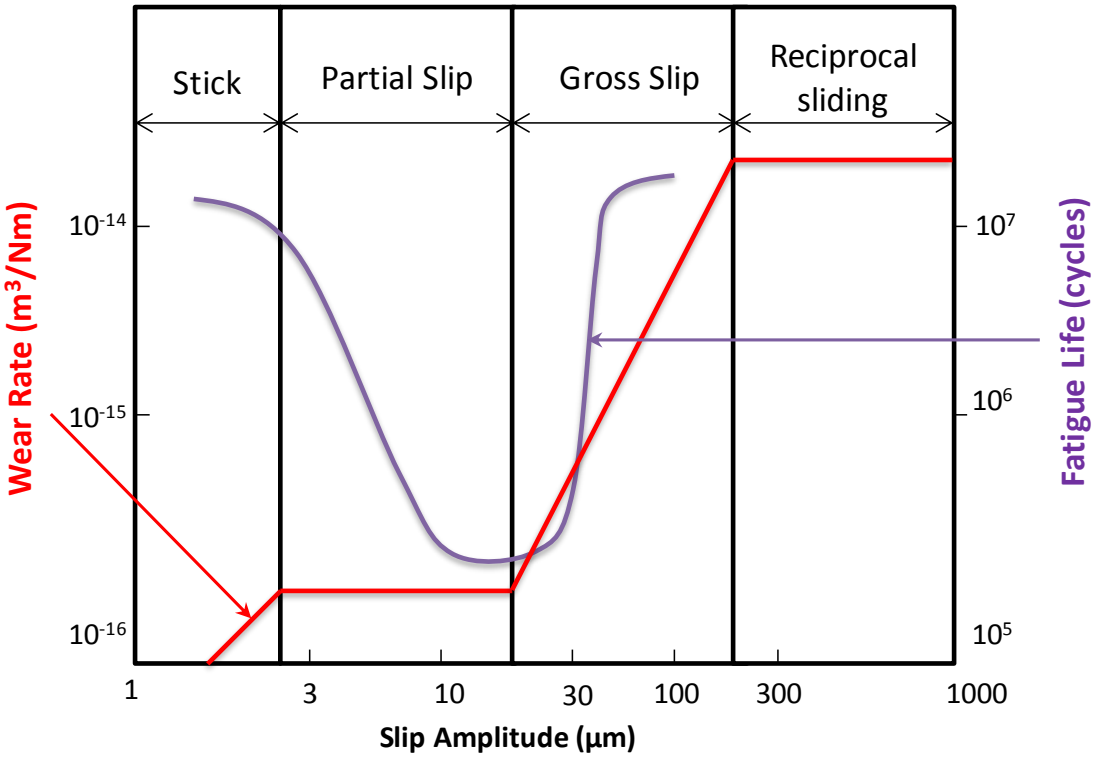

Figure 2.16: Schematic fretting map shows the effect of slip regime on fatigue life and wear rate (Vingsbo and Söderberg, 1988).

Figure 2.17(a) shows the running condition fretting map (RCFM); this illustrates the relationship between normal load, displacement amplitude and different

fretting regimes. The material response fretting map (MRFM) (Figure 2.17(b)) shows the typical damage response for materials (Fouvry et al., 2003; Zhou and Vincent, 1999) describing the characteristics of PSR and GSR. Cracking is observed to occur in PSR, with the damage taking place within the slip band and near the trailing edges of contact (Araújo and Nowell, 2002). In the GSR, larger frictional energy is dissipated and this generates more wear volume than in PSR.

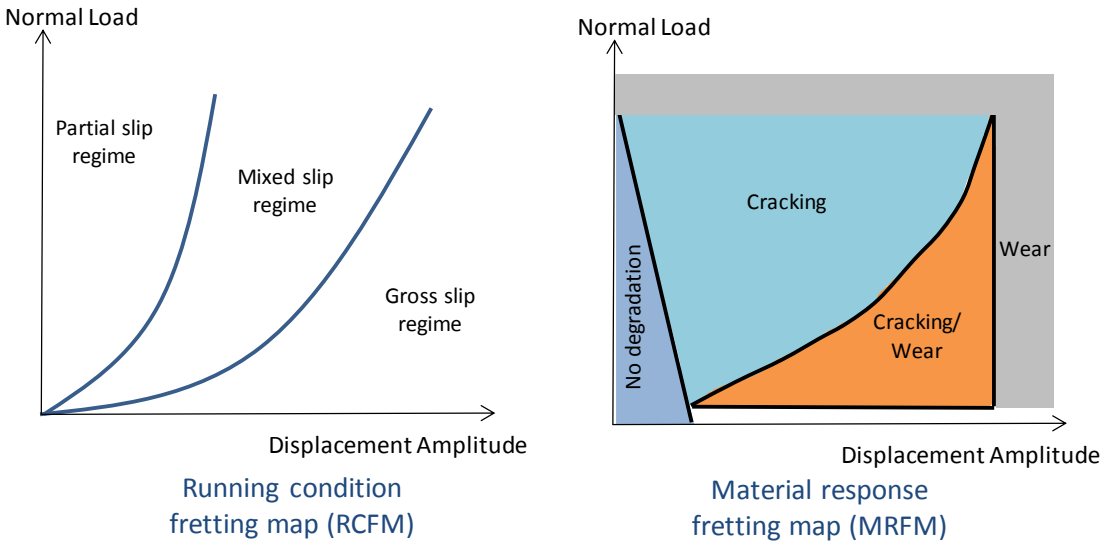

(a) (b)

Figure 2.17: Schematics of (a) running condition fretting map (RCFM) and (b) the material response fretting map (MRFM) for different combinations of displacement amplitude and normal load

Major efforts have been made on researching fretting fatigue and wear in mechanical components. The Cattaneo-Mindlin (Cattaneo, 1938; Mindlin, 1949) solution for partial slip (see section 2.3.3) has proved invaluable in the analysis and design of Hertzian contacts within engineering with respect to fretting fatigue. More recently researchers (Ciavarella et al., 1998; Ciavarella and Macina, 2003) have

developed analytic solutions for rounded punch-on-flat contact cases. However, in engineering, real mechanical components are often much more complex due to their geometry and/or loading conditions. For these components, analytical solutions do not suffice to solve the fretting problem; thus experimental and computational modelling must be considered. In some cases, experimental modelling may not be a viable option due to either economic or time reasons. Numerical simulation of engineering components experiencing fretting has become increasingly popular due to increasing computational power availability. Computational modelling has been used for a wide variety of fretting problems, such as gas turbine blade/disc dovetail joints (Papanikos et al., 1998), railway axles (Ekberg, 2004), riveted panels (Szolwinski and Farris, 1996), spline couplings (Leen et al., 2003), steel rope (Cruzado et al., 2013) and hip implants (Zhang et al., 2013a).

2.6.2. Fretting fatigue

There are many different fatigue damage parameters (or FIPs) (Li et al., 2015), such as SWT and FS parameters as previously discussed (Section 2.5.3). Fretting is a multiaxial fatigue problem, so that critical plane approach (Szolwinski and Farris, 1996) is often used to predict fretting fatigue life. This approach finds the maximum value for a FIP over a number of different planes and thus predicts life based on the critical plane. Many researchers have used this critical plane approach to successfully predict fretting fatigue life (Araújo and Nowell, 2002; Sum et al., 2005; Zhang et al., 2011).

A contact size effect for fretting fatigue life prediction was observed in experiments carried out by Araújo and Nowell (2002) on Al4%Cu and To-6Al-4V; it

was observed that under nominally similar stress conditions, the fretting fatigue life increased as the contact width decreased. This is consistent with the previous theory that crack initiation is dependent on the volume of material stressed and on the stress gradient (Neuber, 1958). Araujo and Nowell (2002), for example, applied a volume averaging process on the FIP parameter (SWT and FS) to qualitatively explain the contact size effect observed experimentally. The length-scale of the process volume is comparable to the size of the material microstructure.

Sum et al. (2005) modelled an experimental spline coupling geometry under complex loading conditions using elastic-plastic response with regard to fretting performance. They predicted partial slip under large bending moments and the predicted stick-slip boundary was consistent with the fretting fatigue crack locations from the experiments. This work showed that it is possible to capture the contact size effect in fretting through detailed finite element modelling. This is due to the FE simulation averaging the stress field over an element volume; this is similar to the volume averaging method implemented by Araújo and Nowell (2002).

Fretting fatigue life prediction is related to the process by which micro-cracks nucleate and develop until macroscopic crack initiation. At this stage, the fretting fatigue crack propagation becomes more rapid and fracture mechanics can then be implemented. Cracks can cause local steep stress gradients; therefore, crack growth can be modelled using fracture mechanics as described previously (see Section 2.5.4).

2.6.3. Fretting wear

As stated previously, fretting wear is the progressive material removal from connecting bodies. As wear takes place, the profile of the contact evolves, and thus the contact pressure and sub-surface stresses also evolve. Therefore, it is important to know the effect of wear on the fretting behaviour of a mechanical component. Figure 2.16 shows the interaction between fretting wear and fatigue life. Contact geometry plays a role in fretting wear.

McColl et al. (2004) and Ding et al. (2004) developed and experimentally validated an FE-based approach for fretting wear simulation (via incremental material removal) using the Archard wear equation (described in Section 2.4.2). This method was applied to a Hertzian geometry to predict the wear-induced evolution of contact geometry and its associated effect on contact surface and sub-surface variables, such as contact pressure, slip and sub-surface stresses. Key fretting phenomena due to material removal, such as the effect on slip amplitude on the evolution of multiaxial contact stresses and FIPs (SWT and FS) were predicted. (Ding et al., 2007b) developed a finite element model to simulate the effect of debris on fretting wear by considering the accumulated debris on the fretting interface as a layer structure with mechanical properties; this model also incorporated migration of the wear particles within the fretting surface. Madge et al. (2007a, 2007b) combined the Archard wear simulation with a finite element based multiaxial fatigue prediction to successfully predict the effect of fretting wear on fretting fatigue life in the elastic conditions, with experimental validation against Hertzian round-on-flat and rounded punch-on-flat fretting fatigue cases for Ti-6Al-4V. Mohd Tobi et al. (2009) used linear and nonlinear

kinematic hardening models to show the evolution of plastic strain effects on incremental plasticity during fretting wear.

Wear coefficient calculations are normally based on experimental tests; the Archard wear coefficient is a function of wear volume, stroke and normal load. The Archard wear coefficient is found to vary depending on slip regime (gross or partial) and for different loads. Madge et al. (2007a) and Ding et al. (2009) have extrapolated the Archard wear coefficient based on experiments (Magaziner et al., 2004) and modified it with the cycles jumping factor numerically.

Numerical fretting wear models have also been developed. Hills et al. (2009) presented a solution for long term wear for Hertzian contact. They assumed that the wear has proceeded for a long time so that the final modified contact is wholly adhered. Nowell (2010) expanded this research to focus on transient wear and presented an efficient numerical method based on quadratic programming which can be used to analyse fretting wear. More recently, Dimaki et al. (2014) presented a rapid simulation methodology for fretting wear based on the method of dimensionality reduction (MDR). A three-dimensional contact is transformed into a one-dimensional profile using MDR (Heß, 2013; Popov and Heß, 2014); the incremental wear in each point of the contact area can then be calculated using the Reye-Archard-Khrushchov wear criterion (Archard and Hirst, 1956; Khrushchov and Babichev, 1960; Raye, 1860). Both of these approaches provide alternatives to a full finite element analysis, thus is much less computationally expensive.

2.6.4. Surface damage parameter for fretting

Surface damage has been studied by a number of researchers for different engineering applications such as dovetail joints between blade and disc of a typical gas-turbine (Ruiz et al., 1984) and spline couplings (Ding et al., 2007c).

Ruiz (1984) proposed two fretting parameters, F_1 and F_2, that can affect fretting wear and fretting fatigue, respectively. These parameters combine mechanical variables such as relative slip amplitude, δ, surface shear traction, τ, and sub-surface tensile stress parallel to the surface σ, in the form of $F_1 = \tau\delta$ and $F_2 = \sigma\tau\delta$. F_2 combines a surface damage parameter ($\tau\delta$) and sub-surface stress (σ). Based on experimental and FE results (Ruiz et al., 1984), a relationship between F_2 and fretting fatigue life was proposed as:

$$N = N_{40}\sqrt{\frac{k_{40}}{F_2}} \tag{2.48}$$

where N_{40} and k_{40} are the fatigue life and F_2 parameter obtained for the 4 - 40 kN loading range, respectively. The F_2 parameter was successful in predicting the crack nucleation position at the contact edge.

The F_2 parameter is a simplified parameter and does not account for the transition from one slip regime to another and the associated change in fatigue life (Ding et al., 2011). Neu and Pape (1998) found that the F_2 parameter failed to observe that cracks tend to grow initially at an oblique angle and did not account for the local multiaxial stress state. From this, Vidner and Leidich (2007) developed an enhanced Ruiz fretting fatigue damage parameter (FFDP), with a combined energetic-multiaxial enhancement parameter (eFFDP), where specific frictional power was assumed to control fatigue damage.

At the same time, a modified SWT approach was developed (Ding et al., 2007c) which incorporates the effects of slip on crack initiation and surface wear damage, using a fretting fatigue damage factor, D_{fret}.

Two empirical damage parameters were proposed: D_{fret1} and D_{fret2}, given by:

$$D_{fret1} = \Delta^* \left\langle 1 - \frac{\Delta^*}{\delta_{th}} \right\rangle^r P^m \tag{2.49}$$

where Δ^* is applied displacement amplitude, P is applied normal load, δ_{th} is a threshold limit beyond which wear becomes dominant and there is no crack formation, and r and m are two further tribological constants.

And

$$D_{fret2} = \left(1 - C\tau\delta\right)^m \left\langle 1 - \frac{\tau\delta}{\tau\delta_{th}} \right\rangle^n \tag{2.50}$$

where $\left(1 - C\tau\delta\right)$ is an empirical estimation of enhanced possibility of crack formation under frictional work, $\tau\delta$. $\left\langle 1 - \frac{\tau\delta}{\tau\delta_{th}} \right\rangle^n$ is introduced to characterise the effects of fretting wear. $(\tau\delta)_{\text{th}}$ is the threshold limit beyond which wear becomes dominant over cracking.

The D_{fret} parameter is implemented with the SWT as follows:

$$SWT = \sigma_{\max} \Delta\varepsilon_a D_{fret} \tag{2.51}$$

The modified SWT parameter gives more accurate predictions for fretting fatigue life and locations. D_{fret1} shows good correlation between test data and fretting fatigue life in terms of the running condition of contact displacement and normal load. A linear relationship between D_{fret1} and fretting fatigue life is presented which provides a reasonably quick and accurate means to estimate fretting fatigue life from running

conditions. D_{fret2} is a more complex parameter which has the ability to capture the effect of relative slip on fretting fatigue life and fretting fatigue contact size effect.

2.6.5. Role of lubrication in fretting

There are many methods for reducing friction and thus, reducing or preventing fretting damage and wear while still allowing relative displacement between contacting surfaces; these include lubrication, surface texturing or thin film coating. Different forms of lubrication are used for reducing fretting damage, for example, solid (powder graphite, polymeric film), liquid (oil) or semi-solid (grease) lubricants. Under fretting conditions, where slip amplitude is small, lubricant penetration into the contact can be limited. It has been shown (Warmuth et al., 2016) for oil-lubricated fretting that the concept of covered width (i.e. the width of contact which never comes out of contact throughout a fretting stroke) can be used to identify regimes of fretting behaviour where the oil is continuously replenished into the contact area to provide a protective tribofilm. In this work (Warmuth et al., 2016), it was argued that lubrication was only effective when the covered width fell to zero. McColl and co-workers (McColl et al., 1995; Shima et al., 1997) investigated the effect of lubricant viscosity and slip amplitude on the lubrication process. It was shown that, for grease-lubricated contacts, the fretting regimes depend on pressure and the penetration of the lubricant into the contact zone, and hence, on the formation of a lubricant tribofilm. Zhou et al. (Zhou and Vincent, 1999; Zhou et al., 1998) showed that, in lubricated fretting, the higher the viscosity of the lubricant the slower the transition towards a low tribofilm-lubrication interface. It was also shown that the coefficient of friction depends on slip amplitude for grease-lubricated fretting: lower friction values were observed for tests carried out

at larger displacement amplitudes. Recently, Haviez et al. (2015) quantified the tribological response of grease-lubricated fretting contacts using a friction energy wear approach for partial slip, gross slip and near reciprocal sliding cases. It was shown that for grease-lubricated fretting, wear volume is mainly controlled by metal-on-metal contact and can be formalised using a modified effective friction work approach.

Grease lubricant has been shown to restrict oxygen from the contact area, preventing oxide debris from developing (McColl et al., 1995; Wang et al., 2011). Fretting damage is dependent on oxygen penetration into the contact area (Wright, 1952; Zhou and Vincent, 1999). Wright (1952) found that the concentration of oxygen in the air is about six times that in lubricant and that the rate of oxygen diffusion within lubricant is approximately proportional to the inverse of its viscosity. Neyman and Sikora (2008) have shown that for fretting contacts with higher viscosity lubricants, higher wear rates are observed. This has been attributed to the exclusion of oxygen from the contact, restricting the production of beneficial oxidised wear particles, which reduce the wear rate since wear particles are less abrasive than steel-on-steel fretting (Neyman and Sikora, 2008). The presence of lubricant at the fretting contact also hinders the escape of debris from the contact (Neyman and Sikora, 2008). Characterisation of grease-lubricated fretting wear behaviour can be undertaken using standard test methods (ASTM International, 2011, 2010).

2.7. Experimental characterisation of fretting behaviour

2.7.1. Introduction

In engineering, experimental testing is essential for the identification of relevant material properties, as well as calibration and validation of numerical modelling techniques. In this section, a review of various experimental techniques employed by researchers to characterise fretting will be discussed. Fretting is difficult to replicate in a laboratory environment due to the small displacements required to cause crack initiation and/or wear. Typically, two different experimental rigs are used to investigate fretting behaviour, i.e. fretting fatigue rigs to investigate crack initiation and fretting wear rigs to investigate wear.

2.7.2. Fretting fatigue rigs

Simplified test rigs are often designed to study particular loading parameters such as contact pressure or pad displacement. De Pauw et al. (2011) provides a review and classification of fretting test rigs. A schematic of fretting fatigue is shown in Figure 2.18. A constant normal force (P) puts an indenter (pad) into contact with a fatigue specimen. The indenter is moved cyclically with an amplitude of Δ. Fretting fatigue (cracking) takes place if the resulting contact slip is typically in the partial slip regime. Fatigue is introduced to the specimen by an alternating bulk stress, σ_{app}.

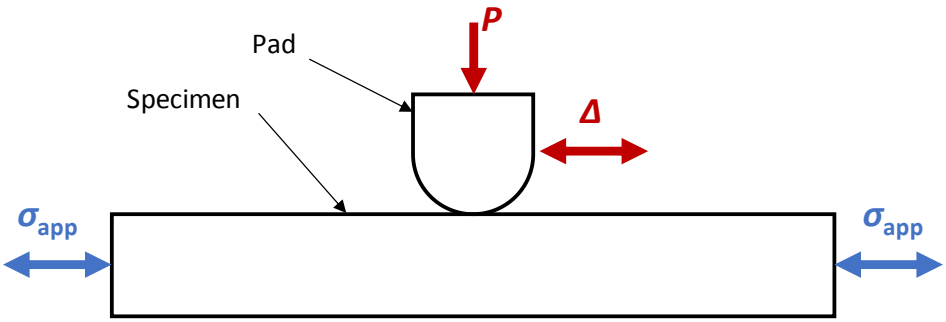

Figure 2.18. Schematic of fretting fatigue experimental set-up

Initially, bridge-type fretting pads arrangements were used (Goh et al., 2006; Pape and Neu, 1999) to replicate fretting fatigue under lab conditions. This was due to the simple arrangement that could be easily adapted for different materials, pad radii, contact pressures and displacements. Jin and Mall (2004) used a variation of the bridge-type arrangement, which was first introduced by Nishioka and Kenji (1972). In this arrangement, the fretting pad has two feet (similar to pads in Figure 2.19)) on either side of the specimen that are clamped in place but are not in contact with the frame or rig. The relative displacement in the contact zone is provided due to the larger cyclic displacement in the specimen relative to the fretting clamps; this leads to friction induced displacement at the contact. McCarthy et al. (2013) used a proving ring as the clamping mechanism for the fretting pads, as shown in Figure 2.19.

Wittkowsky et al. (1999) proposed a method for calculating relative slip δ^* using the following formula (also see Figure 2.20):

$$\delta^* = \delta_{AB} - \left(\delta_{ext} + \delta_{DC}\right) \tag{2.52}$$

where:

$$\delta_{AB} = \left(\frac{P - 2Q}{SE} \right) l_{AB} \tag{2.53}$$

$$\delta_{DC} = -\alpha Q l_{DC} \tag{2.54}$$

where δ_{AB} is the displacement between A and B (see Figure 2.20), δ_{ext} is the displacement measured by the extensometer and δ_{DC} is the compliance of the fretting pad fixture system. P, Q, α, S, E are the normal force, tangential force, compliance constant, cross-sectional area and Young's modulus, respectively. l_{AB} and l_{DC} are the distances from points A to B and D to C, respectively.

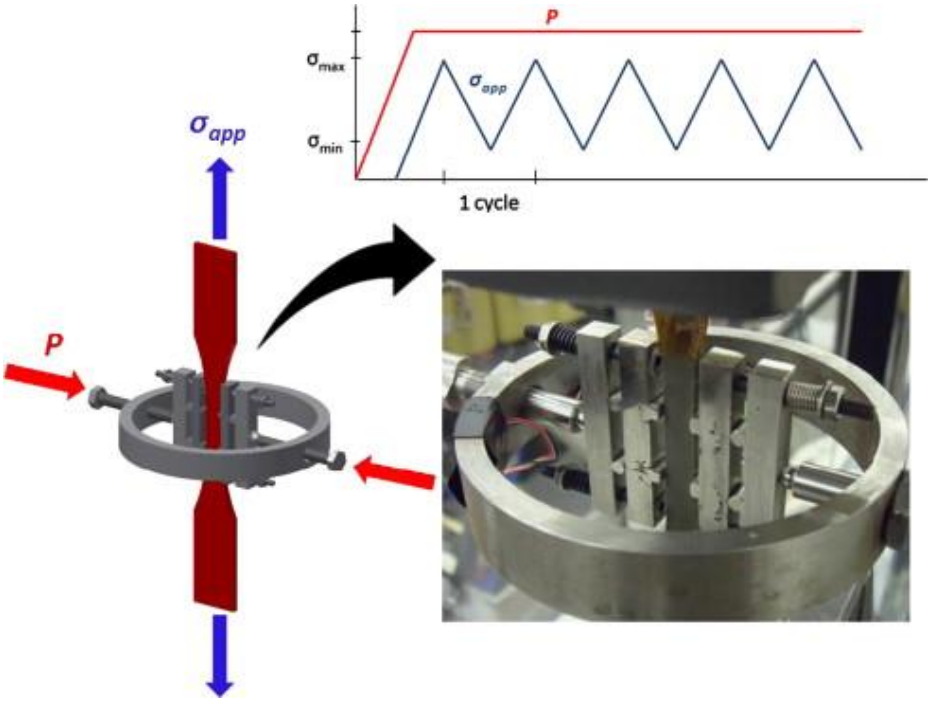

Figure 2.19. Simple schematic highlighting the fatigue specimen clamped between the fretting feet and cyclically loaded (σ_{app}) within the servo hydraulic testing machine along with the load history (image from McCarthy et al. (2013)).

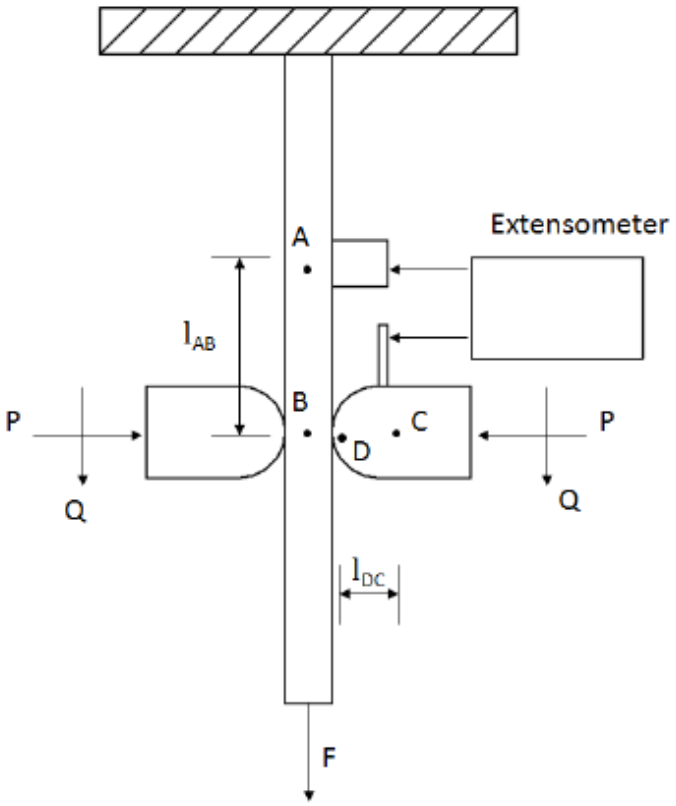

Figure 2.20. Representative schematic of (Jin and Mall, 2004) fretting fatigue rig.

Experimental rigs have been designed to replicate loading scenarios true to those imposed on in-service components, such as: the combined cycling and torque of aero engine spline couplings (Houghton et al., 2009; Wavish et al., 2009) and dovetails in turbine blades (Conner and Nicholas, 2006; Golden, 2009; Golden and Calcaterra, 2006; Golden and Nicholas, 2005; Ruiz et al., 1984).

Kartal et al. (2011) used digital image correlation to measure displacement close to the contact interface in the test rig shown in Figure 2.21 (Mulvihill et al., 2011). This method provides whole field deformation of a surface by cross-correlating surface features in two slightly different images obtained before and after a load is applied remotely. This test rig has been used to test materials, and contact geometries such as

those used in the aero-space industry, turbines. This test rig was designed using D-shaped bronze holders between two rails, which formed adjustable grips (Mugadu et al., 2002b); this insures that the tangential force is applied along the plane of the contact and no rocking moment occurs in the contact region.

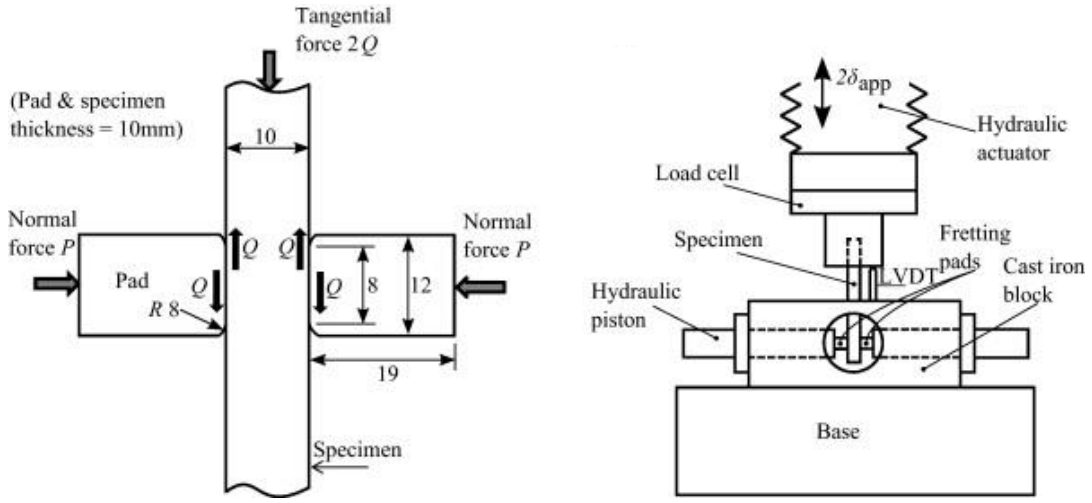

(a) (b)

Figure 2.21. Linear fretting test setup (Kartal et al., 2011; Mulvihill et al., 2011): (a) pad and specimen geometry (dimensions in mm), and (b) schematic diagram of the pads and specimen mounted in the testing machine (image from Mulvihill et al. (2011).

2.7.3. Fretting wear rigs

The primary purpose of conducting fretting wear tests is to identify friction and wear coefficients, therefore, gross slip conditions are necessary. For a fretting wear rig, the displacement of the fretting pads must be controlled while they are in contact with the specimen. Normal loading is generally applied using dead loads or a spring system. Different forms of actuation can be used to oscillate the fretting pads, such as electromagnetic vibrator force transducers (Ding et al., 2009) or magnostrictive or

piezoelectric actuators (Leonard et al., 2012). The tangential force is typically measured with a force sensor. A linear variable differential transformer (LVDT) or differential variable reluctance transducer (DVRT) can be used to measure the pad displacement. The local relative slip between the pad and the substrate is an important parameter in fretting life. However, as in fretting fatigue rigs, the local displacement at the contact surface of the specimen is different from the global applied displacement, Δ^*; this is a result of rig compliance (Jin and Mall, 2004). The following equation has been developed to estimate local slip, δ^* (Sabelkin and Mall, 2005):

$$\delta^* = \Delta^* \left(\frac{C_{CoF}}{C_{RIG}} \right) \tag{2.55}$$

where C_{RIG} is the effect of rig compliance and C_{CoF} is the effect of CoF on compliance. Fridrici et al. (2001) modified extensometer measurements with a compliance factor to obtain the local relative slip where a tension-compression hydraulic machine applied displacement to the specimen.

Pearson (2013) developed a gross-slip fretting wear test rig for cylinder-on-flat test specimen pairs with tangential displacement applied using an electromagnetic vibrator (EMV) and a dead weight normal load, as shown in Figure 2.22(a - b). This test rig has the capacity to test at elevated temperatures, up to 650°C (e.g. Pearson, 2013; Warmuth et al., 2016), this is ideal for testing of high-temperature components, such as spline couplings. Researchers using this rig (e.g. Lemm et al., 2015) typically define the contact slip, δ^*, from fretting loops, as the measured the displacement at zero force, as illustrated in Figure 2.22(c).

Fouvry et al. (e.g. 1996) developed a fretting wear test rig that can test in PS, MS and GS regimes, as illustrated in Figure 2.23. This allows for fretting behaviour of

materials to be studied based on a fretting map approach. In this work, local contact displacement is estimated using the following equation:

$$\delta(t) = \Delta(t) - CQ(t) \tag{2.56}$$

where C is the system compliance determined by subtracting the theoretical contact compliance from the measured compliance, as described by Fouvry et al. (1995).

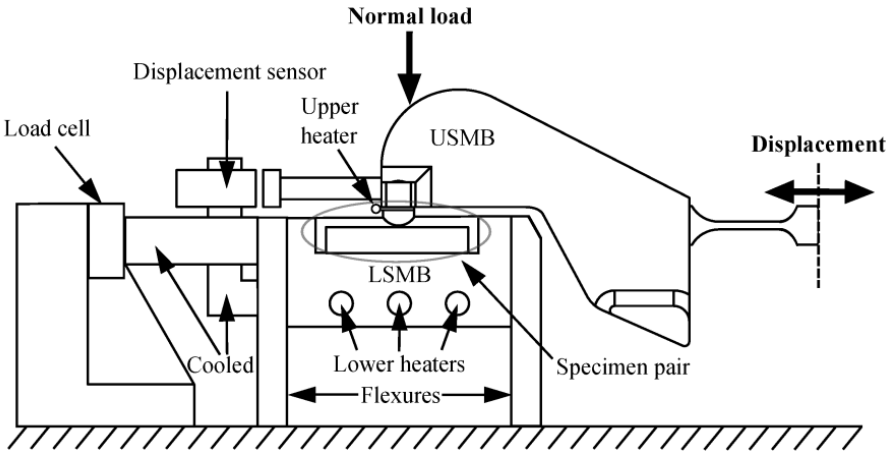

(a)

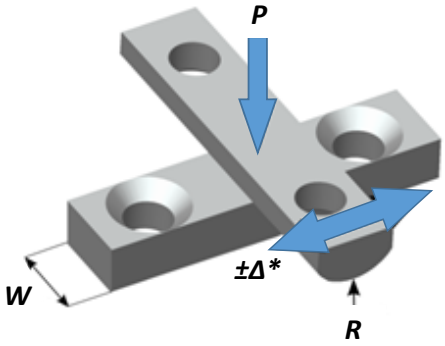

(b)

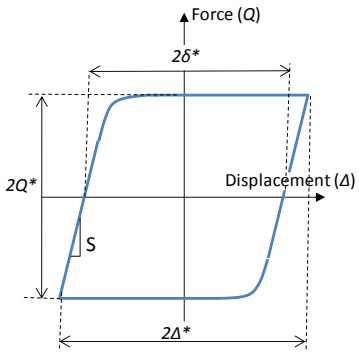

(c)

Figure 2.22. (a) Illustration of the main components of the fretting apparatus used in this study (Pearson, 2013), (b) crossed cylinder-on-flat specimen configuration often utilised in fretting tests, (c) idealised fretting loop indicating maximum local contact slip, δ^*.

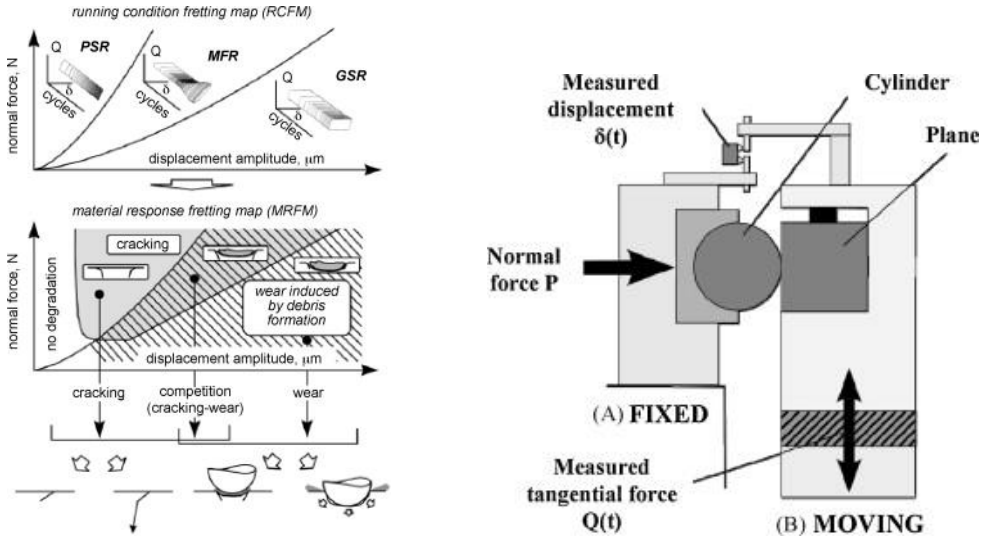

(a) (b)

Figure 2.23. (a) Fretting maps; running condition fretting map (RCFM); material response fretting map (MRFM) (Heredia and Fouvry, 2010), (b) fretting wear setup used by Fouvry et al. (e.g. 1996, 1995), (image from Heredia and Fouvry (2010)).

2.8. Flexible marine riser technology

2.8.1. Modelling of flexible marine risers

The introduction of flexible marine risers to the oil and gas industry has allowed for hydrocarbon extraction at higher pressures and deeper waters that the alternative rigid steel risers. The complex cross-sectional design of flexible risers give them a much lower bending stiffness than rigid structures, this leads to increased ability to undergo large deformations due to sea current loadings, vortex-induced-vibrations (VIV), motions of the FPSO and during installation. However, the complex design of flexible risers also leads to difficulty in the analysis of the structure under these loading conditions. Efficiency and accuracy are required in calculating the structural response,

as well as energy dissipation due to frictional slip between layers, the hysteretic response and the fatigue damage. There are currently two methods of riser analysis, namely, analytical and finite element models.

Analytical models have the benefit of being relatively efficient, however, often are limited to a particular range of applications due to simplifying assumptions made during their formulation. Féret and Bournazel (1987) developed a theoretical model to calculate the stresses and contact pressures between layers due to asymmetrical loads and also, the stresses and relative slip between layers due to bending. This model assumed small displacements and strains and that the layers remain in contact constantly, with a constant interlayer contact pressure. Harte and McNamara (Harte and McNamara, 1993; McNamara, 1992) developed an analytical model composed of individual isotropic and orthotropic layers, each with a unique stiffness for bonded risers. The total stiffness matrix for the whole model was calculated by the summation of all the stiffnesses. The model was designed to give detailed deformations and stresses in various layers so that wear, slip, rupture and debonding may be estimated. However, this model does not include contact or frictional effects. Witz and Tan (1992a, 1992b) researched the axial-torsional and flexural structural behaviour of flexible risers assuming frictionless contact between layers. It was found (Witz and Tan, 1992b) that the lay angle of helix layers is critical to the risers resistance to "Bird-caging" and that the lay angle has a significant influence on the axial-torsional load-displacement relationship. "Bird-caging" is failure that occurs when tensile armour layers buckle radially, usually due to compressive axial loading of the riser, and layer separation occurs. This work was then extended (Witz and Tan, 1992a) to investigate the flexural behaviour of marine cables, umbilicals and flexible risers. It was shown that the flexural response of these structures is dominated by relative movement

between layers once a critical curvature is exceeded. They presented a hysteretic bending moment-curvature relationship for generic flexible structures.

MCS International (now Wood Group), developed a finite element package (Flexcom) to analysis offshore structures under dynamic loading. A general finite element solution for problems involving articulated offshore loading towers and attached mooring arms was presented by Haverty et al. (1982). This solution could be extended for other applications. McNamara and Lane (1984) presented an efficient method for the analysis of the linear and non-linear static and dynamic motions of offshore systems. This method was based on the FE approach using convected coordinates for arbitrary large rotations and includes loads such as buoyancy, gravity, random waves, currents, ship motions and Morison's equation. This was later extended to the 3D frequency domain computational dynamic analysis of deep-water multi-line flexible risers (McNamara and Lane, 1992). Lane et al. (1986) found excellent agreement between results from time domain and frequency domain finite element programs, showing that frequency domain is a reliable and accurate technique for a broad range of applications. More recently, advanced frequency domain analysis of SCR (steel cantenary riser) fatigue (Lane et al., 2001) and CALM (cantenary anchor leg mooring) buoys offloading system (Lang et al., 2005) is compared to time domain results with a high level of accuracy.

O'Brien et.al (1988) presented a 3D finite element model of marine risers, pipeline and offshore loading towers based on the separation of the rigid body motions and deformations of elements under conditions of finite rotations. The finite element model was validated against independent calculations for the case of a vertical cantilever under bi-directional loading and axial torque. Computational efficiency and accuracy was achieved through a single-step implicit time integration operator with a

variable increment size and by assuming an equivalent single layer representing all layers of the riser. McNamara et al. (1988) developed a method for the static and dynamic analysis of flexible risers and pipeline in the offshore environment under large displacement due to wave and vessel motions. A hybrid beam element formulation was developed where axial force is combined with the corresponding axial displacements via a Lagrangian constraint. In the same year, McNamara and O'Brien (1988) also presented a review of flexible marine riser design process including static and dynamic analysis. Newly defined measures of beam deformations (O'Brien et al., 2002) to provide precise measure of rotation deformation to convected axes have been developed; these new terms do not assume that the deformation rotations behave as vectors, as assumed in previous models. This development increased the robustness of the analysis technique, allowing for larger time steps with rapid convergence. The issue of accuracy of finite element for flexible beams undergoing extreme states of 3D finite displacements and rotations, i.e. during installation of flexible pipe, severe operational loading conditions or emergency deployment situations, was addressed by O'Brien et al. (2003). Smith et al. (2007) developed a state-of-the-art bending hysteresis model as part of an analysis tool to allow inherent over-conservatism in design procedures to be removed, resulting in safe use of lower-cost solutions. Connaire et al. (2015) used the method of convected coordinates, Euler-Bernoulli beam theory, the principal of virtual work and finite element method to develop two quasi-rotation measures. These measures allow for accurate definitions of coupled axial, bending and torque response for beams with significant deflection. This allows for the accurate FE analysis of subsea risers with computationally sensitive load cases and highly non-linear loading regimes using fewer elements compared to alternative solutions.

From this work, other finite element programs were also developed. DeepRiser is a FE analysis based on non-linear hybrid beam finite elements; the software can accurately model contact between risers and lateral hull guides (Lang et al., 2001). FE results have been compared to full-scale offshore measurements (Lang et al., 2001). The FE results were shown to have reasonable agreement with the measurements and areas of response sensitivity in the software were highlighted. The advancements made in computational efficiency and accuracy has allowed for the development of on-board operational guidance technology to be developed. Riser management system incorporates advanced FE models of the riser system, coupled with measured riser response data to predict the operational envelope for the vessel under the prevailing metocean conditions in pseudo-time (Lang et al., 2006). Lang et al. (2007) presented an on-board simulation tool designed for use on dynamically positioned drilling rigs that can be used to plan deployment or retrieval and drift running operations.

Other researchers have focused on developing local riser FE models using existing commercial finite element packages, such as Abaqus. For example, simplified finite element models have been presented to investigate failure mechanisms such as burst (Neto et al., 2013) dry and wet collapse (Neto, 2015, 2011; Neto et al., 2016) and failure due to crushing loading (Malta et al., 2013).

2.8.2. Experimental testing of risers

Risers and their materials are tested by the manufacturer prior to installation of the riser in an offshore environment. These tests include global and local strength, fatigue capacity and material corrosion (DNV, 2003). Damage detection, such as rupture and leakage, is also used to identify failure modes. Testing and monitoring of

the riser's integrity also take place during operation (Myren, 2007). The majority of experimental testing in the literature is fatigue testing, focusing in particular on the tensile armour layers and welded joints. Osawa et al. (2013) developed a fatigue testing machine for fatigue testing on welded joint specimens subject to wave loading with high-frequency vibration. Saevik (2011) describes the MARINTEK full-scale test rig to investigate dynamic stresses and fatigue in flexible marine risers. The test rig applies tension loading via a hydraulic cylinder and bending moment via two further hydraulic cylinders. De Sousa et al. (2012) presented an experimental program to analysis the fatigue performance of a 6 inch flexible riser with broken tensile armour wires. It was found that increased number of broken wires (up to 5) significantly reduces the fatigue life of the pipe. Researchers (Clarke et al., 2011; Jacques et al., 2010) applied non-destructive testing techniques to a flexible riser in a full-scale dynamic loading test, as shown in Figure 2.24. One of the techniques used was readings from optical fibre sensors based on Bragg gratings (Figure 2.24(b)) and acoustic emission for direct comparison.

Perera et al. (2007) performed fretting tests on pressure armour specimens. These tests consisted of two interlocked pieces of profiled pressure armour wire subjected to axial stress, which represented hoop stress; the nub-groove contact was pressed together with a controlled normal pressure and controlled tangential displacement was applied to the specimen.

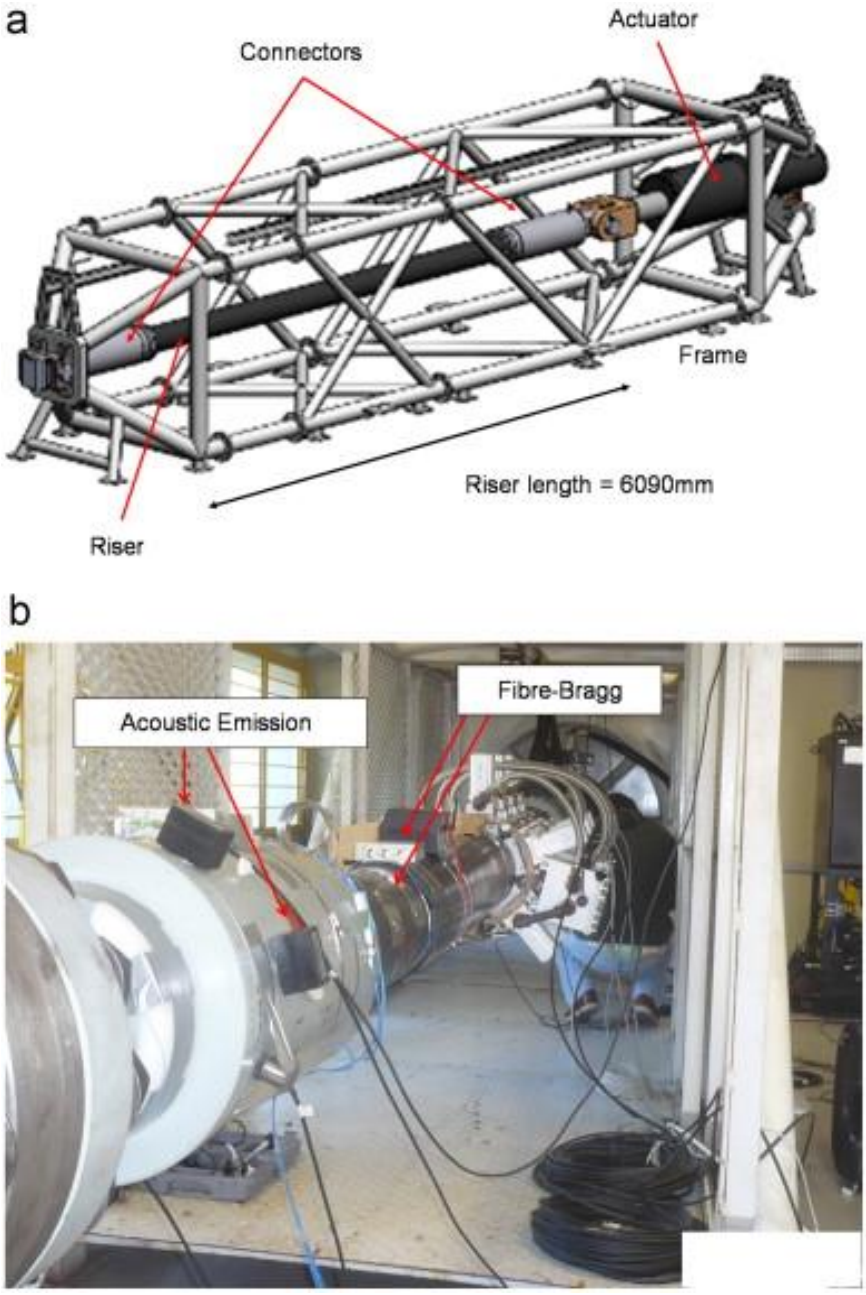

Figure 2.24. (a) Schematic drawings of the test frame with riser assembly and actuator and (b) photograph of test setup showing several NDT techniques including acoustic emission and optical fibre Bragg grating (image from Jacques et al. (2010)).

2.8.3. Fretting in flexible marine risers

Løtveit and Bjaerum (1994) identified fretting of the pressure armour wire as a potential failure mode for flexible marine risers. The problem of fretting in the pressure armour layer of flexible marine risers was presented by Burke and Witz (1995) at an industrial conference. Here, the problem of contact mechanics, frictional contact and wear were highlighted as areas that required further research. To the author's knowledge, Perera et al. (2007) were the first to investigate fretting in the pressure armour layer of flexible marine risers, plotting contact pressure distributions and experimentally characterising the fretting behaviour. This research described a full-scale experimental test program on pressure armour layer nub-groove contacts. These experiments showed that it was possible to generate fretting in the pressure armour samples under certain conditions (high normal load and low displacement amplitude). Fretting cracks initiated at the contact edges, where high contact pressure was predicted. Significant surface damage due to wear was also observed for gross slip cases. However, Perera et al. (2007) concluded that the issue requires further investigation. Since then little or no research has been published on this aspect of riser design.

2.9. Summary and conclusions

The literature on fretting is quite extensive, with a sizable proportion of developments in this literature developed during investigation into fretting of specific components, such osteosynthesis plates and screws, bolted and riveted joints, steel wires, blade-disc dovetail connections in gas turbines and spline couplings in gas

turbines used in aero-engines. Researchers have developed numerical and computational techniques to predict the fretting wear and fatigue performance of frictional fretting contacts. Experimental rigs have been developed to investigate fretting fatigue and tribological (friction and fretting wear) behaviour of materials. These computational and experimental methods can be adapted for investigation into the fretting behaviour of various contacts, such as nub-groove contacts in flexible marine risers. Various methods of modelling flexible marine risers and experimental fatigue testing to identify fatigue behaviour of risers have been discussed in this chapter. However, there is a notable shortcoming in the literature in relation to investigations into fretting in the nub-groove contact of the pressure armour layer in flexible marine risers. The following highlights these shortcomings and outlines how this thesis will address these specific gaps in the current literature.

A significant amount of work has been carried out to date on fretting of simplified contacts, such as cylinder-on-flat revealing a significant effect of loading conditions on the slip regime and hence, on predicted wear and life of a component. The framework proposed in Figure 1.4 outlines the fundamental requirements to incorporate such effects within a fretting design tool, namely:

- Identification of the relevant fretting geometry of the nub-groove contact within the pressure armour layer,
- Determination of key tribological (friction, wear) and mechanical (yield strength, ductility, fatigue) parameters via experimental analysis of pressure armour material under realistic loading conditions,

- Development of representative nub-groove contact finite element models for partial- and gross-slip conditions and investigation into the contact pressure, slip and substrate stresses of the fretting contact,
- Implementation of a combined wear-fatigue finite element model to determine the influence of loading conditions on wear and hence, on predicted fatigue life of the nub-groove contact.
- Development of an analytical fretting wear and fatigue design tool.

As different loading conditions can result in significantly different damage mechanisms, and hence, predicted lives as shown in Figure 2.16 and 2.17, there is a need to develop an understanding of the loading conditions on the pressure armour layer and in particular on the local nub-groove contact. This will facilitate representative material testing and hence, accurate simulation of fretting in the nub-groove contact. To date, no research has investigated the effect of global riser dynamic loading conditions on the local nub-groove fretting wear and fatigue behaviour of the pressure armour material. Building on the current literature for other components, this gap will be bridged by the development of a fretting wear-fatigue modelling framework for the accurate prediction of pressure armour layer fretting service life in flexible marine risers.

There has been relatively little research on the fretting performance of pressure armour material, hence it is necessary to characterise the fretting performance of the material experimentally. For the first time, a suite of laboratory experiments will be conducted on pre-service and representative pressure armour layer material. This will require the dissection of a section of pre-service riser for extraction of pressure armour material, design of test specimens from the formed material, characterisation of

chemical composition of the material and identification of representative material. Monotonic tensile and low-cycle fatigue testing will be carried out on the pre-service material. Dry and grease-lubricated fretting wear tests will be conducted, using a well-established test rig, on representative pressure armour material. Further fretting wear tests will also be conducted on pre-formed pressure armour material on a newly developed fretting wear test rig. The test program will provide relevant critical parameters, such as coefficient of friction, wear coefficient and fatigue parameters to be used in computational models.

As it can seen from the review of the literature on modelling of flexible marine risers, there is a need within the industry for computationally efficient modelling techniques that can provide significant accuracy for the analysis of risers. Therefore, a fretting design tool will be developed that is, (i) computationally efficient, (ii) robust for use with various contact geometries and loading conditions, and (iii) accurate. This thesis will outline the step-by-step approach to the development of a design methodology and fretting design tool for the pressure armour layer of flexible marine risers.

Chapter 3: Design of fretting test rig

3.1. Introduction

In this chapter, a review of fretting rig design is discussed, the requirements for a new test rig are outlined and the development of a new fretting rig is presented. A variety of novel experimental fretting test rigs have been developed to investigate the variables that affect fretting behaviour. A fretting rig must be able to:

i. Apply a fixed normal load as a clamping force between specimens.

ii. Apply a (typically) controlled (unidirectional) micro-scale reciprocating tangential displacement (or force) between the specimens, with the superimposed normal load.

iii. Be capable of high frequency testing, in order to allow large numbers of fretting cycles in reasonable time frame.

Some rigs have been designed to allow real time control of the normal load, tangential displacement and frequency (Fouvry, 2001; Kartal et al., 2011); high-temperature fretting tests and humidity controlled tests have also been developed (Pearson, 2013).

In addition to the mechanical requirements for the design of fretting test rigs, the test rig must be capable of measuring and recording the cyclical variation of:

i. Displacement at the contact (or as close to the area of contact as possible).

ii. Tangential force.

The sampling frequency of these measurements must be large to provide high resolution hysteresis fretting loops (see figure 2.1), which are used to identify fretting parameters, such as friction and energy dissipation.

3.2. Review of fretting wear rig designs

3.2.1. Specimen geometry and alignment

There are no standards for fretting test rigs design, therefore, researchers have developed a variety of test rig designs. A variety of fretting contact geometrical test configurations have been previously developed. These can be divided into three basic categories: point contacts (e.g. sphere-on-flat), line contacts (e.g. cylinder-on-flat) and complete contacts (e.g. flat-on-flat) (see Figure 3.1). A rounded flat-on-flat geometry is often investigated in fretting tests also (e.g. Mulvihill et al., 2011), this contact is not defined as a line or a complete contact. Each of these cases has benefits and drawbacks with respect to fretting wear characterisation. Fouvry and co-workers (Fouvry et al., 2009; Merhej and Fouvry, 2009) have demonstrated that the wear coefficient is dependent on the radius of curvature for cylinder-on-flat and sphere-on-flat unlubricated fretting.

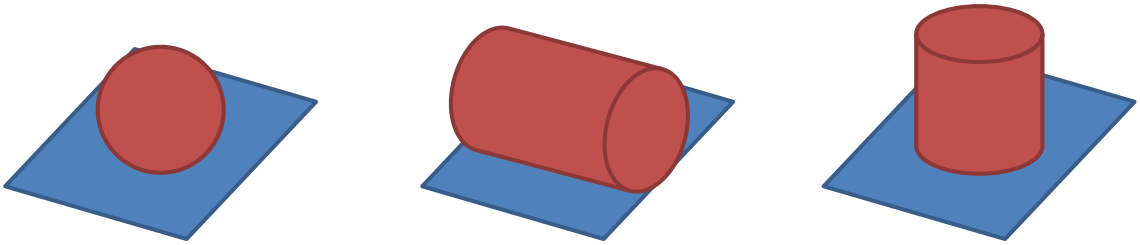

(a) (b) (c)

Figure 3.1. Diagram of the three main types of experimental fretting contacts, (a) point contact, (b) line contact, and (c) complete contact.

A point contact can be either a sphere-on-flat (Figure 3.1(a)) or crossed cylinder geometry. The point contact is a widely used geometry throughout the literature (Barril et al., 2002; Bill, 1983; Hamdy et al., 1981; Johnson, 1955; Leonard et al., 2012; Marui et al., 1998; Mohrbacher et al., 1995; Ramesh and Gnanamoorthy, 2006; Söderberg et al., 1986; Tomlinson et al., 1939; Tomlinson, 1927). The major advantage of this geometry is the natural self-alignment behaviour of a point contact; this simplifies the test design and also improves the repeatability of tests. The elastic contact surface and substrate stresses in the unworn geometry can be defined using analytical solutions developed by Hertz (1882), Cattaneo (1938) and Mindlin (1949) (see Chapter 2 Section 2.2). However, as wear develops the contact becomes three-dimensional, increasing its complexity and making it more difficult to analysis and, therefore, interpret.

A common line contact fretting test geometry is a cylinder-on-flat geometry (Figure 3.1(b)). Although not as widely used as the point contact, there are numerous examples of test rigs that employ this geometry configuration (Barril et al., 2002; Fouvry, 2001; Halliday, 1956; Halliday and Hirst, 1956; Iwabuchi, 1991; Lemm et al., 2015; Leonard et al., 2012; McColl et al., 2004; Mugadu et al., 2002; Pearson, 2013).

Similar to the point contact, the elastic surface and sub-surface stresses can be found by using analytical solutions (Cattaneo, 1938; Hertz, 1882; Mindlin, 1949). A line contact theoretically, maintains its two-dimensional nature, in the direction of the line contact (i.e. across the specimen width) as a wear scar develops, making the evolving contact less complex to analyse compared to a point contact. Also, profilometry of a wear scar from a line contact is easier that other specimen geometries, since no corrections for specimen geometry are required for the flat specimen.

An example of a complete contact (Figure 3.1(c)) is a flat-end punch pressed against a flat substrate in perfect alignment. Such a contact is representative of many engineering applications contacts, such as shaft-hub connections (Shen et al., 2013), and some types of riser nub-groove geometries (Saevik and Ye, 2009); however, there are significant alignment challenges associated with these types of geometries. Even so, there are many examples of researchers utilising such contacts in experimental test rigs (Aldham et al., 1985; Barril et al., 2002; Kartal et al., 2011; Leonard et al., 2012; Mulvihill et al., 2011; Ohmae and Tsukizoe, 1974; Tomlinson et al., 1939; Uhlig et al., 1953; Varenberg et al., 2002; Wavish et al., 2009).

3.2.2. Drive line and reciprocating displacement

Two main types of reciprocating displacement have been used in fretting rigs, namely (i) rotational, (ii) linear. Rotational fretting rigs were commonly used in early fretting rigs (Halliday, 1956; Halliday and Hirst, 1956; Johnson, 1955; Tomlinson, 1927; Tomlinson et al., 1939; Uhlig et al., 1953). For this set-up the contact displacement is a function of radial distance from the centre of the contact; Waterhouse (1922) claimed that this allows for tests to be conducted at different displacement

amplitudes simultaneously. The main advantage of a rotational fretting rig is that once the axis of rotation is defined, (large) input displacement amplitudes can be reduced to fretting scale motions using a lever arm mechanism; similarly contact displacement measurements can be amplified to measurable levels. This was a major advantage prior to the introduction of highly accurate micro-nano scale sensors. However, a disadvantage of using rotational displacement is that the center of rotation will have zero angular displacement amplitude. Rotational fretting rigs can also be implemented in an attempt to approximate linear displacement, as shown in Figure 3.2. This is achieved by using a large radius of motion in relation to the contact displacement amplitude.

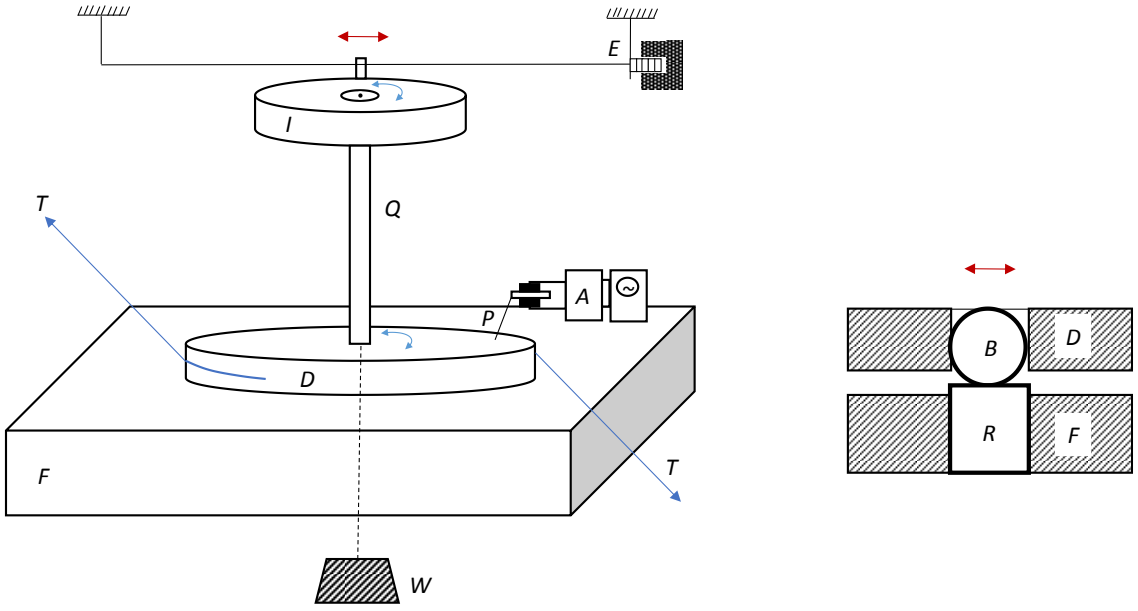

(a) (b)

Figure 3.2. (a) Schematic of apparatus used by Johnson (1955). Normal load is provided by dead weight, *W*. Static shear forces are applied by strings *T* . Oscillating shear forces are applied by torsional vibration of the disk *I* and the displacements measured by the pick-up *P* and amplifier *A*, (b) Ball (*B*) on flat (*F*) specimen configuration in the test rig.

For linear fretting rigs, the reciprocating displacement is typically provided by a linear actuator. In a similar manner to rotational fretting rigs, the linear motion must be constrained using a bearing or a joint. However, joints can be vulnerable to fretting damage, e.g. they may have a tolerance of similar magnitude to the applied fretting displacements. In order to ensure no out-of-plane motion takes place, ball bearings (Antler, 1982; Budinski, 1982), non-contacting hydrostatic-bearings (Kennedy et al., 1982) and flexible vanes (Lemm et al., 2015; Pearson, 2013) have been used. Flexible vanes have been shown to easily introduce unexpected and undesirable degrees of freedom to a test rig, due to their compliance in directions other than the primary direction of flexure (Berthier et al., 1988).

Numerous methods of generating reciprocating motion can be found in the literature. The primary method of providing rotational motion is a cam and electric motor configuration (Budinski, 1982; Colombié et al., 1984; El-Sherbiny and Salem, 1982; Smallwood et al., 1988; Uhlig et al., 1953; Varenberg et al., 2002). Tests can be conducted at a range of displacement amplitudes simply by changing the cam used for each test. There are a variety of methods of producing direct linear motion for fretting tests, including electromagnetic vibrators (EVMs) (Halliday, 1956; Hamdy et al., 1981; Iwabuchi, 1991; Lemm et al., 2015; Pearson, 2013), magnetostrictive vibrators (Vingsbo and Schön, 1993), hydraulic rams (Aldham et al., 1985; Kusner et al., 1982), oscillating lead screws (Antler, 1982; Bailey et al., 1954) and piezoelectric stacks (Barril et al., 2002; Leonard et al., 2012; Marui et al., 1998; Söderberg et al., 1986). The primary benefit of a source of direct linear motion is the reduced number of linkages required to control the motion compared to rotational motion; this can allow for active control of the displacement throughout the test.

3.2.3. Applying normal loading

There are three primary methods of applying normal loading during a fretting test:

(i) Dead-weight: this is the simplest form of applying a constant normal load during testing. Some samples of dead-weight loading used in fretting risers can be found in the literature (Hamdy et al., 1981; Lemm et al., 2015; Marui et al., 1998; Pearson, 2013; Tomlinson, 1927; Varenberg et al., 2002). Figure 2.18 shows an example of dead-weight normal loading (Pearson, 2013).

(ii) Hydraulic methods: hydraulic mechanisms for applying normal load are widely used (Aldham et al., 1985; Fouvry, 2001; Kartal et al., 2011; Mugadu et al., 2002; Mulvihill et al., 2011; Uhlig et al., 1953). This methodology allows for control of the load and also, for testing at high normal loads. However, the use of hydraulics to apply normal load during fretting tests requires pressurised fluid, which can be a source of faults and break-downs. Figure 2.21 shows an example of hydraulic normal loading (Mulvihill et al., 2011).

(iii) Spring loaded: An example of the use of springs to apply normal loading is the use of a proving-ring (as shown in Figure 2.19); this is common in fretting fatigue test rigs (McCarthy et al., 2013). Examples of spring-loaded normal loading in fretting wear test rigs can be found in (Barril et al., 2002; Kusner et al., 1982; Tomlinson et al., 1939). One problem with the use of springs, is that as a wear scar develops and evolves, the

load will decrease. Therefore, it may not be possible to achieve a constant load during fretting wear.

3.3. Requirements for new fretting test rig

A cylinder-on-flat fretting fatigue test rig was previously developed by McCarthy et al. (2013), using a proving-ring mechanism to apply normal load, with a bulk fatigue stress applied to a dog-bone test specimen using the Instron Servo-hydraulic machine in NUI Galway (as shown in Figure 2.19). Fretting pads as indenters on the dog-bone test specimen were used to represent fretting fatigue conditions. However, this test rig did not allow for local (close to the contact) displacement to be measured since no extensometer or DVRT was used. Also, little wear was observed in the specimens. Hence, wear tests were carried out using a tribometer (Zhang et al., 2013). This test rig allowed for testing of a ball-on-flat specimen under normal loads of up to 10 N and reciprocating tangential displacements of ± 2 mm. For tests conducted at 2.25 Hz, the data acquisition was 35 Hz (Zhang, 2013); this implies that there were only 15 or 16 data points per cycle. This test set-up is not a fretting test, since the tangential displacements are too high, the normal loads are low and the data acquisition is not sufficiently accurate.

Hence, there was a requirement for development of a fretting wear test rig to provide an experimental capability at NUI Galway for fretting testing of pressure armour wire of flexible risers and for other more fundamental fretting research. The following features were considered essential for the new fretting rig design:

1. Controlled oscillating contact displacements of the order of micrometres.
2. Normal applied load to achieve contact pressures of 500 MPa to 1500 MPa to represent typical engineering applications of interest, using dead weight loading since it has been proven to be reliable.
3. Ability to control the frequency of the tests.
4. Closed loop control of the applied displacement amplitude.
5. The data acquisition for displacement and force measurements must be sufficient to get reliable fretting loops at high operating frequencies (up to 20 Hz).
6. The data must then be stored in a format that is easy to process using standard common desktop software including, MS Excel, Fortran, MatLab, DIAdem, for example.

For the purpose of designing a new fretting rig in NUI Galway, a linear drive line has been chosen, with a piezoelectric actuator to provide the linear motion. The normal load will be applied using a dead load, for simplicity and proven track record. The specimen geometry selected for the new design will be crossed cylinders initially, since there are less alignment issues associated with crossed-cylinders specimen compared to other possible geometries, but the specimen connection will be designed so that alternative geometries can be investigated also.

3.4. Development of new fretting rig

3.4.1. Design

A new fretting test rig was designed and developed to measure coefficient of friction and quantify fretting behaviour of materials. Figure 3.3 and 3.4 are schematics of the newly designed fretting rig in NUI Galway with the main rig components labelled. The main components include a linear drive line with a piezoelectric actuator to produce reciprocating displacement and a collet to fix the test specimen in place, dead weight normal loading and displacement (DVRT) and force sensors connected to a PC via a data acquisition unit. The following sections will provide a description of these components.

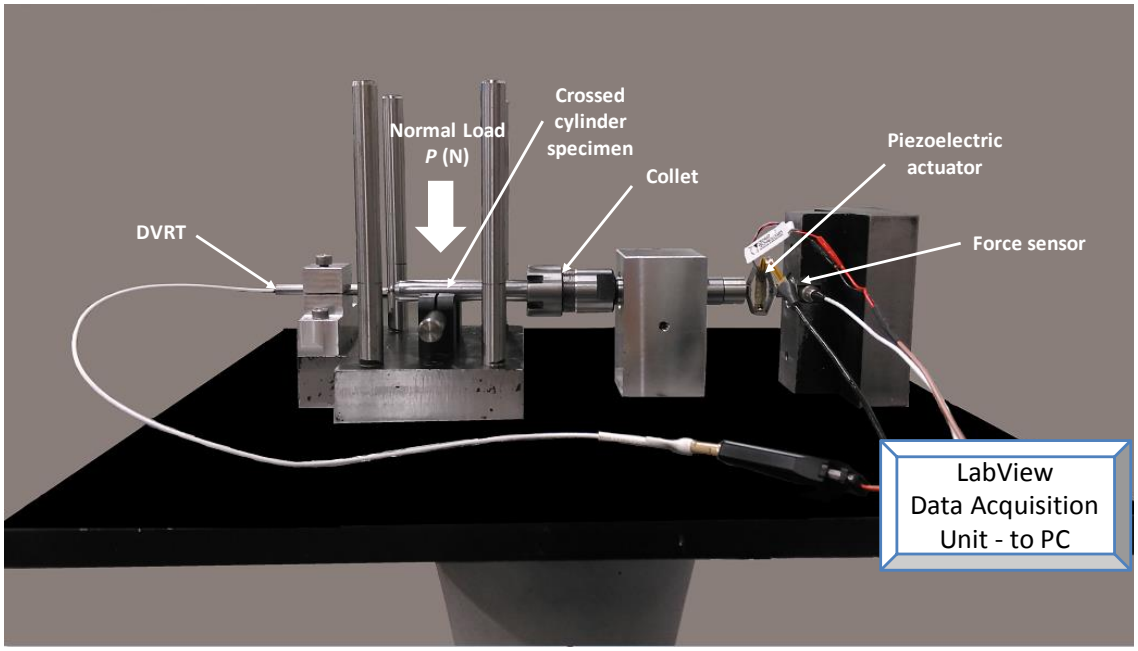

Figure 3.3. Design of fretting rig, without dead weights.

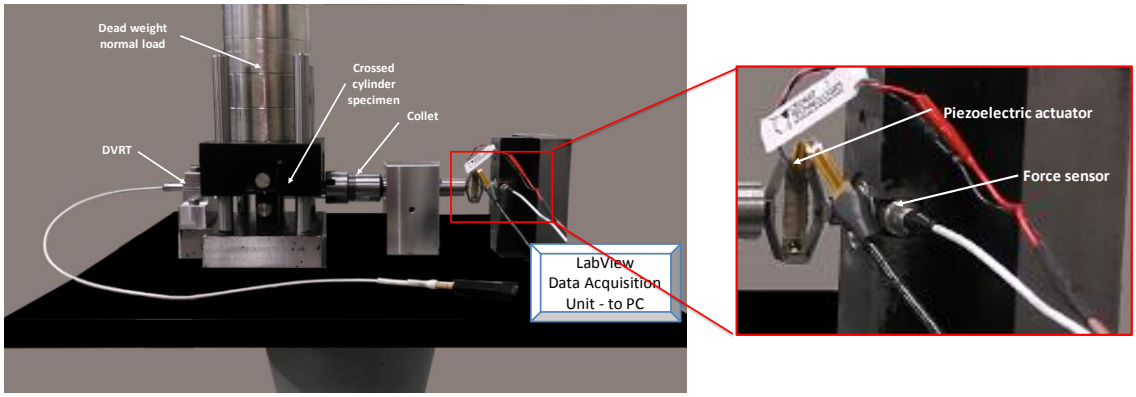

Figure 3.4. Fretting rig with dead weight normal load applied, zoom in on piezoelectric actuator and force sensor.

3.4.2. Drive line and actuator

Based on the expected displacements in the nub-groove region of flexible marine risers, a linear drive line was chosen for this new test rig. This allows for testing of pressure armour material under realistic testing conditions. This set-up also limits the number of connections along the drive line, and therefore, fewer areas in the rig where fretting can take place. Using a linear drive line also allows for greater control of the applied displacement.

The actuator used to produce the reciprocating displacement is an amplified piezoelectric actuator manufactured by Cedrat Technologies (part no. APA40SM). The principle of a piezoelectric actuator is based on the deformation of a ceramic stack caused when the stack is electrically charged. The ceramic stack is aligned along the major axis of the actuator (see Figure 3.5(a)). A small displacement of the major axis then creates a large displacement along the minor axis (as shown in Figure 3.5(a)). This actuator can operate under high forces (up to 172 N blocking force) and low displacements (stroke of ± 15 μm) with high resolution (in the range of nm) and has a

predicted life greater than 10^{10} cycles. The resonance frequency of the actuator is 4100 Hz. These properties, in particular, low stroke, make the piezoelectric actuator ideal for use in a fretting rig. The actuator is driven using a linear amplifier (LA75A) (see Figure 3.5(b)). The linear amplifier is designed to drive capacitive loads like piezoelectric actuators with extremely low noise. A strain gauge sensor (SG75-1) was included with the actuator to provide closed loop feedback along with a PID (Proportional, Integral, Derivative) controller (UC45), explained later in Section 3.4.6.

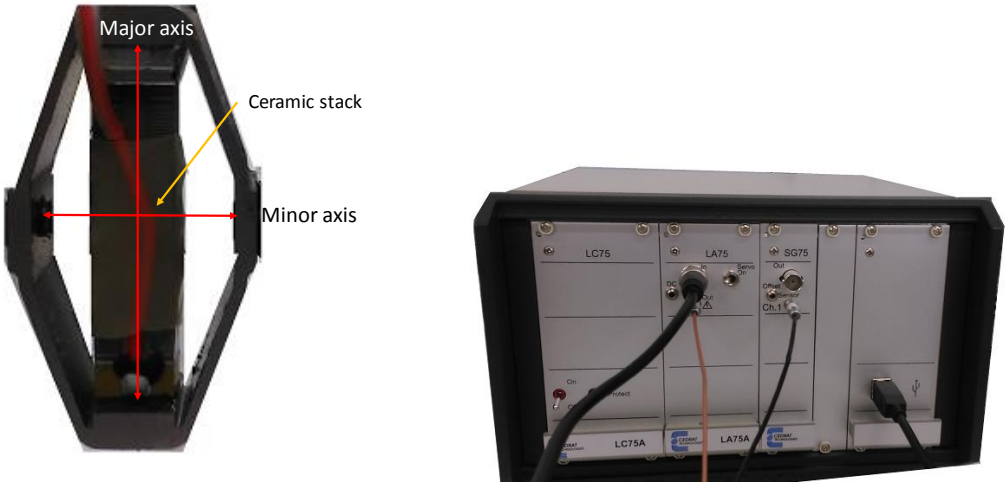

(a) (b)

Figure 3.5. (a) Piezoelectric actuator (APA40SM) with strain gauge sensor (SG75-1) and (b) Linear amplifier (LA75A) and strain gauge signal conditioner.

A linear bearing was used to carry the weight of the driving shaft, and allows accurate, low-friction linear relative movement, thereby minimising bending of the actuator. The linear bearing used is self-lubricating and therefore, causes minimal additional frictional force during testing.

3.4.3. Specimen and normal load application

A crossed cylinder configuration has been implemented in this design. This configuration has less alignment problems compared to alternative specimen geometries discussed previously (Section 3.2.1). The crossed-cylinder configuration consists of two stationary cylindrical specimens (top and bottom) and one reciprocating cylindrical specimen (middle) (see Figure 3.6). Therefore, there are two pairs of wear scars per test. The bottom stationary specimen is clamped to the base of the test rig; the top stationary specimen is clamped to the loading platform. The middle, reciprocating specimen is held in the rig using a collet that is attached to the drive shaft. The reciprocating specimen can be modified to allow for cylinder-on-flat tests.

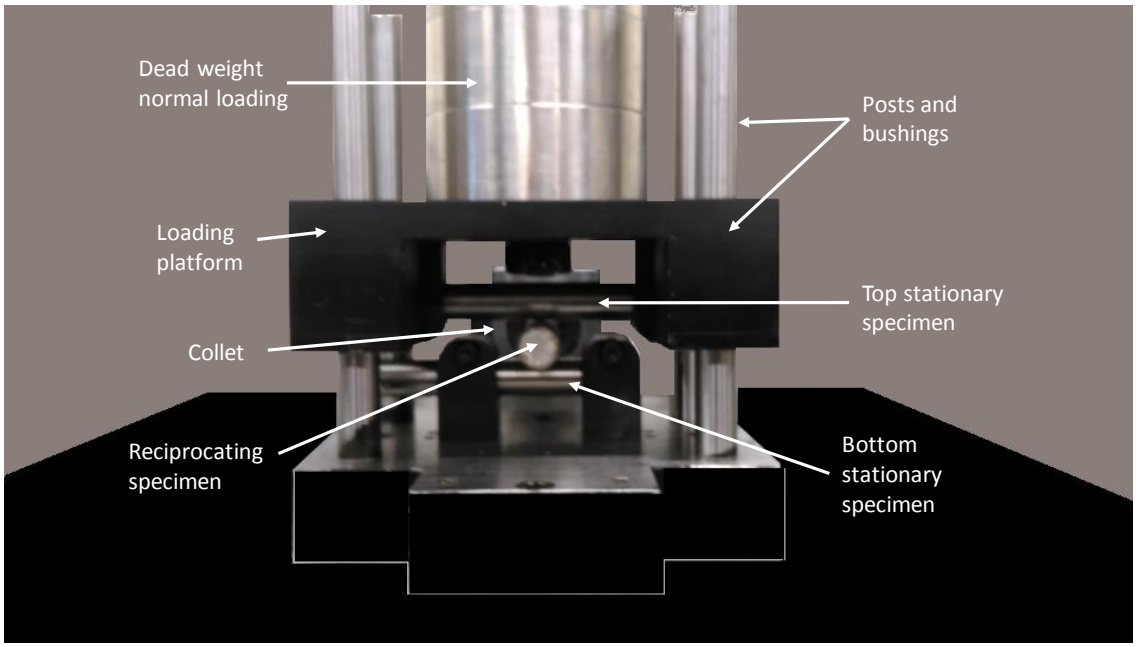

Figure 3.6. Photograph of crossed-cylinder specimen and dead weight normal loading.

Normal load is applied to the specimen using dead weights on the loading platform. The loading platform slides on four posts and bushings; these bushings prevent lateral motion during the fretting tests (see Figure 3.6).

3.4.4. Displacement measurement

The displacement can be measured at two points in the test rig: (i) at the actuator, from strain gauge (SG75-1) readings, and (ii) at the free end of the reciprocating specimen from a highly accurate DVRT (Differential Variable Reluctance Transducer). Since the location of the DVRT measurement is closer to the contact than the strain gauge, it provides more accurate measurement of contact displacement and therefore, is used for postprocessing analysis. The DVRT is clamped in place during the tests with the spring-loaded tip touching the free end of the specimen. The DVRT must be powered on 20 minutes prior to testing taking place, to allow for signal stabilisation. A polynomial fit for sensor output (x) in volts versus displacement (Δ) in μm has been derived from calibration of the DVRT (Equation (3.1)). This polynomial fit gives an error of less than 0.1 μm in the displacement measurement (see Appendix A for calibration certificates).

$$\begin{aligned}\Delta = &-255.11 + 103.629x - 3.6586x^2 - 3.17884x^3 + 1.60274x^4 \\ &+ 0.448693x^5 - 0.00626209x^5 + 0.000346283x^6\end{aligned} \tag{3.1}$$

A graphical representation of this relationship is shown in Figure 3.7. This has been incorporated into the programming system used for data acquisition explained later.

Calculations were conducted to ensure that the operating frequency would not cause lift-off of the DVRT arm tip (i.e. lose contact) from the specimen due to the increased inertia of the DVRT arm. Assuming a sinusoidal displacement profile, the DVRT will remain in contact with the reciprocating specimen at frequencies lower than the critical frequency of, ω_{crit}:

$$\omega_{crit} = \sqrt{\frac{T_s + k\Delta^*}{m\Delta^*}} \tag{3.2}$$

where k is the spring stiffness of the internal spring in the DVRT, taken here as 1.5 × 10^{-2} Nm^{-1}, Δ^* is the displacement amplitude (15 μm), m is the mass of the arm tip of the DVRT, taken here as 0.004 kg and T_s is the pre-load force (1 N) in the DVRT spring at the zero position. The critical frequency for lift-off of the DVRT is ~250 Hz, which is far in excess of the test frequencies expected for the rig, thus precluding DVRT arm tip lift-off.

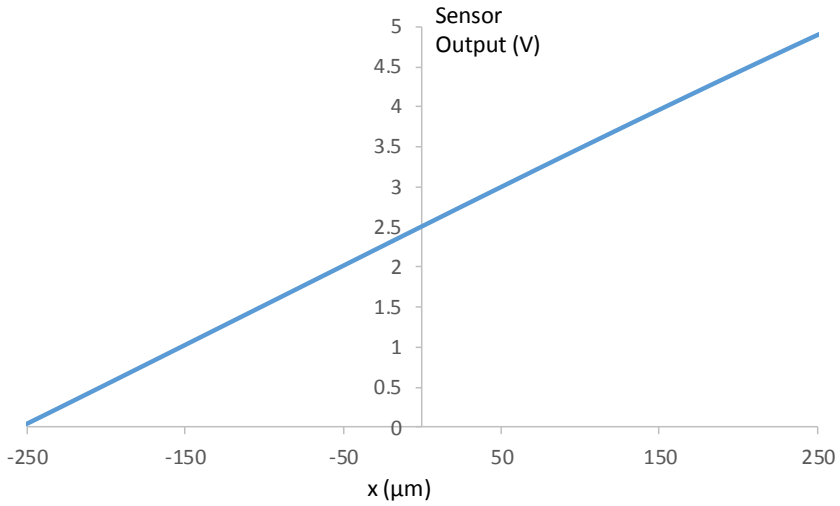

Figure 3.7. Relationship between DVRT sensor output in volts and displacement, as described in Equation (3.1).

3.4.5. Tangential force measurement

A dynamic (piezoelectric) force sensor is mounted on the drive line to measure the tangential force due to the actuator. The resolution of the sensor is 0.0311 N, with a maximum force in compression of 4448 N and a maximum force in tension of 222 N.

The force, Q, is linearly proportional to the sensor output, x, as follows (see Appendix A for calibration certificates):

$$Q = 0.023x \tag{3.3}$$

One disadvantage of using a piezoelectric force sensor is that it is not able measure static loads. This is due to the nature of the sensor, i.e. a change in force is required to produce a signal from the sensor. The time constant for the force sensor used here is 5 s; this makes the piezoelectric sensor suitable for quasi-static loading in the newly designed fretting rig i.e. no constant force is expected for greater than 5 s during fretting testing. This gives a minimum operational frequency of approximately 0.1 Hz.

It can be seen from Figure 3.3 that the force sensor is located behind the actuator; therefore, the force measured by the sensor is the reaction force from the actuator. The force sensor also measures an additional inertial force (F_I) due to the acceleration of the mass of the moving components (m).

$$F_I = ma \tag{3.4}$$

here m is known to be 1.1 kg. The acceleration can be calculated from the operating frequency (2 Hz) and displacement amplitude (15 μm). This gives an inertia force of < 1.85 N; this is accounted for in the postprocessing stage. The calculation of the inertial force has been validated via zero contact force tests. In addition to this, a zero contact force test of 100 cycles is conducted prior to each fretting experimental test to verify the exact inertial force for each test; this accounts for any change in F_I due to different test specimen.

3.4.6. Control

The control of the piezoelectric actuator has been programmed by the author in LabView, a programming language developed by National Instruments (NI). It is a multi-platform graphical programming language, where the program is represented graphically instead of by text. LabView allows for communication with NI devices, such as the data acquisition device used for this test rig (NI USB-6009). The NI USB-6009 has analog and digital input and output terminals; this allows for an output signal to be sent to the device while simultaneously reading input signals.

All reference to input signals in this section refer to signals from the NI USB-6009 to drive and control the actuator, likewise, all reference to output signals refer to signals from the sensors to the NI USB-6009 and onto the PC data acquisition program.

A schematic of the rig layout and control is shown in Figure 3.8. A PC sends a signal to the actuator via the NI USB-6009 (shown in green in Figure 3.8), this voltage then passes through a linear amplifier before getting to the actuator. Output signals (shown in purple in Figure 3.8) from each sensor (force, SG75-1, DVRT) are passed through signal conditioners to convert the current produced by the sensors to voltage, which is read by the NI USB-6009. The sensor output signals are then sent to the PC via the NI USB-6009.

To control the actuator, an analog signal is sent to the linear amplifier (LA75A) via the NI USB-6009. For the purpose of tests conducted for this work, a sinusoidal signal has been used; however, this can easily be changed. The LA75A amplifier allows for also links up to a Cedrat Technologies software “Highly Dynamic Precise Motion 45” (HDPM45) for PID control of the signal (see Figure 3.9). A PID (proportional, integral and derivative) controller continuously calculates an error value as the

difference between a desired set-point and a measured process variable and applies a correction based on proportional (P), integral (I), and derivative (D) terms, respectively. The PID controller ensures optimum response behaviour of the actuator to its input commands, reducing error in velocity, acceleration and position.

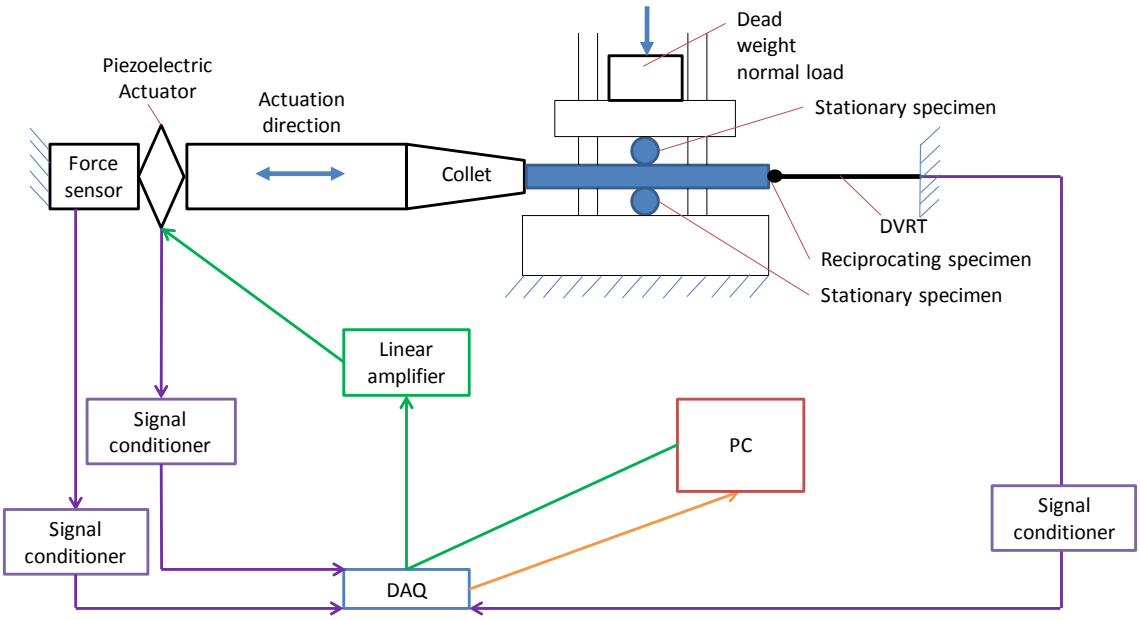

Figure 3.8. Schematic of rig layout and overall control and data acquisition using a PC and LabView NI USB-6009.

The signal sent to the LA75A can be between -1 V and +7 V, this is then amplified linearly to the actuator to between a minimum voltage of -20 V and a maximum voltage of 150 V; the HDPM45 program allows for control of the linear amplifier. These voltage differences cause the ceramic stack to expand (or contract), resulting in motion of the drive line.

A sinusoidal input signal is written into the graphical user interface (GUI) in Figure 3.10 for the actuator, following the work of Pearson (2013). A limitation of the NI USB-6009 is it allows a maximum of 150 samples per second to generate a signal

(i.e. input to drive the actuator); this limits the maximum frequency of the actuator (to 20 Hz for a sinusoidal wave). However, this maximum frequency can be increased to 75 Hz by using a triangular signal rather than sinusoidal; it can be increased further by using a different DAQ.

The relationship between the input voltage to the actuator and the displacement can be found in the calibration certificate for the actuator in Appendix A.

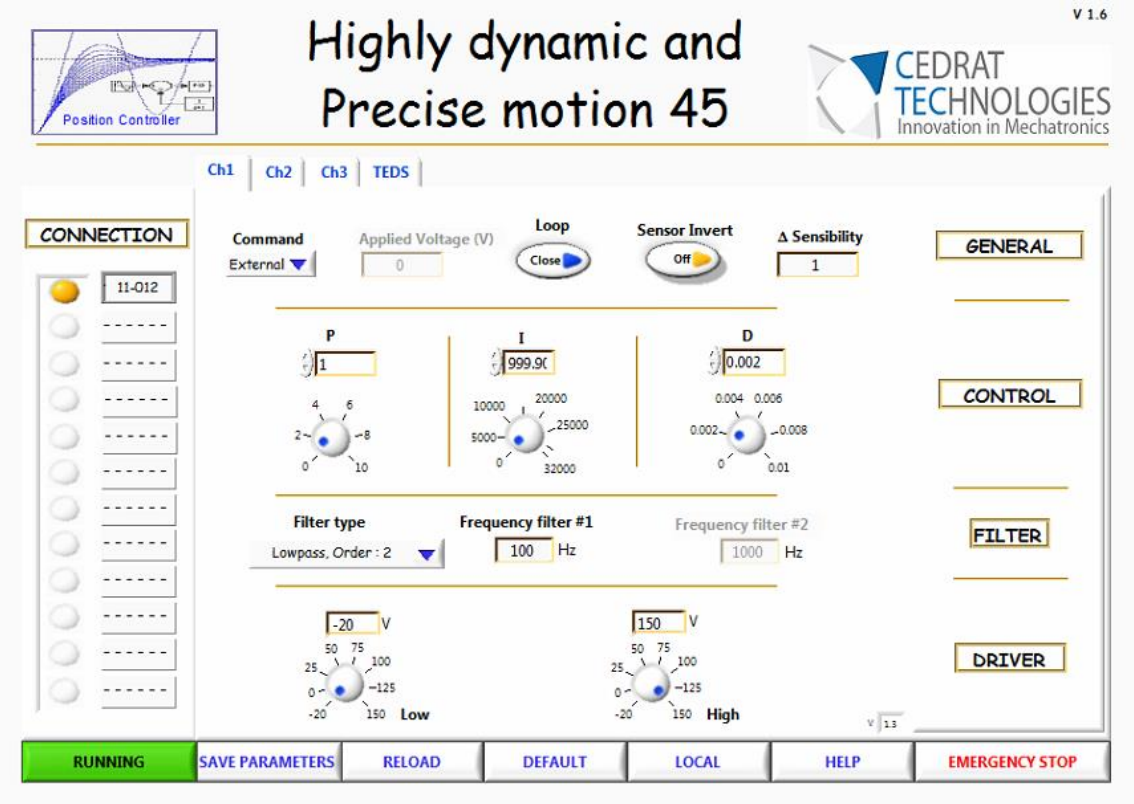

Figure 3.9. HDPM45 software interface, for control of the actuator.

3.4.7. Data acquisition and post-processing

Data acquisition from the sensors is conducted in parallel with the generation of the input signal that drives the actuator via the NI USB-6009. The LabView GUI (graphical user interface) is shown in Figure 3.10. This program allows for the

production of a signal of between 0 and 5 V to be sent to the LA75A while also reading in the output signals from the strain gauge at the actuator (SG75-1), force sensor and DVRT. The readings are stored in ".lvm" (LabView measurement) format, and a new file is written once the file size exceeds 0.8 GB. This allows multiple files per test and therefore, tests to be conducted up to a large number of cycles. The LabView program also allows for real time monitoring of the input signal to the actuator and sensor outputs, and of test progress via the progress bar or cycle counter. The sensor output signals are recorded at 500 Hz, this ensures 250 data points per fretting cycle for tests at a frequency of 2 Hz.

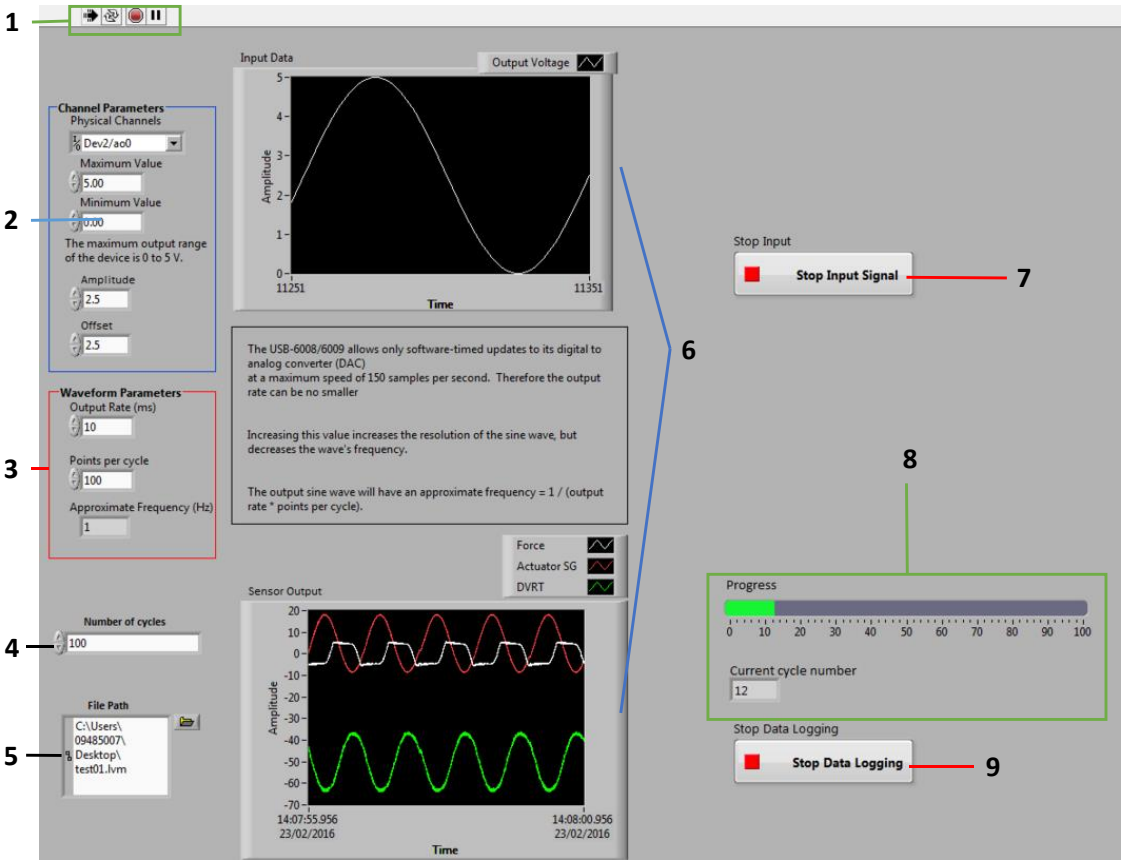

Figure 3.10. LabView program GUI.

Figure 3.10 shows the LabView user interface for control of the test rig and data acquisition. Labels 1 - 9 are defined as follows:

1. LabView commands to Run, Refresh, Stop and Pause the program.
2. Channel parameters for input (sinusoidal) signal to actuator. This allows the user to pick the channel on the NI USB-6009 for the output signal, it also allows for a minimum and maximum voltage to be specified as well as the offset (from 0 V) and amplitude of the output signal.
3. Waveform parameters allows for the frequency of the output signal to be set by specifying output rate in ms and number of points per cycle (maximum 150, due to DAQ USB-6009 digital to analog converter (DAC)).
4. Number of cycles for the test.
5. File location of the .lvm results files for the test.
6. Real time visualisation of (top) the input wave to the actuator and (bottom) the output signals from the sensors (force in N, DVRT in μm and SG75-1 in μm).
7. Stop button to stop sending the output frequency to the actuator.
8. Progress bar and cycle counter for tests.
9. Stop button to stop logging input data from the sensors.

The force sensor and DVRT signals are passed through a 5^{th} order Buttersworth low pass frequency filter (Pearson, 2013). A post-processing program has been written in MatLab which incorporates the frequency filter, and also plots the evolution of fretting loops, CoF (Coulomb, 1821), ECoF (Fouvry et al., 2004) and GICoF (Jin et al., 2016) with number of fretting cycles (as described in Chapter 2).

3.5. Summary and conclusions

A review of experimental methodologies for fretting has been presented. This includes specimen geometry and selection, methods of generating and controlling reciprocating micro-scale displacement required for fretting and methods of applying normal load.

The requirements for a newly designed test rig in NUI Galway have been outlined. A review of previous methods used by researchers in NUI Galway has also been discussed. The design of the new fretting rig has been presented and details on specimen geometry, actuation, normal load application, force and displacement measurements, control of the rig and data acquisition have been presented.

The use of a piezoelectric actuator allows for displacements of ± 1 to 15 μm and a maximum tangential force of 172N (typical of riser nub-groove contact conditions); this is significant improvement on the capabilities of previous test rig used for fretting wear tests in NUI Galway. A piezoelectric force sensor and DVRT are used to measure the tangential force and displacement, respectively. The LabView program allows for simultaneous actuator control and data acquisition to take place. Any input wave shape (i.e. triangular, sinusoidal or square) at frequencies from 0.1 to 75 Hz can be used to drive the actuator. The LabView GUI allows for the selection of amplitude, frequency and number of cycles of the output sinusoidal wave to the actuator, as well as real-time visualisation of the input (to the actuator) and sensor output signals and a progress bar with a cycle counter. A postprocessing program has been written which incorporates a frequency filter and graphs the fretting loops from test data and calculates the coefficient of friction value using three methods, CoF, ECoF and GICoF. In the next chapter, fretting wear test results from this test rig will be presented.

Chapter 4: Fretting and fatigue experimental characterisation of pressure armour material

4.1. Introduction

This chapter presents the results of fretting and fatigue experimental testing of pressure armour material. The primary focus of this work is to characterise the tribological (friction and wear) and mechanical (yield strength, ductility, fatigue) performance of the material. The test programs have been designed to experimentally simulate nub-groove contact of the pressure armour layer, as detailed in Figure 1.4. The results from these tests will allow for identification of parameters such as friction and wear coefficients, elastic material properties and low-cycle and high-cycle fatigue parameters.

Various material forms were used for testing; this was due to limitations in material availability and test rig specimen requirements. Section 4.2 describes the material used and the manufacture of specimens for each test. This section also outlines the primary rationale behind each test conducted.

In the manufacturing of flexible risers, grease-lubricant is often used as the pressure armour layer is being laid. Therefore, it is possible that grease will remain in the nub-groove contact of this layer throughout the service life of the riser. The effect of grease-lubrication investigated using the University of Nottingham (UoN) fretting wear test rig is discussed in Section 4.3. The effect of geometry and loading conditions on

grease-lubricated fretting variables, such as the evolution of friction coefficient and wear volume, is also studied. A description of testing conducted on the newly-designed fretting rig described in Chapter 3 is given in Section 4.4. This section provides details of tests conducted for partial and gross-slip regimes under high contact pressure. Test conditions and results for the UoN and the newly-designed test rig at NUI Galway are compared in Section 4.5.

Mechanical testing of pre-service riser pressure armour material is outlined in Sections 4.6. Results from mechanical testing provide material data for input into analytical and computational models, such as Young's Modulus, yield stress, ultimate tensile strength. Low-cycle fatigue results allow for a plasticity material model to be defined and also, LCF parameters to be used within a multiaxial fatigue model.

4.2. Material and specimen manufacture

4.2.1. University of Nottingham test specimen

Fretting wear experiments were conducted on 080M40, a pearlitic steel with essentially the same chemical composition and hardness as that used in the pressure armour layer of flexible marine risers (see Table 4.1). A general-purpose grease (AFB-LF Grease, THK), developed with a Li-based consistency enhancer, using refined mineral oil as the base oil, was used as the lubricant throughout this work. The test methodology employed was based on ASTM standard test methods (ASTM International, 2011, 2010). A cylinder-on-flat specimen configuration was used to represent the pressure armour wire nub-groove contact, as illustrated in Figure 4.1. The

flat and cylindrical specimens were ground on a linear and cylindrical grinder, respectively, giving a roughness (*Ra*) of 0.1 to 0.3 μm for the flat specimen and of 0.4 to 0.7 μm for the cylindrical specimen.

Table 4.1. Chemical composition of 080M40 steel (from data sheet).

Element	Fe	C	Mg	Si	P	S
Weight (%)	Balance	0.36-0.44	0.60-1.00	0.10-0.40	0.050 Max	0.050 Max

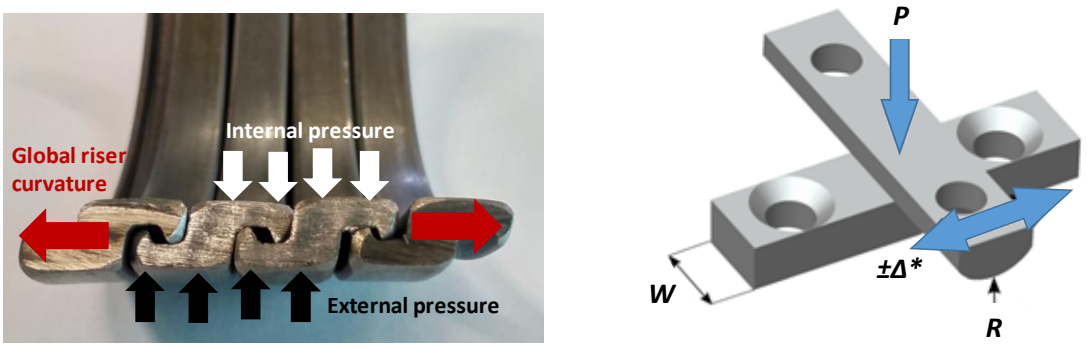

(a) (b)

Figure 4.1. Local nub-groove conditions represented as crossed cylinder-on-flat specimen configuration utilised in fretting tests.

4.2.2. Newly designed fretting rig test specimen

Fretting experiments were conducted using the newly-designed fretting test rig described in Chapter 3 on pre-drawn pressure armour, pearlitic steel material supplied by

NV Bekaert SA, Belgium. This material has the same chemical composition as the riser material; however, the microstructure is different to that of the cold formed pressure armour wire profile. A crossed cylinder specimen configuration was used, as described in Chapter 3 and shown in Figure 4.2. This configuration allows for high contact pressure tests to be conducted, representative of nub-groove contact pressures. The specimens were ground giving a roughness (*Ra*) of 0.4 to 0.7 μm. The test methodology employed, here was also based on ASTM standard test methods (ASTM International, 2011, 2010).

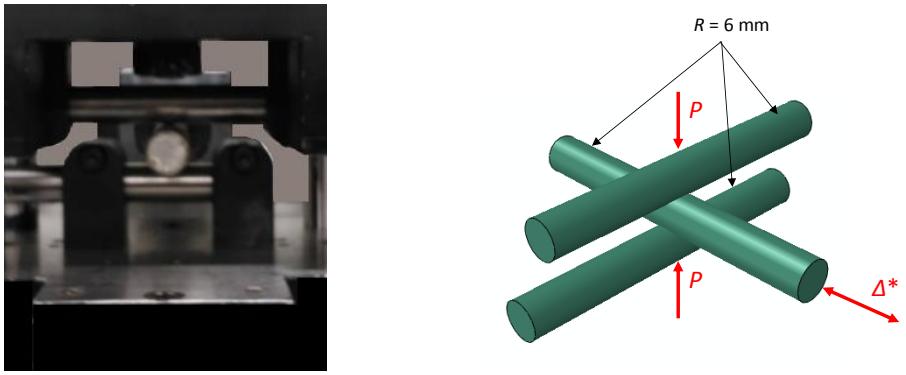

(a) (b)

Figure 4.2. (a) Picture of the crossed cylinder configuration of the newly-designed fretting rig at NUI Galway, (b) schematic of the loading conditions on the cylindrical specimen in the test rig.

4.2.3. Tensile and low-cycle fatigue test specimen

A pre-service flexible marine riser was dissected to obtain pressure armour wire material to manufacture test specimens (see Figure 4.3(a)). The pressure armour is helically wound at approximately 85° to the longitudinal section of the riser. This material was used for monotonic tensile test and low-cycle fatigue (LCF) test specimen. A modified fatigue specimen geometry, based on the ASTM E606-04 (2010) standard

for strain-controlled fatigue testing, has been designed to facilitate the use of formed pressure armour wire, following straightening. Figure 4.4 illustrates the test specimen geometry used for these tests. The measured chemical composition of this material is presented in Table 4.2.

Details of the riser dissection process are provided in Appendix B.

(a) (b)

Figure 4.3. (a) Helically wound pressure armour wire in the dissected riser, and (b) pressure armour layer material extracted from the pipe

Table 4.2. Measured chemical composition of pressure armour material.

Element	Fe	C	Mg	Si	P	S
Weight (%)	98.2	0.38-0.43	0.75-0.77	0.30-0.31	0.012-0.015	0.006-0.008

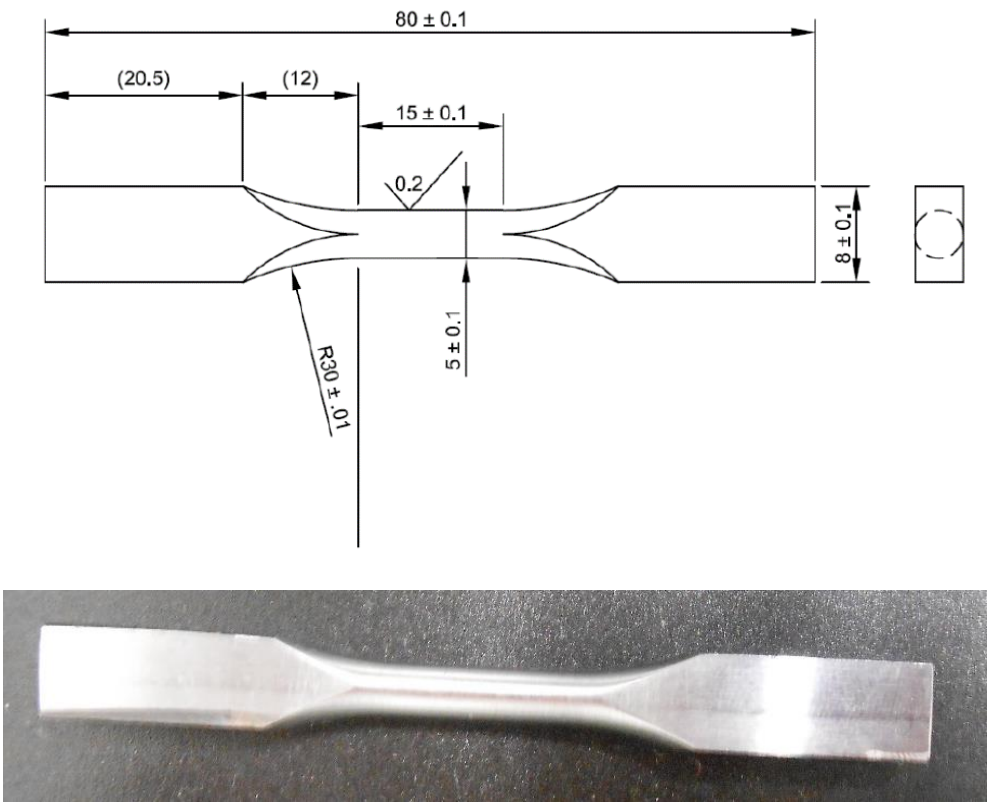

Figure 4.4. Test specimen used for monotonic tensile and low-fatigue tests.

4.2.4. Test material and specimen summary

Table 4.3 presents a summary of the various materials for each test, a description of each material is also provided. The tests include: fretting wear at the University of Nottingham (UoN), fretting tests at NUI Galway and monotonic and low-cycle fatigue (LCF) tests. The desired parameters from each test are also provided; these include wear and fatigue coefficients, Young's modulus, yield strength, ultimate tensile strength, ductility and Coffin-Manson constants.

Table 4.3. Summary of material used for testing.

Test	Material	Rationale
Fretting wear (UoN)	080M40 – a representative pressure armour material	Wear and friction coefficients for cylinder-on-flat configuration
Fretting (NUI Galway)	Pre-drawn pressure armour material (NV Bekaert SA, Belgium)	Wear and friction coefficients for high contact pressure cases
Monotonic tensile	Pressure armour material from pre-service riser	Young's modulus, yield strength, ultimate tensile strength, ductility
LCF	Pressure armour material from pre-service riser	Coffin-Manson constants, cyclic behaviour for plasticity model

4.3. Effect of grease-lubrication on fretting variables

4.3.1. Introduction

This section paper presents an experimental investigation into the effects of contact conformity, contact pressure and displacement amplitude on the gross-slip fretting behaviour grease-lubricated cylinder-on-flat contacts in the context of flexible marine riser pressure armour wire, and compares behaviour with that observed in unlubricated conditions. Characterisation of friction and wear is critical to fretting fatigue life prediction in flexible risers since friction directly controls trailing-edge fretting

stresses and hence fatigue crack initiation, on the one hand, and on the other hand, directly affects wear via relative tangential slip (displacement). Wear can have a beneficial or detrimental effect on fatigue crack initiation and propagation, depending on relative slip and slip regime.

4.3.2. Test conditions and procedures

The UoN fretting test rig used is described in detail elsewhere (Jin et al., 2015; Pearson, 2013; Warmuth et al., 2015). The flat specimen is mounted on the lower specimen mounting block (LSMB) which is stationary and the cylindrical specimen is mounted on the upper specimen mounting block (USMB) (Pearson, 2013). For the lubricated tests, grease was applied to both the flat and cylindrical specimens before the specimens were brought into contact. No more lubrication was applied during the testing process; this represents the method by which grease can enter the nub-groove contact region of flexible risers during laying of the pressure armour wires in the riser manufacturing process. A dead-weight and lever configuration was used to load the USMB, resulting in a normal load, P, being applied to the (cylindrical) specimen. The layout and components of the rig can be seen in Figure 2.22(a). The linear displacement of the cylindrical specimen is achieved via USMB using an electromagnetic vibrator (EVM). The displacement of the USMB (cylindrical specimen), Δ, is monitored and controlled throughout the test using a capacitance displacement sensor mounted on the LSMB, to achieve a specific displacement amplitude, Δ^*.

The tangential force, Q, is measured and recorded throughout the test by a piezoelectric load cell which is connected to the quasi-stationary LSMB (see Figure

2.22(a)). Both displacement and load sensors have been calibrated (both externally and in-situ) under static conditions. The load and displacement signals are sampled at a rate of two hundred measurements per fretting cycle for all of the experiments (Pearson, 2013).

Real-time visualisation of the fretting loops allows for monitoring of the fretting contact behaviour throughout the test. A gross-slip fretting loop is shown in Figure 4.5. The measured displacement amplitude, Δ^*, is always slightly larger than the contact slip amplitude, δ^* due to rig compliance and elastic deformation of the specimen since the fretting contact region is separated from the location of the displacement sensor. δ^* can be derived by measuring the displacement at zero force, as illustrated Figure 4.5. There are many methods of measuring the coefficient of friction, (Coulomb, 1785; Fouvry et al., 2004; Jin et al., 2016), for example. In this work, the ECoF parameter proposed by Fouvry et al. (2004), is used. It was observed (Fouvry et al., 2004) that the tangential force does not remain constant through the sliding part of the fretting loop, as illustrated in Figure 4.5, and thus they proposed that the energy dissipated per cycle could be used to define a coefficient of friction which is more representative of the overall behaviour of the contact.

The energy coefficient of friction (ECoF) (Fouvry et al., 2004) is defined as follows

$$ECoF = \frac{E_d}{4P\delta^*} \tag{4.1}$$

where E_d is the dissipated energy per cycle (area of the fretting loop, see Figure 4.5) (Fouvry et al., 2004).

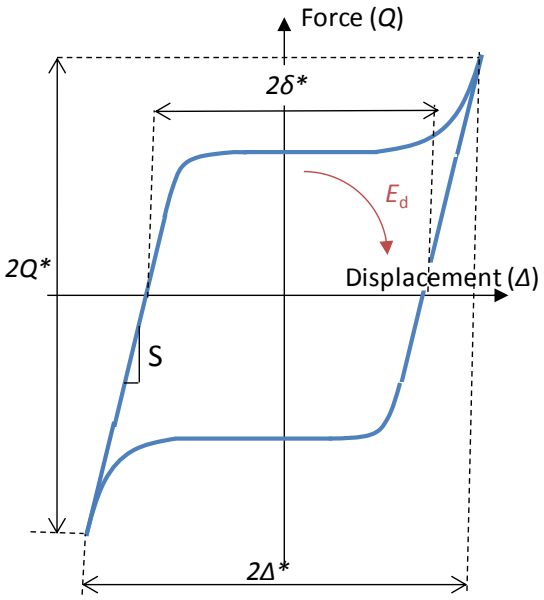

Figure 4.5. Schematic diagram of fretting loop with high tractional force peak at the ends of gross sliding.

Cylinder-on-flat fretting tests were conducted with cylinder radii, R, of 6 mm (less-conforming contact pair) and 160 mm (more-conforming contact pairs). The flat specimen has a width, W, of 10 mm, as seen in Figure 4.1 (this defines the contact length). Experiments were conducted for a range of Hertizian contact pressures, p_o, and applied displacement amplitudes, Δ^*, as summarised in Table 4.4. The experiments were conducted with and without grease lubricant at ambient temperature (typically 22^{o}C), at a frequency of 20 Hz, for a duration of 100,000 cycles.

4.3.3. Estimation of wear volume and surface topography

Following the methodology of Jin et al. (2015) and Warmuth et al., (2015), the test specimens were swabbed lightly with methylated spirits to remove loose debris and

residual grease after testing. The profile of the wear scar on each specimen was scanned and measured using a Bruker Contour GT-I interferometer (vertical resolution ~ 0.15 nm and lateral resolution of 4 μm). The scan area is depicted in Figure 4.6; the scan area includes part of the unworn surface (away from the wear scar). This allows for a reference surface to be defined (Elleuch and Fouvry, 2002) (see Figure 4.7).

Table 4.4. Summary of the fretting test parameters.

Lubricant temperature	Ambient
Cylinder radii, *R*	6, 160 mm
Displacement amplitudes, *Δ**	15, 30, 50, (100) μm
Test duration, *N*	100,000 cycles
Normal Load, *P*	250, 500 N
Hertizian contact pressure, p_o	370 & 525 (6 mm radius), 70 & 100 (160 mm radius) MPa
Initial contact width, *a*	43 & 61 (6 mm radius), 221 & 313 (160 mm radius) μm
Oscillation frequency	20 Hz
Lubricant	Dry, Li-based grease

Specific wear (Archard wear coefficient) and transfer rates for the contact pair are calculated as follows:

$$\frac{dV^-}{dN} = \frac{V^-}{4PN\delta^*} \tag{4.2}$$

$$\frac{dV^+}{dN} = \frac{V^+}{4PN\delta^*} \tag{4.3}$$

where δ^* is the average test slip amplitude, P is the normal load, N is the number of cycles per test, V^- and V^+ are the total wear and transfer volumes, respectively, for the contact pair, given by:

$$V^- = V^-_{flat} + V^-_{cyl} \tag{4.4}$$

$$V^+ = V^+_{flat} + V^+_{cyl} \tag{4.5}$$

where V^-_{flat} and V^-_{cly} are the volumes of the void below each reference surface is the wear volume for the flat and cylindrical specimens, respectively (see Figure 4.7). Similarly, V^+_{flat} and V^+_{cyl} are the volume of (transferred) material above the reference surfaces for the flat and cylindrical specimens, respectively (see Figure 4.7). Note that this may contain displaced metal or oxide debris, and therefore, may be originally from either specimen.

The energy wear coefficient, α, (as described in Chapter 2) is defined as follows:

$$\alpha = \frac{V^-}{\sum E_d} \tag{4.6}$$

where E_d is the energy dissipation per fretting cycle as shown in Figure 4.5.

Since this work focuses on the effect of loading conditions, contact conformity and lubrication on fretting wear behaviour of pressure armour material, it is essential to determine the error associated with each wear coefficient. This allows for any differences

to be deemed significant or irrelevant. The overall error can be calculated if the error of the individual input factors is known (Doebelin, 1975). For a given function, F, with n independent variables, u_1, u_2,… u_n.

$$F = f(u_1, u_2, ..., u_n) \tag{4.7}$$

and the variables have errors of $\pm\Delta u_1, \pm\Delta u_2, ..., \pm\Delta u_n$, respectively. The probable overall error is given by:

$$E_{overall} = \sqrt{\left(\Delta u_1 \frac{\delta f}{\delta u_1}\right)^2 + \left(\Delta u_2 \frac{\delta f}{\delta u_2}\right)^2 + ... + \left(\Delta un \frac{\delta f}{\delta u_n}\right)^2} \tag{4.8}$$

For the Archard wear coefficient, errors in V^-, P and δ^* were considered. Using Equations (4.2) and (4.8) and, the probable overall error is:

$$E_{overall} = \sqrt{\left(\Delta V^- \frac{1}{4PN\delta^*_1}\right)^2 + \left(\Delta P \frac{-V^-}{4P^2 N\delta^*}\right)^2 + \left(\Delta\delta^* \frac{-V^-}{4P^2 N(\delta^*)^2}\right)^2} \tag{4.9}$$

where $\pm\Delta V^-$, $\pm\Delta P$ and $\pm\Delta\delta^*$ are the errors associated with V^-, P and δ^*, respectively.

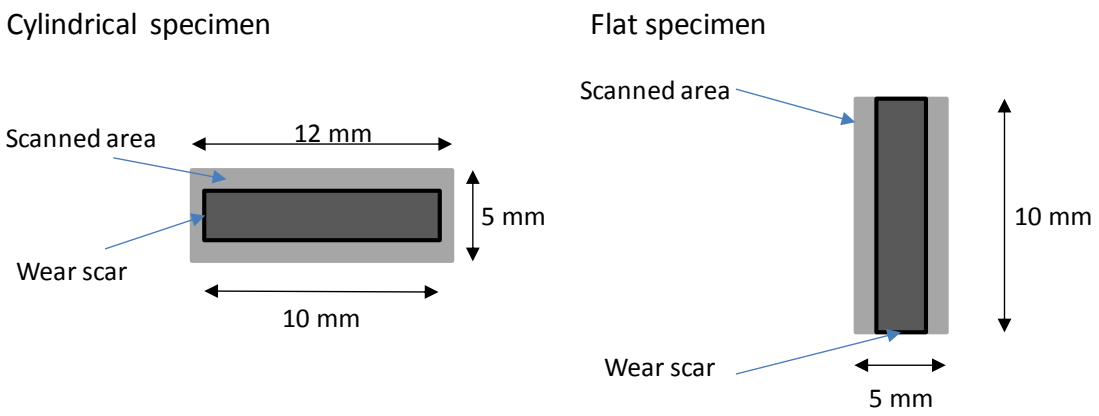

Figure 4.6. Illustration of the area measured by profilometry with respect to the fretting wear scar.

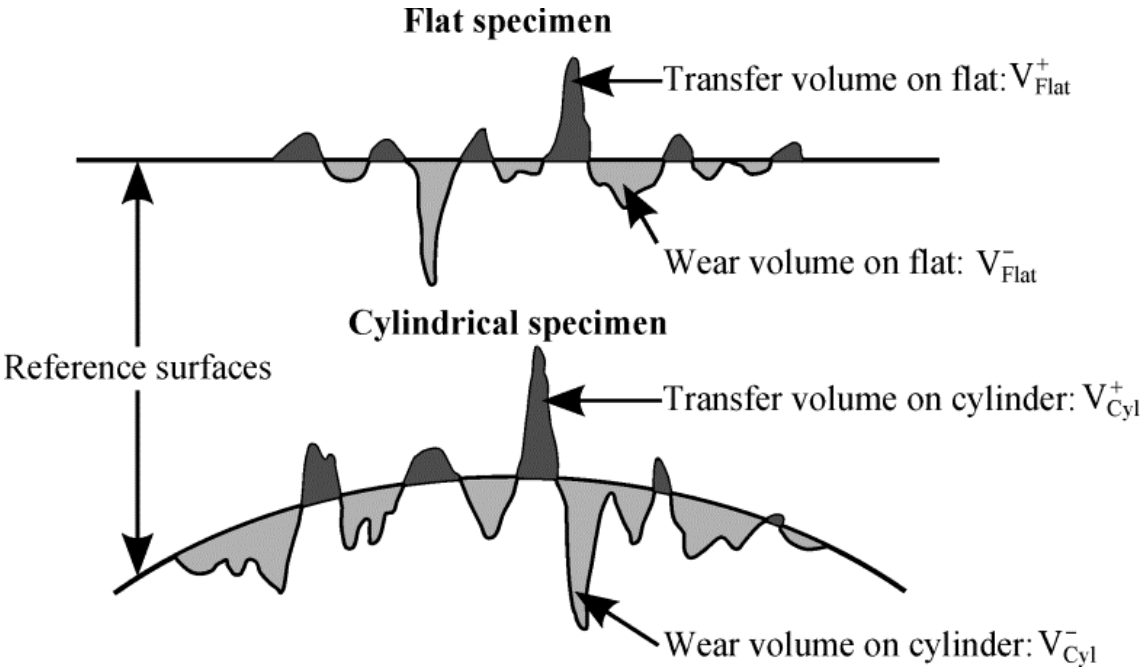

Figure 4.7. Illustration of the definition of wear and transfer volumes in a fretting scar for both the flat and cylindrical specimen (Warmuth et al., 2016).

4.3.4. Characterisation of wear scars and debris

The nature of the fretting wear scars was characterised using scanning electron microscopy (SEM) (Philips XL30 SEM). Back scattered electron (BSE) images were used to distinguish oxide from metallic material (Jin et al., 2015; Warmuth et al., 2015). Iron oxide (debris which forms in the wear scar) has a lower average atomic number; therefore, it appears darker in the BSE image than the steel. The identification of oxide was confirmed qualitatively by energy-dispersive X-ray spectroscopy (EDX) analysis.

4.3.5. Effect of lubrication

Figure 4.8 shows the development of ECoF over the duration of the tests for R = 6 mm with P = 250 N, for the dry fretting cases. An initial rapid rise in ECoF was observed over the first ~500 cycles; this then falls gradually to a steady value over the next ~9000 cycles. Similar results were observed for all dry fretting tests. The measured range of stabilised ECoF for all unlubricated tests was from 0.61 to 0.68, indicating little effect of tangential displacement for the tested conditions. Figure 4.9 presents graphs of dissipated energy against wear volume for dry fretting tests. The energy wear coefficients are 5.5×10^{-5} and 1.4×10^{-5} for 6 mm and 160 mm radius specimen, respectively.

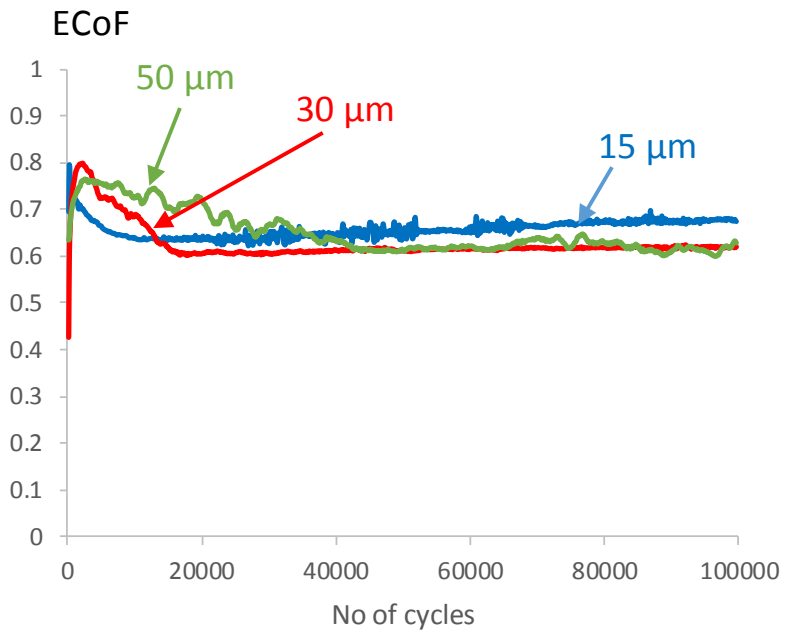

Figure 4.8. Plots of development of ECoF with number of fretting cycles for dry fretting contacts with cylinders of radius 6 mm, applied displacements of 15, 30 and 50 µm and normal load of 250 N (p_o = 370 MPa).

(a) R = 6 mm

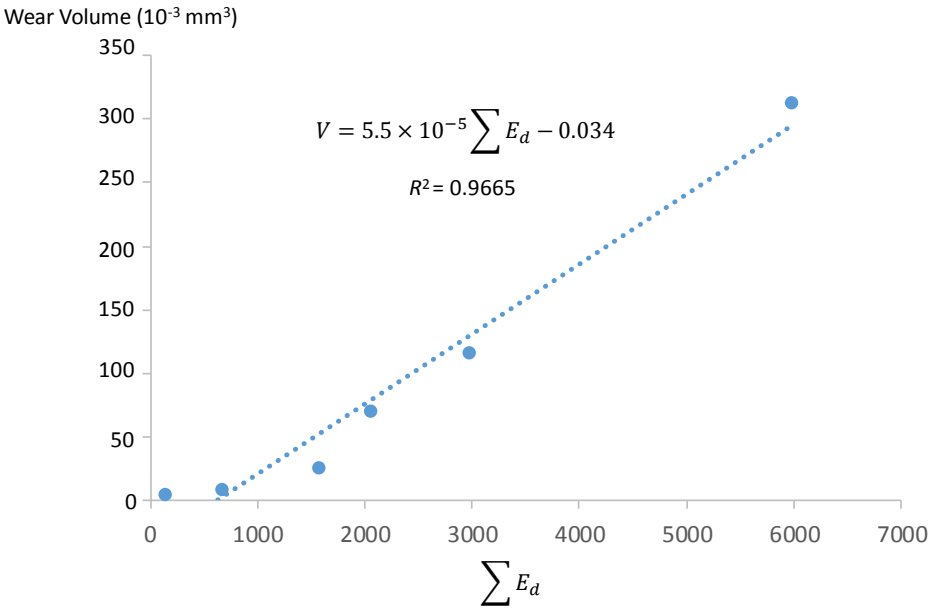

(b) R = 160 mm

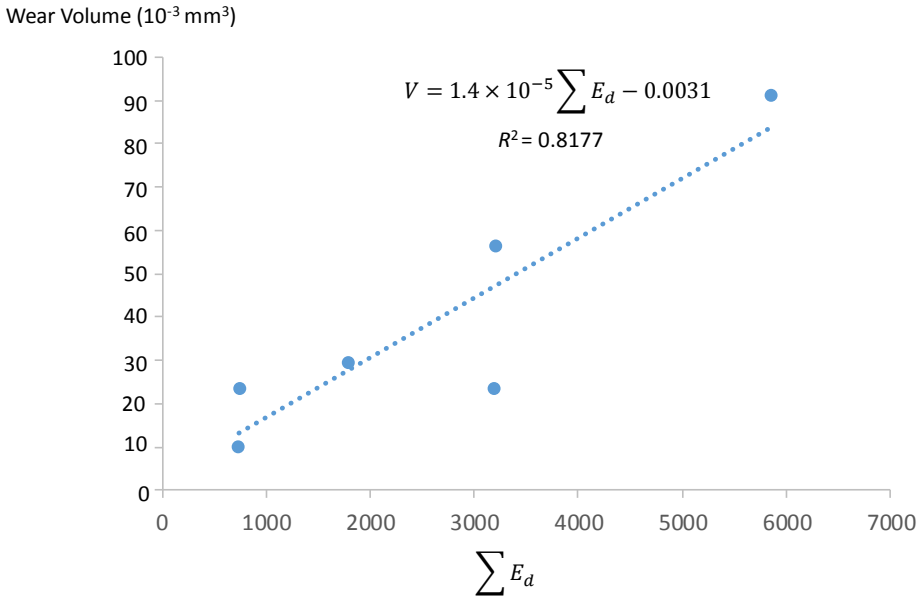

Figure 4.9. Energy dissipation Vs wear volume for (a) 6 mm and (b) 160 mm radius cylinder-on-flat dry fretting tests.

Figure 4.10(a) shows the development of ECoF over the duration of the tests for R = 6 mm with P = 250 N, for grease-lubricated cases. A significant effect of tangential displacement was observed; specifically, ECoF was found to decrease with increasing tangential displacement (dynamic riser curvature). Comparison of Figure 4.10 (a) and Figure 4.10 (b) shows that extrusion of grease from the contact increased for larger normal load (500 N) i.e. ECoF value rises faster. At the lower load (Figure 4.10 (a)), a steady ECoF of 0.12 was measured for displacement of 50 μm, whereas, at lower displacements (30 and 15 μm), the ECoF was higher and more unsteady. The ECoF values after 10^5 cycles were 0.26 ± 0.08 at 30 μm and 0.40 ± 0.18 at 15 μm. The detrimental effect of low tangential displacement (15 μm) is observed for higher normal load (500 N) test also (Figure 4.10 (b)) where a low ECoF value of ~0.13 ± 0.08 was measured for displacement of 50 μm, but at lower displacements (30 and 15 μm), the ECoF was higher and more unsteady. The ECoF values after 10^5 cycles were 0.21 ± 0.49 at 30 μm and 0.38 ± 0.4 at 15 μm. Overall, lubrication retention in the contact is promoted by lower normal load and larger tangential displacements. The most detrimental case is the combination of high normal load (500 N) and low tangential displacement (15 μm). As can be seen in Figure 4.10 (b), this case gives more unsteady and large ECoF values.

Specific wear rates (Archard wear coefficients) for tests with 6 mm radius cylindrical specimens are presented in Figure 4.11. For dry tests, the specific wear rate increases with tangential displacement. However, for grease-lubricated conditions, specific wear rate falls as displacement amplitudes increases. At lower normal load (250 N), the dry specific wear rates were higher than grease-lubricated values (Figure 4.11(a)). However, slightly higher Archard wear coefficient was observed for lubricated tests at higher normal load (500 N) and at lower displacements (15 μm and 30 μm) than the corresponding dry cases (see Figure 4.11(b)).

(a) P = 250 N

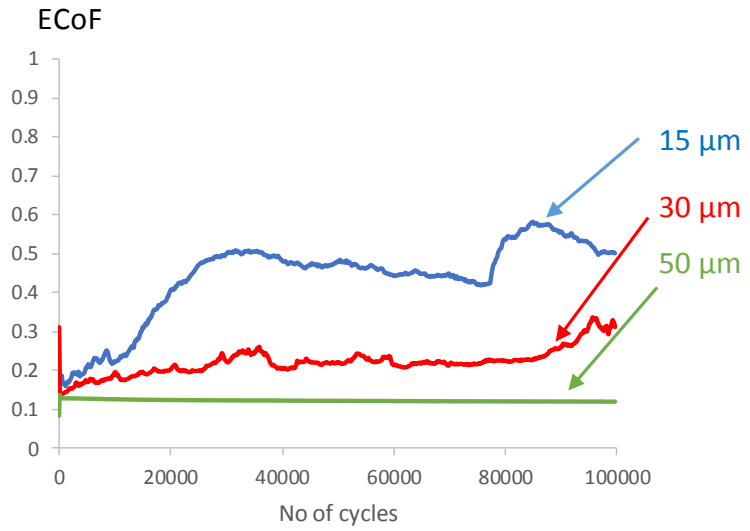

(b) P = 500 N

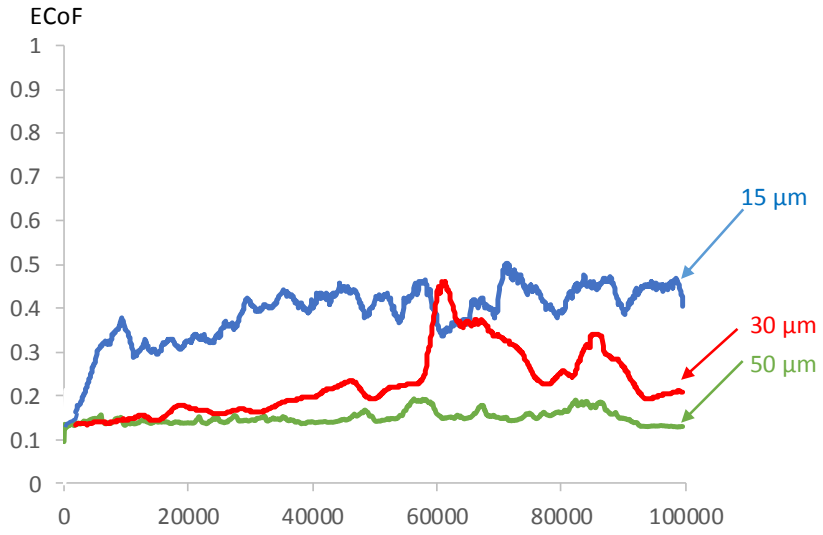

Figure 4.10. Effect of tangential displacement on evolution of ECoF with number of fretting cycles for grease-lubricated contact, with radius 6 mm and normal loads of (a) 250 N (p_o = 370 MPa) and (b) 500 N (p_o = 525 MPa).

Figure 4.12(a) presents the average 2D wear scar across the worn flat specimen surfaces for both dry and grease-lubricated tests conducted with 6 mm radius cylindrical specimens with a normal load of 250 N and a displacement amplitude of 50 µm. Figure

4.12(b, c) presents BSE images of the fretting wear scars on these flat specimen. The damage is reduced considerably for the grease-lubricated condition compared to the dry condition; in dry conditions, extensive damage can be observed with the surface being largely covered with an oxide debris layer, whereas in the lubricated case, there is evidence of only very slight damage and no evidence of any oxide debris formation.

(a) P = 250N

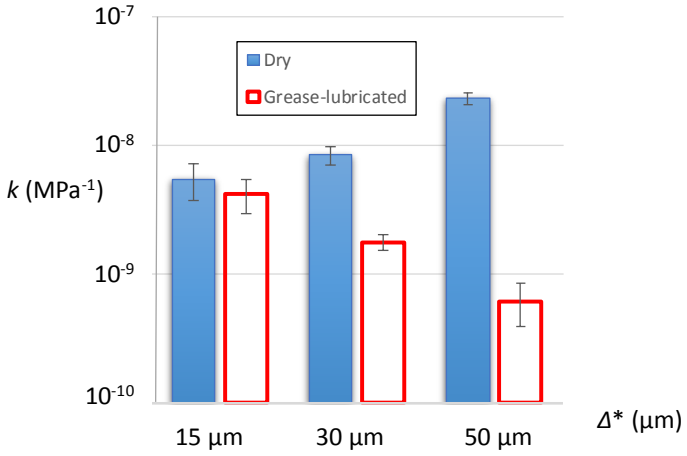

(b) P =500 N

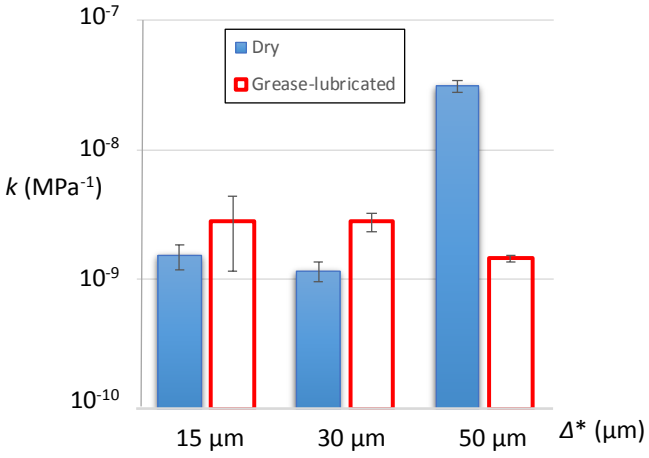

Figure 4.11. Archard wear coefficient, k (specific wear rate), including error bars calculated from Equation 9, for dry and grease-lubricated tests with cylinder of radius 6 mm, an applied displacement of Δ^* and normal loads of (a) 250 N (p_o = 370 MPa), and (b) 500 N (p_o = 525 MPa).

(a) Wear profile

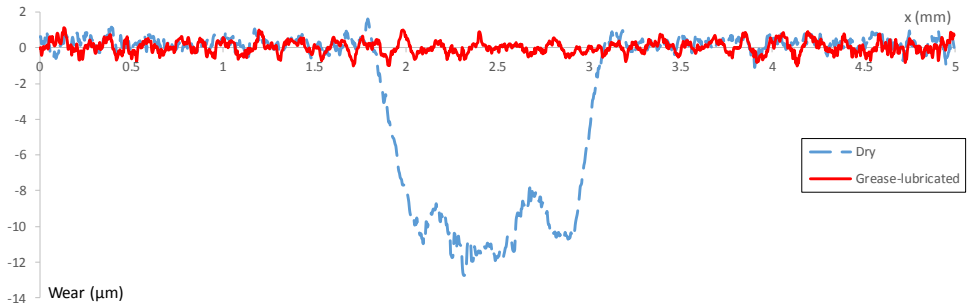

(b) BSE image of dry fretting

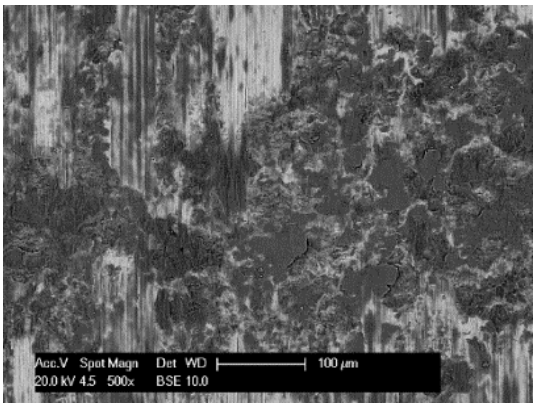

Direction of stroke

(c) BSE image of grease-lubricated fretting

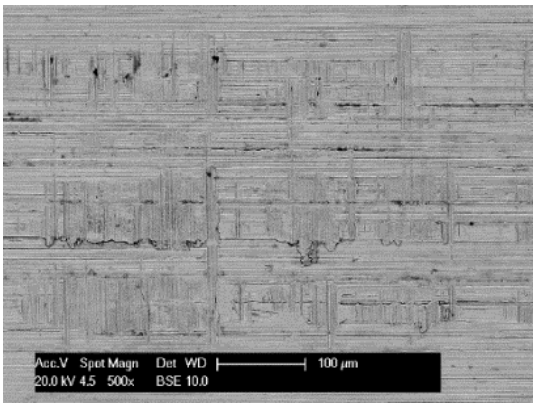

Figure 4.12. (a) Wear profiles and (b, c) BSE images (plan view) of the flat specimen wear scars at high magnification for cylinder radius 6 mm, normal load 250 N (p_o = 370 MPa) and applied displacement 50 μm, under dry and grease-lubricated conditions.

Figure 4.13 presents fretting loop evolution for the test cases presented in Figure 4.12. The fretting loops show that gross slip occurs for these tests; the peak tangential force is lower for the grease-lubricated case compared to the dry case; this is consistent with the ECoF values presented in Figures 4.8 and 4.10.

(a) Dry

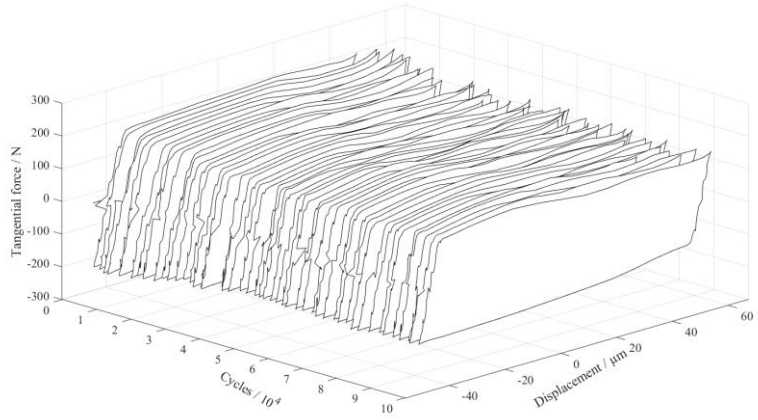

(b) Grease-lubricated

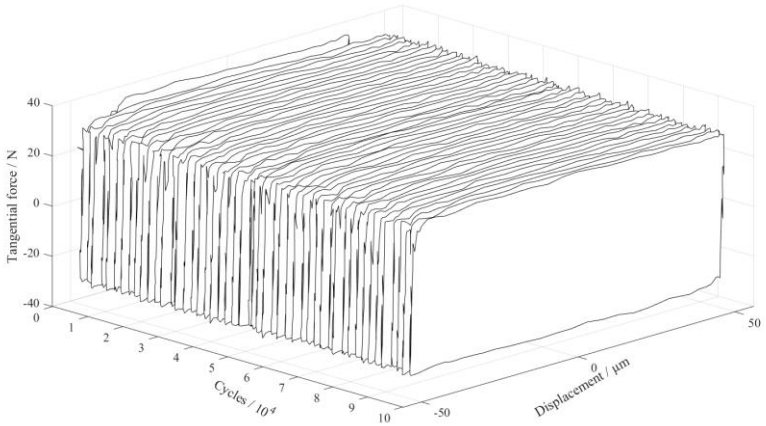

Figure 4.13. Fretting loop evolution for cylinder radius 6 mm, normal load 250 N (p_o = 370 MPa) and applied displacement 50 μm, under (a) dry and (b) grease-lubricated conditions.

4.3.6. Effect of loading conditions

Figure 4.14 presents the effect of applied displacement on evolution of ECoF for a more conforming contact geometry (R = 160 mm) with the same normal loads examined in the tests with the less conforming contacts (R = 6 mm) (presented in Figure 4.10). For grease-lubricated cases, at both of the applied loads examined, full lubrication (as observed for tests with R = 6 mm and a displacement amplitude of 50 μm (see Figure 4.10)) was not observed at either applied load. Hence, the test matrix was extended to a higher displacement amplitude (100 μm). With the inclusion of this higher displacement amplitude, the general behaviour for the more-conforming contacts is observed to be very similar to that observed with the less-conforming contacts, namely that a low value of ECoF can only be maintained once the applied displacement amplitude is greater than a certain value. Moreover, in cases where a low value of ECoF cannot be maintained (similar to work by McColl et al. (1995) and Haviez et al. (2015)), ECoF rises more quickly with higher applied load and with lower applied displacement amplitude. It is also notable that in these cases, the rate at which ECoF rises is lower for the more-conforming contacts (Figure 4.14) than it is for the less-conforming contacts (Figure 4.10).

The specific wear rates (Archard wear coefficients) for tests with the more-conforming contact geometry (R = 160 mm) are presented in Figure 4.15. for the lubricated tests (with values for the unlubricated tests presented alongside to provide context). For grease-lubricated cases with high ECoF values, viz. with displacement amplitudes of 15 μm and 30 μm (see Figure 4.14), the specific wear rate is higher than or close to the corresponding dry fretting tests. The specific wear rate decreases

significantly (by around an order of magnitude) for the grease-lubricated tests at the largest amplitudes.

(a) P = 250 N

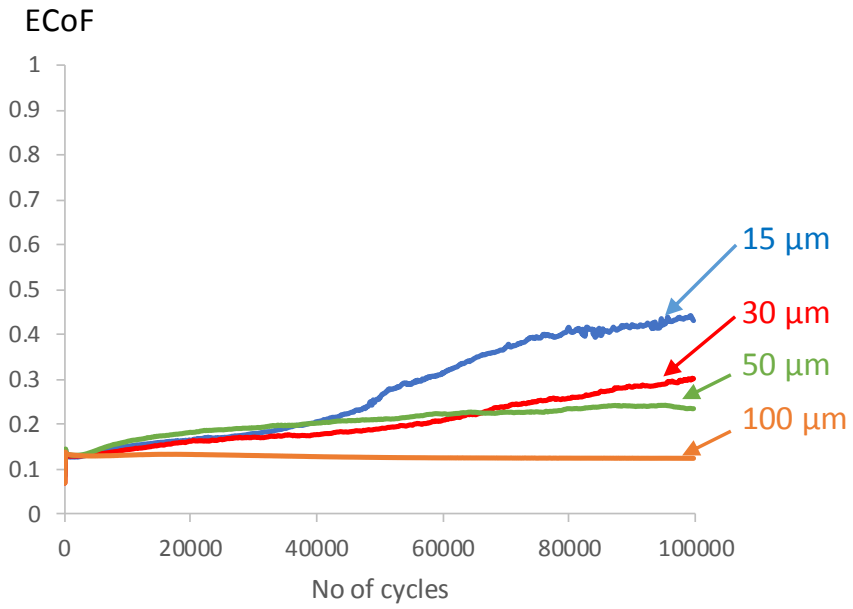

(b) P = 500 N

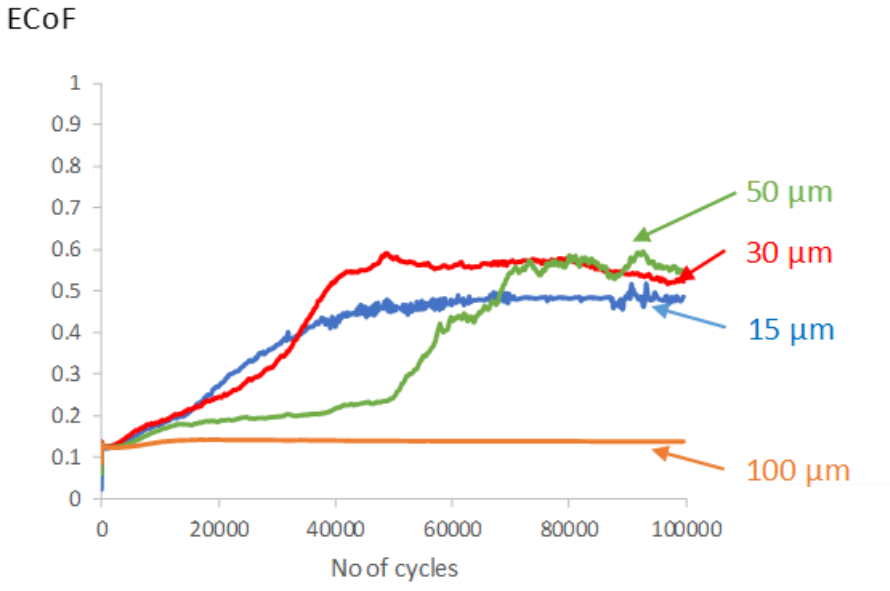

Figure 4.14. Effect of tangential displacement on evolution of ECoF with number of fretting cycles for grease-lubricated contact, with radius 160 mm and normal loads of (a) 250 N (p_o = 70 MPa) and (b) 500 N (p_o = 100 MPa).

(a) P = 250 N

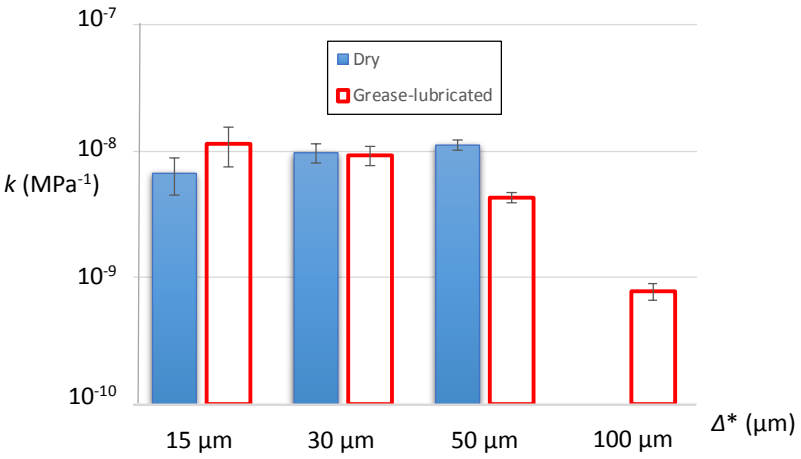

(b) P = 500 N

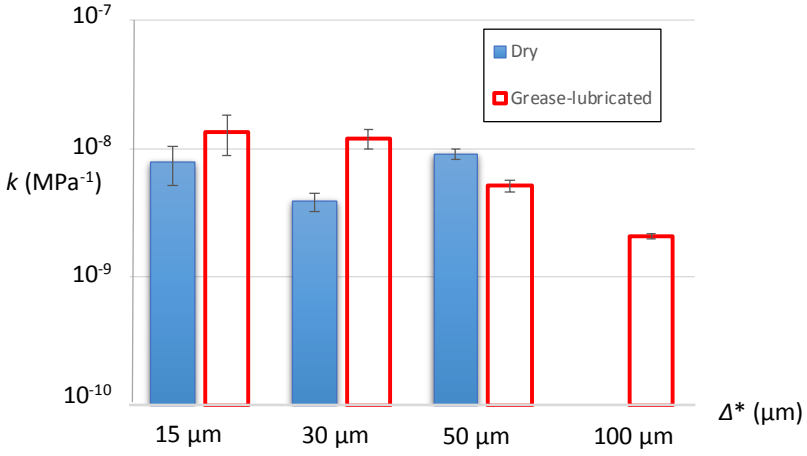

Figure 4.15. Archard wear coefficient, k (specific wear rate), for dry and grease-lubricated tests with cylinder of radius 160 mm, an applied displacement of Δ^* normal load of (a) 250 N (p_o = 70 MPa) and (b) 500 N (p_o = 100 MPa).

Average 2D wear scars across the worn flat specimen surfaces following grease-lubricated tests with the more-conforming contact geometry (R = 160 mm) are presented in Figure 4.16(a). BSE images of sample fretting wear scars on the flat specimens for

these tests are presented in Figure 4.16(b, c, d). With higher loads, lubrication becomes less effective and more fretting damage is observed. However, increasing tangential displacement from 50 μm to 100 μm reduces the damage considerably.

Figure 4.16 presents fretting loop evolutions for these tests. The fretting loops show that gross slip occurs for these tests; an increase in the tangential force occurs at the end of the sliding part of the fretting loop for tests where a rise in ECoF is also observed i.e. Figure 4.16(a - b). Fretting loops in Figure 4.16(c) are steady throughout the test, this is consistent with the steady (low) ECoF observed for this test in Figure 4.14.

4.3.7. Durability of the low friction conditions

Low friction and damage has been observed under certain conditions in the tests run for 10^5 cycles. In other cases, following 10^5 cycles, ECoF had risen to high values (around 0.5) whereas in other cases again, it had risen from its baseline (fully-lubricated) value, but was still relatively low. As such, two cases were selected for extended testing to examine how ECoF would continue to develop. Tests were conducted with both 6 mm and 160 mm radius specimen under 250 N normal load and 50 μm tangential displacement for 10^6 cycles; Figure 4.18 shows the development of ECoF for these tests. A constant and low value of ECoF of ~0.12 was observed for the less-conforming contact (R = 6 mm) with no indication of any changes over this test duration. For the more-conforming contact (R = 160 mm), the ECoF rises (consistent with the results plotted in Figure 4.14(a)) and continues to do so, reaching a value of ~ 0.24 at around 6.5×10^5 cycles, whereupon it continually fell to a value of ~ 0.18 after 10×10^5 cycles.

(a) Wear profile

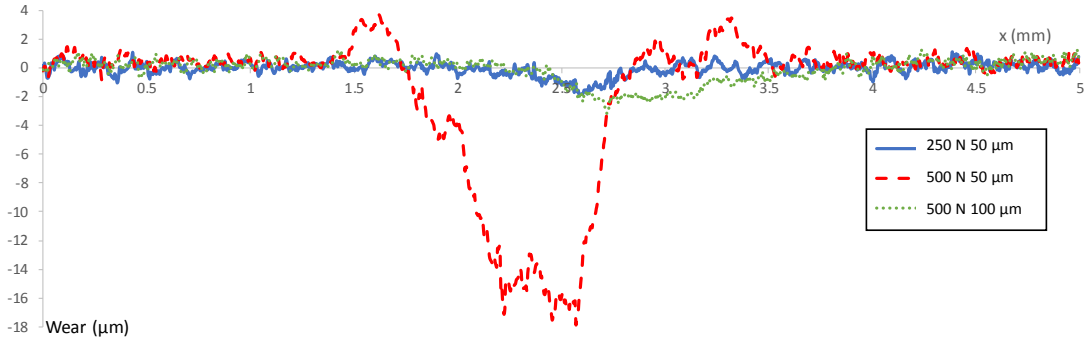

(b) P = 250 N p_o = 70 MPa Δ^* = 50 µm

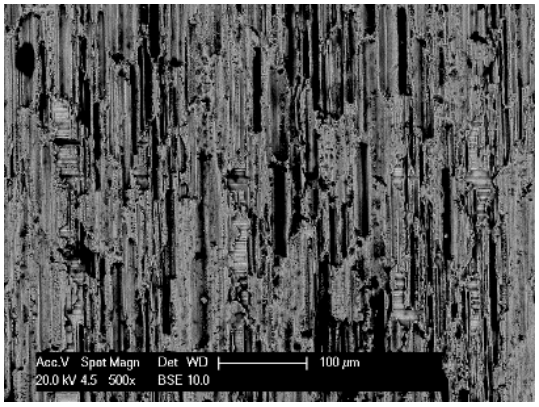

(c) P = 500 N p_o = 100 MPa Δ^* = 50 µm

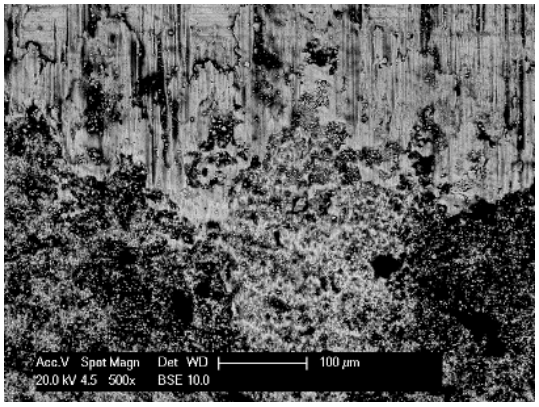

(d) P = 500 N p_o = 100 MPa Δ^* = 100 µm

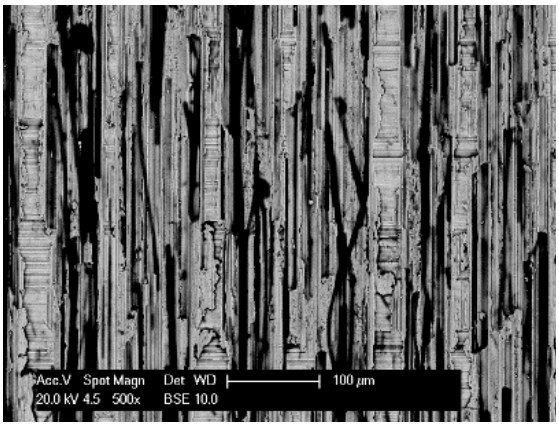

Direction of stroke

Figure 4.16. (a) Wear profiles and (b, c, d) BSE images (plan view) of the flat specimen wear scars high magnification for cylinder radius 160 mm and grease-lubricated conditions.

(a) P = 250 N (p_o = 70 MPa), Δ^* = 50 μm

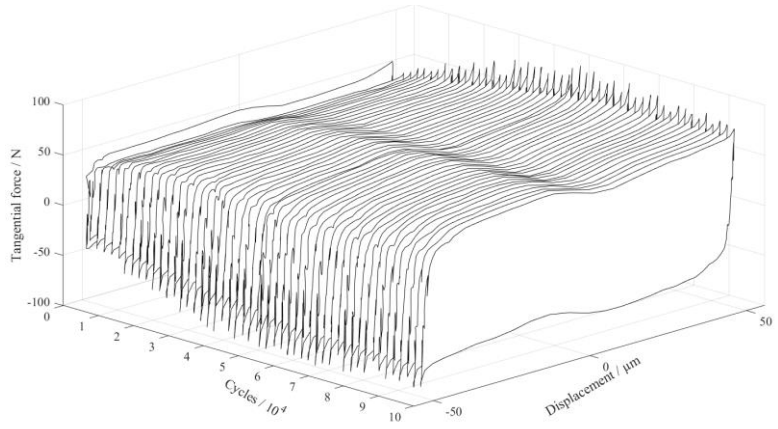

(b) P = 500 N (p_o = 100 MPa), Δ^* = 50 μm

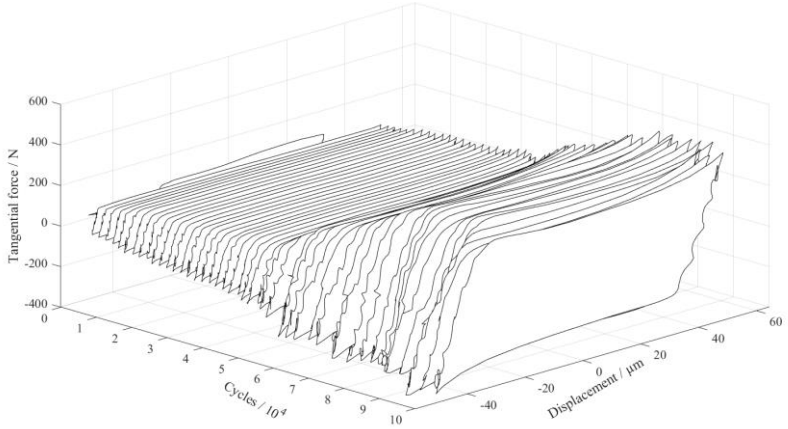

(c) P = 500 N (p_o = 100 MPa), Δ^* = 100 μm

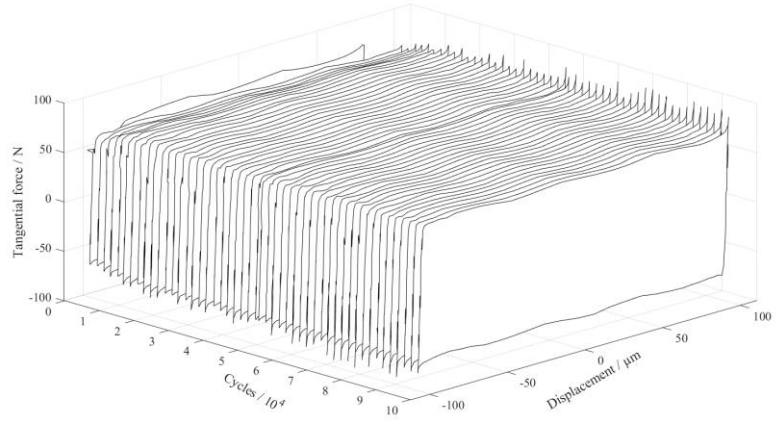

Figure 4.17. Fretting loop evolution for cylinder radius 160 mm and grease-lubricated conditions.

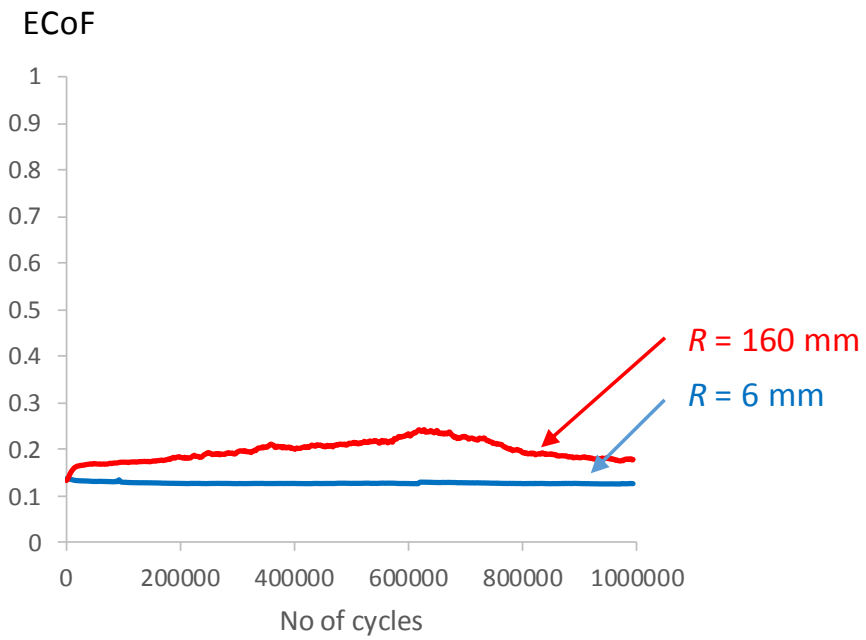

Figure 4.18. Development of ECoF for extended tests (10^6 cycles) for grease-lubricated contact cylinders of radius *R* with applied displacement 50 µm and normal load 250 N.

4.4. Discussion

The ECoF values after 10^5 cycles for grease-lubricated tests are lower than the values for dry tests, as shown in Figure 4.8, 4.11 and 4.15. The ECoF values for dry tests are broadly independent of loading conditions and conformity. The initial ECoF values were in the range 0.4 to 0.6, representing material transfer and adhesion during metal-on-metal contact. An increase in ECoF (up to ~0.79 after between 10 and 100 cycles) was then observed due to abrasive action during the accumulation of oxidised debris. Upon development of a compacted debris layer, the ECoF stabilised to a constant value of between ~ 0.60 and 0.68 after ~ 4×10^4 cycles, with the ECoF itself being relatively insensitive to applied displacement and normal load.

In contrast, the results for lubricated-fretting tests show that the fretting behaviour depends more significantly on loading conditions and contact geometry (see Figure 4.9 and 4.14). For a lubricant to provide effective protection, it must (i) penetrate the contact, and (ii) remain in the contact area to provide a protective film. It was previously shown (Warmuth et al., 2016) for oil-lubricated fretting that the concept of covered width can be used to identify regimes of fretting behaviour where the oil is continuously replenished into the contact area to provide a protective tribofilm; in this work (Warmuth et al. 2016), it was argued that lubrication was only effective when the covered width (i.e. the width of contact which never comes out of contact throughout a fretting stroke) fell to zero. However, in the current work with a grease lubricant, this does not appear to be applicable; full and stable lubrication is observed for the following cases: (i) R = 6 mm, P = 250 N and Δ^* = 50 μm; (ii) R = 160 mm, P = 250 N and Δ^* = 100 μm; (iii) R = 160 mm, P = 500 N and Δ^* = 100 μm. And in these three cases, the covered width is greater than zero (the smallest value of the covered semiwidth is for the first of these three cases where it is 16 μm).

Despite the failure of this concept to describe the behaviour of fretting in grease lubricated conditions, there are obvious trends in the behaviour observed. There is a clear link between the applied displacement and the evolution of ECoF with fretting cycles (shown in Figure 4.10 and Figure 4.14). For the less conforming contact (6 mm radius), friction is low in all cases initially (see Figure 4.10). For the smallest tangential displacement (15 μm) the lubricant is pushed out of the contact by the fretting action which results in a rise in ECoF and wear rate which is approximately the same as that observed in the the dry case (Figure 4.11). As tangential displacement is increased to 30 μm, the evolution of ECoF indicates that it takes longer (more fretting cycles) to remove the lubricant from the contact (Figure 4.10) and the wear rate is correspondingly smaller

(Figure 4.11). At a tangential displacement of 50 μm, the ECoF indicates that the lubricant is effectively retained in the contact (Figure 4.10), and that this behaviour appears to be stable for the long-term (Figure 4.18); there is also a commensurate reduction in specific wear rate (Figure 4.11). In addition, it is clear that the extrusion of grease is more rapid as the applied load is increased.

Comparison of Figure 4.10 and Figure 4.14 indicates that for the more conforming contact (160 mm radius), it takes longer (more fretting cycles) to extrude the grease out of the contact, i.e. the rise in ECoF takes longer than for less conforming contacts due to the larger distances over which the grease must be extruded (larger elastic contact width) and the lower contact pressures. Again, with the more-conforming contacts (Figure 4.14), it is observed that the extrusion of grease from the contact is accelerated by increased normal load. For the more-conforming contact, full and stable grease lubrication requires a higher displacement amplitude (100 μm) than was required for the less-conforming contact (50 μm). However, an extended test of a more-conforming contact where ECoF had been seen to initially rise ($\Delta^* = 50$ μm and P = 250 N) demonstrated that changes in surface morphology due to fretting could result in that contact developing a state of full and stable lubrication (Figure 4.18).

For fretting design of the nub-groove contact in flexible risers, reliable determination of ECoF is important for sliding regime and fatigue stresses. If friction is over-estimated, this will lead to under-prediction of contact slip and hence, slip regime (i.e. partial slip instead of gross slip conditions). In contrast, if friction is under-estimated, slip will be over-predicted, leading to possible over-prediction of fatigue life (in gross slip regime) if beneficial wear effects are accounted for (see Chapter 6).

Jin and Mall (2002) have presented an experimental study on the effects of contact geometry and normal load (for a rounded punch-on-flat and a round-on-flat) on the fretting fatigue (with substrate fatigue load) behaviour of Ti-6Al-4V. It was shown that (minimum) fretting fatigue life is independent of contact geometry and normal load. It is convenient to consider fretting damage as having two contributions, a tribological contribution and a mechanical contribution. This work has highlighted the dependence of tribological effects of conformity (and other variables), highlighting, in particular, the beneficial effects of less conforming contacts (lower contact widths) under grease lubrication conditions for friction and wear. FE predictions (presented in Chapters 5 and 6) show that low values of nub-groove coefficient of friction (e.g. ECoF = 0.1) increase fretting fatigue life by up to 10^7 cycles in comparison to high values (e.g. ECoF = 0.8). In contrast, however, previous work by Zhang et al. (2011), for example, demonstrated the detrimental effect of smaller contact conformity (width) on the mechanical contribution to fretting damage (including the mechanical effects of wear), on the assumption of friction (and specific wear rate) being independent of contact conformity. It is suggested here that, on the one hand, smaller contact width leads to decreased tribological damage under grease-lubrication conditions, whereas, on the other hand, a smaller contact width leads to increased mechanical damage; these opposing effects may (in certain situations) cancel each other out, which is consistent with the observation of Jin and Mall (2002) of a negligible overall effect on minimum fretting fatigue life.

These results highlight the effects of contact conformity and displacement amplitude on tribological damage for flexible riser design. It is clear that, in order to reliably design for optimum fatigue life in flexible risers, both tribological and mechanical aspects need to be considered. This can potentially be achieved by designing the riser nub-groove conformity so that the contact width is small compared to the nub-

groove displacement, and hence, low coefficient of friction values will be achieved under grease-lubricated conditions, but subject to analysis of the mechanical damage implications.

4.5. Fretting wear tests using piezoelectric fretting rig

4.5.1. Introduction

In this section, fretting tests conducted on crossed cylinder specimen using the NUI Galway fretting rig are presented. The material tested was supplied by NV Bekaert SA, Belgium; this is pressure armour material supplied in rod form, prior to being cold formed into the pressure armour profile. Crossed cylinder specimen geometry was chosen to facilitate tests to be conducted under high contact pressure loading cases and for testing under partial and gross slip conditions. The experimental set-up results from these tests will be compared and contrasted to the dry fretting tests described in the previous section (from cylinder-on-flat tests at the University of Nottingham). This will also allow for validation of results from the newly-designed piezoelectrically-actuated fretting rig. The fretting tests conducted at UoN and NUI Galway have facilitated fretting testing to be conducted under the range of loading and geometrical conditions possible in the nub-groove contact of the pressure armour layer of flexible marine risers, and identification of tribological parameters, such as wear and friction coefficients.

4.5.2. Test conditions and procedures

The fretting test apparatus used is described in Chapter 3. Two stationary cylindrical specimens were mounted, one to the base of the rig and the other to the loading platform. The reciprocating cylindrical specimen was mounted in the collet on the drive line. A dead-weight configuration on the loading platform was used to provide a constant normal load, P, throughout the test. The layout of the rig components can be seen in Figures 3.2, 3.3 and 3.5. As described in Chapter 3, the linear displacement of the reciprocating specimen is achieved using a piezoelectric actuator. This displacement, Δ^*, is also measured close to the contact using a DVRT throughout the test. Similarly, the tangential force is measured using a piezoelectric force sensor. The load and displacement signals are sampled at a rate of 250 per fretting cycle for all the experiments (i.e. 500 Hz).

As shown in Figure 3.9, real-time visualisation of sensor outputs allows for monitoring of the fretting contact behaviour throughout the test. This data is processed to give fretting loop evolution for each test; an idealised gross slip fretting loop is shown in Figure 4.19(a). An example of a partial slip fretting loop is shown in Figure 4.19(b). The measured displacement amplitude (at the DVRT), Δ^*, is not the same as the contact slip due to elastic deformation of the specimen and rig compliance. Since the fretting contact region is separated from the location of the displacement sensor, the measured displacement amplitude, is always slightly larger than the contact slip amplitude, δ^*; this is due to elastic deformation of the specimen and rig compliance. The contact slip amplitude (δ^*) can be derived by measuring the displacement at zero force, as illustrated in Figure 4.19.

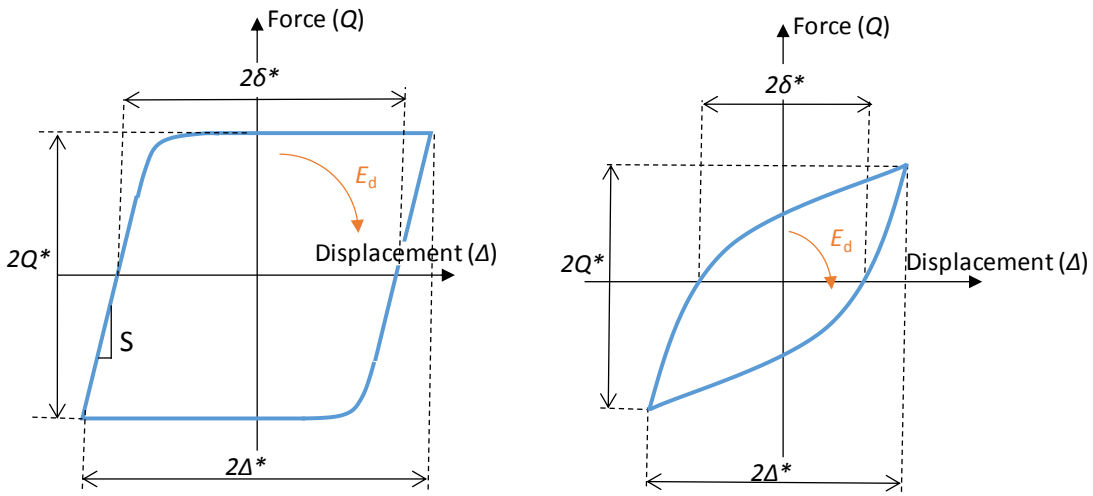

(a) (b)

Figure 4.19. Schematic diagram of an ideal fretting loop in the (a) gross slip regime, and (b) partial slip regime.

Experiments were conducted for a range of normal loads, P, represented by the weight of each loading block. A summary of the fretting parameters is provided in Table 4.5. Tests were conducted at ambient temperature (typically ~20 °C), at a frequency of 2 Hz for a duration of 300,000 cycles. Using Young's modulus of 189 GPa and a Poisson's ratio of 0.33 for this steel, Hertzian contact mechanics (Hertz, 1882) for crossed cylinder contacts were used to predict the initial contact semi-width, a, and initial maximum contact pressure, p_o. The values of a and p_o are presented in Table 4.5 for the test conditions examined. Contact semi-width ranges from 81 μm to 157 μm and maximum contact pressure ranges from 891 MPa to 1729 MPa.

Table 4.5. Summary of the NUI Galway fretting test parameters.

Test temperature	Ambient (typically 20°C)
Cylinder radii, *R*	6 mm
Displacement amplitudes, *Δ**	1 to 6 μm
Test duration, *N*	300,000 cycles
Normal load, *P*	12 to 90 N
Maximum Hertzian pressure, p_0	890 to 1730 MPa
Initial contact width, *a*	80 to 157 μm
Oscillation frequency	2 Hz
Lubricant	None

4.5.3. Characterisation of wear scars and debris

After testing, the specimens were swabbed lightly with methylated spirits to remove loose debris, following the methodology of other researchers (Jin et al., 2015; Warmuth et al., 2015). A 2D profile of the wear scar was measured using a Taylor-Hobson Surftronic 3+ profilometer (vertical resolution of 10 nm). The measurement lengths for the specimen are shown in Figure 4.20; the scan length includes part of the unworn surface (away from the wear scar). This allows for a reference surface to be defined (Elleuch and Fouvry, 2002).

V^- is the total wear volume, for the two contact pairs, given by:

$$V^- = V_1^- + V_2^- + V_3^- + V_4^- \tag{4.10}$$

where V_i^- is the volume of the void below each reference surface, *i*; for each test, there are two pairs of wear scars, and therefore, four wear scars and reference surfaces in total. The wear volume for the crossed-cylinder test specimen is calculated by assuming the wear scar geometry is axisymmetric about its centre. The measured area is revolved around the centre axis of the wear scar (as shown in Figure 4.20(a)) and the volume is calculated using a numerical integration method. The assumption that the wear scar is perfectly axisymmetric will lead to errors in the volume measurement. This could be as large as ± 20%, based on the variation about the centre axis of the 2D wear profiles. This is significant and can lead to an over- or under-prediction of wear rate. Since the specimens are cylindrical, the curved reference surface of the specimen is accounted for in the revolution and calculation of the wear volume, as shown in Figure 4.20(b).

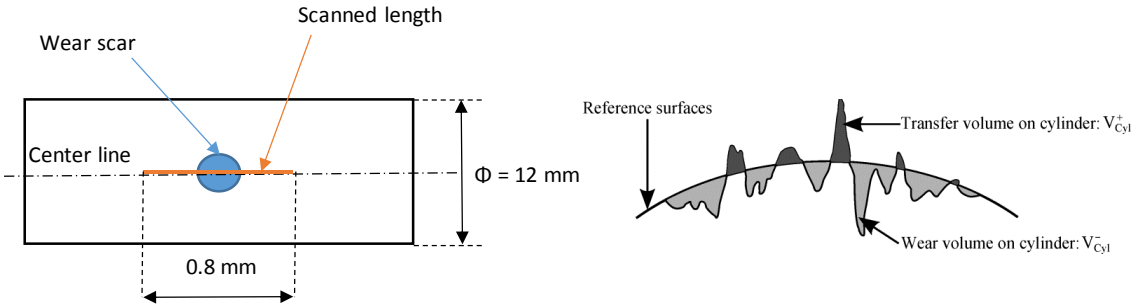

(a) (b)

Figure 4.20. Schematic of (a) the plan view and (b) the end view of the wear scar from crossed-cylinder tests, showing example wear scar.

4.5.4. Results

Figure 4.21 presents the measured evolution of ECoF with number of fretting cycles for crossed-cylinders with normal loads. Development of frictional coefficient

(ECoF) for gross slip fretting is presented in Figure 4.21(a); the stabilised ECOF values ranges from 0.59 to 0.65 in GS. At higher normal loads, the ECoF value is lower, resulting in partial slip conditions. Development of traction coefficient (ECoF) for partial slip fretting is presented in Figure 4.21(b). The ECoF is unstable for the test conducted with a normal load of 43 N (contact pressure ~ 1350 MPa); this is consistent with the MS fretting loops shown in Figure 4.24(b). In partial-slip, the stabilised ECoF value reduces with increased normal load.

Figure 4.22(b - c) presents optical microscopy images of the wear scars from crossed-cylinder tests conducted for GS and PS conditions (contact pressures of 1270 MPa and 1600 MPa). These images are at low magnification due to the curved surface of the cylindrical specimen; therefore, it is difficult to focus the image at larger magnifications. The wear scars in Figure 4.22 are circular, this indicates that there is good alignment between the crossed-cylinders specimen i.e. aligned at 90° to each other. The reddish-brown colour in the images indicates iron oxide debris in the wear scars.

A plot of wear volume, V, against total dissipated energy, ΣE_d, for crossed-cylinder tests is presented Figure 4.23. As total energy dissipation increases, the total wear volume also increases. The energy wear coefficient is given by the slope of the graph and is calculated as 6.3×10^{-9} MPa^{-1}.

Measured fretting loop evolutions for (a) GS, (b) MS and (c) PS conditions are presented in Figure 4.24. Gross slip loops are observed for the low contact pressure (1270 MPa); partial slip occurs at higher contact pressure (1600 MPa). Mixed-slip fretting loops are observed for the test conducted with a contact pressure of 1350 N (Figure 4.24(b)).

(a) GS

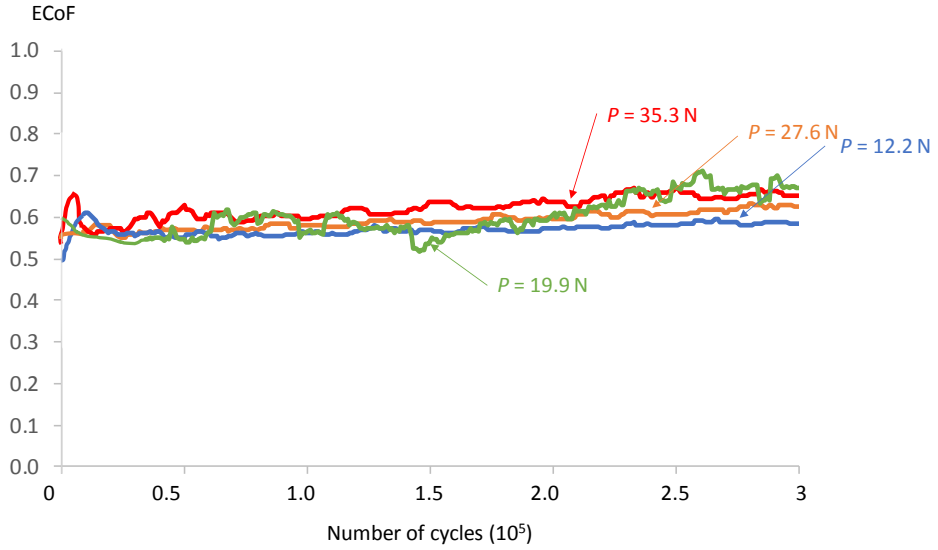

(b) PS

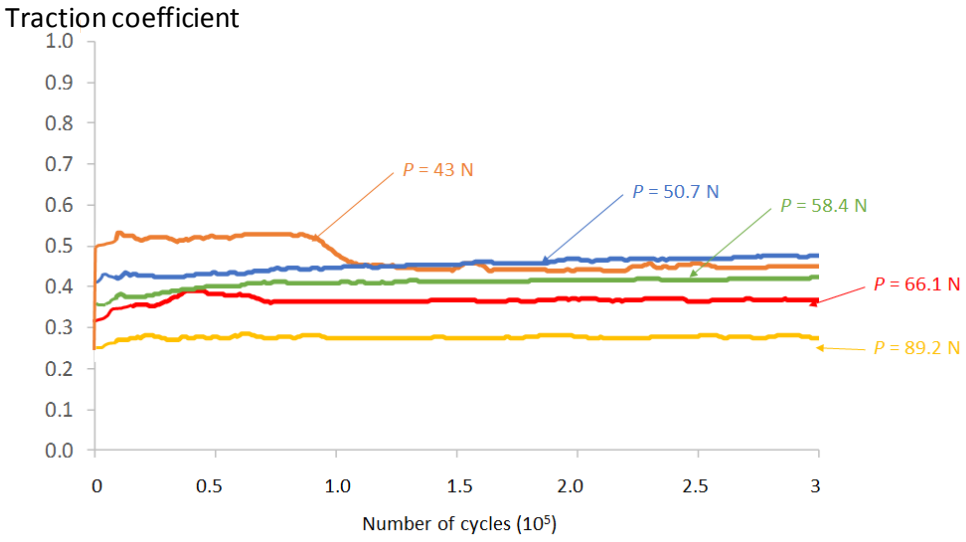

Figure 4.21. Measured evolution of ECoF and tration coefficients with number of fretting cycles for specimen with normal load of *P* for (a) gross-slip (contact pressure between 890 and 1270 MPa), and (b) mixed and partial slip conditions (contact pressure between 1350 and 1730 MPa).

(a) Wear scars

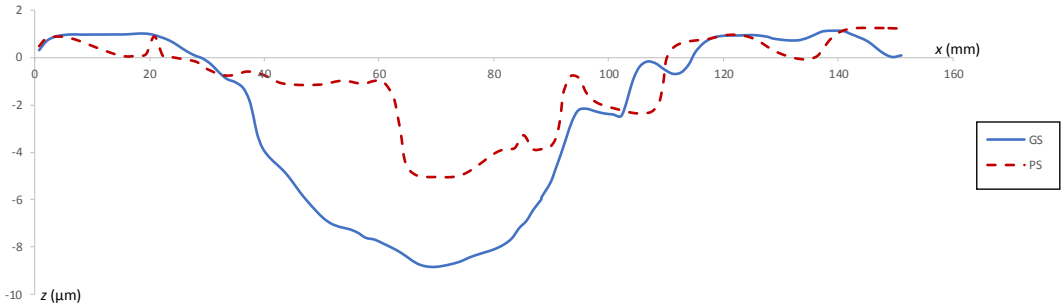

(b) Gross slip (c) Partial slip

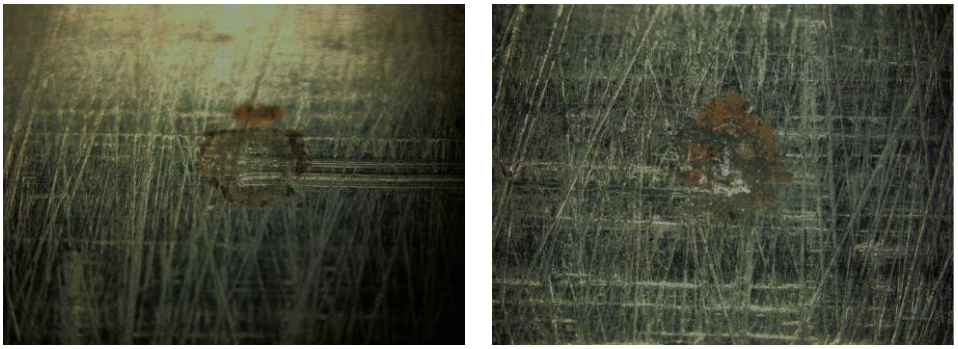

Direction of stroke

Figure 4.22. (a) Measured 2D wear scar for partial- and gross-slip tests, (b - c) optical microscopy images of wear scars for tests with partial (contact pressure of 1600 MPa) and gross slip conditions (contact pressure of 1270 MPa).

4.5.5. Discussion

Crossed-cylinder tests were conducted to characterise fretting behaviour of pre-formed pressure armour material under high contact pressure and low tangential displacement conditions. The fretting loops from tests showed that both PS and GS regimes were achieved using the newly-designed piezoelectrically-actuated fretting test rig. Partial slip conditions were achieved by increasing the normal load and hence, the contact semi-width (as shown in Table 4.5). The ECoF values for the crossed-cylinder

specimen in gross slip give a friction coefficient of 0.59 - 0.68. As the normal load increases, giving partial slip conditions, the ECoF value decreases (as shown in Figure 4.21). The wear scars for the crossed-cylinders are round and symmetric as shown in Figure 4.22. This shows that there is good alignment between specimen, i.e. the reciprocating specimen is at 90° to the stationary specimens. This allows for the 2D wear profile to be revolved about the centre axis to give a 3D wear profile, and hence, wear volume calculation. Energy wear coefficient is calculated as 6.3×10^{-9} MPa^{-1} from PS and GS results, as shown in Figure 4.23, with ~73 % accuracy. The threshold energy, $E_{d,th}$, is the energy required for wear to take place, this energy is used in the formation of a tribologically transformed structure (Saufer et al., 2000).

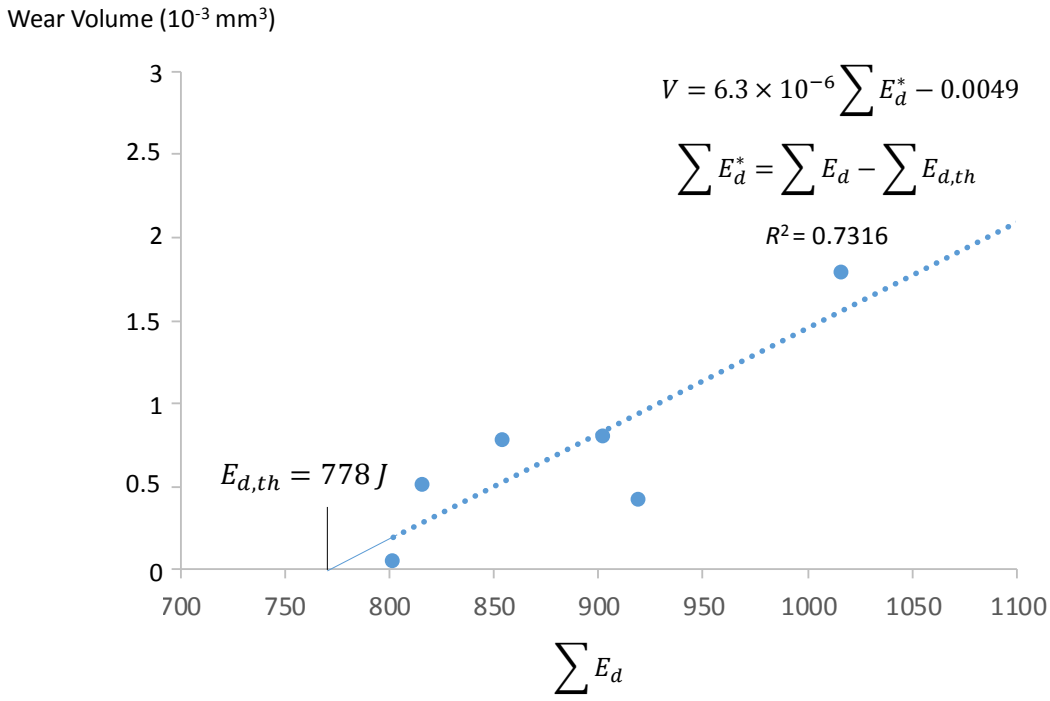

Figure 4.23. Plot of wear volume, V, against total dissipated energy, ΣE_d, for crossed-cylinder tests

(a) Gross-slip

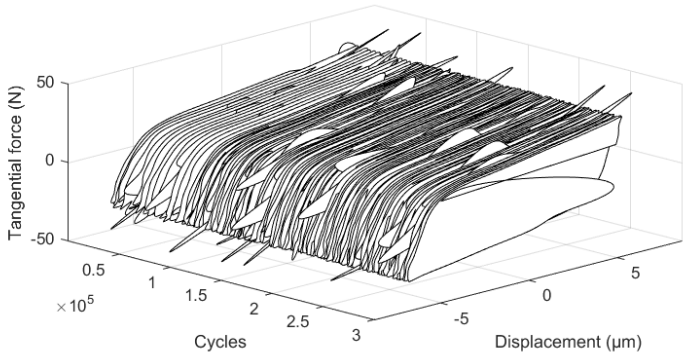

(a) Mixed-slip

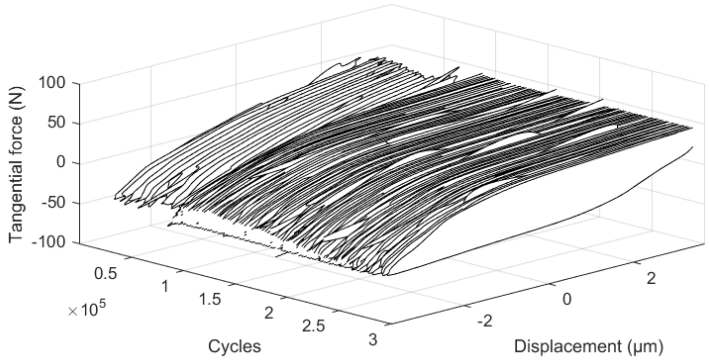

(c) Partial-slip

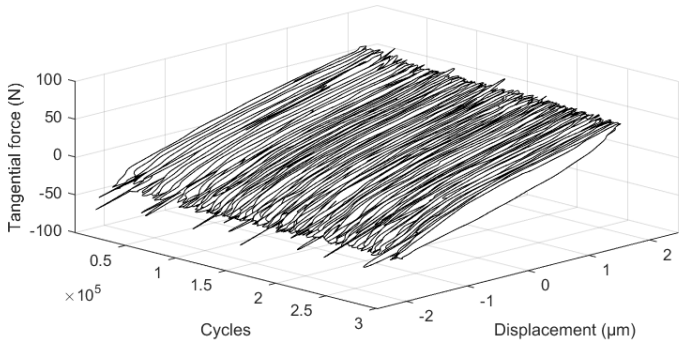

Figure 4.24. Measured evolution of fretting loop for tests with (a) gross slip conditions (contact pressure of 1270 MPa), (b) mixed slip conditions (contact pressure 1350 MPa), and (c) partial (contact pressure of 1600 MPa).

4.6. Comparison of fretting tests

4.6.1. Comparison of rigs

A crossed-cylinder configuration was employed for fretting testing in the newly designed test rig in NUI Galway. The fretting rig piezoelectric actuator is limited to a maximum of 200 N tangential force; therefore, in order to ensure safe loading of the rig, normal load, P, was in the range of 12.2 N to 89.2 N. This loading resulted in maximum initial (unworn) contact pressures between 891 MPa and 1729 MPa. These pressures are similar to the maximum contact pressure in flexible marine risers under normal riser operating conditions for internal fluid pressure (25 to 30 MPa). The contact semi-width was between 81 μm and 157 μm. The piezoelectric actuator gives low applied displacements i.e. $\Delta^* < 10$ μm. These loading conditions allowed for testing in GS and PS. The loading conditions are representative of pressure armour contact pressures (see Chapter 5). However, the contact geometry of crossed cylinders is not representative of the contact in the pressure armour wire in flexible marine risers (see Figure 4.3(b)). See Table 4.6 for normal applied load, P, applied displacement, Δ^*, peak unworn contact pressure, p_o, unworn contact semi-width, a and slip regime for 6 mm crossed-cylinders tests at NUI Galway.

In contrast, the University of Nottingham fretting test rig uses an EVM and a lever-arm configuration to apply normal load, giving higher normal load and applied displacement values than the NUI Galway test rig. However, the specimen configuration means that higher contact pressures are achieved using the NUI Galway test rig. Cylinder-on-flat specimen configuration was used to better represent the nub-groove contact in flexible marine risers. Two contact conformities were examined; the less conforming contact had a cylinder radius of 160 mm and the more conforming contact

radius 6 mm cylinder specimen. Normal loads, *P*, of 250 N and 500 N were used to achieve maximum contact pressures of 371 MPa to 525 MPa and 72 MPa to 102 MPa for the 6 mm and 160 mm radius cylindrical specimens, respectively. Initial contact semi-widths of 43 μm and 61 μm were calculated for the 6 mm radius cylinder contact and 221 μm and 313 μm for the 160 mm radius cylinder contact. The EVM applies larger applied displacements than the piezoelectric actuator, giving GS conditions for all tests conducted on the University of Nottingham test rig. See Table 4.6 for applied displacement, Δ^*, peak unworn contact pressure, P_0, unworn contact semi-width, a and slip regime for 6 mm and 160 mm cylinder-on-flat tests at University of Nottingham.

Overall, testing has been conducted on three contact geometries (6 mm crossed-cylinders, 6 mm and 160 mm cylinder-on-flat), giving initial, unworn, peak contact pressures of between 72 MPa and 1729 MPa and semi-widths between 43 μm and 313 μm. Using applied displacements between 1 μm and 50 μm has resulted in both PS and GS test conditions.

4.6.2. Comparison of dry fretting results

Stabilised ECoF values for all GS dry fretting tests are between 0.59 and 0.68 (see Table 4.7). The ECoF development with number of fretting cycles is similar for both test rigs, NUI Galway and University of Nottingham (UoN) (see Figure 4.8 and Figure 4.21(a)). For all tests, ECoF value is initially 0.4 - 0.7 representing material transfer and adhesion during metal on metal contact. An increase in the ECoF is then observed due to abrasive action during the accumulation of oxidised debris. The ECoF stabilises to a

constant value (0.59 - 0.68) as the abrasive action decreases due to the formation of compacted debris.

Table 4.6. Applied displacement, Δ^*, peak unworn contact pressure, p_o, unworn contact semi-width, a and slip regime for 6 mm crossed cylinders tests at NUI Galway and 6 mm and 160 mm cylinder-on-flat tests conducted at the University of Nottingham.

Test	**6 mm crossed cylinders (NUI Galway)**	**6 mm cylinder-on-flat (UoN)**	**160 mm cylinder-on-flat (UoN)**	**Typical values for riser contact**
Δ^* (µm)	1 to 6	15 to 50	15 to 50	0 to 200
p_o (MPa)	891 to 1729	371 to 525	72 to 102	500 to 2000
a (µm)	81 to 157	43 to 61	221 to 313	40 to 100
Slip regime	PS and GS	GS	GS	PS and GS

Wear coefficients calculated here depend on contact geometry (see Table 4.7). For the point contact (crossed-cylinders) the wear coefficient is lower than for the line contact (cylinder-on-flat). The less conforming cylinder-on-flat contact (6 mm) has the largest value for wear coefficient. The energy wear coefficient is higher than the Archard wear coefficient for all gross slip tests. Merhej and Fouvry (Fouvry and Merhej, 2013; Merhej and Fouvry, 2009) showed an asymptotic decrease of wear rates associated with increasing contact size.

A greater range of Archard wear coefficients are calculated for the cylinder-on-flat cases; this is due to the larger range of loading conditions for cylinder-on-flat tests.

There is a greater error associated with the energy wear coefficient results from the crossed-cylinder tests due to the assumption that the wear is axisymmetric. However, since Archard wear coefficients were only calculated for GS cases, there is less of a range of loading conditions for the crossed-cylinder than for the cylinder-on-flat cases.

The data point fit to the energy wear coefficient plot (see Figure 4.23) is 73% for the crossed-cylinders compared to 97% and 82% for the 6 mm and 160 mm cylinder-on-flat cases, respectively. The lower percentage fit for the crossed-cylinder tests can be attributed to the greater error associated with the wear volume calculated for these tests.

Table 4.7. Stabilised ECoF values, Archard wear coefficient and energy wear coefficient for 6 mm crossed-cylinder (NUI Galway test rig) and 6 mm and 160 mm cylinder-on-flat (University of Nottingham test rig) specimen configurations.

Test	**6 mm crossed-cylinders (NUIG)**	**6 mm cylinder-on-flat (UoN)**	**160 mm cylinder-on-flat (UoN)**
Stabilised ECoF (GS)	0.59 - 0.65	0.6 - 0.63	0.61 - 0.68
Archard wear coefficient (MPa^{-1})	1.36×10^{-9} - 2.04×10^{-8}	1.17×10^{-9} - 3.12×10^{-8}	1.17×10^{-9} - 1.12×10^{-8}
Energy wear coefficient (MPa^{-1})	6.3×10^{-9}	5.5×10^{-8}	1.4×10^{-8}

4.7. Tensile and low-cycle fatigue tests

4.7.1. Test conditions and procedures

Monotonic tensile tests have been conducted on the pressure armour material extracted from a pre-service flexible marine riser, using the NUI Galway Instron 8500 servo-hydraulic testing machine with hydraulic grips. The tensile test was conducted using displacement control at a rate of 1×10^{-3} mm/s per mm gauge length; a video extensometer was used to measure the strain in the gauge region of the specimen.

A programme of low-cycle fatigue (LCF) tests has been conducted on pressure armour material extracted from a pre-service flexible marine riser. Strain-controlled cyclic tests were carried out using the Instron 8500 servo-hydraulic testing machine, with servo-hydraulic grips and a contact extensometer for strain feedback. Tests were conducted at strain ranges of 0.8%, 1%, 1.25% and 2%. A cyclic strain ratio R_c of -1 and a strain rate of 0.01 s^{-1} were used.

4.7.2. Results

Measured tensile behaviour of the pressure armour material is presented in Figure 4.25(a). The elongation at failure was measured to be 18.9%, the yield strength is 748 MPa, the ultimate tensile strength is 903 MPa and the Young's modulus was measured as 189 GPa. Localised necking at the crack site is observed, as shown in Figure 4.25(b).

(a)

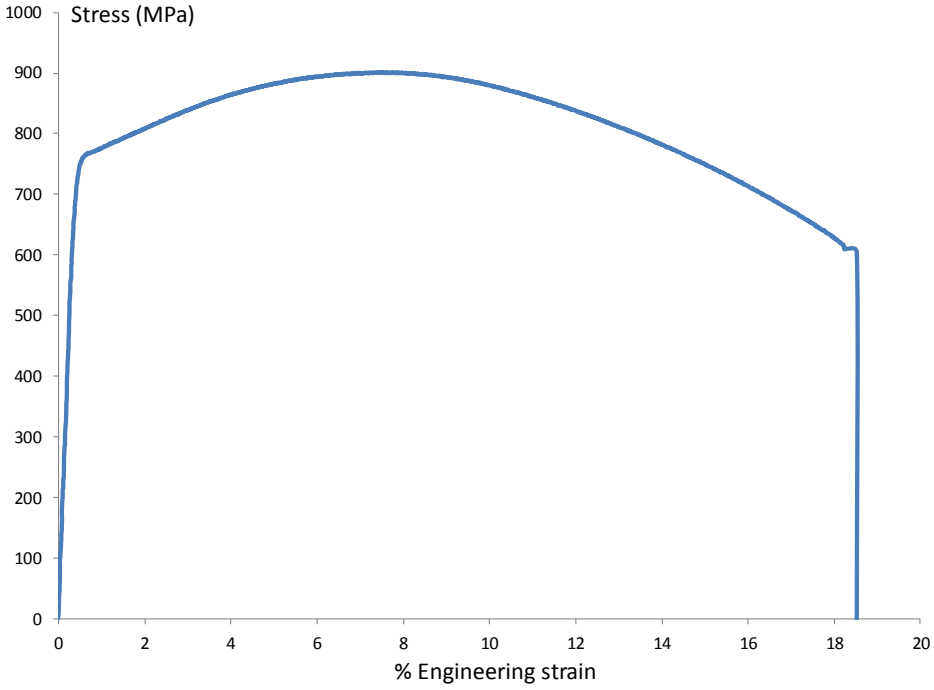

(b)

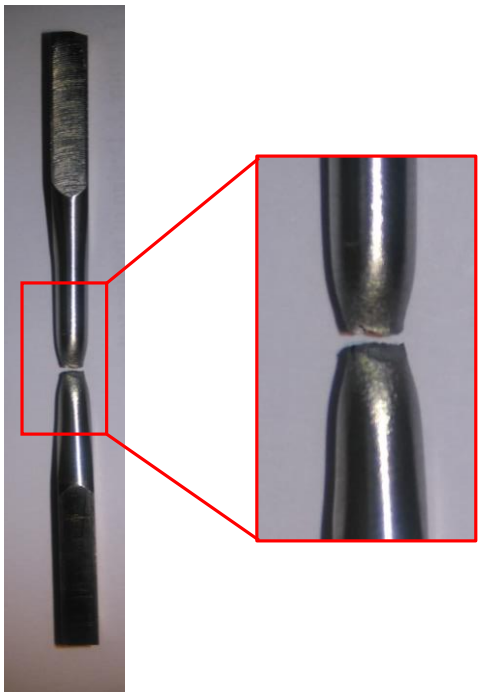

Figure 4.25. (a) Measured tensile test stress-strain curve for pressure armour material, (b) Failed tensile test specimen showing localised necking.

Figure 4.26(a) presents the measured evolution of the cyclic stress range for LCF tests at controlled cyclic stress ranges of 0.8%, 1%, 1.25% and 2%. The material cyclically softens; this is consistent with other cold formed steels (Hassan et al., 1994). Initial softening occurs within the first 100 cycles. Thereafter, a stabilised stress range occurs until a sudden drop in stress range, corresponding to the termination of the test due to a 20% load drop in tension; this is taken as failure. Figure 4.26(b) presents detailed evolution of stress-strain hysteresis loops for ±0.5% applied stress range; cycle 2060 is the last cycle before failure.

The Coffin-Manson (as described in Chapter 2) fit to experimental data is presented Figure 4.27(a). The Coffin-Manson (1954) relationship between plastic strain amplitude and the fatigue life for low-cycle fatigue (lCF) is as follows:

$$\frac{\Delta\varepsilon_p}{2} = \varepsilon'_f (2N_f)^c \tag{4.11}$$

where $\Delta\varepsilon_p$ is the plastic strain amplitude, ε'_f is the fatigue ductility coefficient and c is the fatigue ductility exponent. Stabilised hysteresis loops for each strain range tested are presented in Figure 4.27(b). From Figure 4.27(a), Coffin-Manson constants (ε'_f and c) were obtained and used in a computational fatigue model (described later in Chapter 5). Coffin-Manson constants for the pressure armour material are provided in Table 4.8.

(a)

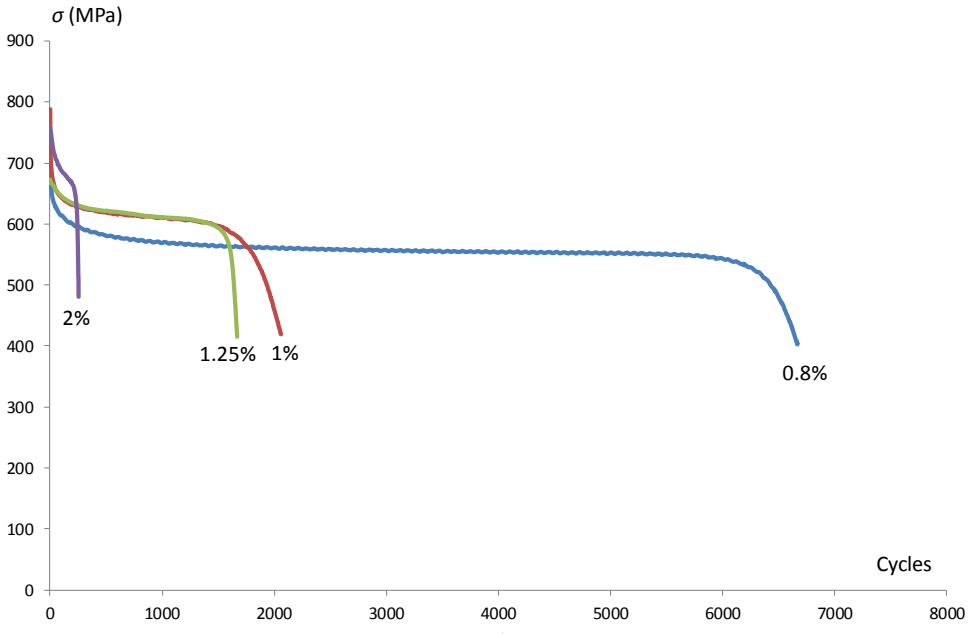

(b)

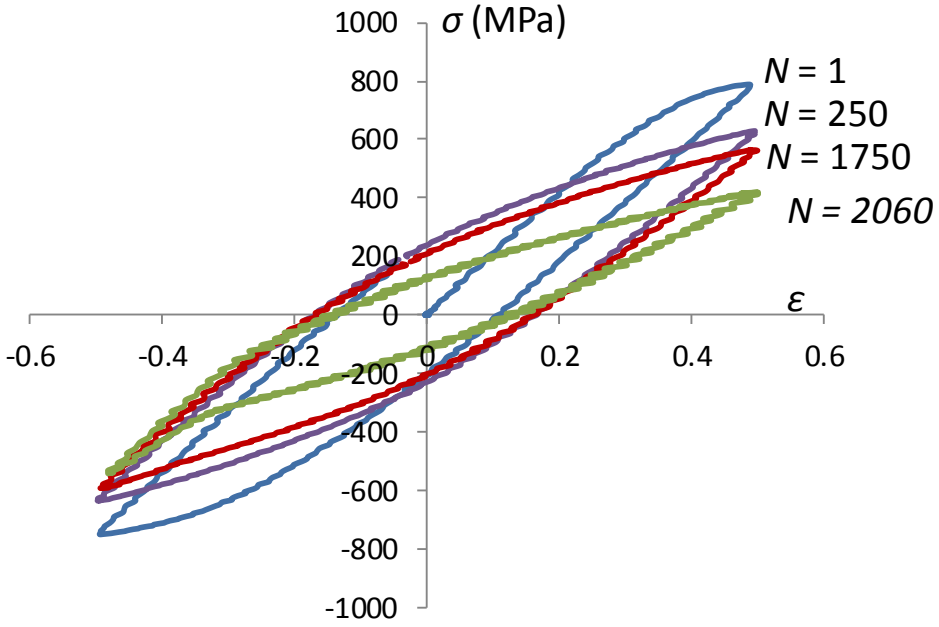

Figure 4.26. (a) measured evolution of the cyclic stress range for LCF tests at controlled cyclic stress ranges; (b) evolution of stress-strain hysteresis loops for ±0.5% applied stress range.

(a)

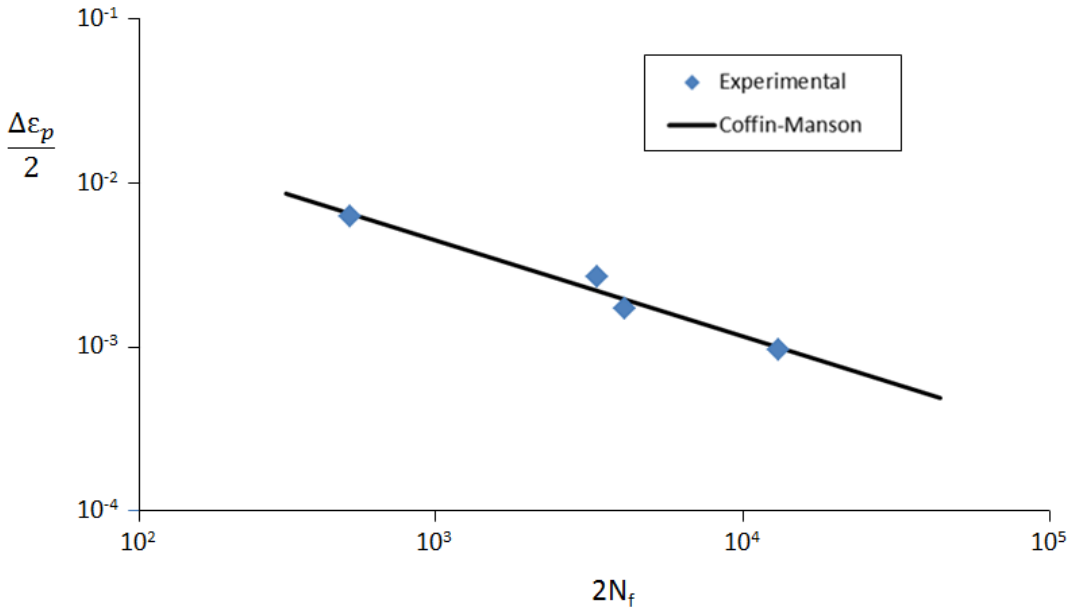

(b)

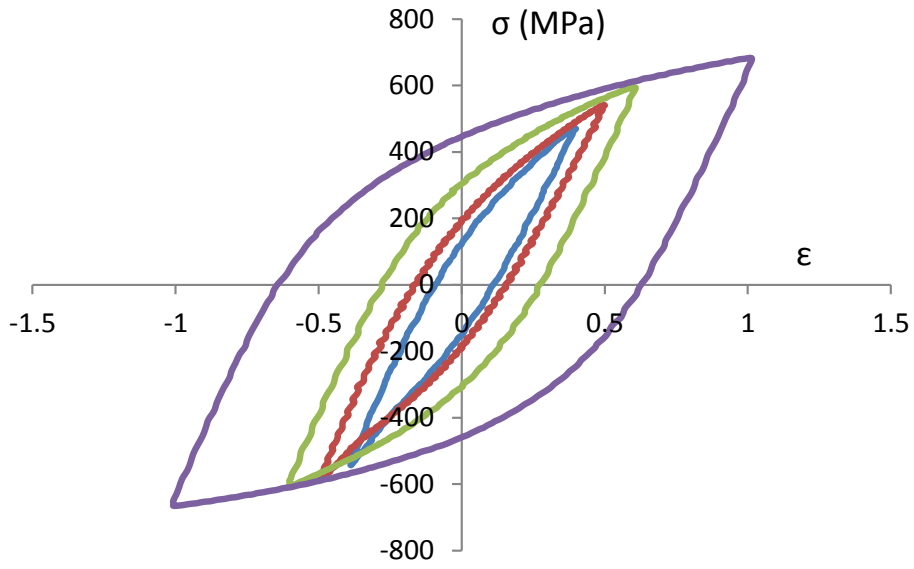

Figure 4.27. (a) LCF experimental test results with Coffin-Manson fit; (b) measured hysteresis loops for different controlled strain-ranges.

Basquin parameters (σ'_f and b) have been estimated from monotonic tests data (see Figure 4.25) using the universal slopes method (Cruzado et al., 2013; Manson, 1965). This method gives estimated fatigue coefficients based on monotonic tensile test results for ultimate tensile strength, σ_{UTS}, e.g. $\sigma'_f = 1.9\sigma_{UTS}$, and $b = -0.12$. Basquin (1910) relationship between stress amplitude and the fatigue life for high-cycle fatigue (HCF) is given by:

$$\frac{\Delta\sigma}{2} = \sigma'_f (2N_f)^b \tag{4.12}$$

where $\Delta\sigma$ is the stress range, σ'_f is the fatigue strength coefficient and b is the fatigue strength exponent.

Table 4.8. SWT parameters from LCF testing of pressure armour wire (ε'_f and c) and universal slopes method (σ'_f and b).

Parameter	Value
σ'_f	1710 MPa
ε'_f	0.2355
b	-0.12
c	-0.5742

4.8. Summary and conclusions

Experimental characterisation of pressure armour material has been discussed in this chapter. An outline of the materials used and specimen design is provided. Characterisation of both tribological (friction and wear) and mechanical (monotonic and fatigue) properties is critical to fretting fatigue life prediction in flexible risers. The experimental results and observations (i.e. nub-groove geometry) of this chapter will provide a basis for the modelling of fretting in the pressure armour layer of flexible marine risers, as outlined in Figure 1.4.

Dry and lubricated fretting tests have been conducted at the University of Nottingham fretting wear test rig. These tests were on two different cylinder-on-flat contact geometries, and hence, representative of pressure armour nub-groove contact in flexible marine risers. For dry tests, friction was found to be independent of loading conditions and geometry; however, wear rate increases with applied displacement. The effect of Li-based grease on ECoF and wear coefficient has been investigated. It is shown that friction and wear are higher for dry conditions than for grease-lubricated conditions. If grease can be retained in the contact by fretting displacements above a critical value, low conformity and low normal load, low wear rates and coefficient of friction are observed.

Fretting tests have been conducted on the newly designed fretting rig, described in Chapter 3. These tests utilised crossed-cylinder specimen geometry, giving large contact pressures, representative of contact pressures in the nub-groove contact region of flexible marine risers. PS and GS fretting conditions were tested since the slip conditions in the nub-groove contact can range from stick to gross-slip. A comparison between NUI Galway and University of Nottingham test rig test conditions and results is discussed.

The UoN test geometry is more representative of the nub-groove contact; however, the loading conditions (contact pressure, contact semi-width) tested at NUI Galway are more representative of the loading conditions in flexible marine riser nub-groove contacts.

Monotonic and LCF tests were conducted on pressure armour wire material from a pre-service flexible marine riser. The dissection process of the pre-service riser provided an example nub-groove geometry for finite element models and also material for testing. Monotonic tests provided Young's' modulus, yield stress, ultimate tensile strength and ductility parameters for the riser material. LCF tests provided data for the identification of Coffin-Manson coefficients and also allowed for the development of a plasticity material model to be implemented in the finite element modelling of the pressure armour layer; this will be described in Chapters 5 and 6.

Chapter 5: Modelling of fretting in pressure armour layer

5.1. Introduction

This chapter describes the development of a model for fretting contact using analytical and finite element (FE) computational methods. A 3D riser segment model for the analysis of global riser bending is developed, allowing for determination of relative slips and contact pressure due to dynamic motions of flexible riser in marine environment. Fretting models for cylinder-on-flat are presented and a comparison between analytical and FE models is conducted. The development of a simplified pressure armour layer axisymmetric finite element model is discussed. The pressure armour model uses a round-on-flat nub groove contact based on measurements from the riser dissection (described in Chapter 4). A J_2 plasticity material model is introduced for the pressure armour. The material model has been calibrated against LCF test data for pressure armour material. Crack initiation predictions are made for nub-groove fretting contact, using the three-dimensional critical plane Smith-Watson-Topper multiaxial fatigue parameter (Sum et al., 2005). 3D global riser modelling combined with sub-modelling techniques are discussed and validated against nub-groove contact conditions from axisymmetric models. The effect of non-symmetric loading on nub-groove contact conditions is investigated using 3D riser modelling techniques.

5.2. Modelling of fretting contact

5.2.1. Analytical model

The analytical model used for validation of the FE model is the general solution for contact mechanics, as described in Chapter 2 (Section 2.3.6). This allows for comparison of substrate stresses between analytical and FE fretting models. Schematics of the fretting geometry modelled in shown in Figures 4.1(b) and 5.1. Equations 2.19 to 2.21 have been implemented using a numerical integration scheme to allow prediction of stresses for arbitrary two-dimensional contact pressure and shear tractions. This is employed here to validate the computational contact model for a cylinder-on-flat contact under partial and gross slip conditions.

5.2.2. Cylinder-on-flat finite element model

Finite element models have been developed for gross-slip and partial-slip cylinder-on-flat contact cases. The loading conditions are shown in Table 5.1. The finite element code used is Abaqus, the general-purpose, nonlinear finite element (FE) code.

Table 5.1. Loading conditions: Gross and partial-slip case.

Slip regime	**Normal Load (kN/mm)**	**Tangential stroke (GS) or Load (PS)**
Gross	50	10 μm
Partial	50	25 kN

A 2D, plane strain assumption has been assumed for each case. The material used is a carbon steel, with Young's modulus of 200 GPa and a Poisson's ratio of 0.3. The radius of the cylinder is 6 mm based on test specimen dimensions used for fretting wear tests as described in Chapter 4 and conducted by other researchers (McCarthy et al., 2013; Warmuth et al., 2015).

A coefficient of friction (CoF) of 0.8 is used, based on the assumption that after a sufficient number of cycles, surface modifications within the slip zone will raise the local CoF from an initial value of approximately 0.3 to a stable value, typically between 0.7 and 0.9, as described in Hills et al. (1996) and McColl et al. (2004), for example. This CoF behaviour with fretting cycles is consistent with experimental results described in Chapter 4.

Since the analysis is a frictional contact problem, two-dimensional, 4-noded, quadrilateral, plane strain elements are used due to their accuracy and stability for these loading conditions (McColl et al., 2004). A mesh sensitivity study was used to establish a converged mesh; the resulting mesh is highly refined in the contact region, becoming coarser further from the contact area, as shown in Figure 5.1. The contact element size is approximately 4 μm × 4 μm. The transition between fine mesh and coarse mesh is achieved by reducing the mesh density through an unstructured mesh interface region between the fine and coarse mesh regions (see inset Figure 5.1).

The dimensions of the substrate material were made significantly larger than the contact area so that the assumption of an elastic half-space remained valid. The bottom edge of the substrate was restrained in the *z*-direction and the left and right edges were restrained in the *x*-direction (see Figure 5.1 for axis definition). The normal load per

unit length, P, is applied to the cylinder, with a superimposed cyclic tangential load (Q) for PS or displacement (Δ) for GS applied as shown in Figure 5.2.

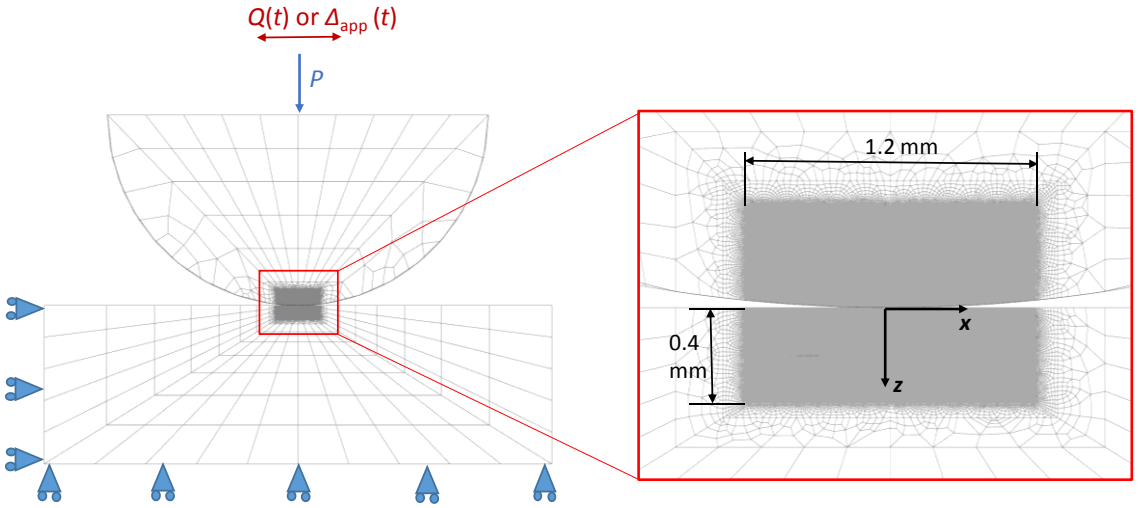

Figure 5.1. Mesh refinement and loading conditions for cylinder on flat contact.

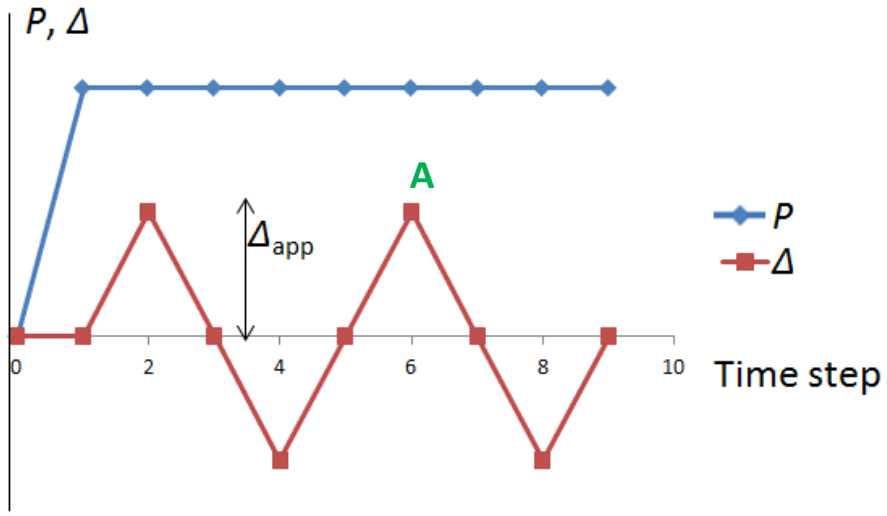

Figure 5.2. Applied stroke and loading condition

The master-slave algorithm with finite sliding contact within Abaqus was used to define the surface interaction for both models. The maximum allowable penetration depth between master and slave nodes was set to 1 μm. The adjustment tolerance for the initial geometry was set to 0.001 μm. Since the Coulomb-Amontons' law is assumed for sliding friction, the exact stick condition is ensured by implementing Coulomb friction based on the Lagrange multiplier contact algorithm.

5.2.3. Comparison between finite element and analytical models

Figure 5.3 shows a comparison of the analytical and FE results for the cylinder on flat sliding contact case. These samples are presented for instant *A* of the loading cycle (see Figure 5.2). The results are sampled for the set of integration points closest to the surface (depth z = 4.8 μm). Qualitatively, the FE solution predicts the peak trailing edge tensile stress at the same location as the analytical solution. The location of maximum shear stress differs by less than 1% between the two models. The FE solution predicts peak trailing edge tensile and maximum shear stresses that are 1% and 7% lower, respectively, than the analytical solution.

Figure 5.4 shows the comparison between analytical and FE solutions for the partial-slip case for the same time instant and depth. The FE solution again predicts the peak trailing edge tensile stress at the same location as the analytical solution and the predicted location of maximum shear stress differs by 10% between the two models. The FE solution predicts the same trailing edge tensile stress values; however, the FE maximum shear stress is 14% lower than the analytical solution. This is attributed to small differences between the contact shear distribution predicted by the FE model and the corresponding analytical distribution.

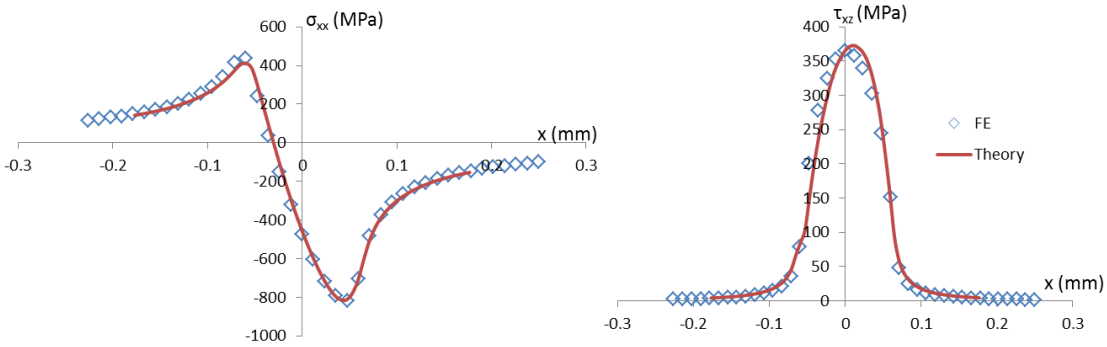

(a) (b)

Figure 5.3. Comparison of σ_{xx} and τ_{xz} stress results from FE to the analytical solution for sliding case (P = 50 kN, Δ_{app} = 10 μm).

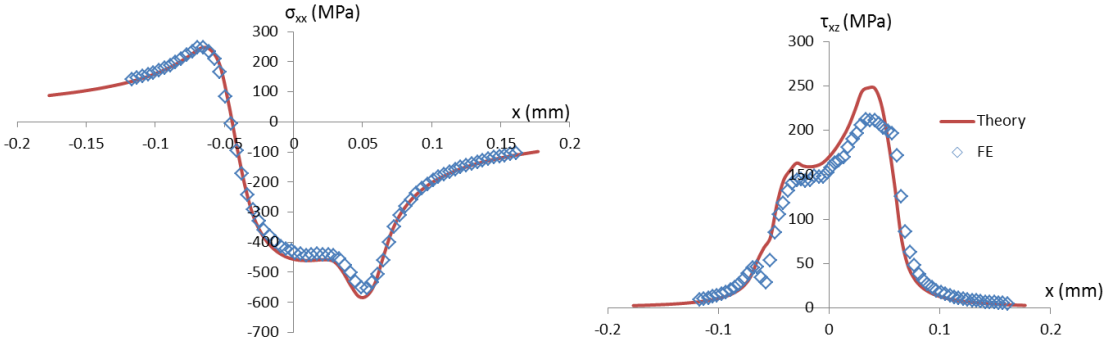

(a) (b)

Figure 5.4. Comparison of σ_{xx} and τ_{xz} stress results from FE to the analytical solution for partial-slip case (P = 50 kN, Δ_{app} = 1 μm).

5.3. Local pressure armour layer fretting FE model

5.3.1. Axisymmetric riser model

Figure 5.5 shows the axisymmetric FE model developed for the flexible riser section with pressure armour wire nub-groove contact. The riser model has been developed based on riser data from flexible riser data sheets (provides riser specification, e.g. OD, ID etc). The model was designed to focus on the nub-groove contact region of the pressure armour wire. Thus, the internal and external layers are modelled as two monolithic layers. The contact region of the pressure armour wire was modelled as a round nub-on-flat groove.

The pressure armour wire of a flexible pipe is helically wound at an angle of approximately 5° with the circumferential direction of the pipe, i.e. approximately circumferential to the pipe. Hence, it is assumed that the helix angle of the pressure armour wire can be ignored for the purpose of these simulations, so that the riser can be modelled as axisymmetric. Furthermore, a repeated axial segment of the riser pressure armour wire was modelled to reduce computational time (see Figure 5.5).

A detailed mesh refinement study was carried out to ensure convergence with respect to contact variables and substrate stresses in the nub and groove region. The element size in the contact region is 2 μm × 2 μm. 4-node bilinear axisymmetric quadrilateral elements (CAX4) are used. The contact interactions are described in Section 5.2.2.

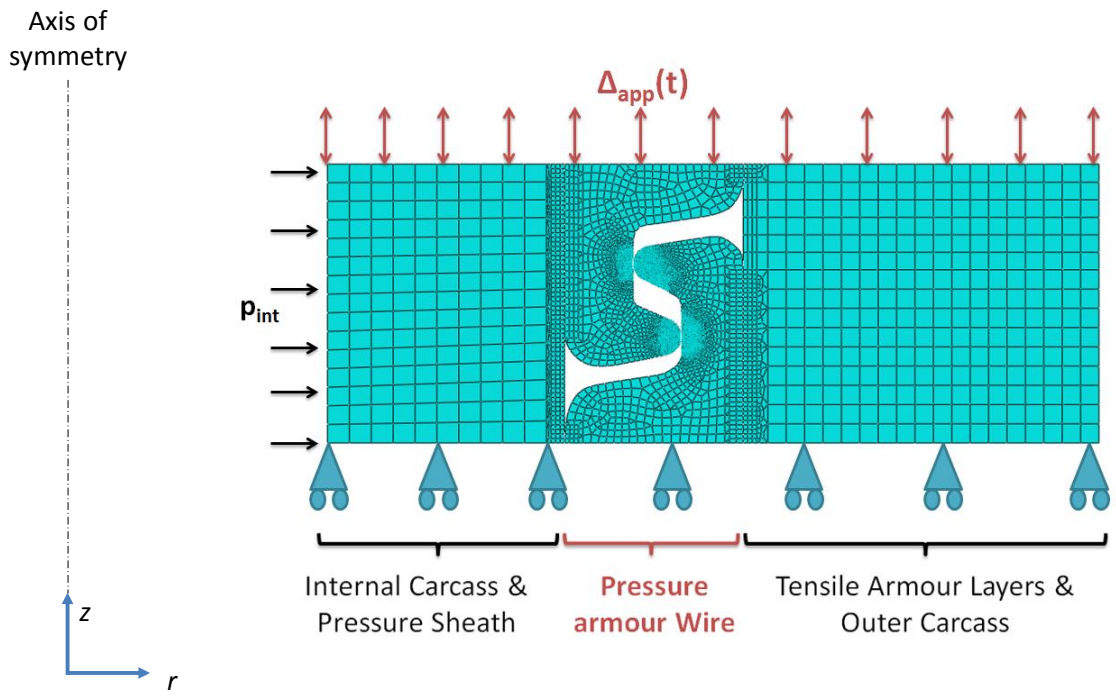

Figure 5.5. Boundary conditions and loadings on the pressure armour wire model.

Three internal pressure conditions are considered: design pressure (p_d), operating pressure (p_o) and a pressure below regular operating conditions (p_l). These conditions represent normal operating conditions and two extreme cases for internal pressure. The internal pressure (p_{int} in Figure 5.5) is assumed to be constant for the purpose of these models and thus does not presently account for possible pressure fluctuations, e.g. due to *"slugging"* (variations in the internal fluid density causing variations in internal pressure), for example, in the internal fluid. The bottom surface of the riser model is held in the axial direction (see Figure 5.5). A cyclic axial displacement (Δ_{app}) is applied to the top surface of the riser section (as in Figure 5.2 and Figure 5.5). Due to the typically observed evolution of CoF from an initial low value to a (typically) steady state high value under continuous fretting, e.g. see Figure 4.24(a), Chapter 4, the effect of variation of CoF has been investigated. The range in CoF values

studied also corresponds to the range in observed CoF values experimentally under dry and grease lubricated conditions (as discussed previously in Chapter 3).

5.3.2. Pressure armour material model

Both elastic and J_2 plasticity models have been investigated for the pressure armour axisymmetric model. The elastic properties used in the models are shown in Table 5.2; these are results from monotonic tensile tests described in Chapter 4.

The J_2 plasticity model incorporates non-linear kinematic hardening (NLKH) to simulate the Bauschinger effect combined with nonlinear isotropic hardening (or softening), as described in (McCarthy et al., 2014; Sweeney et al., 2014). The model is based on the von Mises yield function:

$$f = \left(\frac{3}{2} (\boldsymbol{\sigma}' - \mathbf{x}') : (\boldsymbol{\sigma}' - \mathbf{x}') \right)^{\frac{1}{2}} - k - r(\varepsilon_{eq}^{pl}) \tag{5.1}$$

where $\boldsymbol{\sigma}'$ and $\mathbf{x}'$ are the deviatoric stress and deviatoric back-stress tensors, respectively, k is the initial cyclic yield stress and $r(\varepsilon_{eq}^{pl})$ is the isotropic hardening function, where ε_{eq}^{pl} is the equivalent plastic strain given by:

$$\varepsilon_{eq}^{pl} = \int \sqrt{\frac{2}{3} d\boldsymbol{\varepsilon}^{pl} : d\boldsymbol{\varepsilon}^{pl}} \tag{5.2}$$

Isotropic hardening (softening) evolution is given by:

$$dr\left(\varepsilon_{eq}^{pl}\right) = b(Q - r) d\varepsilon_{eq}^{pl} \tag{5.3}$$

where Q is the saturation value of the isotropic parameter and b is the rate of decay towards saturation. The non-linear evolution of back-stress **x** is given by the Frederick-Armstrong rule for the Bauschinger effect:

$$d\mathbf{x} = \frac{2}{3} C d\varepsilon_p - \gamma \mathbf{x} d\varepsilon_{eq}^{pl} \tag{5.4}$$

The J_2 constants, shown in Table 5.2, were identified using the results of the low cycle fatigue tests carried out on the pressure armour layer material, extracted from the pressure armour wire material, as described in Chapter 4. The identification process used here for the cyclic plasticity constants is described in detail by Barrett et al. (2013), for example, among others. A comparison between the measured experimental and FE hysteresis stress-strain loops for the strain-controlled test conditions is shown in Figure 5.6.

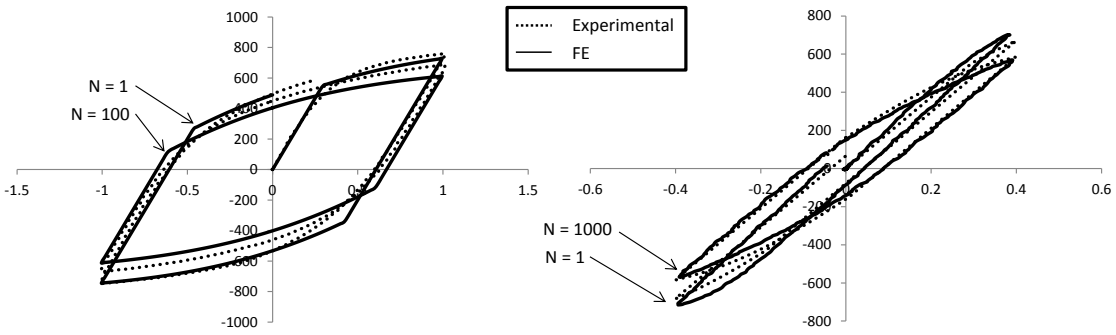

(a) (b)

Figure 5.6. Experimental and FE fretting loops for (a) 2% strain range, and (b) 0.8% strain range.

Table 5.2. Elastic-plastic material constants.

Parameter	Value
σ_y	750 MPa
E	189 GPa
v	0.3
Q	-130 MPa
b	15.48
C	48.3 GPa
γ	154

5.3.3. Local nub-groove contact results

Figure 5.7 shows the highly localised von Mises contact stress concentration predicted for the pressure armour layer.

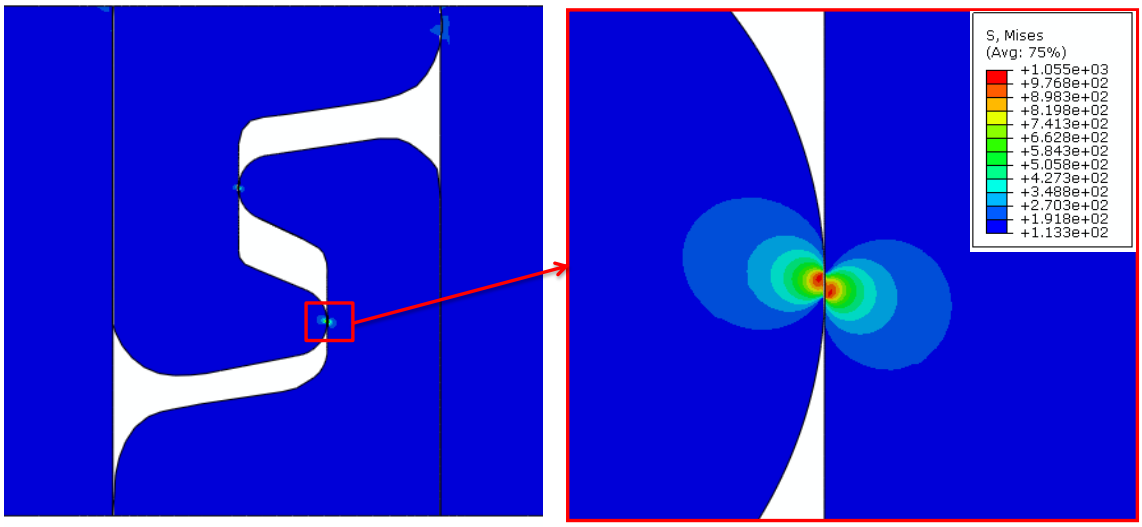

Figure 5.7. Von Mises contour plot of riser model.

After a sufficient number of cycles (McColl et al., 2004), surface modifications (tribological transformations) within the slip zone cause an increase in the local CoF from an initial low value (e.g. ≤ 0.3, approximately) to between 0.7 and 1.0 dependent on stroke, load and other factors (McColl et al., 2004). Figure 5.8 and Figure 5.9 shows the effects of CoF on substrate stresses in the groove of the pressure armour layer for (a) the elastic FE model, and (b) the elastic-plastic FE model. For a higher CoF (μ ~ 0.8) the predicted peak tensile stress location (Figure 5.8) in the elastic-plastic model is further out, from the contact edge, than for lower CoF values and the elastic model. There is a significant reduction (relaxation) in trailing edge tensile stress and maximum shear stress (Figure 5.9) for the elastic-plastic models in comparison to the elastic models.

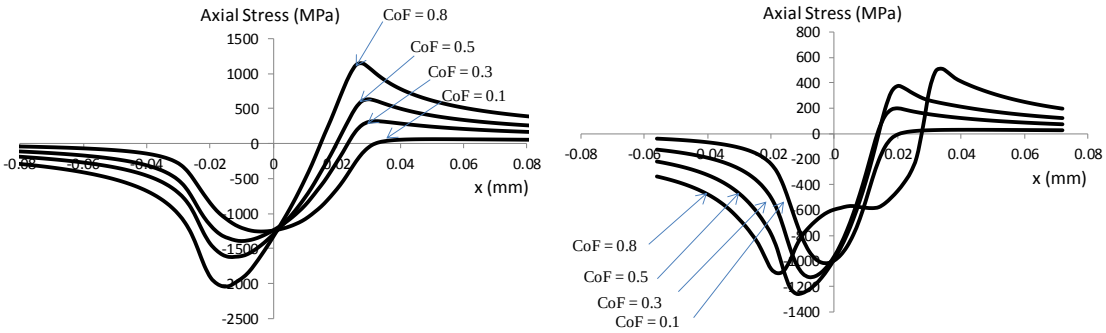

(a) (b)

Figure 5.8. Comparison of axial stresses for different CoFs for (a) elastic model, and (b) elastic-plastic model ($p_{int} = p_d$, Δ_{app} = 10 μm).

Figure 5.10 shows the effects of CoF on contact slip in the groove of the pressure armour layer for (a) the elastic FE model, and (b) the elastic-plastic FE model. There is a significant effect of CoF on contact slip amplitude. All values of CoF are

predicted to give gross slip under these loading cases; the values are close to the applied displacement. As the CoF increases, the contact slip decreases. The occurrence of localised negative contact slip in the +x region can be attributed to elastic and elastic-plastic deformation due to the change in slip direction during the cyclic loading history.

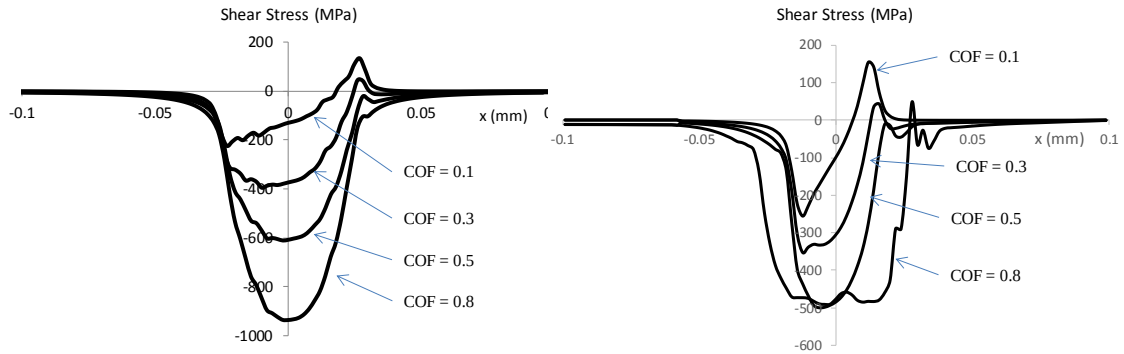

(a) (b)

Figure 5.9. Comparison of shear stresses for different CoFs for (a) elastic model, and (b) elastic-plastic model ($p_{int} = p_d$, Δ_{app} = 10 μm).

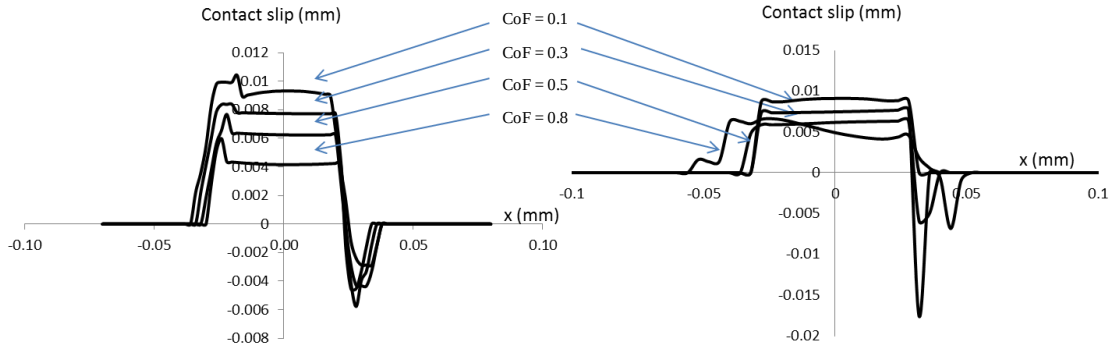

(a) (b)

Figure 5.10. Comparison of contact slip for different CoFs for (a) elastic model, and (b) elastic-plastic model ($p_{int} = p_d$, Δ_{app} = 10 μm).

5.4. Fatigue model

5.4.1. Fatigue indicator parameter

For fretting fatigue cracks, the stress range is a primary parameter for the calculation of fatigue life. High shear stress (τ_{xz}) ranges are generally considered to be responsible for fatigue crack initiation, and high tangential (trailing edge) stress (σ_{xx}) ranges for Mode I fatigue crack propagation. Since the contact loading is cyclic, a material point can experience a high shear stress and a low (compressive) tangential stress at one instant in a cycle, and subsequently at a later instant (e.g. half-cycle later) a low shear stress and a high (tensile) tangential stress; this behaviour increases the possibility of crack formation and growth due to fretting. Fretting fatigue crack initiation and growth can occur under both low and high cycle fatigue conditions, depending on local stresses, material strength, frictional and wear conditions, etc.

The Smith-Watson-Topper (SWT) fatigue parameter (Smith et al., 1970) considers both the Coffin-Manson equation for low cycle fatigue (LCF) and the Basquin's equation for high cycle fatigue (HCF), as follows.

$$SWT = \frac{\sigma_{\max}\Delta\varepsilon_a}{2} = \frac{(\sigma'_f)^2}{E}(2N_i)^{2b} + \sigma'_f\,\varepsilon'_f\,(2N_i)^{b+c} \tag{5.5}$$

where σ_{max} is the maximum normal stress on the critical plane (for mean stress effect), $\Delta\varepsilon_a$ is the maximum normal strain amplitude on the same plane, E is Young's modulus σ'_f and b are fatigue strength coefficient and exponent, ε'_f and c are the fatigue ductility coefficient and exponent, and N_i is the number of cycles to crack initiation. The total number of cycles to failure (N_f) is given by:

$$N_f = N_i + N_p \tag{5.6}$$

N_p is the number of cycles of crack propagation prior to failure (typically taken as the occurrence or measurement of a 2.5 mm long crack).

5.4.2. Critical plane approach

The critical plane approach for multiaxial fatigue has been previously successfully applied to the complex multiaxial stress-strain histories associated with fretting fatigue prediction (e.g. Madge et al., 2008; Sum et al., 2005; Zhang et al., 2012). The critical plane approach essentially identifies the plane of the greatest fatigue damage at a material point, in terms of the chosen fatigue parameter, in this case, the SWT parameter.

Figure 5.11 shows the procedure used to determine the critical plane and SWT life from FE simulation output (see Sum et al., 2005). Stress and strain time history data is read in from elements at the surface of the substrate for each time increment in each step. Data from the top row of integration points are used for the calculation of SWT life, as the stresses and strains are most critical close to the surface for fretting fatigue. In the two-dimensional case, the stresses and strains are then transformed for 36 different planes (5° apart) using the following transformation equations.

$$\sigma_{11}' = \frac{\sigma_{11} + \sigma_{22}}{2} + \frac{\sigma_{11} - \sigma_{22}}{2}\cos 2\theta_i + \tau_{12}\sin 2\theta_i \tag{5.7}$$

$$\varepsilon_{11}' = \frac{\varepsilon_{11} + \varepsilon_{22}}{2} + \frac{\varepsilon_{11} - \varepsilon_{22}}{2}\cos 2\theta_i + \gamma_{12}\sin 2\theta_i \tag{5.8}$$

where σ_{11}' is the transformed stress normal to the plane at angle θ_i, σ_{11}, σ_{22}, and τ_{12}, are the untransformed normal and shear stresses. ε_{11}' is the transformed strain normal

to the plane at angle θ_i, while ε_{11}, ε_{22}, and ε_{12}, are the untransformed normal and shear strains.

This gives stresses and strains for 36 different planes (5° apart, from 0° to 180°) for each element at every time increment. Next the maximum normal stress, σ_{max}, and the strain range, $\Delta\varepsilon_a$ are found. $\Delta\varepsilon_a$ is calculated as the difference between the maximum and minimum strain values over the full period of a load cycle. SWT values are calculated for each element; the maximum SWT value gives the minimum predicted fatigue crack initiation life. N_i is calculated by solving Equation (5.5) using the Newton-Raphson method.

3D implementation of the critical plane SWT was described by Sum et al. (2005). More complex stress transformations are required for the three-dimensional cases, as the extra dimension introduces another plane which must also be considered in the critical plane calculation. Thus, the plane must be defined by two angles θ_h and θ_v as shown in Figure 5.11. Direction cosines of a normal, ***n*** to the plane are given by:

$$n_x = -\sin\theta_v \sin\theta_h;\ \ n_y = \cos\theta_h;\ \ n_z = -\sin\theta_h \cos\theta_v \tag{5.9}$$

The transformed normal stresses and strains for a given plane defined by ***n*** are given by:

$$\sigma' = \sigma_{11}n_x^2 + \sigma_{22}n_y^2 + \sigma_{33}n_z^2 + 2\tau_{12}n_x n_y + 2\tau_{23}n_y n_z + 2\tau_{13}n_x n_z \tag{5.10}$$

$$\varepsilon' = \varepsilon_{11}n_x^2 + \varepsilon_{22}n_y^2 + \varepsilon_{33}n_z^2 + 2\gamma_{12}n_x n_y + 2\gamma_{23}n_y n_z + 2\gamma_{13}n_x n_z \tag{5.11}$$

The present implementation of the SWT critical plane approach has been previously validated against fretting fatigue test results for Ti-6Al-4V (Ding et al., 2007b) for cases with wear (Zhang et al., 2011) and without wear (Ding et al., 2007b); it has also been validated against continuum damage mechanics (Zhang et al., 2012) for

fretting fatigue of Ti-6Al-4V. It has also been shown to give good results for the prediction of tensile crack formation for combined cyclical axial and torsional loading (Shang et al., 2006).

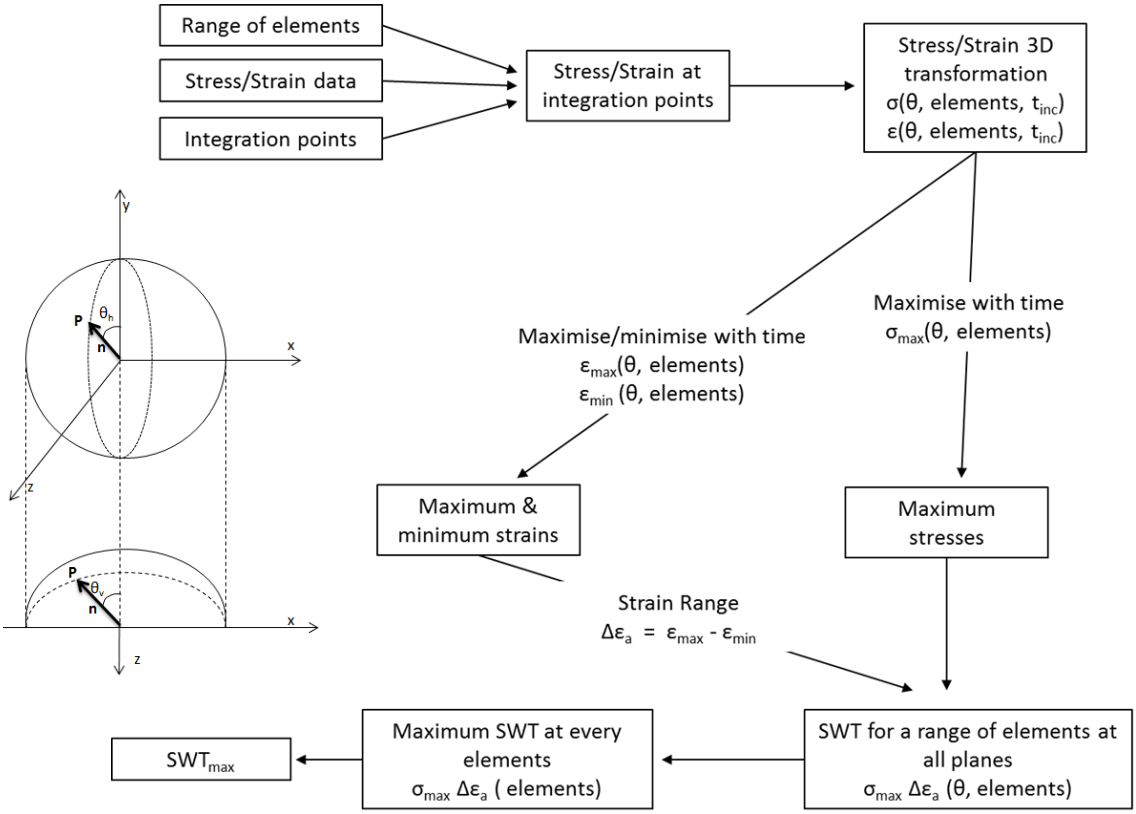

Figure 5.11. Orientation of unit normal vector **n** defined by θ_h and θ_v and implementation of critical plane SWT (adapted from Sum et al., 2005).

Figure 5.12 shows a comparison of the present 3D critical-plane fatigue prediction method for Ti-6Al-4V alloy fretting fatigue test data (Jin and Mall, 2004) for partial-slip. The prediction gives good correlation with the experimental data for this case where cracking is the primary damage mechanism.

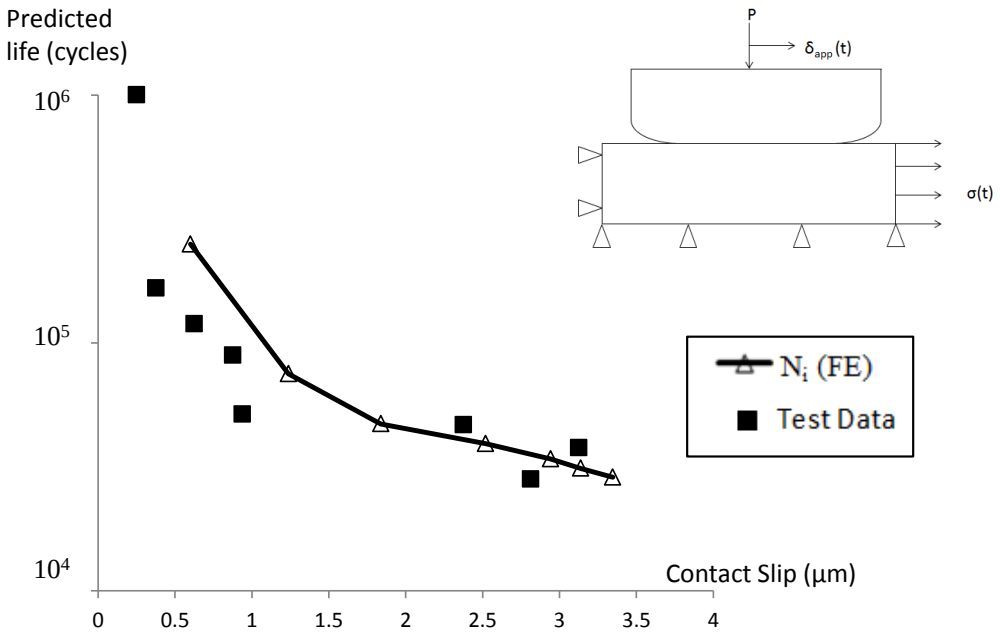

Figure 5.12. Multiaxial fretting fatigue (SWT) validation against experimental results for Ti-6Al-4V under partial slip (Jin and Mall, 2004).

5.4.3. Fatigue constants for pressure armour material

A programme of low-cycle fatigue (LCF) tests has been conducted on pressure armour material extracted from a pre-service flexible marine riser (see Chapter 4). Tests were conducted at strain ranges of 0.8%, 1%, 1.25% and 2%. These tests have provided Coffin-Manson constants (ε'_f and c) for the computational fatigue model (see Table 5.3), as described in Section 4.7.2.

Computational work in this thesis focuses on crack initiation; however, experimental tests (described in Chapter 4) typically give total life to observable cracks. Following Sweeney et al. (2014), a damage approach has been implemented for back-

calculation of approximate N_i for each experimentally applied strain range. Figure 5.13 shows the experimental damage curves evaluated as:

$$D = 1 - \frac{\sigma}{\sigma_{\max,soft}} \tag{5.12}$$

where $\sigma_{\max,soft}$ is the maximum peak tensile stress after initial cyclic softening takes place for each LCF test. A value of 0.008 is chosen for D_c, critical damage for crack initiation, based on a circumferential crack with a depth equal to the standard element size (10 μm) initiating at the free surface. N_s in Figure 5.13is the number of cycles for initial cyclic softening to take place. The resulting N_i data points are shown along with experimental N_f data in Figure 5.14. The Coffin-Manson fits for both crack initiation and failure are also shown in Figure 5.14. The Coffin-Manson constants (ε'_f and c) for crack initiation are presented in Table 5.3.

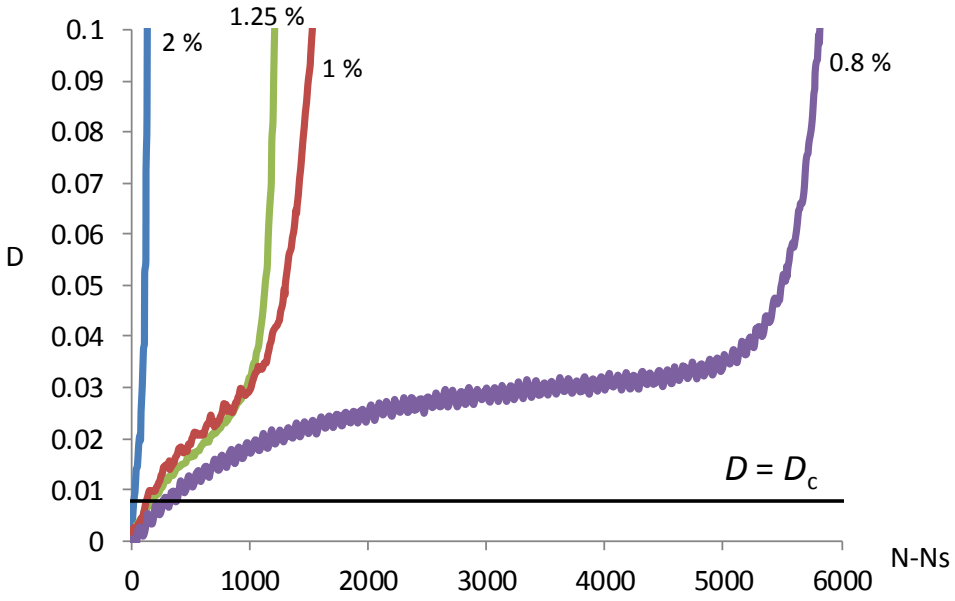

Figure 5.13. Damage evolution during LCF tests, where N_s is the number of cycles for initial cyclic softening to take place.

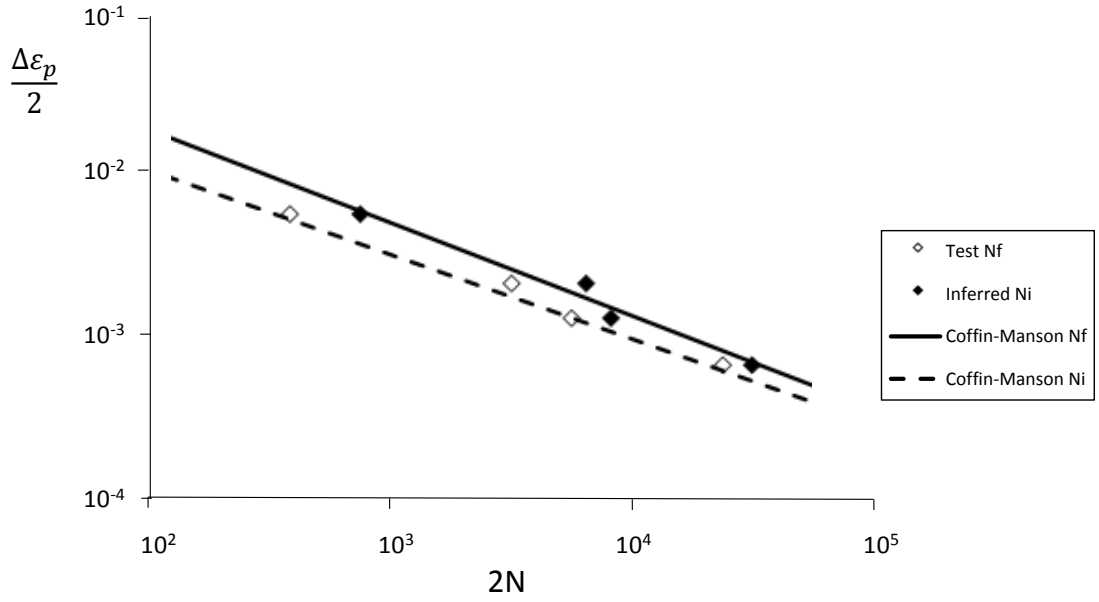

Figure 5.14. LCF experimental test results with Coffin-Manson fit for crack initiation and failure.

The universal slopes method (Cruzado et al., 2013; Manson, 1965) has been used to estimate the Basquin constants (σ'_f and b) for the computational fatigue model (see Table 5.3). The universal slopes method, in which the slopes of the plastic and elastic lines are universalised as -0.6 and -0.12 respectively for all materials, has been widely used, (Cruzado et al., 2013; Del Llano-Vizcaya et al., 2006) for example. This method gives estimated high-cycle fatigue (HCF) coefficients based on monotonic tensile test results for ultimate tensile strength. The universal slopes method has been shown to give a conservative estimate for the fatigue parameters (Park and Song, 1994). For the universal slopes method, about 80% of the data fall within a scatter band of a factor of 3 for both HCF and LCF for a large amount of test data obtained from experiments carried out on a range of different steels (Park and Song, 1994); this is approximately the same scatter found for different estimation methodologies.

HCF constants from the universal slopes method are for number of cycles to failure. The number of cycles to crack initiation was back-calculated following the approach used previously (Houghton et al., 2009; Madge et al., 2008; McCarthy et al., 2013). Using the Paris equation and El-Haddad correction (El Haddad et al., 1979) for small crack growth, the number of cycles for a crack to propagate, N_p, from 10 μm to failure (defined as 2.5 mm) was calculated, N_p was then subtracted from the number of cycles to failure calculated using the Basquin equation and universal slopes constants. This gave the number of cycles to crack initiation and hence, Basquin constants for crack initiation were found. The Basquin constants (σ'_f and b) for crack initiation are presented in Table 5.3.

Table 5.3. Identified low- and high-cycle fatigue constants for pressure armour wire, for crack initiation and failure.

Parameter	Initiation	Failure
σ'_f	1633 MPa	1710 MPa
ε'_f	0.11	0.24
b	-0.11	-0.12
c	-0.52	-0.57

5.4.4. Crack initiation lives for pressure armour layer

The predicted effects of CoF and axial displacement on SWT crack initiation life for the elastic and elastic-plastic models are presented in Figure 5.15(a). The predicted number of cycles to crack initiation decreases considerably as CoF increases.

For a low CoF ($\mu \leq 0.3$) some differences in the predicted life for the elastic and elastic-plastic models are predicted; this is mainly attributed to high plastic shear strain in the nub-groove contact region. However, for higher CoFs (μ = 0.5 to 0.8), negligible difference is predicted.

Figure 5.15(b) shows the effect of bending induced axial displacement on crack initiation in the pressure armour layer. As the applied axial displacement increases, the predicted number of cycles to crack initiation decreases, reaching a minimum (almost constant) value for large displacements. For low axial displacements (1 to 5 μm), the elastic-plastic model is predicted to give longer life than the elastic model; however, for higher applied axial displacements (10 μm) both models lead to similar life predictions.

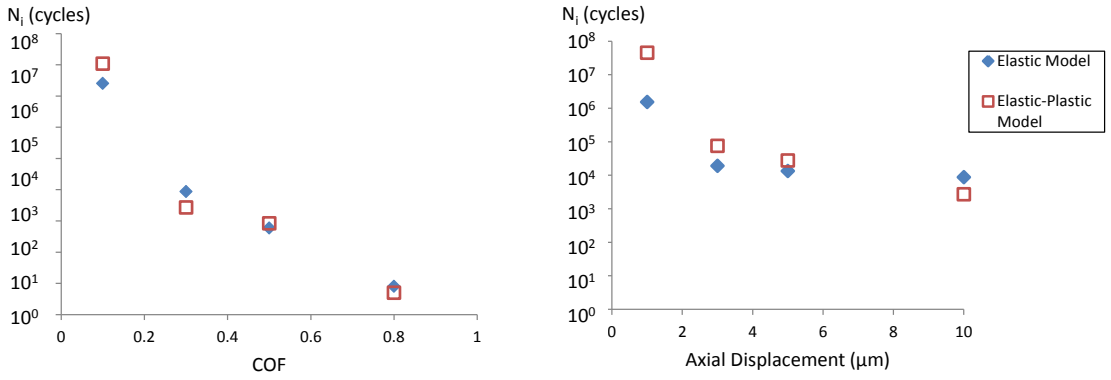

(a) (b)

Figure 5.15. SWT predicted lives showing the effect of (a) CoF ($P_{int} = p_d$, Δ_{app} = 10 μm) and (b) bending induced axial displacement ($p_{int} = p_d$, CoF = 0.3) for elastic and elastic-plastic models.

Table 5.4 presents the effect of internal pressure on predicted number of cycles to crack initiation (for elastic and elastic-plastic models), for the three pressures, p_d, p_o

and p_l, where $p_d > p_o > p_l$. Increasing pressure is predicted to cause significantly increased fatigue damage and hence, reduced life to crack initiation. All cracks are predicted to initiate at an angle of between 5° and 10° to the z-axis (see Figure 5.5), at the edges of contact, which is typical of fretting contacts.

Table 5.4. Predicted effect of internal pressure on fatigue life to crack initiation for elastic and elastic-plastic models (μ = 0.3, Δ_{app} = 10 μm).

p_{int}	**Minimum life –elastic model (cycles)**	**Minimum life –elastic-plastic model (cycles)**
p_d	8.6×10^3	2.7×10^3
p_o	9.4×10^4	8.1×10^5
p_l	1.9×10^6	2.9×10^7

5.5. 3D riser modelling

5.5.1. Sub-modelling approach

Sub-modelling is a technique often used to model a problem that is too large to simulate with a conventional modelling approach in FE. It is an FE technique used to get more accurate results in a region of the model. Creating a sub-model required two steps, as follows:

- Create and analyse the global model (typically with a course mesh).

- Create the sub-model (with a greater level of mesh refinement than the global model) and drive the boundaries of the sub-model with time-dependent variables that were saved during the analysis of the global model.

Sub-modelling is used here to obtain an accurate, detailed solution for the nub-groove contact variables (pressure, shear, slip) and substrate stresses in the nub-groove region under non-symmetric global riser loading, i.e. bending. This technique has been previously used for the analysis of contacting bodies (Rajasekaran and Nowell, 2005) and fretting fatigue in aero engine spline couplings (Houghton et al., 2009).

5.5.2. Global model details

The "global" model used for the sub modelling approach is shown in Figure 5.16. This is a riser cross-section model comprising of the repeated unit element used for the axisymmetric model described earlier revolved helical at 85° to the transverse section of the riser. Periodic boundary conditions are used for nodes on the top and bottom surfaces ensure the repeated element linear momentum of the system is conserved. The other boundary conditions on the model are as shown in Figure 5.16 and as described by Neto and co-workers (Neto, 2015, 2011; Neto et al., 2013). Nodes on the $z = 0$ and $x = 0$ planes have zero displacement in the z-direction and x-direction, respectively. Tie constraints are used to tie the top and bottom surfaces to reference points (RP1 and RP2 in Figure 5.16); loading conditions, such as axial displacement and bending moment, are applied to RP2. Internal and external pressures were applied to the inner and outer surface of the riser, respectively. Elastic material properties were used for this model, as detailed in Table 5.2.

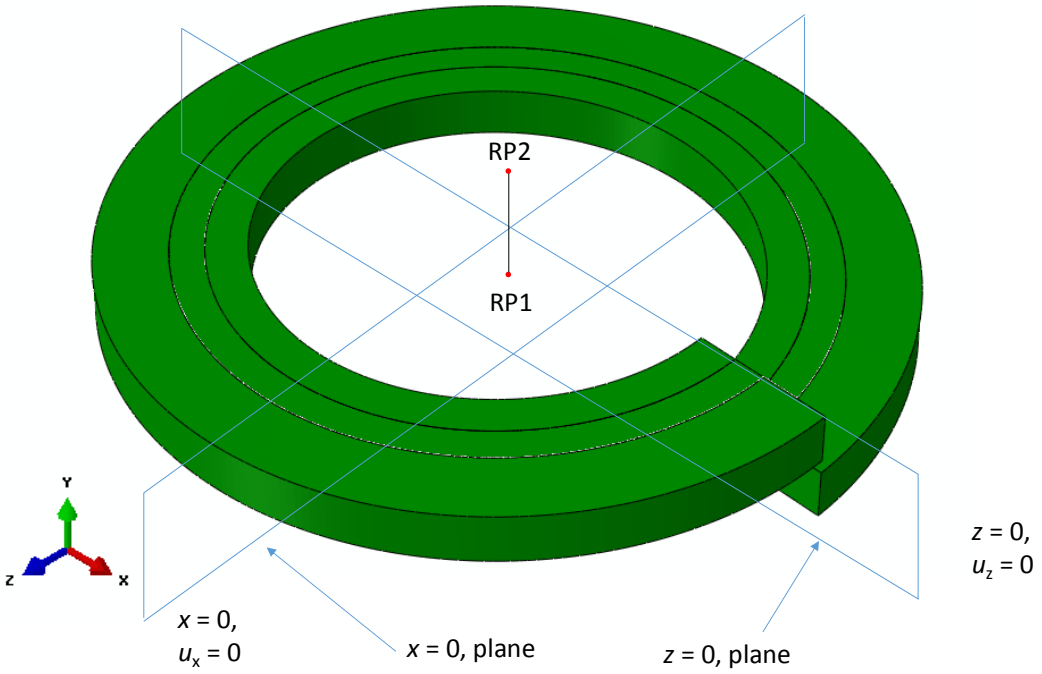

Figure 5.16. Boundary conditions for global model.

Contact interaction was defined as discussed in Section 5.3.1. The master-slave algorithm for finite sliding contact within Abaqus was used to define the surface interaction for both models. The maximum allowable penetration depth between master and slave nodes was set to 1 µm. The adjustment tolerance for the initial geometry was set to 0.001 µm. Since Coulomb-Amontons' Law is assumed for sliding friction, the exact stick condition is ensured by implementing Coulomb friction based on the Lagrange multiplier contact algorithm. The contact between the outer layers and pressure armour layer and between the inner layers and pressure armour layer are assumed to be frictionless; this is due to an anti-wear layer tape that is used between metallic layers in the risers. The coefficient of friction in the nub-groove region is modelled as 0.7; this is the measured dry fretting friction coefficient measured in Chapter 4.

Eight-node brick element with reduced integration (C3D8R) elements were used. The average element size for this model is 2 mm. The mesh is refined at the nub-groove contact; here, the average element size is 50 μm. Figure 5.17(a) and Figure 5.18(a) shows the mesh size and structure.

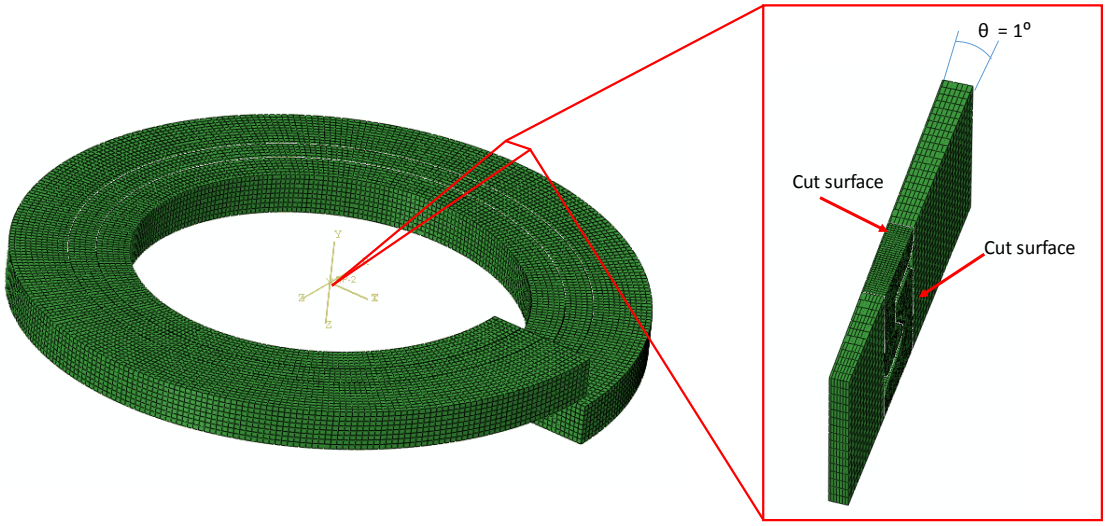

(a) (b)

Figure 5.17. (a) Global riser model showing one revolution of helically wound pressure armour wire, and (b) 1° segment sub-model of helically wound pressure armour wire showing cut surfaces for sub-model driven boundary conditions.

5.5.3. Sub model details

The sub-model used for the sub modelling approach is shown in Figure 5.17. A 1^0 segment of the global model described above is "cut" away and modelled with a finer mesh. The displacement of the cut surfaces (Figure 5.17(b)) is driven using sub-model boundary conditions based on time-dependent variables that were saved during the analysis of the global model. Periodic boundary conditions, tie constraints loading

conditions, material properties and contact conditions used for the sub model are as described for the global model above.

(a)

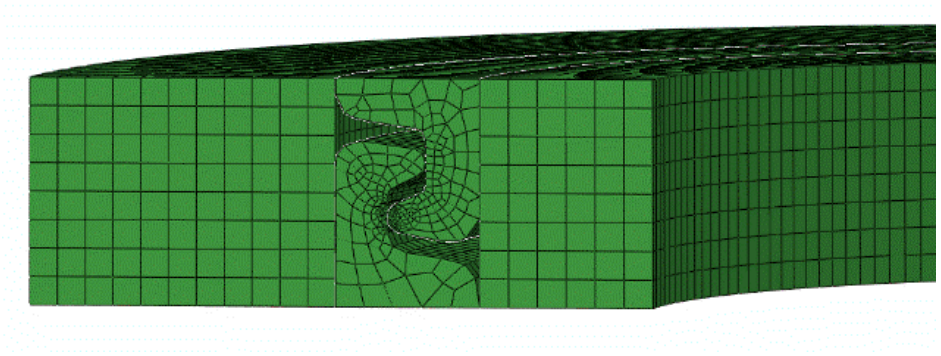

(b)

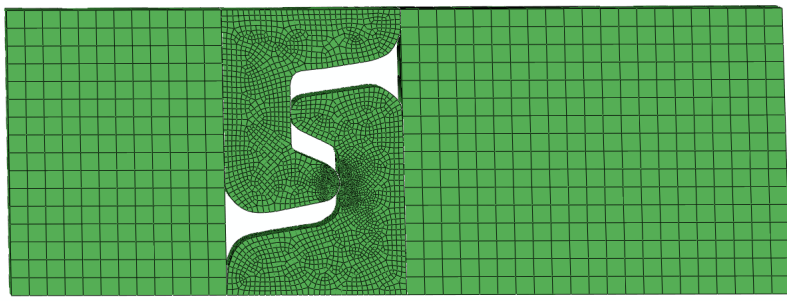

Figure 5.18. (a) Course mesh used for the global model, and (b) fine mesh used for the riser sub-model.

Eight-node brick element with reduced integration (C3D8R) elements were used. A more refined mesh is used for the sub-model than for the global model. The average element size for this model is 0.5 mm. The mesh is refined at the nub-groove contact; here, the average element size is 4 μm. Figure 5.17(b) and Figure 5.18(b) shows the mesh size and structure.

5.5.4. Validation of 3D modelling technique

The sub-modelling finite element approach was validated against results from the axisymmetric model of Section 5.3.1 for fretting contact in the nub-groove of the pressure armour layer. Internal and external pressures of 27.5 MPa and 4 MPa, respectively, were applied to the risers, combined with cyclic axial displacement of amplitude 5 μm.

There was good correlation between both modelling techniques. The peak contact pressure and slip are identical for both models (see Figure 5.19). The contact width (2*a*) differs by 4 μm between the two models.

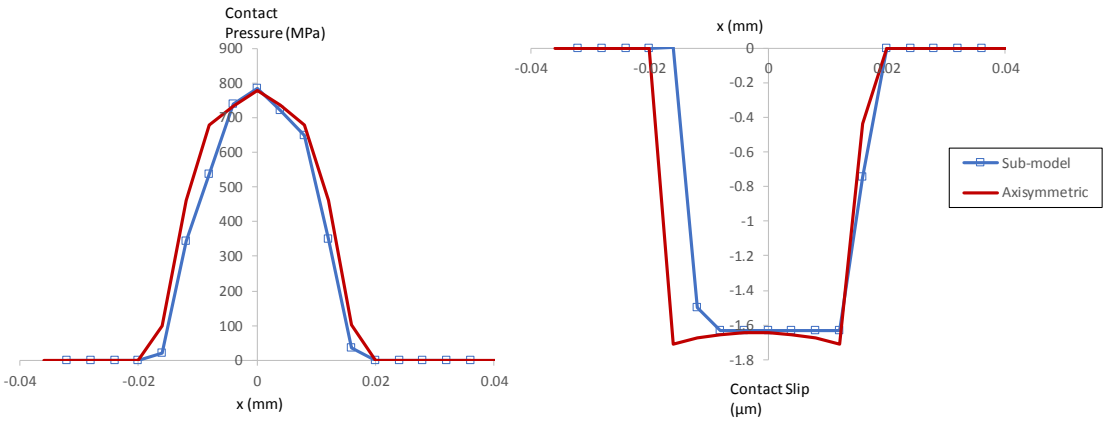

(a) (b)

Figure 5.19. Comparison between contact variable results from axisymmetric model and sub-model for (a) contact pressure, and (b) contact slip.

Figure 5.20 presents a comparison between (a) axial and (b) shear stress distributions from the sub-model and axisymmetric model. Again, this shows good correlation between modelling techniques. However, the trailing edge tensile stress is 30 % lower for the sub-model than for the axisymmetric model.

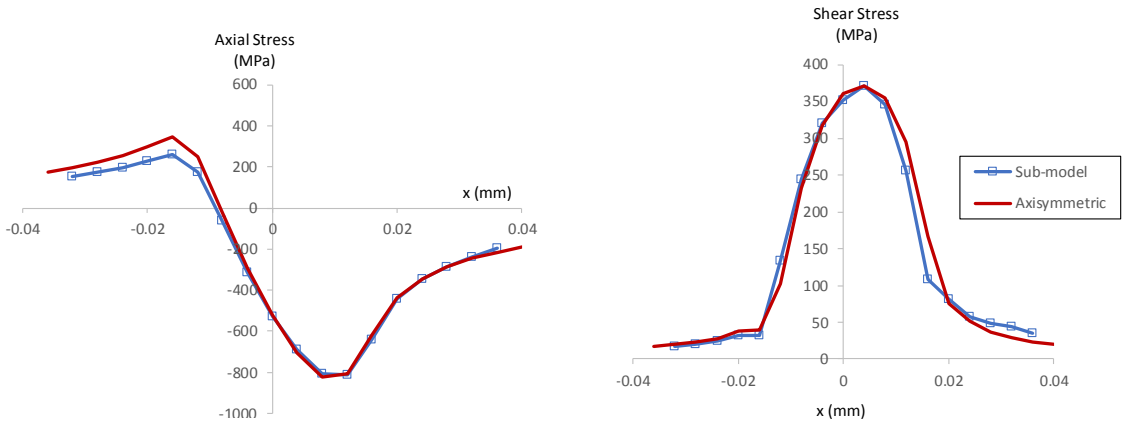

(a) (b)

Figure 5.20. Comparison between substrate stresses results from axisymmetric model and sub-model for (a) axial and (b) shear stress.

5.5.5. Effect of bending moment on nub-groove contact conditions

The primary benefit of using the 3D model over the axisymmetric model is that the effect of non-axisymmetric loading, such as bending moment, on contact conditions can be investigated. In this section, the effect of a bending moment of ± 750 MPa about the *z*-axis, as shown in Figure 5.21, is discussed. This bending moment is a typical bending moment from global dynamic riser curvatures results from Flexcom (as described later in Chapter 7). Both the internal and external nub-groove contacts, as shown in Figure 5.22, are investigated. Material, contact conditions, internal and external pressure and mesh size are as described for the global riser analysis in Section 5.5.2.

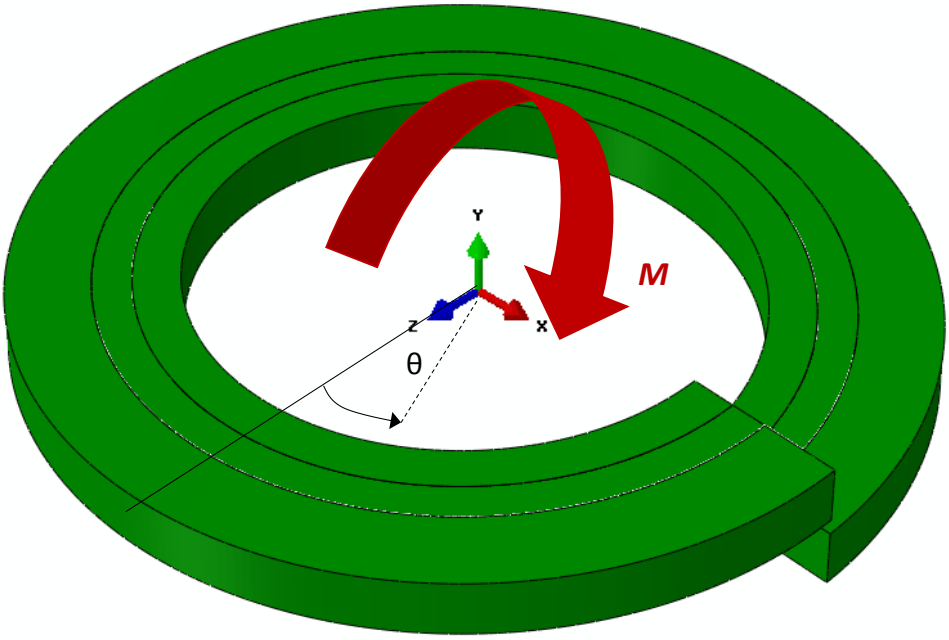

Figure 5.21. Schematic of bending moment about the *z*-axis, direction of θ used in results graphs.

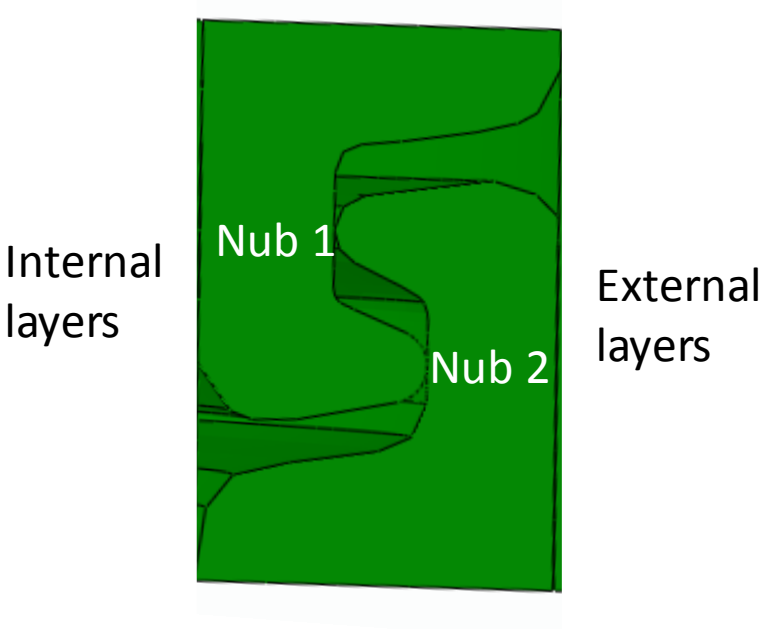

Figure 5.22. Schematic of pressure armour layer, indicating Nub 1 and Nub 2 for results.

Figure 5.23 presents the effect of riser bending on nub-groove contact slip (in the axial direction, *y*-direction in Figure 5.21) circumferentially, where θ is as shown in Figure 5.21 and Nub 1 and Nub 2 are described in Figure 5.22. Contact slip is positive for negative θ and negative slip is observed for positive θ. This is as expected for the loading conditions, where the bending moment results in a range of contact slip conditions around the nub-groove region. However, the contact slip is unstable in the circumferential direction. This can be attributed to the coarse mesh used for this model. It is recommended here that the global model be used to identify areas for further investigation, such as areas where partial slip conditions may occur.

Figure 5.24 presents the effect of riser bending on nub-groove peak contact pressure (in the axial direction, *y*-direction in Figure 5.21) circumferentially, where θ is as shown in Figure 5.21 and Nub 1 and Nub 2 are described in Figure 5.22. Peak contact pressure increases for negative θ compared to the peak contact pressure for the case without bending moment (~600 MPa as shown in Figure 5.19(a)). For the case without bending moment, the peak contact pressure is constant (~600 MPa) in the circumferential direction. The peak contact pressure is unstable in the circumferential direction; again, this can be attributed to the course mesh used for this model. Negative slip is observed in Figure 5.23 for positive θ; here, there is reduced contact pressure; contact pressure is ~ 0 MPa for some regions and other regions experience lift-off of the nub-groove contact.

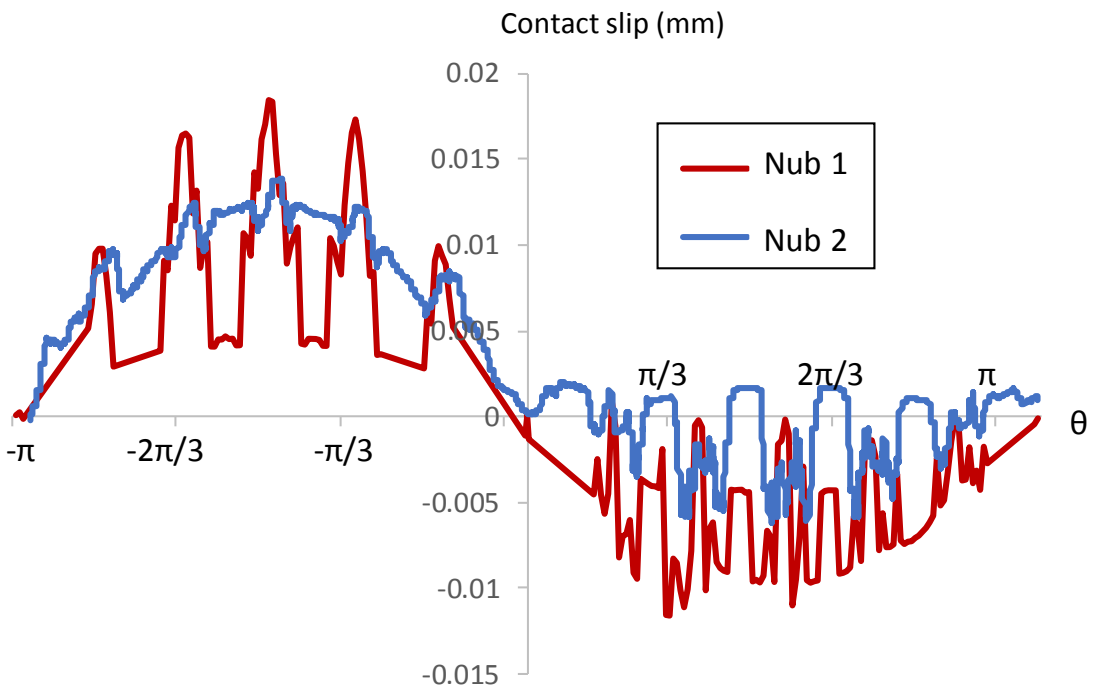

Figure 5.23. Effect of angular position, θ, as shown in Figure 5.21, on nub-groove contact slip due to global riser bending moment, M.

Further investigation is required to investigate the effect of a range of global dynamic riser loading conditions, i.e. internal and external pressure, axial displacement and bending moment, on nub-groove contact conditions, i.e. contact slip and pressure. This will provide a running condition fretting map for fretting in the nub-groove contact region based on global riser conditions. A schematic of a RCFM is provided in Figure 2.17, this map gives the slip regime (PS, MS or GS) based on displacement amplitude and normal load; in the case of risers, both nub-groove displacement amplitude and normal load are dependent on a combination of internal and external pressure, as well as riser bending moment.

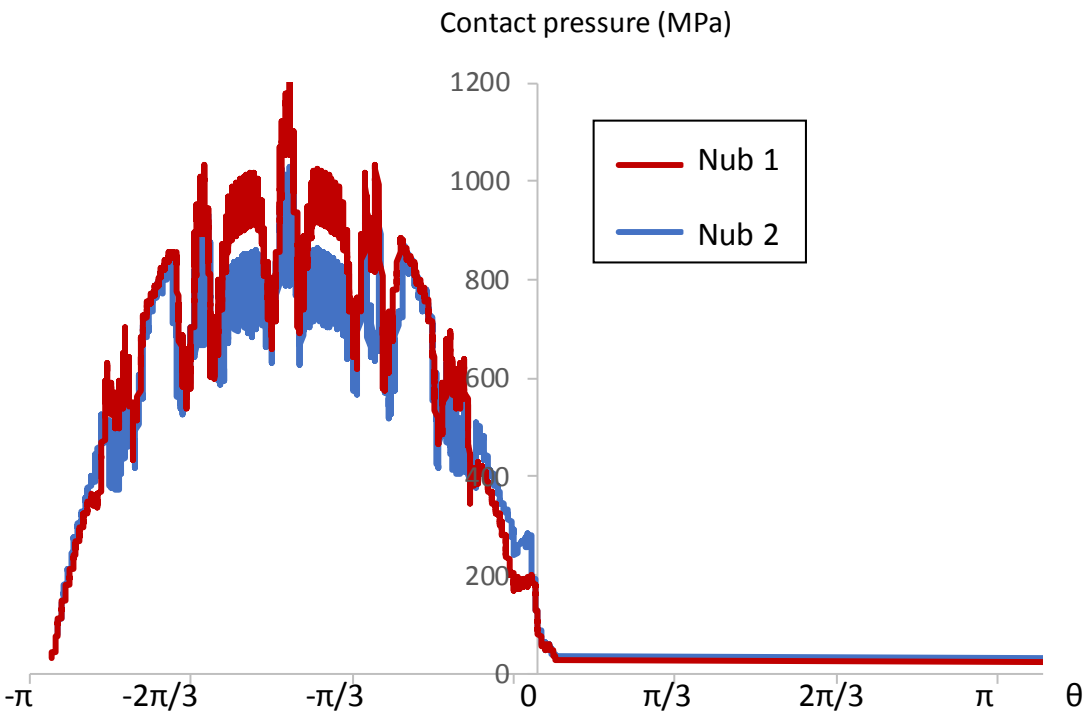

Figure 5.24. Effect of angular position, θ, as shown in Figure 5.21, on nub-groove contact pressure due to global riser bending moment, M.

The computational (CPU) times to run the global and sub-model on an Intel® Core™ i7-3770 processor with 8 cores for parallel processing are ~ 2.8 and ~ 2.2 hours, respectively. The diameter of the riser modelled is 6 inch (152.4 mm), the computational time increases significantly for increased riser diameters. The CPU time increases to ~ 3.6 and ~ 5.5 hours for the global and sub-model, respectively, for a riser of diameter 9 inches (228.6 m).

5.6. Summary and conclusions

An analytical frictional contact model for a Hertzian cylinder-on-flat geometry based on the theory of elasticity has been developed; this can be adopted as the basis for an analytical fretting fatigue life prediction model for the nub-groove contact region of the pressure armour layer flexible risers. Frictional contact FE models of the Hertzian contact have also been developed. The FE model is shown to be in general agreement with the analytical results for Hertzian contact in both partial and gross slip regimes, in terms of minimum tangential and shear stresses, locations and peak values.

An axisymmetric FE model of the flexible riser cross-section is developed incorporating a pressure armour wire contact. This revealed a highly-localised and severe trailing-edge tensile stress concentration due to fretting action. Cyclic plasticity and low-cycle fatigue characterisation of pressure armour wire material, in terms of J_2 plasticity material constants and Coffin-Manson fatigue constants, has been conducted. Attention has been focused on prediction of crack initiation; the modelling of material plasticity had an effect on predicted crack initiation lives.

Crack initiation predictions have been calculated using a 3D critical plane SWT fatigue indicator parameter. CoF evolution and increased bending induced axial displacement are shown to have a significant and detrimental effect on the trailing-edge tensile stresses responsible for fatigue crack initiation. However, in flexible marine risers, higher values CoF may result in lower contact displacements; hence the detrimental effect of high CoF may be counteracted by lower axial displacements. The work presented in this chapter does not include the effects of fretting wear. At high contact displacements (gross slip regime), wear can have a beneficial effect on

predicted fretting fatigue life. Fretting wear effects on contact variables and predicted crack initiation life will be investigated in the next chapter.

A 3D riser model is presented using sub-modelling techniques to accurately predict nub-groove contact conditions. This has allowed the effect of non-symmetric loading, such as bending moment, on nub-groove contact conditions to be quantified, for the first time.

Chapter 6: Combined fretting wear and fatigue model for pressure armour wire contacts

6.1. Introduction

In this chapter, a framework for prediction of combined fretting wear and fretting fatigue for frictional contact in pressure armour wire material of flexible marine risers is outlined. The methods implemented are based on similar previous developments by Madge et al. (2008, 2007a), combining FE-based fretting wear simulation, based on the work of McColl et al. (2004), with the critical-plane approach of Sum et al. (2005) for fretting fatigue multiaxiality. Furthermore, in order to facilitate more rapid design for combined wear-fatigue effects, a fretting fatigue surface damage parameter, originally proposed by Ding et al. (2011, 2007), has been implemented for the pressure armour wire material. This provides a computationally efficient design tool for fretting in flexible marine risers.

6.2. Modelling fretting wear

6.2.1. Adaptive meshing techniques

The fretting wear model implemented here uses an adaptive meshing methodology, with the Abaqus FE code. This has been implemented within the

UMESHMOTION user subroutine to simulate the fretting wear process, based on the Archard wear equation (as described in Chapters 2 and 4), first proposed by McColl et al. (2004). The fretting wear depth is calculated by applying Archard's equation to the local contact conditions along the contact area. The Archard equation was chosen since it can easily be adapted for specific loading conditions, i.e. only one test is required to identify a specific wear coefficient for constant CoF conditions; whereas, multiple tests are required to identify an energy wear coefficient, α, and the threshold energy, $E_{d,th}$, (Pearson and Shipway, 2015). Another advantage of the Archard wear equation is that the Archard wear coefficient can be easily identified from experimental results from the literature (e.g. Mohd Tobi et al., 2011); therefore, riser designers can investigate various materials for optimum design of the pressure armour layer. The local wear depth, using a modified Archard wear equation, is given by (Madge et al., 2008; McColl et al., 2004):

$$\Delta h(x,t) = k_l\, p(x,t)\delta(x,t) \tag{6.1}$$

where $\Delta h(x, t)$, $p(x, t)$ and $\delta(x, t)$ are the incremental wear depth, contact pressure and relative slip at a point x on the contact surface at time t and k_l is the local wear coefficient. McColl et al. (McColl et al., 2004) describe how the FE simulation of wear requires a local wear coefficient, k_l, which is expressed as the wear per unit local slip per unit local contact pressure. However, this is different to the conventional wear coefficient, k, defined in terms of worn volume per unit displacement per unit load (as described in Chapters 2 and 4). It has been argued (McColl et al., 2004; Paulin et al., 2008) that there is a close relationship between the local wear coefficient k_l and the experimentally determined volumetric wear coefficient k.

To reduce the computational time for fretting wear simulations, a cycle jumping technique (Johansson, 1994; Mary and Fouvry, 2007; McColl et al., 2004; Öqvist, 2001) was employed, where it is assumed that the contact pressure and slip distributions remain constant over ΔN cycles. Therefore, Equation (6.1 becomes:

$$\Delta h(x,\tau) = \Delta N k_l p(x,\tau)\delta(x,\tau) \tag{6.2}$$

where τ is the time within on "cycle" corresponding to ΔN wear cycles. Wear simulation is conducted for a total number of cycles, N_t. The implementation of this wear simulation algorithm in Abaqus is represented in the flowchart of Figure 6.1 and the adaptive meshing technique is depicted in Figure 6.2.

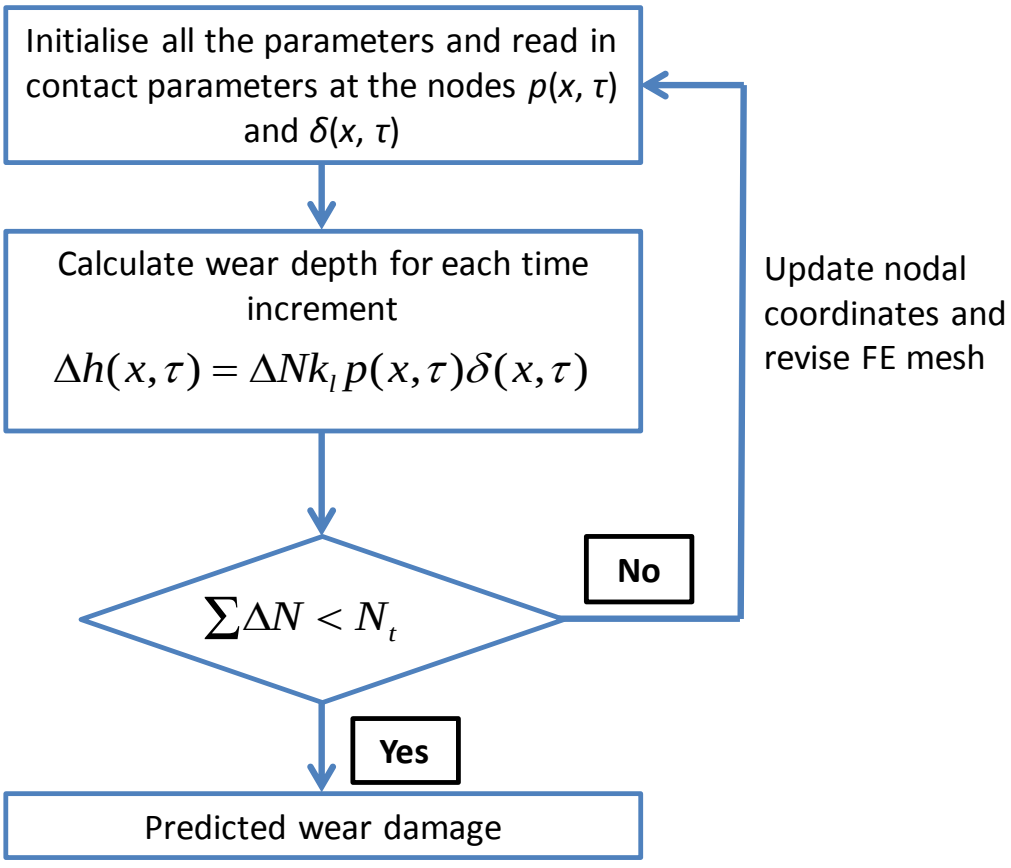

Figure 6.1. Methodology for implementation of the adaptive meshing technique to predict fretting wear damage, where N_t is the total number of fretting cycles modelled.

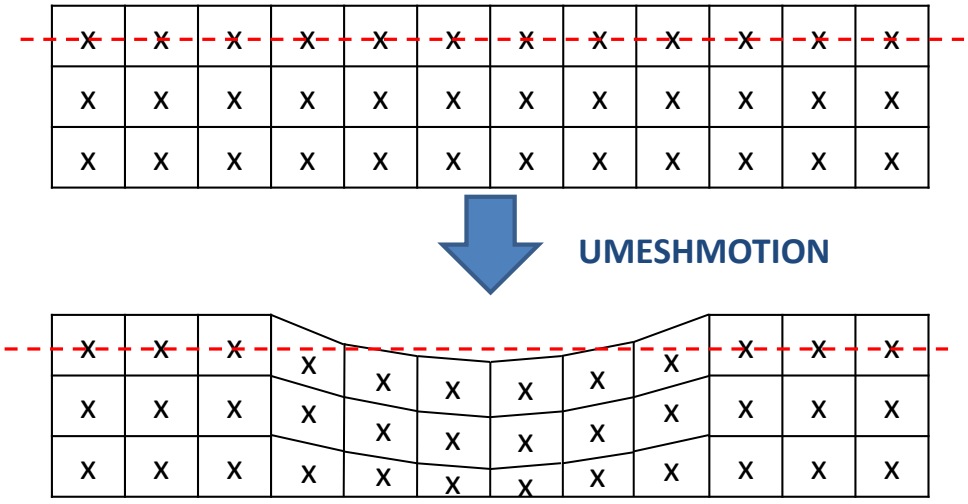

Figure 6.2. Movement of finite element mesh to simulate material removal due to wear via adaptive meshing methodology (based on Cruzado et al., 2013).

The adaptive meshing technique is validated here against 6 mm radius cylinder-on-flat experimental profiles of wear scars measured, as described in Chapter 4, for a 3 mm radius cylinder-on-flat geometry which is intended to be representative of the nub-groove contact in the pressure armour layer (see Figure 6.3). The coefficient of friction and wear coefficient of friction used here are 0.7 and 1.1×10^{-8} MPa^{-1}, respectively, as found for dry fretting test results in Chapter 4. Otherwise, FE contact model conditions are the same as in Chapter 5, Section 5.3.1. The material modelled in this chapter is modelled as elastic; this is a limitation for consistency with use of cycle jumping, since plasticity accumulation could not be correctly computed using cycle jumping. It is worth mentioning, however, that both the elastic and plastic models where shown to lead to similar predicted number of cycles to crack initiation in Chapter 5.

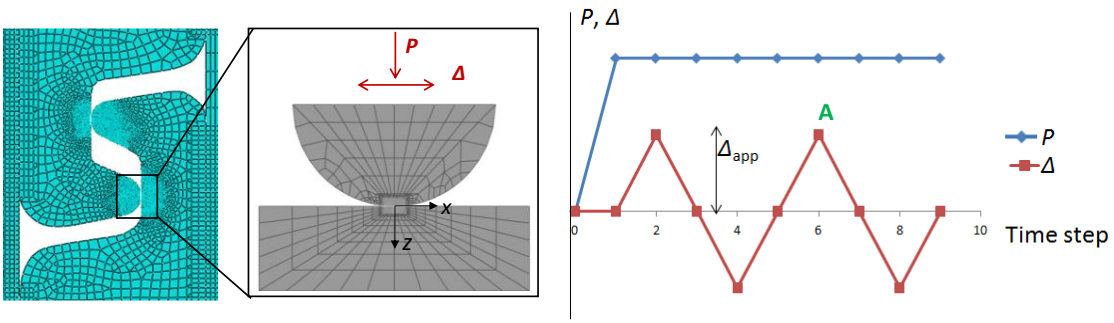

(a) (b)

Figure 6.3. (a) Cylinder-on-flat FE model representation of nub-groove contact for wear simulation; (b) loading history for normal load, P and applied displacement, Δ_{app}.

In Figure 6.4, a comparison is made between the finite element simulated wear scars and experimentally measured fretting wear scars for R = 6 mm under two different loading conditions: (a) P = 500 N, Δ_{app} = 30 µm; and (b) P = 250 N, Δ_{app} = 15 µm after 10^5 cycles of fretting. These loading conditions give a range of contact pressures and relative slips that are representative of nub-groove contact conditions. There is a reasonable correlation between the FE simulated wear scar and the experimentally measured wear scar. The FE model over-predicted maximum wear depth by 11 % (in Figure 6.4(a)) and 13 % (in Figure 6.4(b)) in comparison to the measured experimental values. The width is under-predicted by 6 % in Figure 6.4(a), and over-predicted by 24 % in Figure 6.4(b). In this study, as a simplification, wear of the cylindrical indenter and the effects of debris are not explicitly simulated (Ding et al., 2007b). Therefore, the effect of debris "*pile-up*", for example, as is evident in the experimental wear scar shown in Figure 6.4(b), is not captured in the FE wear simulation.

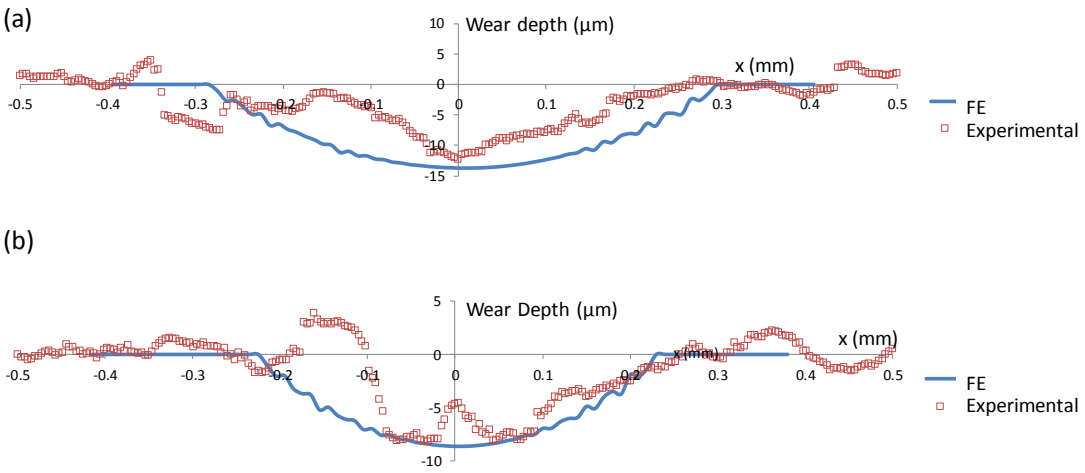

Figure 6.4. Comparison between FE simulated and measured wear scars for R = 6 mm after 10^5 cycles at 20 Hz and: (a) P = 500 N, Δ_{app} = 30 µm; and (b) P = 250 N, Δ_{app} = 15 µm.

6.2.2. Effect of wear on fretting variables

Figure 6.5 presents the evolution of predicted wear with fretting cycles for a 3 mm cylinder-on-flat model under normal load (P) of 50 N/mm and displacement amplitude (Δ_{app}) of 10 µm; these loading conditions give gross slip, and therefore, wear is the dominant fretting damage. Figure 6.6 presents the corresponding predicted contact pressure evolution for the 1st, 25,000th, 100,000th and 200,000th cycles. It can be seen that, as wear evolves, the contact width is predicted to widen and the contact pressure is predicted to redistribute over a wider area; therefore, the peak pressure is dramatically reduced and the pressure becomes much less concentrated with increasing cycles.

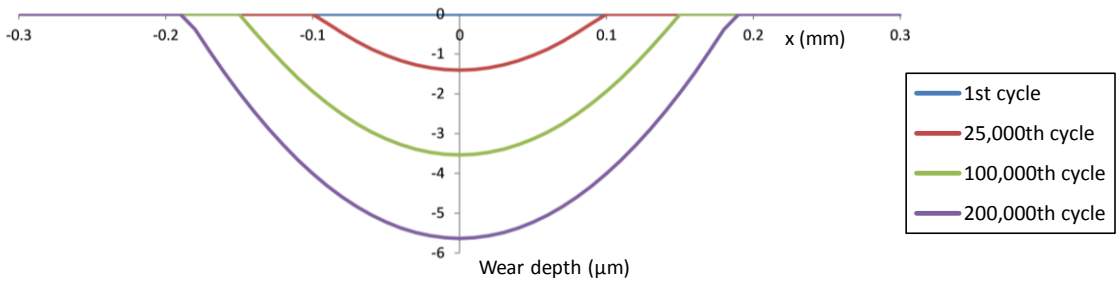

Figure 6.5. FE wear simulation results for gross slip (P = 50 N/mm and Δ_{app} = 10 µm) condition showing predicted evolution of wear scar.

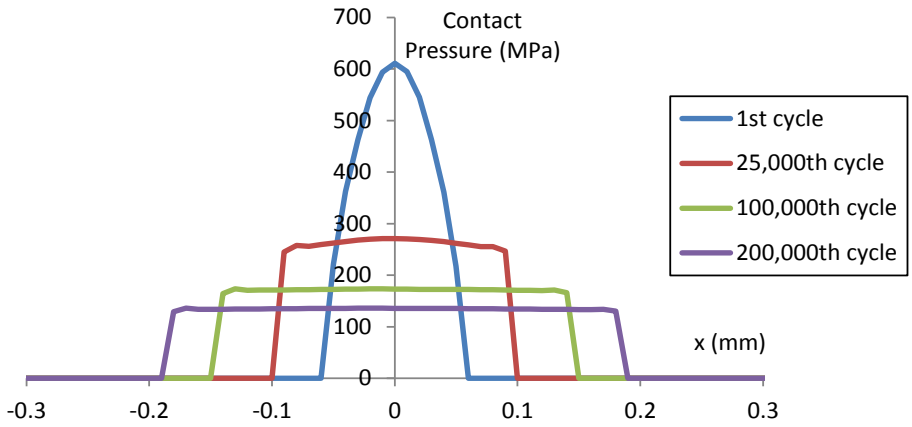

Figure 6.6. FE wear simulation results for gross slip (P = 50 N/mm and Δ_{app} = 10 µm) condition showing evolution of contact pressure.

The predicted effect of the redistribution of contact pressure on (a) tensile (σ_{xx}) and (b) shear (τ_{xz}) stresses is presented in Figure 6.7 for the extreme stroke position (e.g. *A* in loading history of Figure 6.3(b)). The contact width is predicted to increase from 100 to 360 µm over 2 × 10^5 fretting cycles, causing a 55 % decrease in trailing edge tensile stress. The location of the maximum (trailing edge) tensile stress moves outwards as the contact width increases. The maximum shear stress value is initially

located in the centre of contact; however, as the contact width increases, the shear stress is redistributed to an almost uniform value across the contact, which is dramatically reduced relative to the unworn case (about 75 % less that the initial peak value).

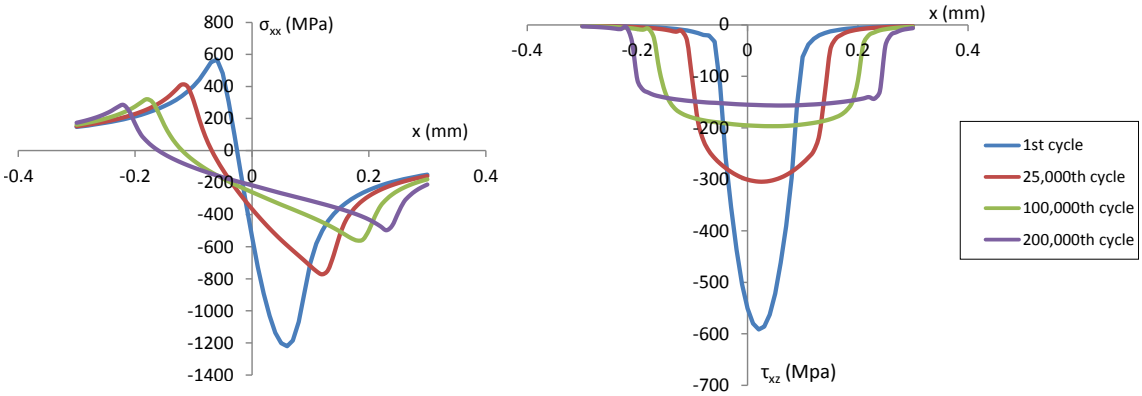

(a) (b)

Figure 6.7. FE wear simulation results for gross slip (P = 50 N/mm and Δ_{app} = 10 μm) condition showing predicted evolutions of (a) tensile stress (σ_{xx}) and (b) shear stress (τ_{xy}) at extreme stroke position, (A in loading history of Figure 6.3 (b)).

6.3. Combined wear-fatigue model

6.3.1. Wear-fatigue damage accumulation

Due to the evolving geometry and stress fields associated with fretting wear, a fatigue damage accumulation model is required for prediction of fretting fatigue life. The Miner-Palmgren rule is used to calculate the damage accumulation, as follows:

$$D = \sum_{i=1}^{N} \frac{\Delta n_i}{N_i} \tag{6.3}$$

where Δn_i is the number of cycles experienced at loading cycle i with an associated SWT value of SWT_i, and N_i is the predicted number of cycles to crack initiation for

SWT_i (given by Equation 5.5). When D = 1, a crack is assumed to have initiated at the SWT-predicted location, orientation and number of cycles. Within the present FE methodology, D is calculated at the location of the centroid of the first row of surface elements in the unmodified mesh (prior to wear taking place).

As discussed in detail by Zhang et al. (2013), in the adaptive meshing technique in the FE simulation, the centroidal position (same as Gauss point position for 4-noded reduced integration quadrilateral elements) of each surface element changes from cycle to cycle, due to movement of the mesh. Therefore, is necessary to track the same centroidal position from cycle to cycle (see Figure 6.2) in order to consistently accumulate damage at specific material points. Hence, following Zhang et al. (2013), a material point mesh (MPM) has been defined, independent of the FE mesh, to calculate the damage accumulation. In this method the MPM has fixed coordinates; the SWT damage is calculated at the centroid of each element and linearly interpolated back to the MPM for calculation of accumulated damage. The spacing for the MPM is determined from the initial location of each element centroid for the unmodified mesh, following Cruzado et al. (2013).

6.3.2. Wear-fatigue life predictions

The initiation SWT constants shown in Table 5.4 as back-calculated from the total life constants, using the method proposed by Madge et al. (2008) based on El-Haddad modified Paris equation (El Haddad et al., 1979) for short crack growth are been used. Fretting crack initiation life predictions have been calculated for element centroidal (integration point) positions at a depth of 5 μm below the surface of the substrate. When a damage of 1 is predicted for an integration point close to the surface,

the element is deemed to have reached crack initiation, with a crack length of 10 μm. This work focusses on the interaction and competition between fatigue crack initiation (damage) and wear-induced material removal, potentially leading to either exacerbated initiation conditions (partial slip) or ameliorated conditions (gross slip). Crack propagation is not explicitly considered here.

Figure 6.8 presents the predicted effect of applied displacement on crack initiation life with and without the effects of wear-induced material removal. In the partial and mixed slip regimes (Δ_{app} < 4 μm), the predicted crack initiation life is essentially the same for both models. However, in the gross slip regime, exclusion of wear effects is seen to significantly underestimate life relative to the "with wear" case. Including wear effects leads to a dramatic increase in life (to almost 10^8 cycles) with increasing stroke (displacement), relative to the minimum value in the partial slip regime. In all cases, the fretting fatigue cracks are predicted to initiate at the edge of contact and the predicted (critical plane) angle for crack initiation is between 10° and 30° to the horizontal.

The predicted increase in crack initiation life, when wear is included, is attributed to the redistribution of stresses, due to the evolution of the contact geometry and widening of the contact width. This trend is consistent with the fretting schematic of Vingsbo and Söderberg (1988), where, as wear rate increases, the predicted fretting fatigue life increases. Hence, for flexible marine riser design, fretting wear is predicted to be an important consideration, particularly in gross-slip conditions, to avoid overly-conservative prediction of crack initiation.

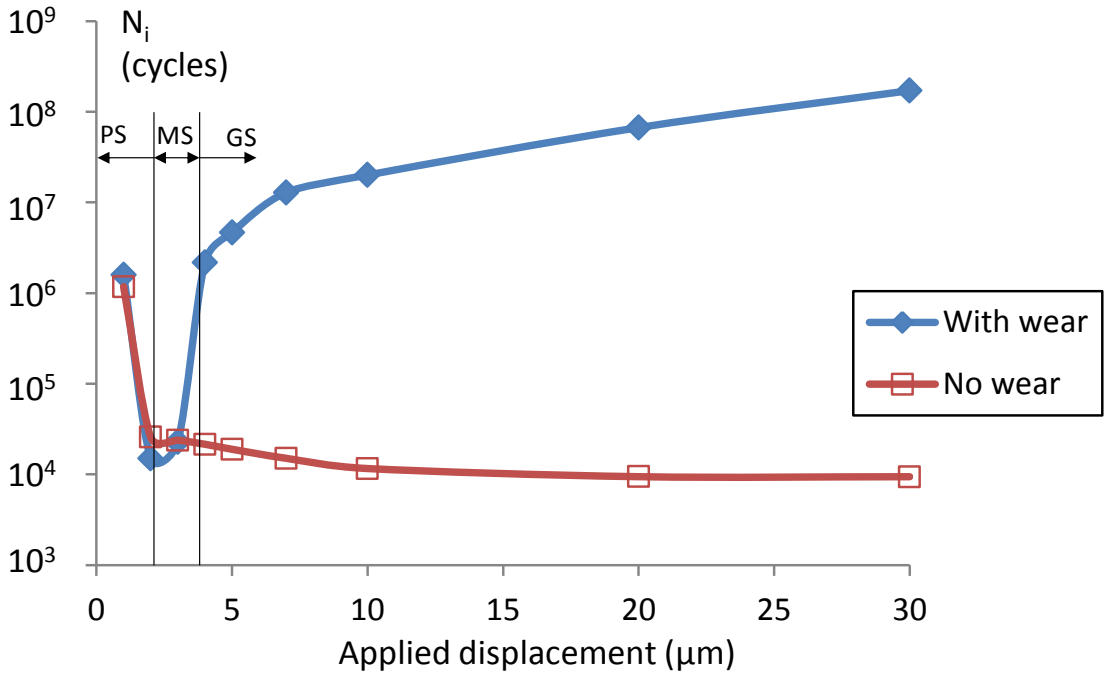

Figure 6.8. Predicted effect of applied tangential displacement on crack initiation life: (i) without effect of wear, and (ii) with effect of wear.

6.4. Fretting wear-fatigue design parameter

The computational time for simulating fretting wear in a full or partial flexible marine riser, with multiple three-dimensional nub-groove contacts, under realistic loading histories, is prohibitively expensive for design purposes. Hence, it is proposed to implement the D_{fret} fretting parameter here for the flexible riser material and contact geometry, based on the original work of Ding et al. (2011) for aeroengine spline couplings. The D_{fret} method introduces a surface damage factor for the effects of fretting wear in conjunction with critical-plane SWT approach, developed to incorporate the effects of slip and surface wear damage on crack initiation, as follows:

$$\sigma_{\max}\Delta\varepsilon_a D_{fret} = \frac{(\sigma'_f)^2}{E}(2N_i)^{2b} + \sigma'_f\,\varepsilon'_f\,(2N_i)^{b+c} \tag{6.4}$$

where D_{fret} is a surface damage factor given by Ding et al. (2011):

$$D_{fret} = (1 - C\tau\delta)\left\langle 1 - \frac{\tau\delta}{(\tau\delta)_{th}}\right\rangle^m \tag{6.5}$$

where C, m, and $(\tau\delta)_{th}$ are material parameters; τ and δ are the local contact shear and slip, respectively. $(\tau\delta)_{\text{th}}$ has been estimated here as a value slightly greater than the value at the partial slip -gross slip transition, based on FE simulations and following Ding et al. (2011). For $\tau\delta < (\tau\delta)_{\text{th}}$, the unmodified SWT value is used (i.e. $D_{\text{fret}} = 1$); for $\tau\delta > (\tau\delta)_{\text{th}}$, the SWT-$D_{\text{fret}}$ value is used (Equation (6.4).

The material parameters C and m were identified here (and by Houghton et al. (2009)) by applying a least squares minimisation method to the following objective function:

$$F(C,m) = \sum_i \left\{SWT_{D,i}(C,m) - SWT_{AM,i}\right\}^2 \tag{6.6}$$

where $SWT_{D,i}(C,m)$ is the D_{fret}-predicted SWT value at sample (element centroid) point i, $SWT_{AM,i}$ is the corresponding wear-simulated SWT value (using the adaptive meshing technique). The resulting material parameters identified here for the pressure armour layer are presented in Table 6.1. A comparison of the wear-simulated $SWT_{\max}$ from the previous section, and the corresponding maximum SWT-D_{fret} value, (from the least squares minimisation method) is shown in Figure 6.9.

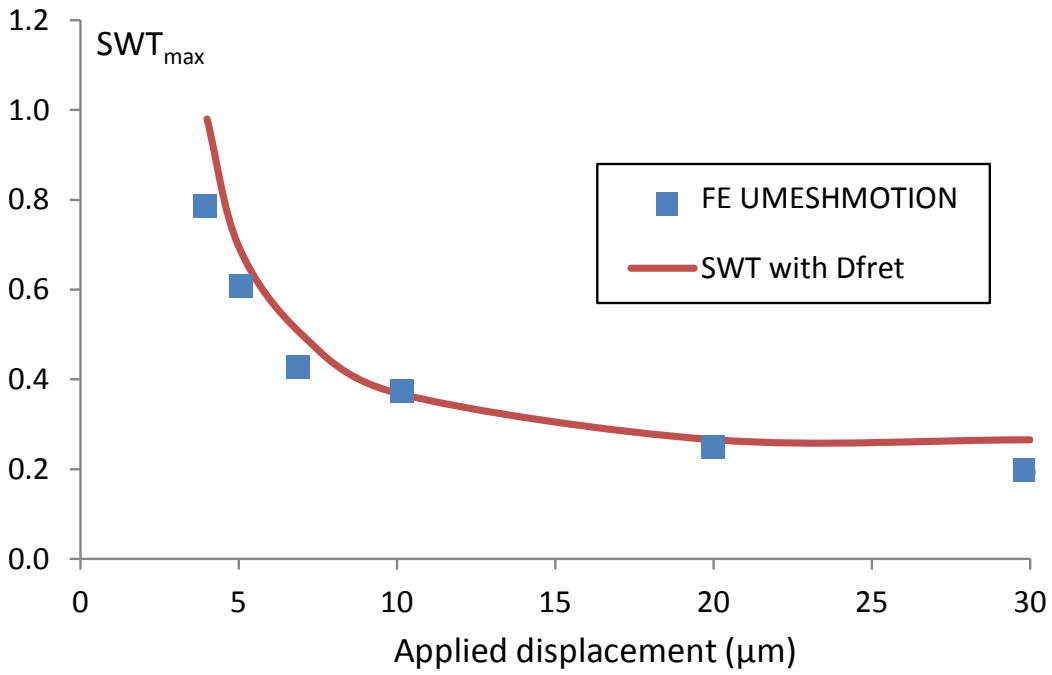

Figure 6.9. Comparison between effect of applied fretting displacement on SWT, as predicted by D_{fret} approach and explicit FE wear simulation approach.

Table 6.1. D_{fret} parameters for pressure armour wire.

Parameter	Value
$(\tau\delta)_{th}$	0.4 MPa mm
C	0.05 MPa^{-1} mm^{-1}
m	-0.85

A comparison between the fretting crack initiation lives calculated using the modified SWT-D_{fret} parameter and wear simulation analysis is presented in Figure 6.10. This shows excellent correlation between the two prediction methods, particularly in terms of the beneficial effect of increasing (gross) slip amplitude. The major advantage of the modified SWT parameter over explicit modelling of wear is the significant

reduction in computational expense. Table 6.2 compares the computational (CPU) time for explicit wear FE simulation of 250,000 cycles and the contact model excluding wear used for D_{fret}; simulations were conducted on an Intel® Core™ i7-3770 processor with 8 cores for parallel processing.

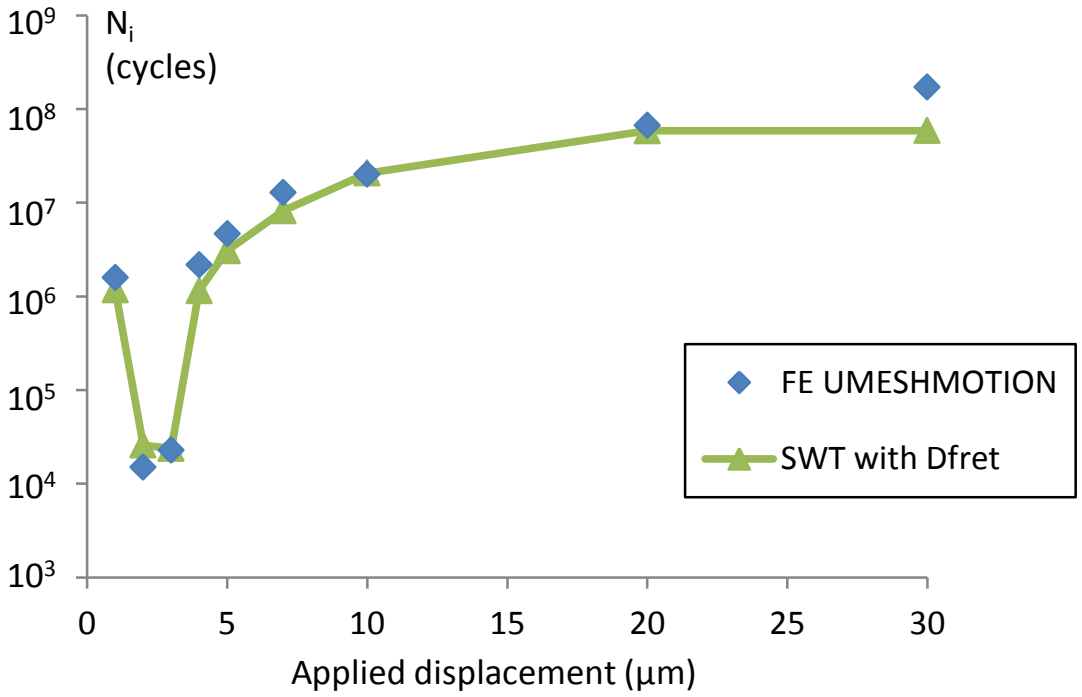

Figure 6.10. Comparison between effect of applied fretting displacement on crack initiation life, as predicted by modified SWT-D_{fret} approach and explicit FE wear simulation approach.

Table 6.2. Computational time for explicit FE UMESHMOTION wear modelling compared to fretting contact FE modelling excluding wear.

Model	**FIP**	**CPU Time**
Explicit wear FE	SWT	~ 6 hrs
No wear FE	SWT-D_{fret}	~ 4 mins

6.5. Summary and conclusions

A finite element computational methodology for combined fretting wear-fatigue analysis of riser material is developed. The method combines fretting wear simulation using an adaptive meshing technique with critical plane multiaxial fatigue life prediction. The fretting wear simulations are validated against cylinder-on-flat fretting wear experimental test results.

The effect of tangential displacement on fretting crack initiation life was investigated. Increased tangential displacement is shown to have a beneficial effect on predicted life to crack initiation. However, experimental validation is required to investigate the increase in life to crack initiation in GSR due to beneficial effects of wear, i.e. fretting cycles up to 10^7 to 10^8 (test duration of between 6 and 60 days at a test frequency of 20 Hz) for applied displacement of ±30 μm.

A fretting wear-fatigue design parameter was shown to successfully capture the effects of wear and tangential displacement on fretting crack initiation life as predicted by the explicit wear fatigue approach. The major benefit of this parameter is the reduced computational expense, since wear does not have to be explicitly modelled.

Chapter 7: Global-local fretting analysis of flexible risers

7.1. Introduction

This chapter presents analysis of fretting in the nub-groove contact region for a realistic flexible riser design based on data provided by the industrial partners, Wood Group Kenny. Global riser analyses are presented to provide loading conditions for local finite element nub-groove fretting analysis. Predictions are made for numbers of cycles to crack initiation and crack propagation, thus providing total fretting fatigue lives for the risers. Running condition fretting maps (RCFM) are developed for three riser geometries. The effects of riser specification (internal diameter) and sea-state load-case are investigated. The aims of this case study are to (i) apply the experimental results and modelling methodologies of this thesis to a realistic industrial design, and thus, (ii) assess the service life of the nub-groove component of candidate risers under realistic environmental conditions.

7.2. Methodology

Figure 7.1 shows the framework for the methodology implemented here. Global and local analysis are combined to predict the fretting fatigue life of the pressure

armour wire nub-groove contact. The global analyse are conducted using the software code Flexcom, to predict dynamic riser response, such as time histories of axial tension, $F(t)$, and riser curvature, $\kappa(t)$, in response to dynamically-imposed vessel motion and sea-state loading conditions. Geometrical and analytical models are used to identify local FE (axisymmetric) riser model loading conditions, such as applied displacement, $\Delta_{app}(t)$ and additional pressure $p_a(t)$, based on global riser curvature, $\kappa(t)$, and axial tension, $F(t)$, respectively, as shown in the flowchart of Figure 7.1. Local nub-groove fretting contact is analysed using the FE axisymmetric model, as described in Chapter 5. Fretting fatigue life is predicted from the resulting contact stresses, slips and surface traction results using the D_{fret}-SWT parameter of Chapter 6. Hence, wear is not explicitly modelled, thus reducing the computational time for local fretting analysis. Crack propagation is estimated using a weight function approach and hence, total life is obtained for the fretting regions of the risers.

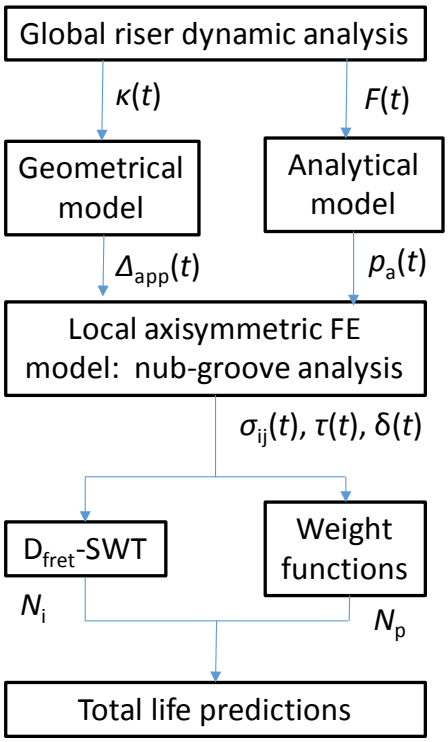

Figure 7.1. Framework for fretting life prediction in flexible marine risers.

7.3. Global riser analysis

7.3.1. General

This study focuses on a single line hybrid riser (SLHR) with a flexible riser jumper connecting to a floating production, storage and offloading vessel (FPSO) as shown schematically in Figure 7.2; three different dynamic flexible riser jumper geometries have been analysed. The water depth from the seabed to MSWL (mean sea water level, as shown in Figure 7.2) is 2030 m. This is close to the boundary between what is considered to be deep and ultra-deep (> 2,133 m) drilling. As oil reserves in shallower waters deplete, the oil and gas industry are pushed to extract oil at depths that were once considered too deep for hydrocarbon exploration and extraction. The configuration of SLHR with riser jumpers is often used to extract hydrocarbons at ultra-deep seas; this is because the flexible riser jumpers fully decouple the SLHR from the vessel motions; in turn, the vessel motions are decoupled from the wellhead at the seabed, making hydrocarbon extraction safer.

Cyclic loading in the dynamic flexible risers due to wave and current loading create axial tension and curvature variations along the risers, leading to micro-scale motion between nub-groove contacts in the pressure armour wires. The full study of the behaviour of the flexible dynamic jumpers requires the consideration of long term cyclic loading.

Global riser analysis was conducted using the software Flexcom, the development of which was discussed in Section 2.8.1. Flexcom uses an established finite element formulation, incorporating a hybrid beam-column element with fully

coupled axial, bending and torque forces, e.g. see Lane et al., (2001, 2005), O'Brien et al., (2003, 2002), Smith et al., (2007) and Connaire et al., (2015).

7.3.2. Riser configuration and geometrical properties

The SLHR and riser jumper configuration of this case study is shown schematically in Figure 7.2. The FPSO and SLHR hang-off points are typically critical sections for fatigue along the flexible riser due to the high tensions and curvature variation. Sag bend location can also be critical for fatigue also, due to the high curvature variation in this area. However, the full length of the risers is analysed here since critical fretting conditions (PS) may not necessarily coincide with the locations of maximum loading or displacement.

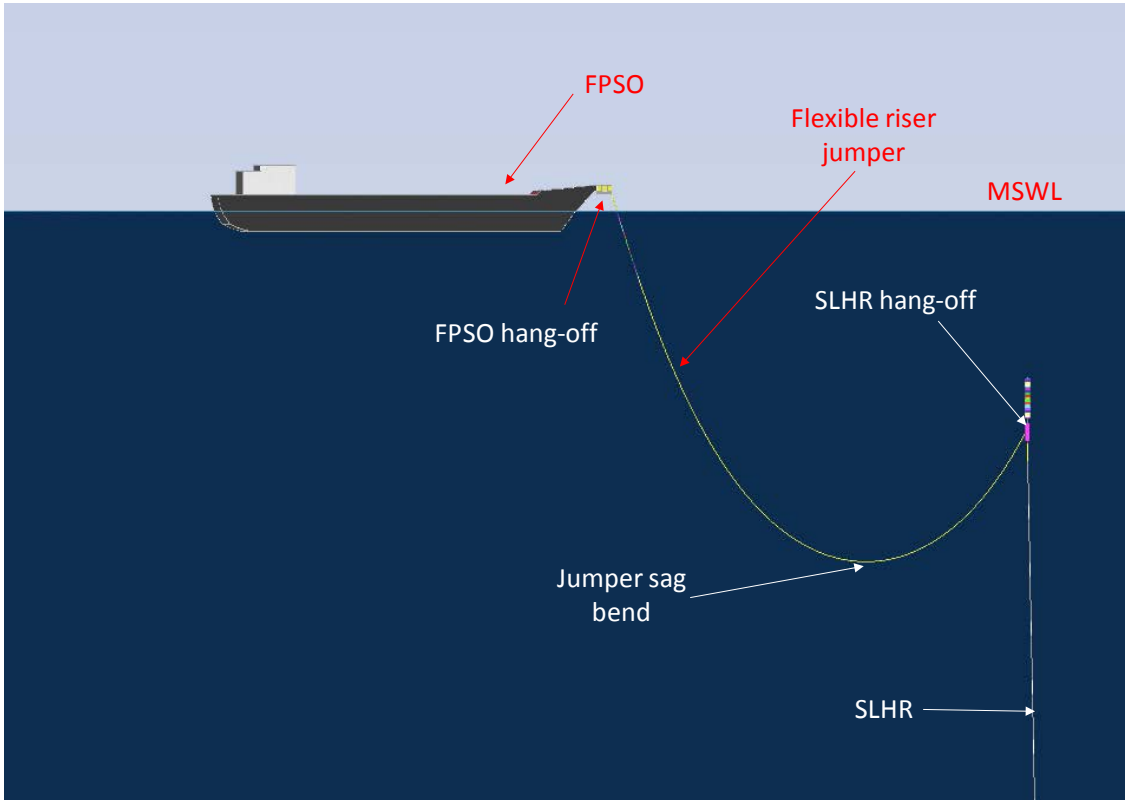

Figure 7.2. Schematic of SLHR and single riser jumper configuration.

The three flexible riser jumper geometries (11 inch, 9 inch and 6 inch) investigated here are listed in Table 7.1. The inner diameter is based on the required capacity and internal pressure of the riser. The external diameter (detailed in Table 7.1) is used for calculation of drag and buoyancy of the riser. The internal diameter and pipe mass are used to calculate the buoyancy contribution of the internal fluid; the pipe mass also influences the resultant axial force. The internal fluid properties (density and internal pressure) for each riser jumper are also provided in Table 7.1. Other geometric properties used for the global riser analysis are provided in Table 7.2. The external (hydrostatic) pressure, which is dependent on depth, and therefore, location along the riser, is zero at the FPSO hang-off; at the SLHR hang-off point, external pressure is 2 MPa.

The submerged sections of the risers experience hydrodynamic forces due to the environmental loading. Generally, drag forces are dominate for extreme waves and inertia forces are dominant for smaller waves. Drag and inertia coefficients are included in the global analysis, modelled as 1.2 and 1.8, respectively, for all riser geometries.

Table 7.1. Riser geometrical and internal fluid data.

Riser	Inner diameter (mm)	Outer diameter (mm)	Internal fluid density (kg/m^3)	Internal pressure (MPa)
11 inch	279.4	404.5	1100	27.3
9 inch	222.25	336.95	285	32.4
6 inch	152.4	362.8	267	27.5

Table 7.2. Riser geometrical data.

Riser	EI (Nm^2)	GJ (Nm^2)	EA (N)	Mass (kg/m)
11 inch	13.4×10^3	133.5×10^3	125×10^6	279
9 inch	37.1×10^3	371×10^3	95.2×10^6	208
6 inch	49.1×10^3	491×10^3	66.2×10^6	165

7.3.3. Vessel and environmental loading

The vessel motions due to the wave action are modelled using vessel response amplitude operations (RAOs). The motion of all points on the vessel are calculated using rigid body dynamics from a reference point (typically vessel center of gravity) and the associated RAOs. A vessel has six degrees of freedom, three translational and three rotational, as shown in Figure 7.3. The RAO data for all six degrees of freedom used for this study were obtained from a database of typical FPSO data for this type of riser configuration and sea conditions (courtesy of Wood Group Kenny).

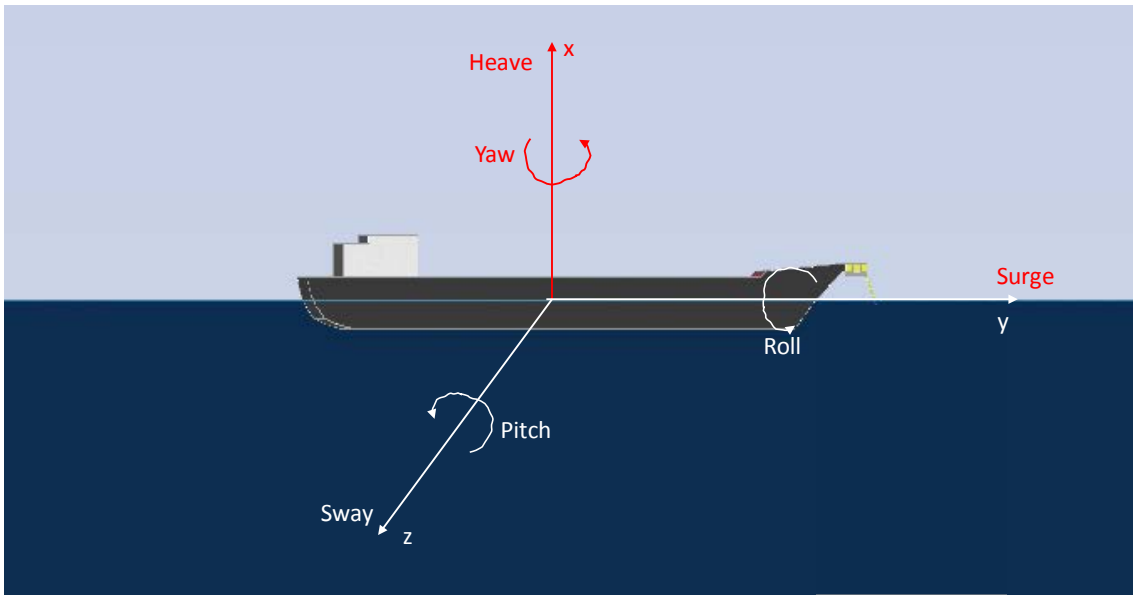

Figure 7.3. Definition of vessel degrees of freedom for RAOs.

A piecewise linear current profile is used to model the horizontal current velocity distribution that can vary in magnitude and direction with depth. The current velocity-depth profile is shown in Figure 7.4. For this study, the direction of the current is assumed to be constant, 0° from the *y*-axis (see Figure 7.3).

The riser system is subjected to six sea state (regular Airy wave) load cases defined by wave height and period (as shown in Table 7.3). These wave heights and periods are representative of extreme dynamic loading on the flexible riser jumper from swell and sea wave conditions (Wood Group Kenny metocean data). A riser can experience up to 10^6 cycles of each load-case in a year of operation.

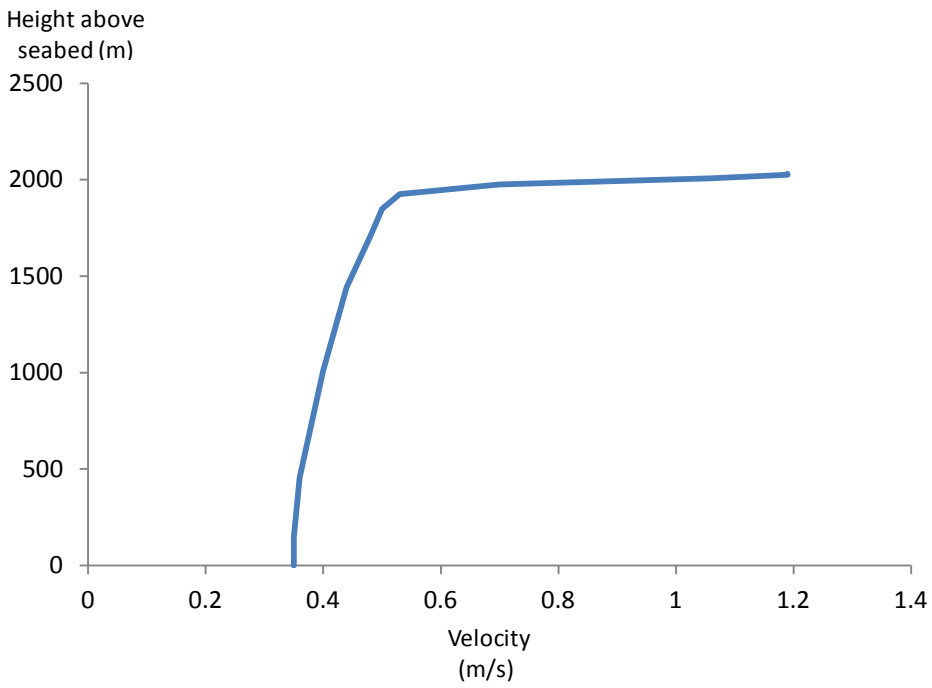

Figure 7.4. Assumed current velocity versus height above seabed.

7.4. Global-local loading conditions

7.4.1. General

This section describes analytical and geometrical models employed to establish global-local relationships, such as (i) global axial force to local nub-groove contact pressure and (ii) global riser curvature to local nub-groove slip, as shown in the flowchart of Figure 7.1.

Table 7.3. Definition of regular wave load-cases for design study.

Load case	Wave height (m)	Wave period (s)
1	2.78	11.5
2	2.36	10.54
3	2.78	11.65
4	1.74	6.94
5	0.93	6.94
6	1.74	14.81

To the author's knowledge, there are no existing methods to identify nub-groove fretting conditions, in particular, contact slip, based on global riser dynamic analysis results. The work of Burke and Witz (1995) identified fretting as a damage mechanism in the nub-groove contact region; however, the nub-groove contact loading conditions were not quantified. Perera et al. (2007) performed fretting wear tests on pressure armour wire to quantify the fretting behaviour; however, the loading conditions used were not based on global riser analysis. Féret and Bournazel (1987) presented a theoretical approach to calculate stresses, contact pressures and slip

between tensile armour layers of flexible pipes under axisymmetric loading. However, the pressure armour layer nub-groove articulations are driven by global riser curvatures rather than axisymmetric loading conditions; therefore, the theoretical approach used by Féret and Bournazel (1987) can not be used for pressure armour layer nub-groove contacts. The aim of this section is to quantify the global-local response and hence, provide data for the formulation of material response fretting maps (MRFM) and running conditions fretting maps (RCFM).

7.4.2. Global riser axial tension

A key design criterion for flexible risers is the avoidance of buckling which occurs under compressive loading. Hence, risers are designed, using software such as Flexcom, to prevent compressive axial forces. Flexible risers are designed so that each layer has a specific function. The function of the tensile armour (wire) layers is to support the axial tensile forces experienced by the riser. The lay angle of the tensile armour layer is typically ±30 to $\pm 40^0$ (to the longitudinal axis of the riser) helically around the riser; therefore, tensile forces on this layer cause the wires to straighten slightly. This straightening causes a pressure on layers under the tensile layer, such as the pressure armour layer. Therefore, global axial tensile force causes an additional external pressure on the pressure armour layer, p_a, expressed using an analytical solution (Lanteigne, 1985), as follows:

$$p_a = \frac{m\left(\frac{F_w \sin^2(\alpha)}{R_w \cos(\alpha)}\right)}{2\pi R_{pa}} \tag{7.1}$$

where m is the number of tensile armour wires in the tensile armour layer, F_w is the axial force in each tensile armour wire, R_w is the radius at which the tensile armour layer lies with a lay angle of α and $2\pi R_{pa}$ is the circumference of the pressure armour layer. This analytical solution has been validated against finite element models and used extensively, e.g. (Hoffman et al., 2001; McNamara, 1992) within the oil and gas industry.

7.4.3. Global riser curvature

In this section, a geometrical model is presented to relate global riser curvature-applied displacement for a local FE model of the riser nub-groove contact, as outlined in Figure 7.1, is described. In order to develop this model, some assumptions are made, as follows:

- Plane sections remain plane
- The outer pressure armour layer slides relative to the inner layer under bending
- No ovalisation of the riser occurs under bending
- The angle of rotation, θ, remains small ($R\theta \approx l$, see Figure 7.5)
- The length of riser modelled, l, is small with respect to the bend radius, R
- Pure bending occurs about the centre line of the riser
- Only elastic behaviour occurs (i.e. plasticity is neglected)
- No additional nub-groove contact pressure occurs due to riser bending

The length of the riser section modelled, l, in the simplified axisymmetric model is 15 mm, as shown in Figure 7.7, and the minimum bend radius of a riser is typically 1.5 to 3 m (this is the storage radius of the pipe - the bend radius during operation is much larger). Therefore, the angle of rotation, θ, remains small (maximum 0.3^0 to 0.6^0), and the section of the riser modelled is small compared to the bend radius (~ 1 %). A schematic of the geometrical model used to develop the riser curvature-applied displacement, κ-Δ_{app}, relationship is shown in Figure 7.5, where curvature κ, is given by the inverse of bend radius, R.

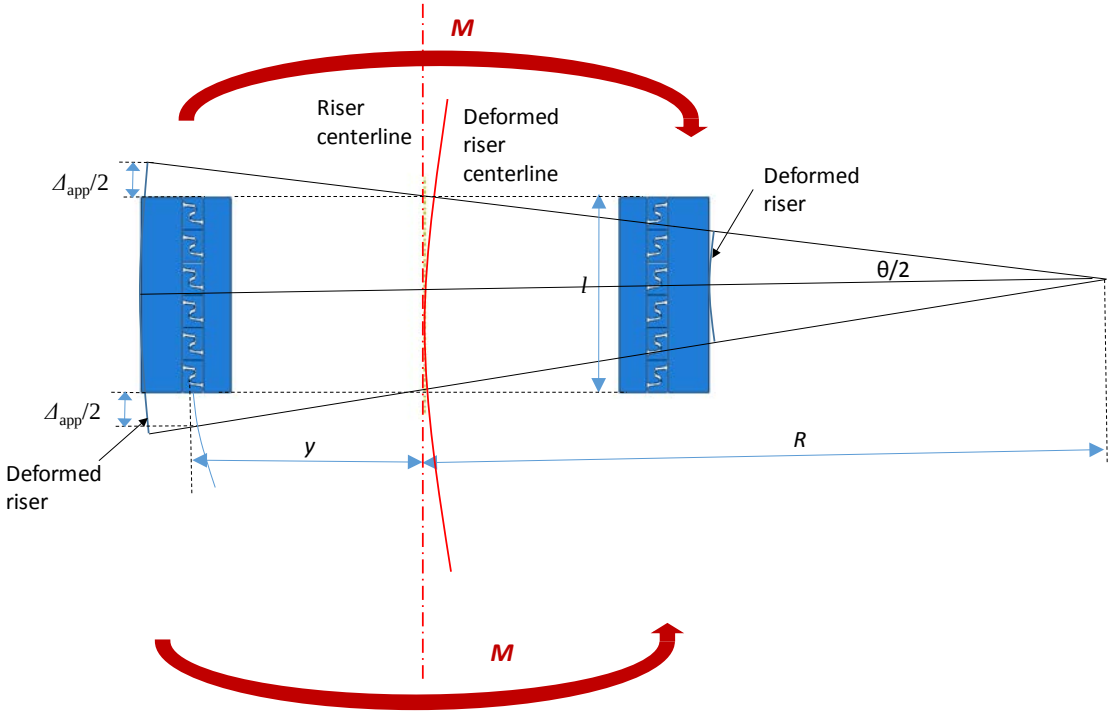

Figure 7.5. Schematic of effect of bending on riser section and the geometrical model used to relate riser curvature to local applied displacement.

From the geometrical construction (model) of Figure 7.5, the angle of rotation, θ, can be expressed in terms of riser bend radius, R, and length of riser section modelled, l, as follows:

$$\theta \approx 2\sin^{-1}\left(\frac{l/2}{R}\right) \tag{7.2}$$

where l and R are as shown in Figure 7.5. Assuming that the outer pressure armour layer slides as a rigid body relative to the inner layer, the relative applied displacement, Δ_{app}, can be approximated as follows, for small θ:

$$\Delta_{app} \approx (R \pm y)\theta - R\theta \tag{7.3}$$

where y is the distance from the central riser axis to the nub-groove interface, as shown in Figure 7.5. In riser design, the riser curvature, κ, is typically used; therefore, Equations (7.2) and (7.3) can be rewritten as:

$$\theta \approx 2\sin^{-1}\left(\kappa\frac{l}{2}\right) \tag{7.4}$$

$$\Delta_{app} \approx \left(\frac{1}{\kappa} \pm y\right)\theta - \frac{1}{\kappa}\theta \tag{7.5}$$

Figure 7.6 presents the linear relationship between riser curvature, κ, and applied displacement, Δ_{app}, described by Equations (7.4) and (7.5) (for the 6 inch riser).

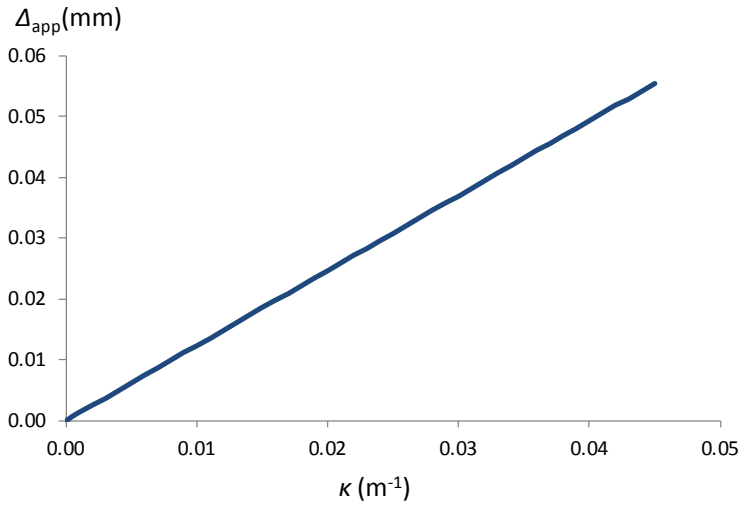

Figure 7.6. Linear relationship between riser curvature and applied displacement for the 6 inch riser.

7.5. Local nub-groove analysis

7.5.1. Finite element analysis

Following the work of Section 7.4.3, the local nub-groove slip, δ, can then be identified as a function of applied riser displacement, Δ_{app}, from the axisymmetric riser model of Figure 7.7. The FE model details are outlined in detail in Section 5.3.1.

In this study the internal and external pressure for the riser are outlined in Table 7.1, the additional pressure due to the straightening of the tensile armour wires, p_a, given by Equation (7.1), is also modelled. The cyclic applied displacement, $\pm\Delta_{app}$, is identified by substituting $\Delta\kappa$ for κ in Equations (7.4) and (7.5), where the global curvature range, $\Delta\kappa$, is given by:

$$\Delta\kappa = \kappa_{max} - \kappa_{min} \tag{7.6}$$

where κ_{max} and κ_{min} are the maximum and minimum curvatures that occur at a specific point on the riser throughout the dynamic simulation, as described in Section 7.3, respectively. The riser curvature histories in this study are typically symmetrical about the neutral axis of the riser (shown in results section, Figure 7.9).

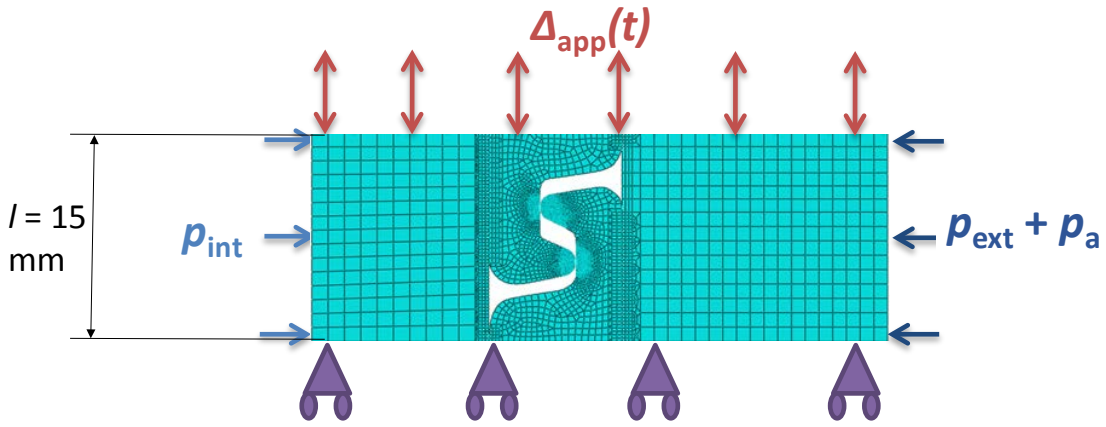

Figure 7.7. Axisymmetric riser model.

7.5.2. Crack initiation

The numbers of cycles to crack initiation (10 μm crack) have been calculated using the methodology outlined in Section 6.5. This implements the fretting damage parameter proposed by Ding et al. (2011), D_{fret}, along with critical-plane SWT for the nub-groove fretting contact in flexible marine risers as outlined in Figure 7.1. Therefore, wear is not explicitly modelled here.

7.5.3. Crack propagation

This section describes the estimation of crack propagation using a weight function approach, as outlined in Figure 7.1. The total fretting fatigue life can then be calculated by the sum of crack initiation and propagation lives. The weight function approach was used for PS regime, where it is assumed that wear rate is low and therefore, wear has little to no effect on substrate stresses. Since wear is not explicitly modelled, the contact stress gradient in the nub-groove contact region is expected to reduce up to a depth where constant stress is observed (far from the nub-groove contact surface). In an attempt to capture the effect of fretting stress relaxation occurs due to wear, stress reduction factors have been estimated based observations from the explicit wear modelling of Chapter 6, this is described in Appendix E. These estimated stress gradients have been used here to estimate crack propagation in the gross-slip regime.

The weight function method used for PS is described below. In fretting experiments, cracks have been observed to grow at a shallow angle initially, typically between 5^0 and 20^0, (Dubourg and Lamacq, 2000), being influenced by the contact load. The crack will grow in this manner for up to 3-grain sizes (Khotsyanovskii,

2010). Next the direction of the crack propagation changes to approximately perpendicular to the contact surface; here the propagation direction is influenced by the bulk stress in the pressure armour wire. This crack growth behaviour is depicted in Figure 7.8.

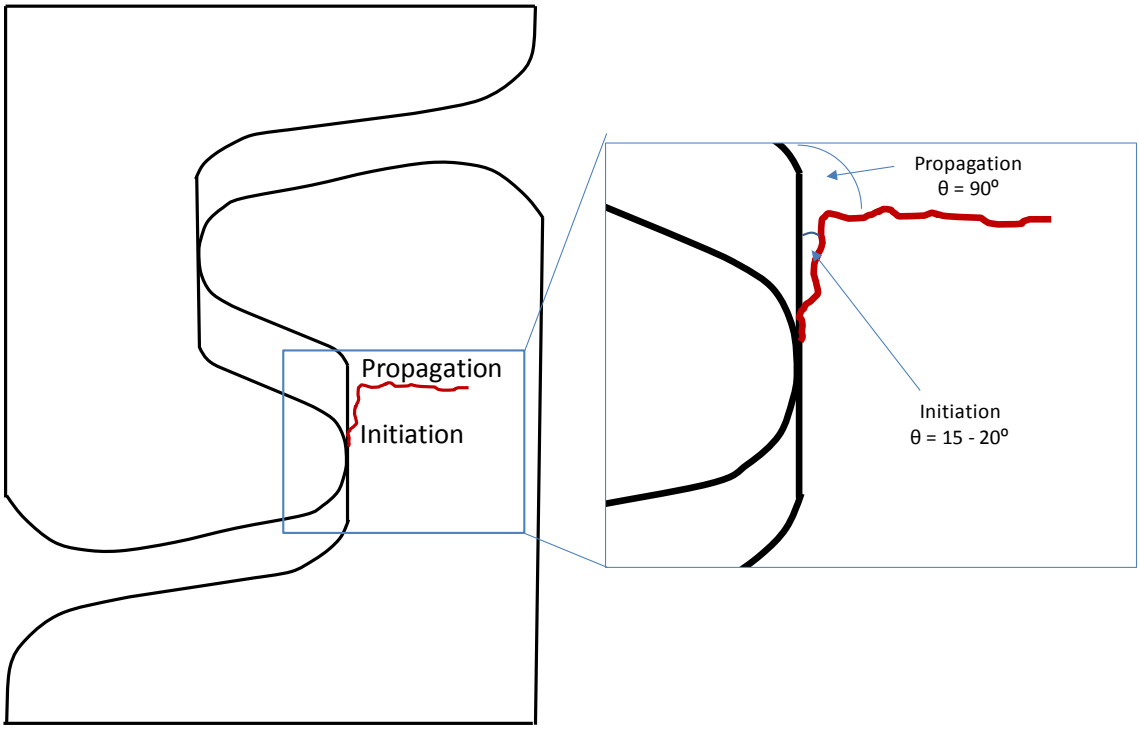

Figure 7.8. Direction of crack initiation and propagation.

Due to stress gradients close to the contact surface in fretting, crack propagate is a complex issue (McCarthy et al., 2013). Houghton et al. (2009) used weight functions based on the work of Nicholas et al. (2003) to analyse the mixed mode cracking of Ti-6Al-4V to predict multiaxial fretting fatigue. Crack location was found from SWT critical plane calculations, then local stress ranges were identified for Mode I and Mode II crack propagation. The weight functions, h_I and h_{II}, for Mode I and Mode II crack growth, respectively, are defined as (Fett and Munz, 1997):

$$h_I = \sqrt{\frac{2}{\pi a}} \frac{1}{\sqrt{1-\rho}} \left[1 + \sum_{\upsilon,\mu} \frac{A_{\upsilon,\mu} \alpha^{\mu}}{(1-\alpha)^{\frac{3}{2}}} (1-\rho)^{\upsilon+1} \right] \tag{7.7}$$

$$h_{II} = \sqrt{\frac{2}{\pi a}} \frac{1}{\sqrt{1-\rho}(1-\alpha)^{\frac{1}{2}}} \left[(1-\alpha)^{\frac{1}{2}} + \sum_{\upsilon,\mu} A_{\upsilon,\mu} (1-\rho)^{\upsilon+1} \alpha^{\mu} \right] \tag{7.8}$$

where $\rho = x/a$ and $\alpha = a/W$, a is the crack length, x is the distance along the crack, W is the specimen width and $A_{\upsilon\mu}$ is the influence coefficient for each weight coefficient (Fett and Munz, 1997). Mode I and Mode II stress intensity factors are defined as:

$$\Delta K_I = \int_0^a \Delta\sigma_{xx}(x) h_I(x,a) dx \tag{7.9}$$

$$\Delta K_{II} = \int_0^a \Delta\sigma_{xy}(x) h_{II}(x,a) dx \tag{7.10}$$

where $\Delta\sigma_{xx}$ and $\Delta\sigma_{xy}$ are the local FE-predicted normal and shear stresses during crack growth in Mode I and Mode II, respectively. The effective stress intensity factor is:

$$\Delta K_{eff} = \sqrt{\Delta K_{I,eff}{}^2 + \Delta K_{II,eff}{}^2} \tag{7.11}$$

where:

$$\Delta K_{I,eff} = \Delta K_I (1-R)^{(1-n)} \tag{7.12}$$

where R is the stress ratio > 0 and n is a material constant, where $0 < n > 1$. In this work, n was chosen to be 0.5. The incremental crack growth, Δa, is defined by:

$$\Delta a = C(\Delta K_{eff} - \Delta K_{th})^m \Delta N \tag{7.13}$$

where ΔN is a cycle jumping factor. The process crack growth calculation is incrementally repeated until the crack length, a, propagates to a length of 2 mm. Previously published Paris coefficients for a dual phase pearlite-ferrite cold-formed steel were used here (Li et al., 2014). This methodology has been validated against

results obtained from the Paris equation (see Section 2.5.4) for a plan fatigue case. This method includes the El-Haddad correction for short crack growth (El Haddad et al., 1979).

7.6. Results

7.6.1. Global analysis

Key output variables from the global analysis are (i) time histories of riser curvature and axial tension and (ii) envelopes of the minimum and maximum riser curvatures and axial tensions along the length of the riser. This data allows for detailed design of flexible risers based on dynamic responses to various sea state loadings. Examples of these results are presented here for the 6 inch riser under load case 1.

Normalised time histories of resultant rise curvature (κ/κ_{max}), axial tension (F/F_{max}) and internal and external pressures (p/p_{max}) results from dynamic riser analysis are shown in Figure 7.9; these results are from the SLHR hang-off point. The internal and external pressure remain constant with respect to time. In all load-cases, riser curvature is seen to be 180^0 out of phase with axial tension. The riser curvature is symettric about the neutral axis of the riser, and the axial force is in tension at all times.

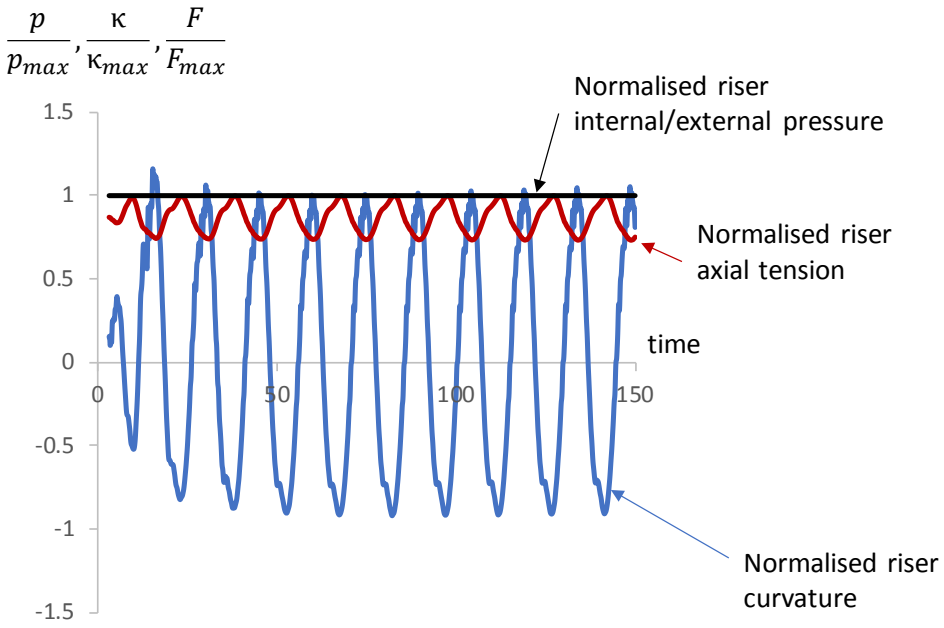

Figure 7.9. Time histories of normalised results from dynamic riser analysis.

The minimum and maximum axial force and riser curvature along the length of the 6 inch riser under load case 1 are presented in Figure 7.10 and 7.11. Note that *l* in these plots is the length of the riser, measured as curvilinear distance along the riser from the FPSO hang-off point (see Figure 7.2). The end-point (*l* = 550 m) corresponds to the SLHR hang-off point. Clearly, the predicted location of maximum axial tension and riser curvature values are at the SLHR hang-off point. The SLHR has a more dynamic response to the sea-state loading than the FPSO, therefore, the SLHR hang-off point is the most dynamically loaded point on the flexible riser. The results from all other load-cases analysed for the three risers are consistent with these also. The complete set of axial tension and curvature envelopes for all risers and load cases are given in Appendix C.

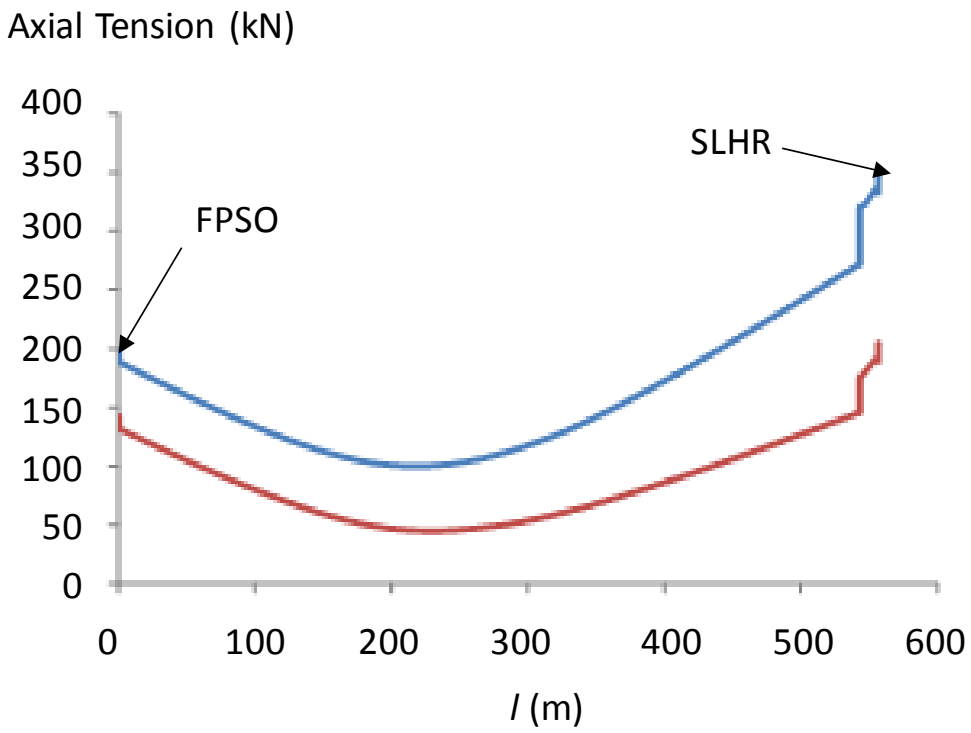

Figure 7.10. Envelope of minimum and maximum axial tensile force along the length of the 6 inch riser jumper.

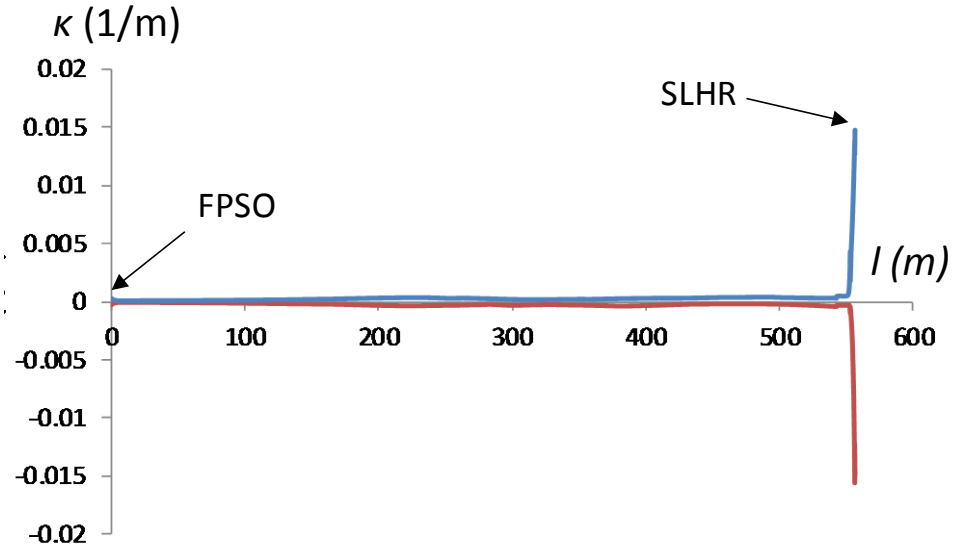

Figure 7.11. Envelope of minimum and maximum riser curvature along the length of the 6 inch riser jumper.

7.6.2. Global-local loading conditions

A typical FE predicted relationship between nub-groove contact displacement (δ) and riser curvature range ($\Delta\kappa$) is shown Figure 7.12. These responses are obtained by calculating an applied load, Δ_{app}, from global riser curvature results and Equations (7.4) and (7.5). This value of Δ_{app} is then applied to the local FE riser model (see Figure 7.7), from which nub-groove contact slip, δ, is predicted. The curvature-slip response shows two types of trends depending on slip regime for finite sliding friction; a quadratic trend is observed for PS and a linear trend is observed for GS. To achieve slip i.e. overcome friction, a certain threshold curvature range, $\Delta\kappa_{th}$, is required; above these threshold values, curvature-slip response is much "softer", i.e. a smaller change in curvature results in a larger change in slip. The value of $\Delta\kappa_{th}$ depends on riser geometry and loading conditions.

This combined geometrical-FE method, as described in Figure 7.1, has been compared to the 3D riser model of Chapter 5. There are differences between the two method, as shown in Figure 7.12 This is due to assumptions associated with both techniques. However, it is important to note that both methods gave results similar curvature-slip responses. For this study, the geometrical-FE method has been used. The analysis of curvature-slip relationship is one that requires further computational investigation and full-scale validation, if possible. Figure 7.13 shows the combined geometrical-FE predicted effect of internal pressure on the curvature-slip relationship (6 inch riser under 4 MPa external pressure, a nub-groove CoF of 0.7). As internal pressure increases, the curvature required to cause a specific slip increases.

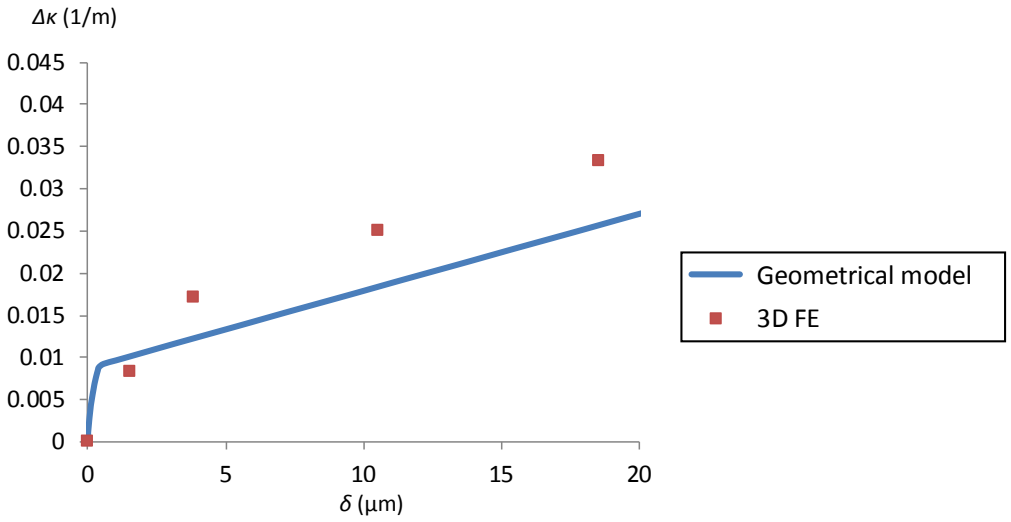

Figure 7.12. Comparison of geometrical and 3D FE models to obtain curvature-slip relationship for the 6 inch riser with nub-groove CoF of 0.7.

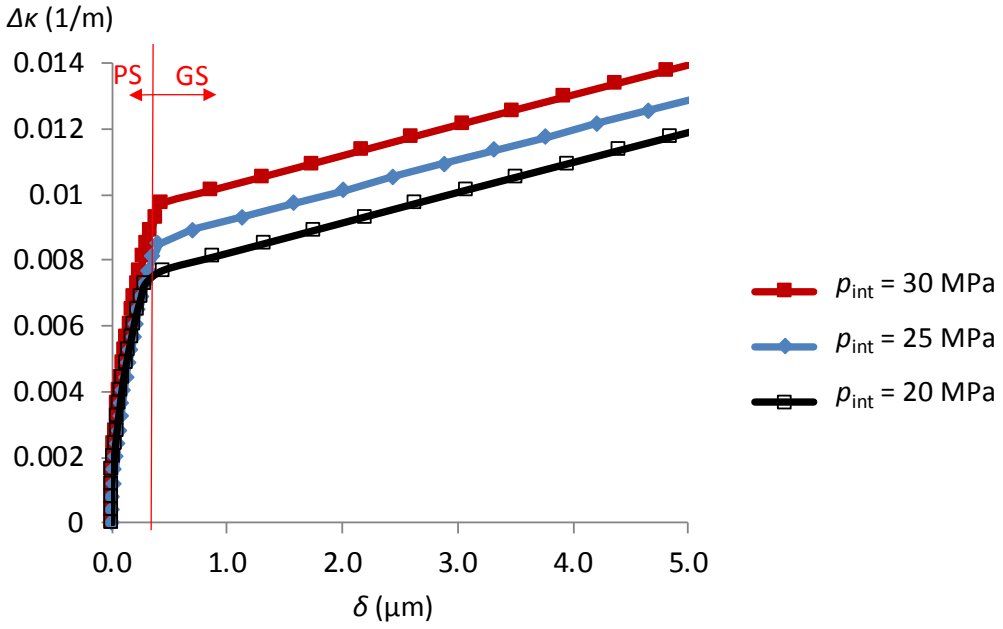

Figure 7.13. Effect of internal pressure on the curvature-slip relationship (6 inch riser under 4 MPa external pressure, a nub-groove CoF of 0.7).

Similarly, Figure 7.14 presents the effect of CoF on the curvature-slip relationship (6 inch riser under 25 MPa internal pressure, 4 MPa external pressure). This shows a linear relationship for the frictionless case and a combined quadratic-linear relationship for non-zero CoF. As CoF increases, the curvature range required to cause gross-slip ($\Delta\kappa_{th}$) increases. The PS-GS transition occurs at larger contact slips as CoF increases. Figure 7.15 shows the curvature-slip relationship for the different size risers. Again, the effect of decreasing riser diameter is the same as that of increasing internal pressure and increasing CoF.

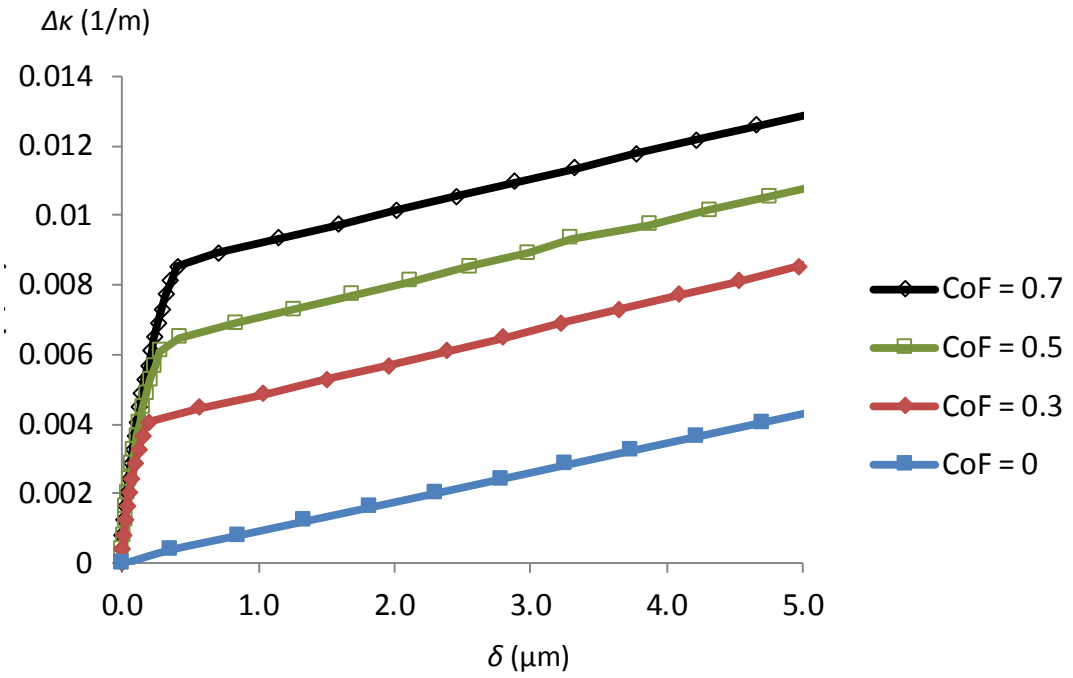

Figure 7.14. Effect of CoF on the curvature-slip relationship (6 inch riser under 4 MPa external pressure and with nub-groove CoF of 0.7).

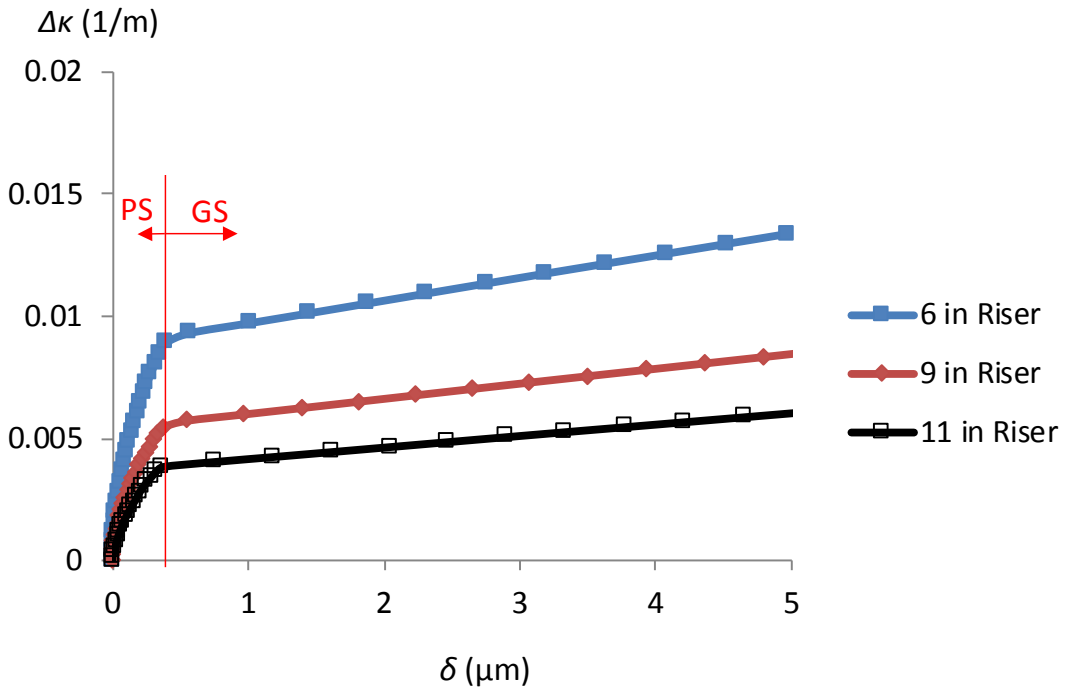

Figure 7.15. Curvature-slip relationship for the different risers used in this study.

Threshold values of curvature range, $\Delta\kappa_{th}$, have been identified as the curvature range at which nub-groove contact transitions from PS to GS regimes, as shown in Figures 7.12 and 7.14; the values of $\Delta\kappa_{th}$ are provided in Table 7.4.

The $\Delta\kappa$-δ relationships shown above can be described by the following equations, for PS and GS:

$$\delta = A(\Delta\kappa)^2 + B(\Delta\kappa) + C \quad \text{(PS)} \tag{7.14}$$

$$\delta = B(\Delta\kappa) + C \quad \text{(GS)} \tag{7.15}$$

where A, B, and C for each riser geometry and nub groove sliding regime are given in Table 7.4. Partial slip occurs at $\Delta\kappa$ values less than $\Delta\kappa_{th}$.

Table 7.4. *A*, *B*, and *C* for each riser geometry and nub-groove sliding conditions

Riser	A	B (PS)	C	B (GS)	C	$\Delta\kappa_{th}$
6 inch	3933.6	7.160	-0.0043	1097.7	-9.7293	8.92×10^{-3}
9 inch	1024.4	11.418	-0.0022	1655.1	-8.9727	5.46×10^{-3}
11 inch	17902.8	18.65	-0.0006	18.65	-0.0006	3.65×10^{-3}

Figure 7.16 shows an example of the accuracy of the Δκ-δ fit using Equations (7.14) and (7.15) to data for 6 inch riser. This plot shows very good agreement between the combined geometrical-FE predicted curvature-slip relationship and the fit using the polynomial equations.

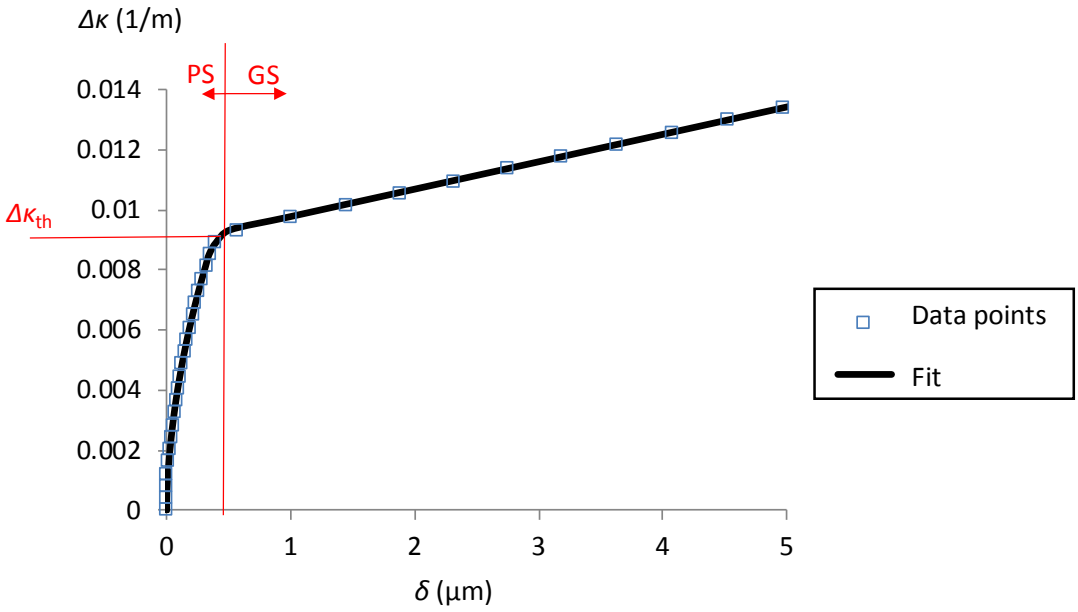

Figure 7.16. Curvature-slip relationship fit to data using Equations (7.14) and (7.15) for 6 inch riser.

The predictive methodology has been applied to the various dynamic load cases for each riser diameter. The results for maximum predicted slip for each riser are shown in Table 7.5 For the minimum loading conditions along the riser lengths, stick is predicted, whereas for the maximum conditions along the riser lengths, gross slip is typically predicted. Therefore, along the riser length, stick, partial slip and gross slip conditions are experienced for most load cases. Load case 5 results in maximum nub-groove contact displacements closest to PS-GS transition. Typically, the larger wave heights (see Table 7.3) result in larger nub-groove slips, i.e. load cases 1 to 3; this is due to larger vessel and SLHR motions associated with wave loading, and hence, larger global riser dynamic motions occur compared to load cases with lower wave heights, i.e. load cases 4 to 6.

Table 7.5. Minimum and maximum nub-groove contact displacements for each riser and load case.

Load case	**6 inch riser δ_{max} (μm)**	**9 inch riser δ_{max} (μm)**	**11 inch riser δ_{max} (μm)**
1	22.8	83	192.1
2	45.4	65.1	192.1
3	78.1	81.9	188.7
4	40.5	44.6	101.8
5	2.1	3.3	4.4
6	29.2	27.2	87.8

7.6.3. Predicted life to crack initiation

Figure 7.17 presents the predicted number of cycles to crack initiation against nub-groove displacement for all three risers. At lower contact slips (< 2 μm) the 11 inch riser is most critical (lower predicted life); however, as contact slip increases (> 4 μm), the 6 inch riser is more critical in terms of predicted number of cycles to crack initiation.

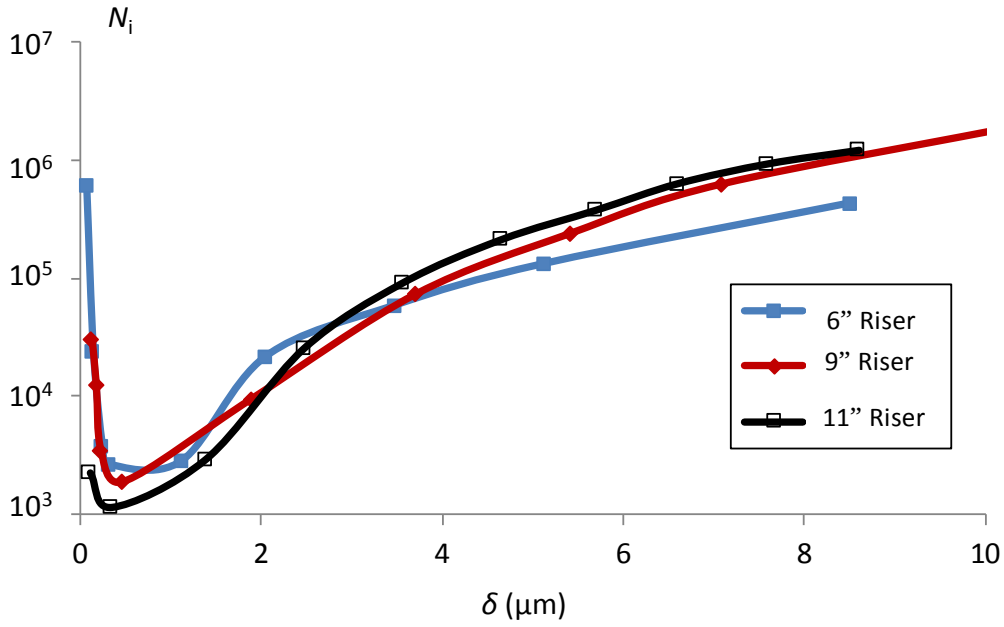

Figure 7.17. Number of cycles to crack initiation against nub-groove displacement for all three risers.

Figure 7.18 presents the effect of riser curvature range, $\Delta\kappa$, on predicted number of cycles to crack initiation for all three risers. The difference between the riser configurations can be clearly seen. The PS regime occurs at much lower curvatures for the larger diameter risers (11 inch and 9 inch) than for the smaller diameter riser (6 inch). This is due to the different curvature-slip relationships for each riser, as shown in

Figure 7.15. Figure 7.18 is an example of a RCFM; this can be used to identify the number of cycles to crack initiation from global riser curvature response.

Figure 7.18 also shows critical curvature range ($\Delta\kappa_{crit}$) that relate to lower predicted lives ($N_i < 5 \times 10^4$) for each riser. The smaller diameter (6 inch) riser has a large range of $\Delta\kappa_{crit}$ than the larger diameter risers (9 inch and 11 inch). These $\Delta\kappa_{crit}$ values can be used in conjunction with global riser analysis results (from Flexcom) to identify locations of the riser where fretting fatigue cracking are likely to occur. For all load cases, $\Delta\kappa_{crit}$ occurs closest to the SLHR hang-off point (between 0.1 m and 5 m from hang-off point) for each of the risers. It must be noted that these values for $\Delta\kappa_{crit}$ are specific to each of these risers under the loading conditions outlined above and with a nub-groove CoF of 0.7.

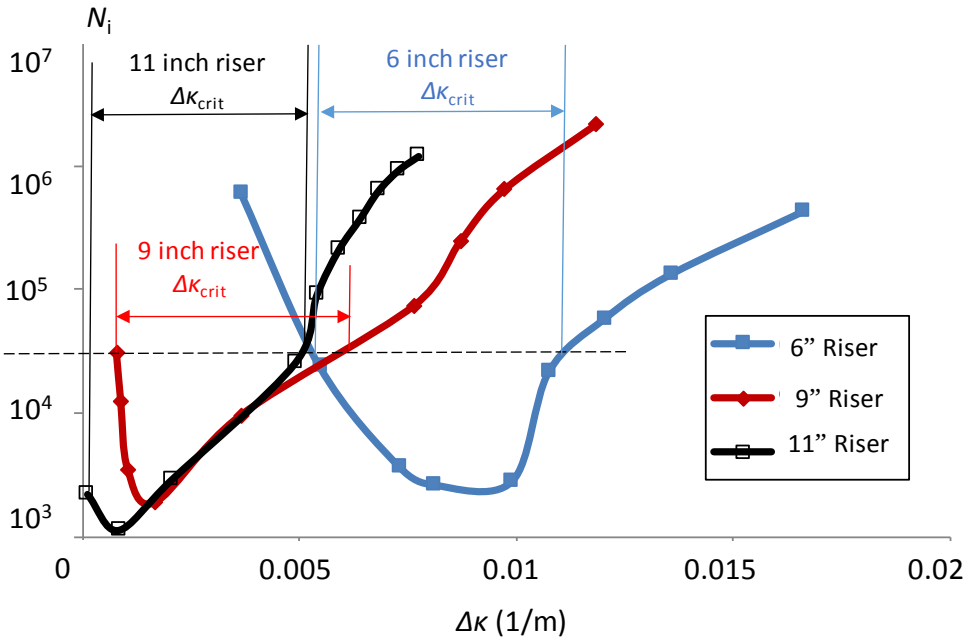

Figure 7.18. Number of cycles to crack initiation against dynamic riser curvature for all three risers and definition of $\Delta\kappa_{crit}$ for each riser case.

The predicted number of cycles to crack initiation for each load case and riser is presented in Figure 7.19. The 11 inch riser is typically most critical riser, in terms of predicted number of cycles to crack initiation, compared to the smaller diameter risers (9 inch and 6 inch). The load case with the most difference between predicted riser lives is load case 5, this corresponds to the load case with the lowest wave height and period. The predicted number of cycles to crack initiation is considerably low. However, the location where $\Delta\kappa_{crit}$ occurs along the riser length is short relative to the length of the riser, typically ≤ 2 m compared to overall riser length of 550 m. This is approximately 0.4 % of the riser length that is critical for fretting design.

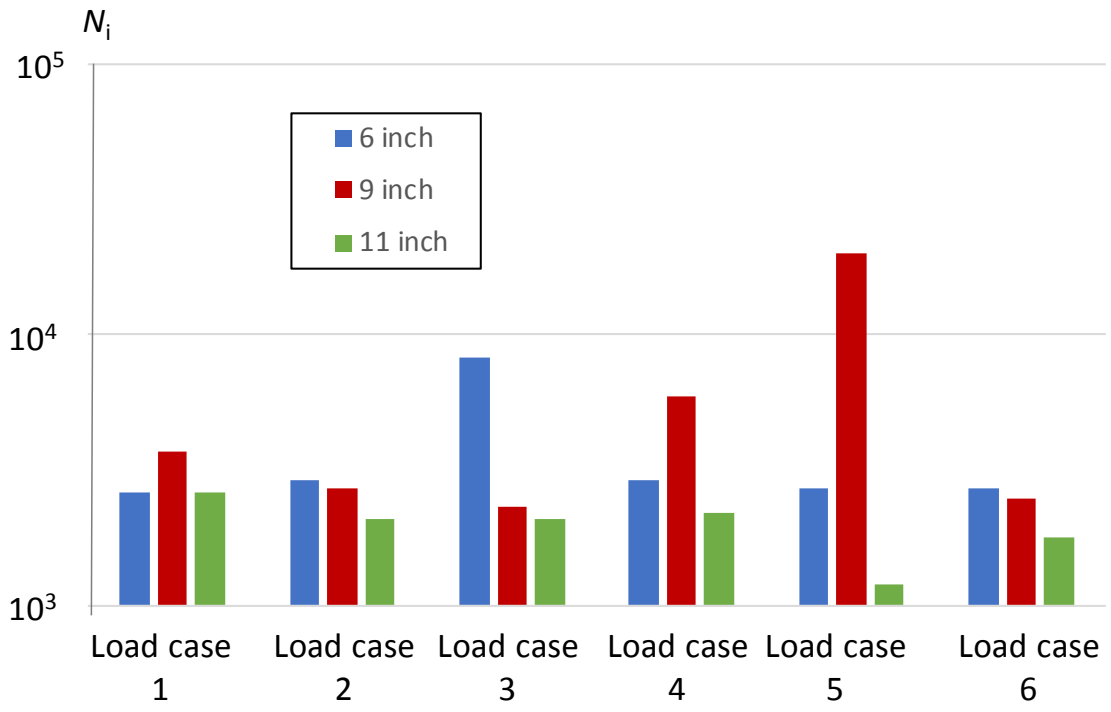

Figure 7.19. Predicted numbers of cycles to crack initiation for all load cases and all three risers.

7.6.4. Crack propagation

Figure 7.20 presents the predicted number of cycles to crack initiation and propagation against nub-groove displacement for the 6 inch riser. Estimated propagation life is much longer than predicted initiation life (typically by two orders of magnitude). This is due to the fact that the high fretting stresses are highly localised close to the nub-groove contact surface (shown in Figure 5.7), and therefore, have little influence as the crack propagates. Figure 7.21 presents the effect of riser curvature range, $\Delta\kappa$, on predicted number of cycles to crack initiation and propagation for the 6 inch riser. Figure 7.22 presents the effect of riser curvature range, $\Delta\kappa$, on predicted number of cycles to crack initiation and propagation for all risers. This is an example of a RCFM and can be used to identify the number of cycles to failure from global riser dynamic response.

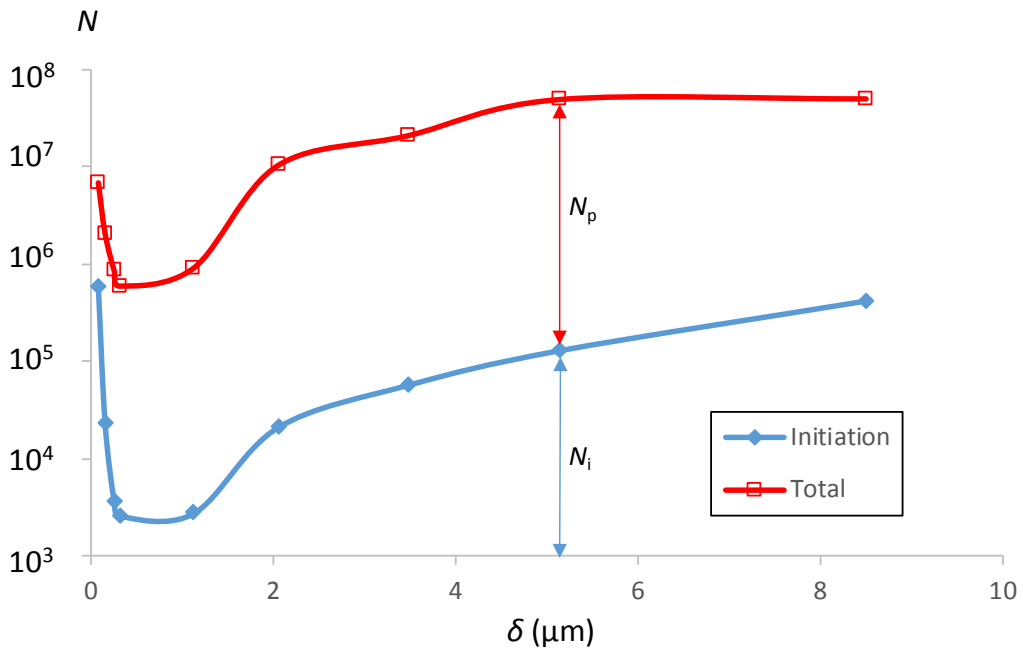

Figure 7.20. Effect of nub-groove contact slip on number of cycles to crack initiation and propagation for the 6” riser.

Figure 7.23 presents the predicted number of cycles to failure for all three risers and all load cases. There is a significant increase in life for all risers and load cases compared to predicted initiation life (shown in Figure 7.19). There is less scatter between the results for failure than for initiation, this because crack propagation is dominant over crack initiation since stresses perpendicular to the surface decrease rapidly, resulting in similar predicted propagation lives for all risers and load cases.

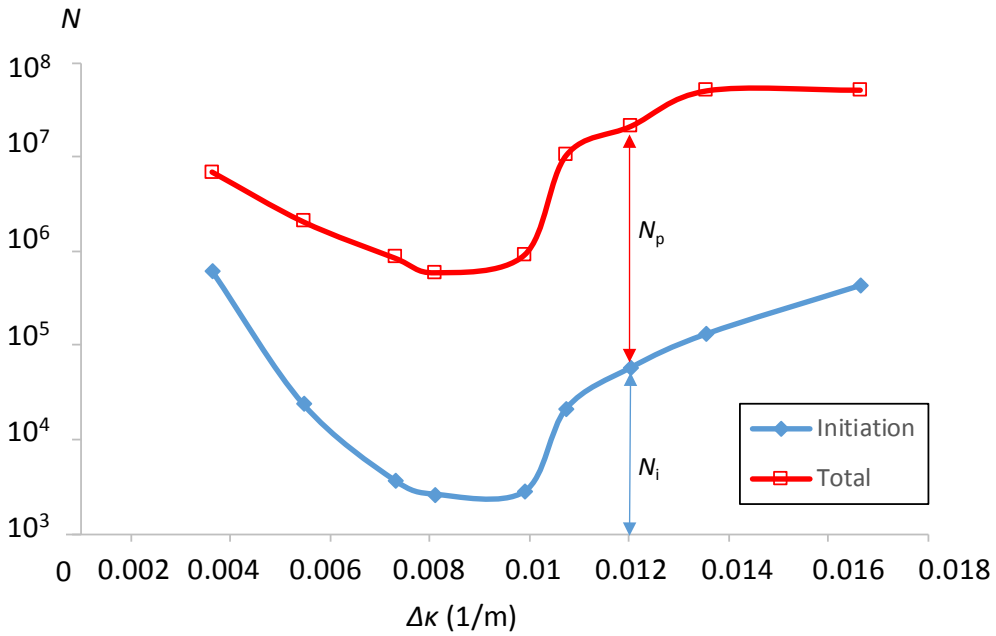

Figure 7.21. Effect of global riser curvature on number of cycles to crack initiation and propagation for the 6 inch riser.

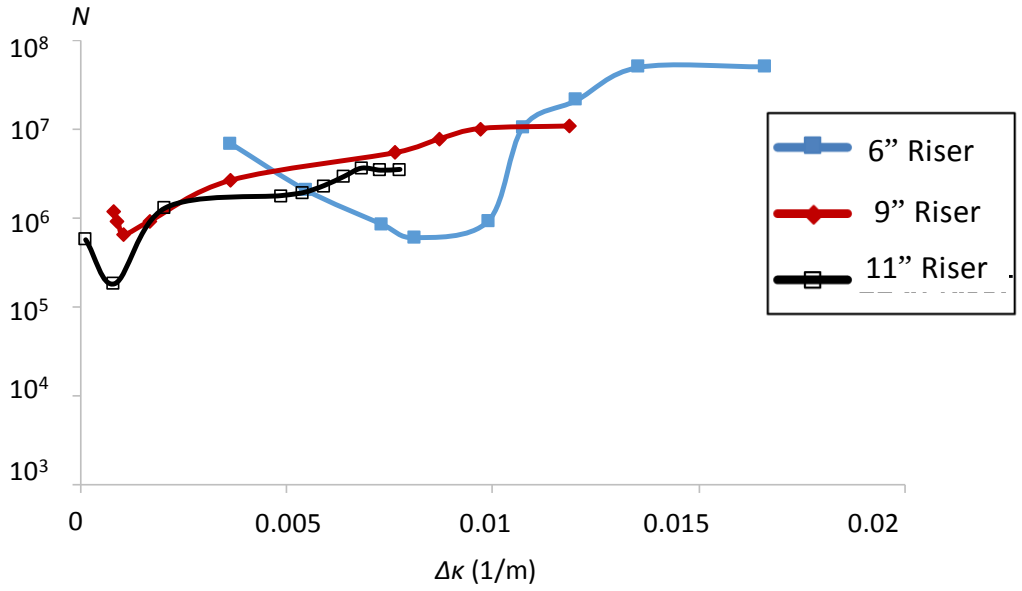

Figure 7.22. RCFM for predicted number of cycles to failure for dynamic curvature range for all three risers.

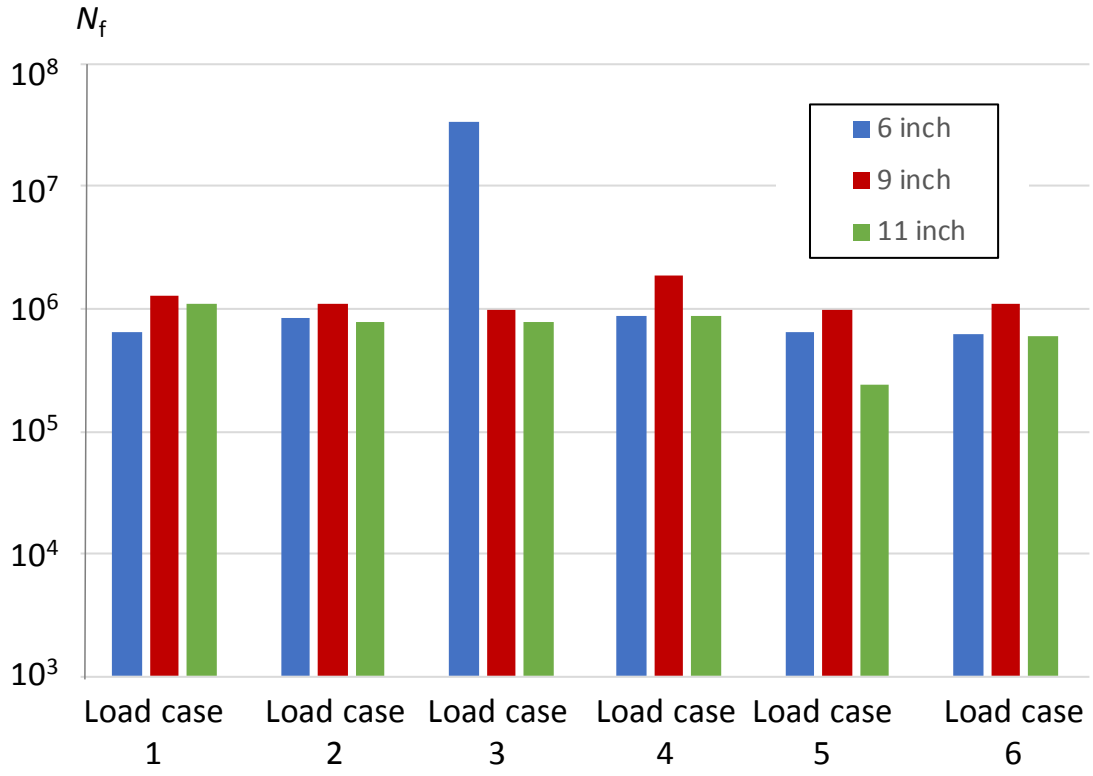

Figure 7.23. Predicted numbers of cycles to failure for all load cases and all three risers.

Currently, there is no standard procedure for the analysis of fretting in the pressure armour layer. Typically, risers are analysed for fatigue behaviour of the tensile armour layer. For this study, the fatigue life of tensile armour layer has also been predicted using Layercom, a tensile armour layer fatigue predictive tool developed by MCS International (now Wood Group). The lives predicted for the tensile armour layer ranged from 5.9×10^5 to 1.3×10^7. This is a similar range to the total fretting fatigue life predicted for the pressure armour layer in this study (see Figure 7.23). The load cases investigated here are extreme loading scenarios; by modelling stochastic sea states, less conservative and more realistic life predictions can be calculated using the same predictive methodologies for both fatigue of the tensile armour layer and fretting fatigue of the pressure armour layer.

7.7. Summary and conclusions

The fretting analysis methodology of this thesis has been implemented in a realistic riser jumper case study. Global riser analysis has been conducted on three riser geometries and six load cases have been investigated for each riser. Global riser dynamic curvature and axial tension histories have been related to local nub-groove loading conditions. Critical dynamic riser curvatures, that result in low predicted lives, have been identified for the various riser geometries. The number of cycles to crack initiation have been predicted for the six load cases for each riser. Predictions of the total number of cycles for failure of the pressure armour wire have been calculated using weight functions. The use of the D_{fret}-SWT method allows for fretting fatigue life predictions to be made in PS and GS; however, computationally efficient, incremental

modelling of wear is required to accurately predict substrate stresses for the predictions of crack propagation using the weight function method employed here for GS. The total lives predicted for fretting fatigue in the pressure armour layer have been compared to fatigue lives of the tensile armour layer. Predicted pressure armour layer fretting fatigue lives are in the same range as the fatigue lives of the tensile armour layer.

Chapter 8: EASY-FRET: An analytical fretting wear-fatigue design tool

8.1. Introduction

EASY-FRET stands for Engineering Analysis SYstem for FRETting; it uses an analytical elasticity theory methodology implemented within a quadratic programming method following the work of Nowell (2010) in MatLab™ to simulate wear and frictional fretting contact for two-dimensional contact geometries and loading conditions, including partial and gross slip regimes, for example. Fretting fatigue life is calculated using the critical-plane multi-axial SWT fatigue parameter, described in previous chapters. EASY-FRET is a computationally efficient method for modelling fretting wear and fatigue and for geometry optimisation against fretting damage. The benefit of this design tool, for industry application, in particular, is that it does not require finite element software or expertise and requires minimal inputs from the designer.

Nowell (2010) presented an efficient numerical method based on quadratic programming to analyse transient wear problems. In this chapter, this analytical solution to calculate contact pressure from initial geometry and loading conditions is expanded to include the calculation of substrate stresses and fretting fatigue life. The analytical design tool is validated against finite element results presented previously in this thesis. EASY-FRET will allow for the accurate and computationally efficient

modelling of fretting in the nub-groove contact in flexible marine risers, as depicted in Figure 1.4. EASY-FRET is readily adaptable for different fretting geometries and loading scenarios.

8.2. Analytic model

For a 2D contact between bodies, quadratic programming (Nowell, 2010) can be used to predict the contact pressure for a given contact geometry with an initial gap function, h_o, as shown in Figure 8.1. Under a normal load, P, the two bodies undergo vertical displacements, $v_1(x)$ and $v_2(x)$ for bodies 1 and 2, respectively. Therefore, the gap function in the loaded state, $h(x)$, is:

$$h(x) = h_o(x) - (v_2(x) - v_1(x)) = h_o(x) - v(x) \tag{8.1}$$

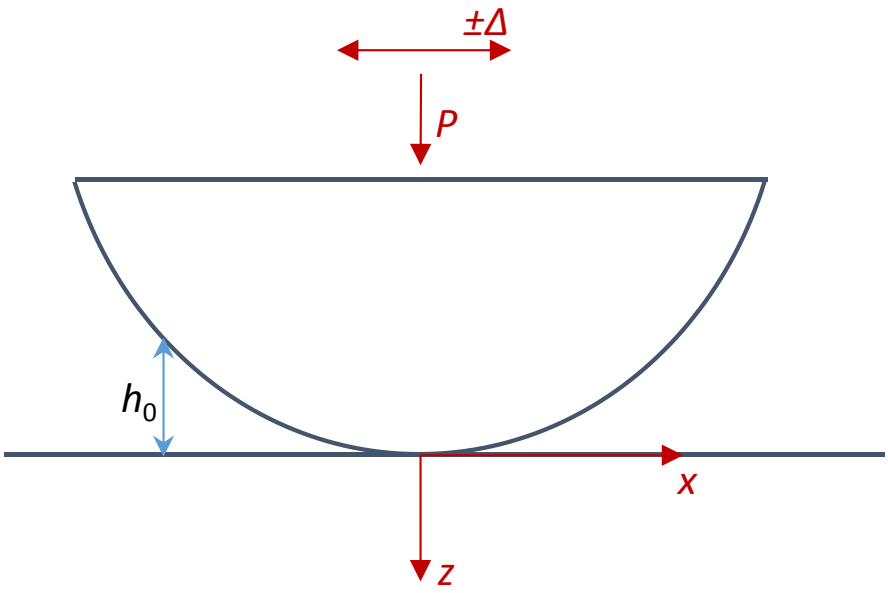

Figure 8.1. Round and flat bodies in contact with initial gap function h_o.

For contact conditions, pressure is positive and the gap function is zero, as follows:

$$p(x) \geq 0 \qquad h(x) = 0 \tag{8.2}$$

For non-contact conditions, pressure is zero and the gap function is positive, as follows:

$$p(x) = 0 \qquad h(x) \geq 0 \tag{8.3}$$

The object function, *I*, for quadratic programing is given as the product of the pressure and gap functions, as follows:

$$I = p(x)h(x) = \int p(x)h(x)dx \tag{8.4}$$

I is minimised subject to constraints, as described by Equations (8.1) to (8.3). For an elastic half-space, the integral of the pressure distribution is equal to the normal load, as follows:

$$P = \int p(x)dx \tag{8.5}$$

To convert these equations to a standard quadratic programming problem, the pressure is discretized; this is achieved by dividing the possible contact area into *M* triangular pressure elements, each of magnitude, p_i. These triangular elements are positioned so that they overlap, as shown in Figure 8.2; this gives a piecewise linear representation of pressure. The object function now becomes:

$$I = \sum_{i=1}^{M} p_i h_i \tag{8.6}$$

where h_i is the gap at the center of pressure element *i*. The constraints now become:

$$h_i = h_{oi} - v_i \tag{8.7}$$

$$p_i \geq 0 \qquad h_i \geq 0 \qquad i = 1,...,M \tag{8.8}$$

$$P = \sum_{i=1}^{M} b p_i \tag{8.9}$$

where 2*b* is the width of each pressure element.

The relationship between vertical displacement and pressure for a single triangular pressure element is given by Johnson (1985):

$$v(x) = -\frac{1-\nu^2}{2\pi E}\frac{p_o}{b}\left((z+b)^2 \ln\left(\frac{x+b}{b}\right)^2 + (z-b)^2 \ln\left(\frac{x-b}{b}\right)^2 - 2x^2 \ln\left(\frac{x}{b}\right)^2\right) + C \tag{8.10}$$

The constant *C* is fixed by the datum chosen for normal displacements and can be chosen arbitrarily. The discretized displacement to pressure relationship is:

$$v_j = \sum_{i=1}^{M} D_{ij}\, p_i \tag{8.11}$$

where D_{ij} is the influence function, obtained by substituting $x = b(j-i)$ in Equation (8.10).

The contact pressure distribution can now be found by minimising Equation (8.6) subject to constraints described by Equations (8.7) to (8.10)

The change in surface profile due to wear can be described using the gap function calculation as follows:

$$h_n(x_i) = h_{n-1}(x_i) + dz_{n-1}(x_i) \tag{8.12}$$

For the Archard wear equation, the change in normal profile, *dz*, is given by:

$$dz = 4k\delta(\Delta N)\, p(x) \tag{8.13}$$

where *k* is the Archard wear coefficient, as described in Chapters 2 and 6.

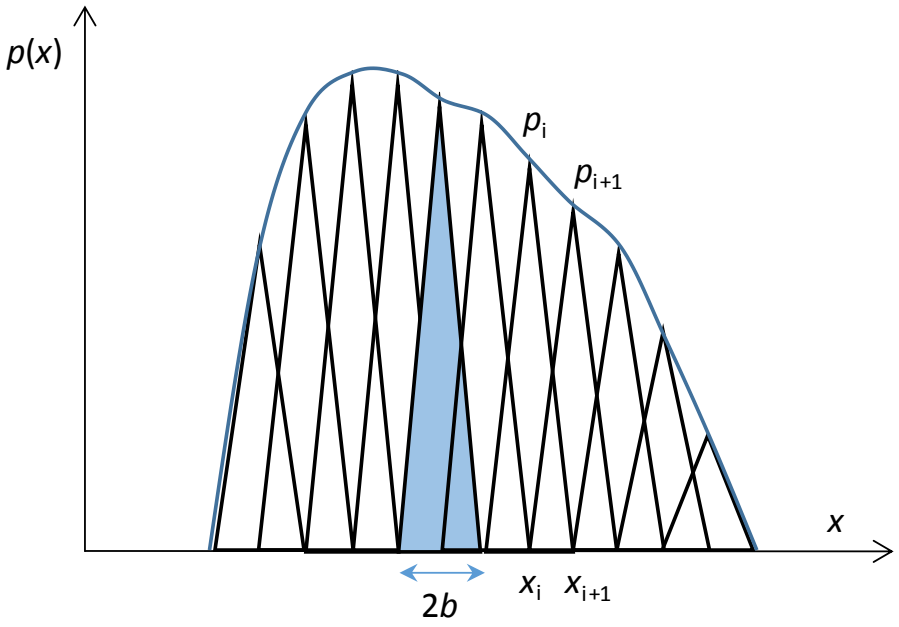

Figure 8.2. Overlapping triangular elements for discretization of pressure distribution

This optimisation methodology has been implemented in MatLab™, which also includes the calculation of substrate stresses based on the theory of elasticity described earlier (see Chapter 5).

The two-dimensional Cartesian stress components are given by (Johnson, 1985; Switek, 1984):

$$(\sigma_{xx}) = -\frac{2z}{\pi}\int_{-b}^{a}\frac{p(s)(x-s)^2 ds}{\left\{(x-s)^2+z^2\right\}^2} - \frac{2}{\pi}\int_{-b}^{a}\frac{q(s)(x-s)^3 ds}{\left\{(x-s)^2+z^2\right\}^2} \tag{8.14}$$

$$(\sigma_{zz}) = -\frac{2z^3}{\pi}\int_{-b}^{a}\frac{p(s) ds}{\left\{(x-s)^2+z^2\right\}^2} - \frac{2z^2}{\pi}\int_{-b}^{a}\frac{q(s)(x-s) ds}{\left\{(x-s)^2+z^2\right\}^2} \tag{8.15}$$

$$(\tau_{xz}) = -\frac{2z^2}{\pi}\int_{-b}^{a}\frac{p(s)(x-s) ds}{\left\{(x-s)^2+z^2\right\}^2} - \frac{2z}{\pi}\int_{-b}^{a}\frac{q(s)(x-s)^2 ds}{\left\{(x-s)^2+z^2\right\}^2} \tag{8.16}$$

where *a*, *b*, *z*, *s*, *ds* and *x* are illustrated in Figure 2.7.

The critical-plane multi-axial fatigue SWT parameter, as described in Chapter 5, has been implemented to calculate the fretting fatigue life to crack initiation. Damage accumulation is calculated using the Miner-Palmren rule, as described in Chapter 6. A flowchart of EASY-FRET is provided in Figure 8.3.

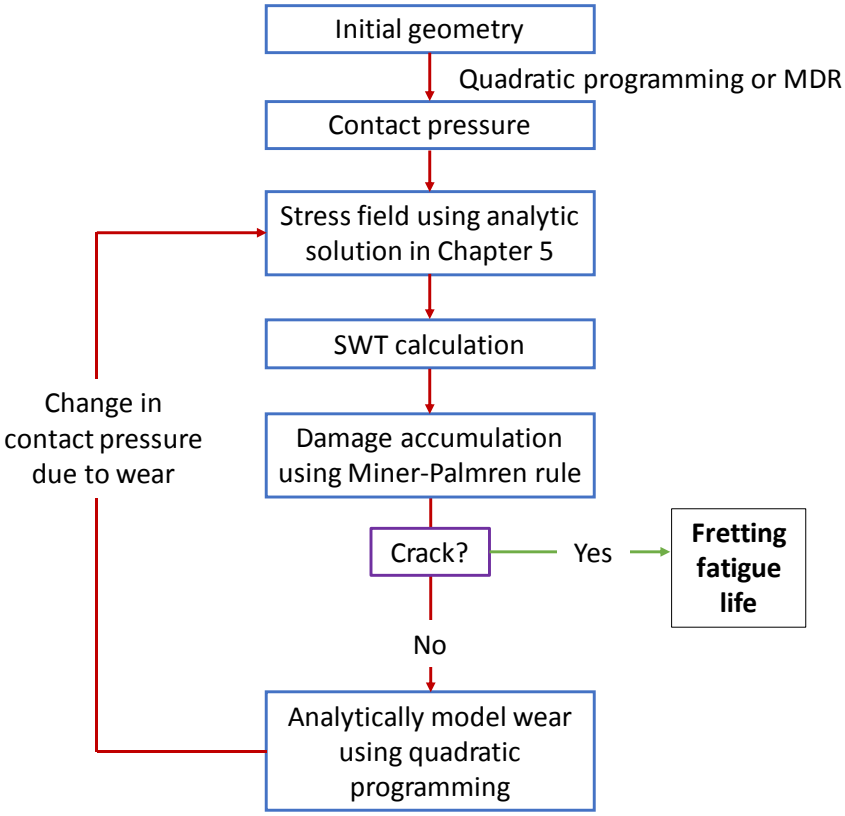

Figure 8.3. Implementation of EASY-FRET design tool for fretting.

8.3. Model validation

8.3.1. Contact pressure distributions

The EASY-FRET methodology of quadratic programming to obtain a pressure distribution from an initial gap function has been validated against known solutions for cylinder-on-flat, punch-on-flat and wedge-on-flat. Figure 8.4 shows a comparison

between contact pressure distributions from EASY-FRET and analytical (i.e. Hertzian) solutions (Johnson, 1985) for (a) punch-on-flat, (b) wedge-on-flat, and (c) cylinder-on-flat. Clearly EASY-FRET gives identical solutions to the analytical for all geometries; peak pressures and contact widths from both methods are essentially the same for all cases.

8.3.2. Stress distributions

The EASY-FRET substrate stress distributions are compared here to the FE results for PS and GS regimes described in Chapter 5, viz. 6 mm radius cylinder-on-flat, with a normal load of 10 N/mm and (i) a tangential displacement of 10 μm for the PS case, and (ii) a tangential force of 25 N for the GS case.

Figure 8.5 shows the comparison for the cylinder-on-flat sliding contact case. The FE results are sampled at the set of integration points closest to the surface (depth z = 5 μm); EASY-FRET stresses are also calculated at this depth with 200 triangular elements along the contact width, as depicted in Figure 8.2. The EASY-FRET predicts the peak trailing edge tensile stress and maximum shear stress at the same location as the FE solution. The peak trailing edge tensile and maximum shear stresses are slightly under-predicted by EASY-FRET relative to the FE results, by approximately 12% and 3%, respectively.

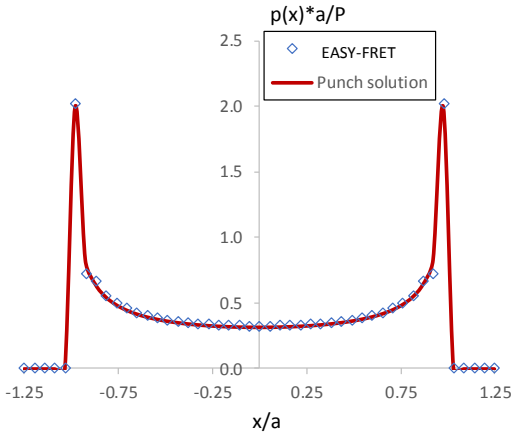

(a) Punch-on-flat

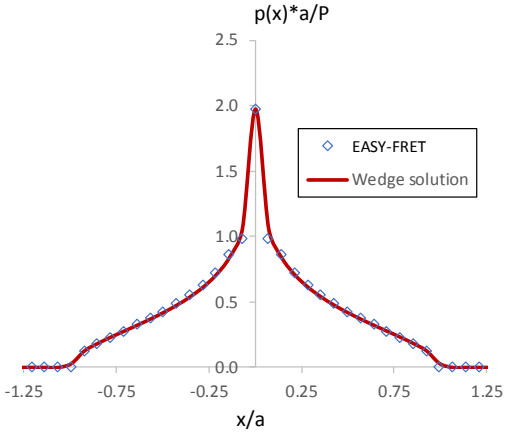

(b) Wedge-on-flat

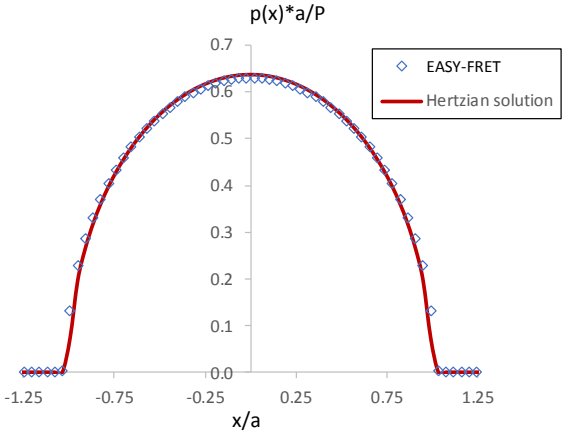

(c) Cylinder-on-flat

Figure 8.4. Comparison of normalised pressure distributions calculated using EASY-FRET and known analytical solutions for different contact geometries.

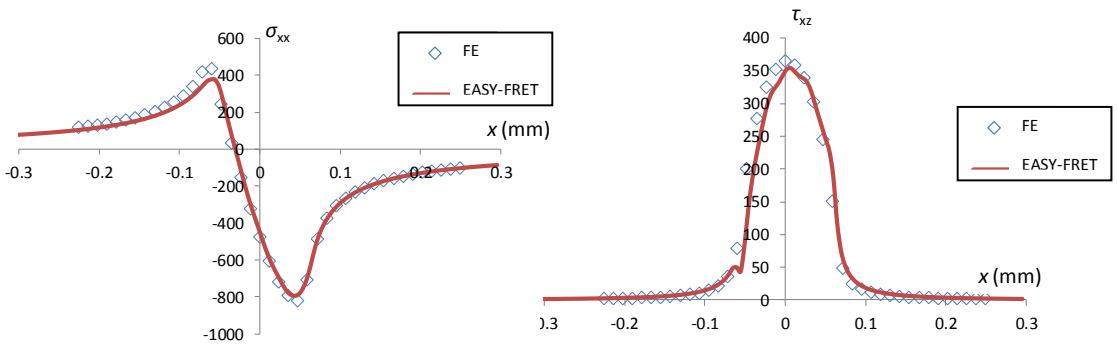

(a) (b)

Figure 8.5. Comparison of σ_{xx} and τ_{xz} stress results from EASY-FRET with FE solution for gross-slip case (P = 50 kN, Δ = 10 μm).

Figure 8.6 shows the comparison between EASY-FRET and FE solutions for the partial-slip case for the same time instant and depth. EASY-FRET again predicts the peak trailing edge tensile stress and maximum shear stress at the same location as the FE; EASY-FRET peak trailing edge tensile and maximum shear stresses are 9% lower and 10% higher, respectively, than the FE.

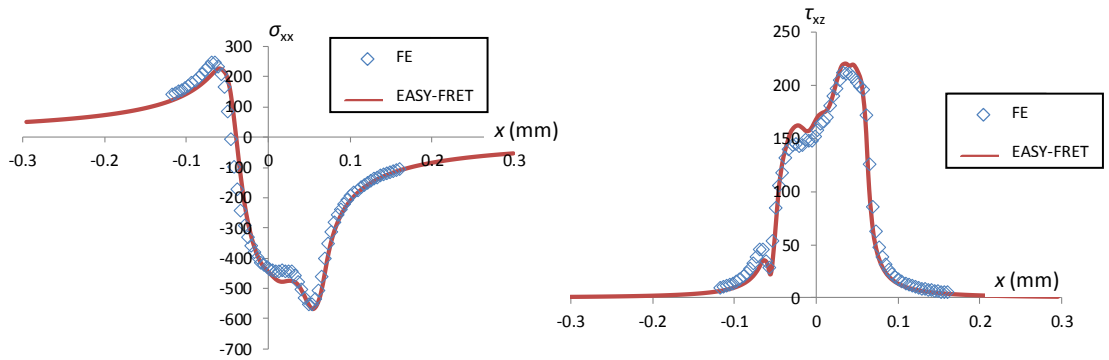

(a) (b)

Figure 8.6. Comparison of σ_{xx} and τ_{xz} stress results from EASY-FRET with FE solution for partial-slip case (P = 50 kN, Q= 25 N/mm).

8.3.3. Wear simulation

Change in contact profile due to wear is simulated, as described by Nowell (2010) and by Equations (8.12) and (8.13); this new contact profile is then used to calculate the contact pressure, as described by the flowchart of Figure 8.3. Similar to the work presented in Chapter 6, cycle jumping is used to speed up the wear simulation. This section presents the effect of cycle jumping on solution stabilisation within EASY-FRET and also comparisons of EASY-FRET and FE results for pressure and stress redistributions due to wear effects.

Ding et al. (2004) discusses the possibility of instability occurring in the results if too large a ΔN is used. Therefore, a critical value of cycle jumping was introduced, ΔN_{crit}. The value of ΔN_{crit} was found to depend on different input parameters, such as tangential displacement and wear coefficient. Ding et al. (2004) found that the instability can be more directly interpreted in terms of a maximum allowed wear depth per increment, Δh_{crit}. In this work, Δh_{crit} has been calculated for a 6 mm radius cylinder-on-flat contact with a normal load of 50 N/mm, tangential displacement of 10 μm, and CoF of 0.7 as shown in Figure 8.7.

This rapid wear simulation methodology has been validated against 3 mm radius cylinder-on-flat FE stress distributions described in Chapter 6. Figure 8.8 presents the comparison of contact pressure for the 1st, 25,000th, 100,000th and 200,000th cycles found using EASY-FRET and FE. There is good correlation between EASY-FRET and the FE results. As wear evolves, the contact width widens and the contact pressure is redistributed over a wider area for both models; therefore, the peak pressure is dramatically reduced and the pressure is much less concentrated than for the initial fretting loading. EASY-FRET under-predicts the wear, and hence, over-predicts

the contact pressure; this can be attributed to the assumed constant contact slip in the EASY-FRET simulation.

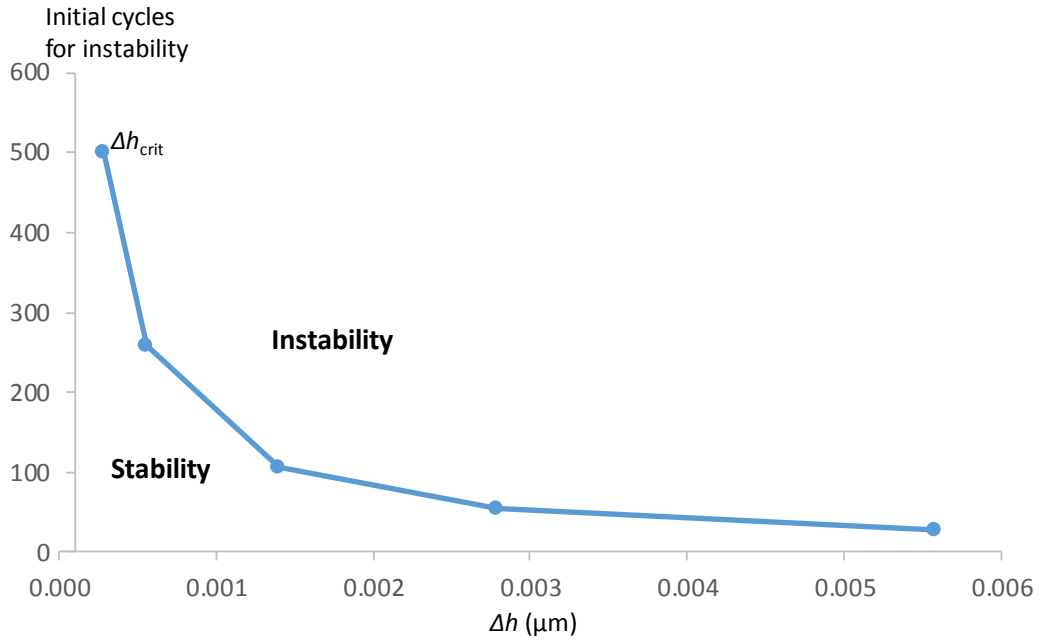

Figure 8.7. Influence of incremental wear depth, Δh, on computational stability

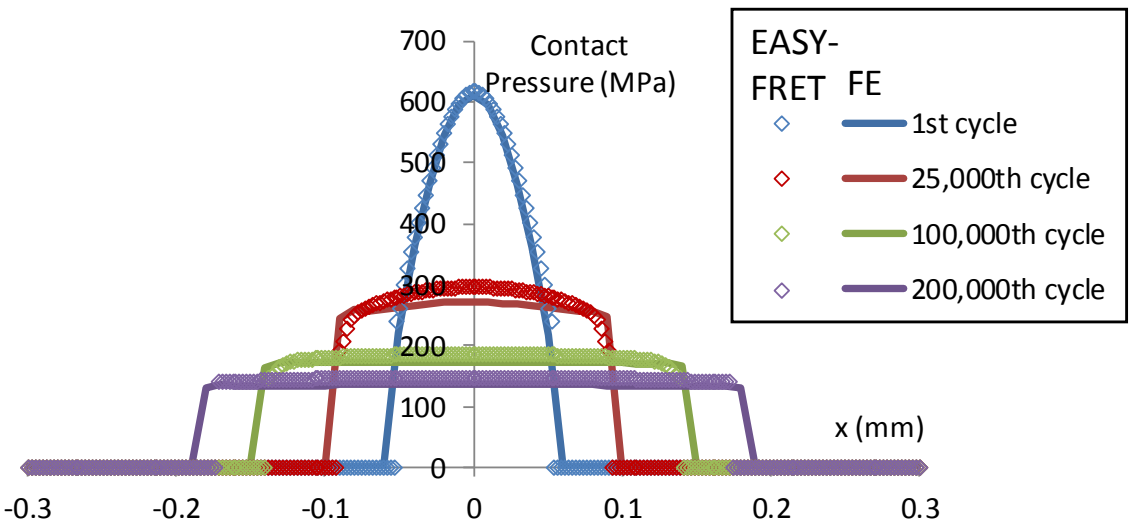

Figure 8.8. EASY-FRET and FE wear simulation results for gross slip (P = 50 N/mm and Δ^* = 10 μm) condition showing evolution of contact pressure.

The effects of the redistribution of contact pressure on (a) tensile (σ_{xx}) and (b) shear (τ_{xz}) stresses predicted using EASY-FRET and FE are presented in Figure 8.9. Since the contact pressures are overpredicted by EASY-FRET, the substrate stresses are also overpredicted, in comparison to the FE results. However, EASY-FRET captures the effect of wear. The EASY-FRET contact width after 2×10^5 fretting cycles is 4% smaller than the FE results. This causes the EASY-FRET trailing edge tensile stress and shear stress to be 17 % and 14 % higher, respectively.

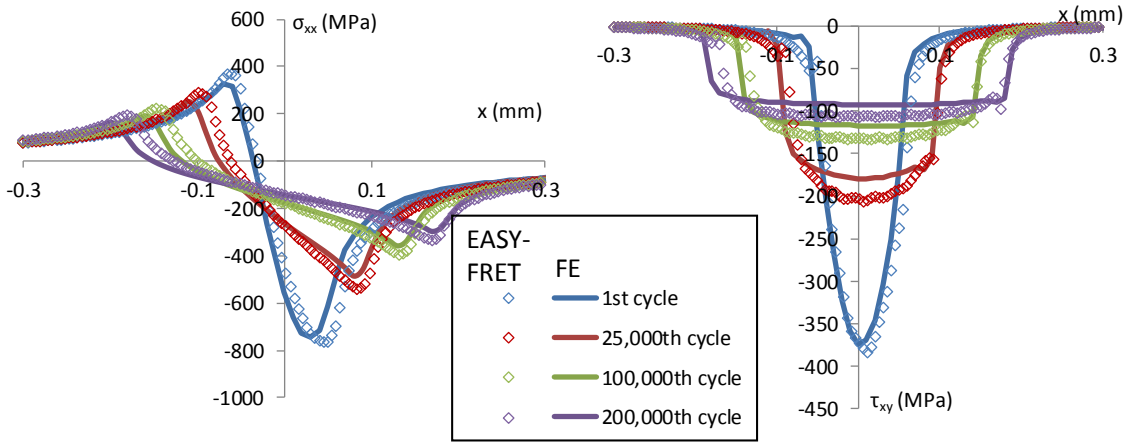

(a) (b)

Figure 8.9. EASY-FRET and FE wear simulation results for gross slip (P = 50 N/mm and Δ^* = 10 μm) condition showing evolution of (a) tensile stress (σ_{xx}) and (b) shear stress (τ_{xy}) at extreme stroke position.

8.3.4. Multi-axial fatigue

As described in Chapter 6, fretting crack initiation life predictions have been calculated for FE centroidal (integration point) positions at a depth of 5 μm below the surface of the substrate. This depth is also used in EASY-FRET. When a damage of 1 is predicted for an integration point close to the surface, the element is deemed to have

cracked so that initiation crack length is 10 μm. Figure 8.10 presents a comparison between EASY-FRET and FE predicted effect of applied tangential displacement on crack initiation life. EASY-FRET gives a conservative life prediction in the GS regime, this is due to the slight under prediction of wear, and hence under prediction of contact pressure and substrate stresses (Figure 8.8 and 8.9). However, the minimum life is over-predicted, compared to FE results, using EASY-FRET in the MS regime. The predicted life calculated using EASY-FRET is approximately twice as high as than that predicted using FE methods. However, it must be stated that in terms of component life design, there is very little difference between 1.5×10^4 and 3.1×10^4 cycles since, 10^4 is considered to be very low, and can occur in a very short period of time.

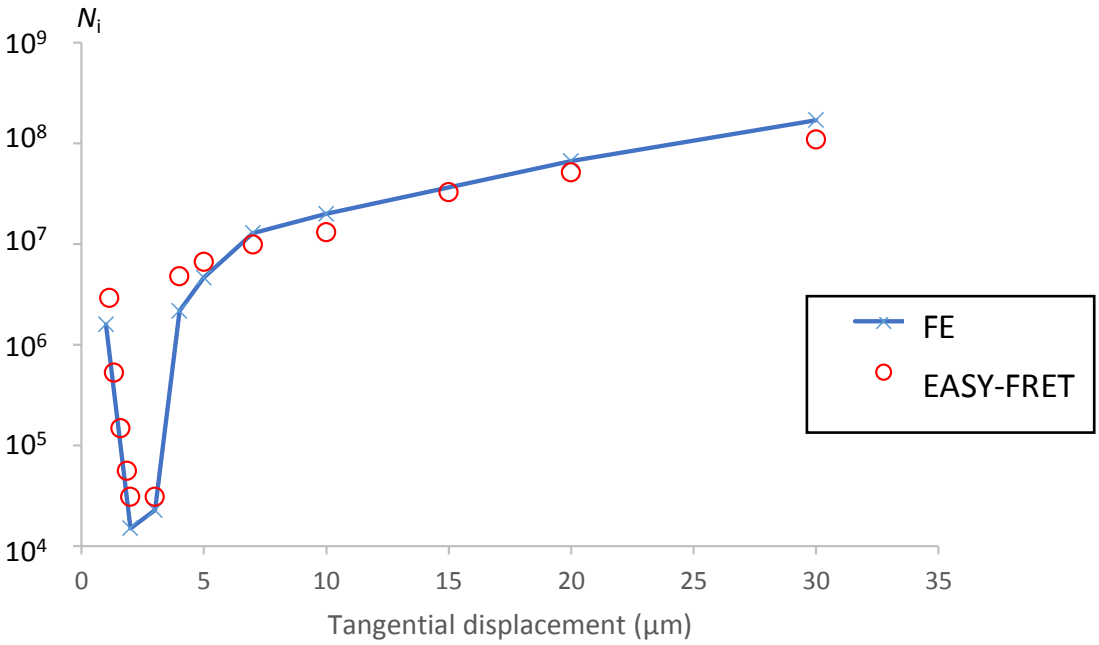

Figure 8.10. Comparison between EASY-FRET and FE predicted effect of applied tangential displacement on crack initiation life.

8.4. Discussion

8.4.1. Computational efficiency

EASY-FRET allows for fretting analysis to be conducted on any contact geometry without the use of computationally expensive finite element models. For example, the optimisation of the contact pressure for each wear block (with M = 500 and N = 50 cycles) takes 0.05 s of CPU time on an Intel® Core™ i7-3770 processor. However, the calculation of substrate stresses takes considerable more computational time; the calculation of 2D stress components for a given pressure distribution takes ~100 s of CPU time on the same PC, for example. Therefore, stress distributions are calculated every 1000 fretting cycles, reducing total computational time.

8.4.2. Further development

At present, this design tool assumes elastic material behaviour; plasticity can be introduced to the program either by assuming a simplified plasticity model or a more complex NLKH J_2 plasticity model. However, since the primary benefit of the ESAY-FRET design tool is its superior computational efficiency compared to FE wear simulation, the addition of plasticity would increase the computational time, and hence, would decrease the benefits of this design tool.

If the initial contact geometry is 3-dimensional, the method of dimensional reduction (MDR) can be implemented to reduce the problem to a 2D contact. After analysis, MDR can be used to go from the 2D solution to 3D. Similarly, stresses can also be calculated to represent axisymmetric conditions.

Bulk substrate stresses can also be added to the model. These additional stresses may represent fatigue loading or hoop stress in pressure armour wires of flexible marine risers, for example. The bulk substrate stress can be modelled as in-phase or out-of-phase with the fretting tangential loading. However, again this will increase the computational time of the simulation.

Finally, the computational time can be increased by varying ΔN to keep Δh constant throughout the simulation. This method has been used by other researchers (McColl et al., 2004; Öqvist, 2001) as a method to balance the simulation time and stability.

8.5. Summary and conclusions

This chapter outlines the development of EASY-FRET (Engineering Analysis SYstem for FRETting) design tool. Results from this design tool has been compared against known contact mechanics pressure distributions for punch-on-flat, wedge-on-flat and cylinder-on-flat. Substrate stresses have been compared to FE results for partial- and gross-slip contacts for worn and unworn cases. The effect of wear on pressure and stress distributions have also been compared. There is good agreement between fretting results found using EASY-FRET and FE adaptive meshing techniques. The computational time to model wear using EASY-FRET is considerably shorter than FE methods; therefore, EASY-FRET is the superior modelling technique for use in industry, in particular.

Chapter 9: Conclusions and recommendations

9.1. Conclusions

The key achievement of this thesis is the characterisation and simulation of fretting in pressure armour nub-groove contacts and the prediction of fretting fatigue damage in flexible marine risers. This has been achieved through a combined experimental-computational methodology, leading to the development and implementation of a design framework for fretting in flexible marine risers, as presented in Figure 1.4. Another important achievement is the development of a stand-alone, computationally efficient, analytical design tool, EASY-FRET, for use in industry, to predict incremental fretting wear and crack initiation.

The dissection of a pre-service flexible marine riser, described in Appendix B, allowed for pressure armour wire material extraction for tensile and fatigue testing and identification and measurement of the local contact geometry. Mechanical testing of pressure armour wire material has provided material properties, such as yield strength, ultimate tensile strength, Young's modulus, ductility and low-cycle fatigue parameters. High-cycle fatigue parameters were inferred from tensile data using the universal slopes method.

Experimental characterisation for dry and grease-lubricated fretting conditions were conducted at the University of Nottingham using 080M40, a pearlitic steel with essentially the same chemical composition and hardness as that used in the pressure armour layer of flexible marine risers. These tests were conducted with a specific focus

on grease lubrication, contact conformity, relative tangential displacement and normal load. Under dry fretting conditions, friction was found to be relatively insensitive to increasing tangential displacement and specific wear rate was found to increase with tangential displacement. Under grease-lubricated conditions, friction and specific wear rate were found to decrease with increasing displacement, particularly for the larger displacements tested. Grease lubrication was shown to be generally beneficial to the fretting behaviour of the tested material, resulting in lower friction and specific wear rates than dry fretting cases. For grease lubrication, a threshold value of displacement for low fretting damage was established, above which friction and specific wear rate remain low. It was also found that as the contact becomes more conforming, this threshold value increases significantly. Grease extrusion out of the contact is accelerated by increased normal load and by reduced contact conformity.

The development of a new fretting test rig, utilising a piezoelectric actuator for high contact pressure (up to 1730 MPa), low displacement (down to ±1 μm) conditions, has been outlined in Chapter 3. This has allowed for testing of pressure armour material under representative nub-groove contact pressure and slip loading conditions, as predicted by the global-local modelling of Chapter 7. This rig was used for fretting tests on pre-drawn pressure armour, pearlitic steel material supplied by NV Bekaert SA, Belgium. The newly-design fretting rig at NUI Galway has been developed for the identification of tribological parameters, such as coefficient of friction and wear coefficient, and testing under PS and GS conditions under high contact pressure conditions. Coefficient of friction and wear coefficient values have been identified using this rig for a crossed-cylinder configuration and compared to corresponding values from the cylinder-on-flat tests at the University of Nottingham. There is good agreement terms of coefficient of friction and wear coefficients. The fretting test rigs at

the University of Nottingham and at NUI Galway are complementary to each other, allowing for investigation of various fretting contact geometries and a wide range of loading conditions. The NUI Galway rig is specifically relevant to flexible riser conditions.

The experimental characterisation (fretting, tensile and fatigue) has allowed for the identification of key tribological parameters, viz. wear coefficient and coefficient of friction, and mechanical properties, viz. elastic-plastic material parameters and fatigue parameters, for use within the computational models developed in Chapters 5 and 6.

Local (axisymmetric) frictional contact analyses of the nub-groove contacts in the pressure armour layer, described in Chapter 5, have revealed a highly-localised and severe trailing-edge tensile stress concentration due to fretting action. Crack initiation predictions have been calculated using a 3D critical plane SWT fatigue indicator parameter. CoF evolution and increased bending-induced axial displacement are shown to have a significant and detrimental effect on the trailing-edge stresses responsible for fatigue crack initiation. Plasticity was shown to have relatively small effect on predicted fretting fatigue lives; therefore, elastic material properties have been used throughout the remainder of the thesis to increase computational efficiency without compromising the accuracy of life prediction methodology. Three-dimensional riser modelling has facilitated, for the first time, quantification of the effect of non-symmetric global riser loading, such as bending moment, on local nub-groove fretting, viz. relative slip and contact pressure. This was key to the representative fretting tests at NUI Galway.

A computational methodology, combining fretting wear simulation using adaptive meshing techniques and critical plane multiaxial fatigue life predictions, has

been developed in Chapter 6. The fretting wear finite element simulations have been validated against cylinder-on-flat fretting wear experimental test results of Chapter 4. In partial-slip, wear rate was low and therefore a detrimental effect of increasing slip on number of cycles to crack initiation was observed. However, in gross-slip, wear has a beneficial effect on crack initiation life, due to the redistribution of stresses associated with material removal caused by wear. The D_{fret}-SWT parameter successfully predicts the effect of wear and tangential displacement on crack initiation life. The major benefit of this parameter is the significantly reduced computational expense since wear does not have to be explicitly modelled. This is a key development in terms of the design of flexible risers against fretting.

The design framework of Figure 1.4 has been implemented in a realistic riser design study for extreme, but realistic, loading conditions. Global-local analyses on a number of riser geometries and load cases has established, for the first time, the functional relationship between global riser variables (dynamic curvature and axial tension) and local nub-groove fretting variables (contact slip and pressure). Novel running condition fretting maps for flexible risers are then developed giving critical dynamic riser curvature ranges for the various riser geometries, including both crack initiation and propagation effects. The methodology developed is a significant improvement on the current analysis techniques (typically only used for fatigue of the tensile armour layer). The predictive methodology currently used is based on S-N curves (stress amplitude versus number of cycles to failure), therefore does not include LCF or stress range effects. This study establishes the effect of global riser bending on local nub-groove contact slip, for the first time. The predicted total fretting fatigue life for the pressure armour layer was found to be similar to the predicted fatigue life of the

tensile armour layer, found using the tensile armour layer fatigue design tool, Layercom.

An analytical design tool has been developed utilising quadratic programming (Hills et al., 2009; Nowell, 2010) and analytical fretting solutions based on the theory of elasticity, the Archard wear equation and critical-plane multi-axial fatigue indicator parameter. The analytical model has been validated against finite element results for pressure and stress distributions for partial-slip, without wear effects, and for gross-slip with incremental wear. Fretting fatigue lives have been successfully validated against the finite element adaptive meshing results of Chapter 6. The analytical model is considerably more computationally efficient than the finite element adaptive meshing technique, giving a CPU time that is approximately 90 to 95 % faster than the finite element adaptive meshing method. An advantage of this analytical tool over the D_{fret}-SWT parameter of Chapter 6 is that since wear is explicitly modelled, the effect of wear on contact pressure and substrate stresses is known throughout the simulation, and hence crack propagation can be predicted.

This work shows that for reliable prediction of fretting stresses in the nub-groove contact of flexible marine risers, designers must account for contact geometry conformity and loading conditions, such as normal load (contact pressure) and relative (tangential) displacement, based on dynamic curvature, as well as the pressure armour material properties, such as friction coefficient. A key fretting design recommendation is that nub-groove contact slip should be large (gross slip). This will ensure longer predicted fretting fatigue life in both grease-lubricated and dry fretting. Effective sustainable (grease) lubrication occurs if the contact slip is larger than the contact width, as shown in Chapter 4. This will reduce the fretting fatigue damage of the pressure armour layer since the frictional contact stresses will be reduced considerably,

as shown in Chapter 5. This, in turn, will be beneficial to increased fatigue endurance of flexible risers. For dry fretting conditions, wear has a beneficial effect for larger contact slips due to wear-induced redistribution of substrate stresses, as shown in Chapter 6. The framework developed and implemented in this work (Chapter 7) has improved the understanding of fretting in the nub-groove contact of marine risers through experimental characterisation and computational simulation. The analytical design tool, of Chapter 8, will help riser engineers to design pressure armour wire against fretting damage for various nub-groove geometries and loading conditions, using relevant pressure armour material properties.

9.2. Recommendations for future work

The work presented here has successfully achieved the overall aim of the research by developing a fretting wear-fatigue design tool for flexible marine risers. However, there are limitations and gaps that require further research.

The newly-designed fretting testing rig is a significant improvement on the micro-scale testing capabilities at NUI Galway; however, there are some areas to further improve the test rig. For example, a more powerful actuator would allow for testing under higher normal load and applied displacement loading conditions. If a more powerful actuator was employed (such as an EMV), a lever-arm set-up could be used to apply the dead weight. A lever ratio would allow for higher normal loads to be applied using the same number of weights that are currently used. One other area where the rig could possibly be improved is by changing the closed loop feedback. At present, the closed loop feedback to the actuator is from the strain gauge (SG45) on the actuator.

This could possibly be improved by changing this to a closed loop feedback from the DVRT since it is located closest to the contact region. This would allow for more accurate control of the contact displacement. However, this would require overwriting the inbuilt HDPM45 software that allows signals to be sent to the actuator at present. With regard to post-processing of fretting test results, 3D measurement of the wear scar would provide greater accuracy for wear volume measurement.

Future work can characterise the high-cycle fatigue and fretting fatige behaviour of pressure armour material. In this work, HCF constants were estimated using the universal slopes method. This method is useful for the industry, because designers may not have access to fatigue data for the material in a riser, but they typically would have access to monotonic tensile test data (i.e. σ_{UTS}, E, ε_f). Fretting fatigue testing of pressure armour material would quantify the difference between plain fatigue and fretting fatigue lives and hence the qualification of a fretting life reduction factor (FLRF) between plain and fretting fatigue lives. McCarthy et al. (2013a) experimentally observed an average life reduction factor of 3.5 between plain and fretting fatigue life for a stainless steel.

This work focuses on a generalised round-on-flat geometry based on observations from the riser cut-up in NUI Galway. However, different manufacturers use different nub-groove contact geometries. A full computational study of the various riser geometries would help determine the most effective geometry against fretting damage. This would also allow for optimisation of nub-groove geometries to account for fretting damage.

Individual grains in the metallic materials are not modelled in this work; therefore, this methodology does not capture local anisotropic effects or local

crystallographic heterogeneity. Hence, scatter due to microstructural effect will not be captured (Ashton et al., 2017). Current parallel work is investigating the effect of the wire profile process on grain size, texture and shape especially in the context of fretting performance of the material. The effect of cold forming the material may increase dislocation density and affect grain orientation and texture. Further experimental characterisation, combined with material modelling would allow for pressure armour material to be designed for optimum fretting performance, potentially including material coatings and lubrication regime.

The study presented in Chapter 7 has highlighted the requirement for further investigation into the effect of global riser curvature on local nub-groove contact slip. To quantify this effect, 3D riser modelling including detailed geometry of each layer and contact pressures and slip between layers is required. These 3D models should be validated using full-scale riser testing; this is a difficult task since contact slip is difficult to measure experimentally, especially in the small space within the pressure armour layer. However, it may be feasible to implement displacement or position sensors to measure the effect of riser curvature on pressure armour wire displacement; FE modelling can then be used to predict local nub-groove contact slip.

Finally, new flexible riser design codes and standards need to be developed to include the findings of this thesis. This thesis has addressed an uncertainty associated with fatigue design of flexible marine risers; therefore, the development of new riser design codes would allow for the safety factors associated with fatigue design of risers (API, 2009) to be decreased.

Appendix A: New fretting rig documents

A.1. Overview

The following Appendix contains calibration certificates for:

1. Piezoelectric actuator manufactured by Cedrat Technologies,
2. DVRT manufactured by LORD MicroStrain,
3. Force sensor manufactured by DYTRAN.

Drawings for the test rig are also provided in this section. Finally, the operational procedure for the test rig is provided.

A.2. Calibration certification for piezoelectric actuator

CEDRAT TECHNOLOGIES
Innovation in Mechatronics

Piezoelectric Actuators

Factory Verification: Cypher_v7.8

Date of test (DD/MM/YY)	Model	Options	Serial Number	Test performed by	Signature	Quality Assurance
04/05/2016	APA40SM	SG	16-001	CS		Date: Signature: Name: Stamp:

09 MAI 2016

CEDRAT TECHNOLOGIES S.A. Quality Control Certificate of Calibration A.M.A department

Electrical Admittance vs. Frequency

Mechanical conditions:
Free-Free

Measurement Apparatus:
Cypher Instruments C60

Resonance Frequency:
15297 Hz

Effective Coupling Coefficient
47 %

Acceptance limits :13600 Hz < Fr < 17600 Hz.

Notes:

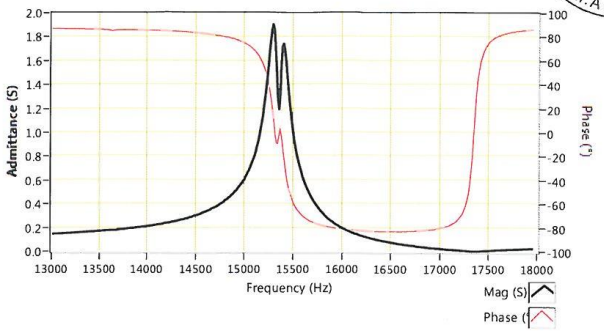

Displacement vs. Input voltage

Mechanical conditions:
Blocked-Free

Measurement apparatus:
Capacitive sensor MC2930

Sensor gain:
50 µm/V

Tension gain probe:
x20.00

Driving frequency
10.00 Hz

Measured displacement :
58.26µm pk-pk for 170.24V pk-pk

Maximum displacement:
58.18µm pk-pk for 170V pk-pk

Acceptance limits : Vmax=150V ; Vmin= -20V; 47 µm < U < 68 µm.

Notes:

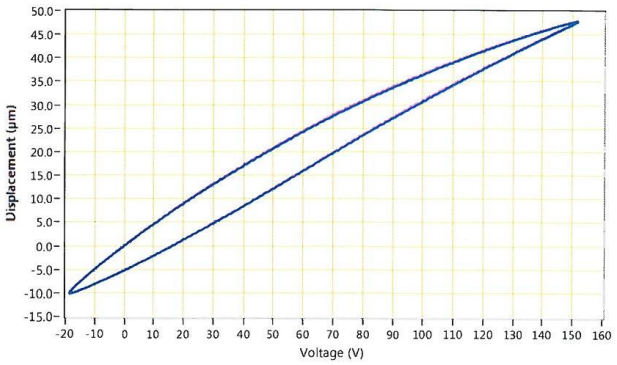

SG vs. Displacement

Mechanical conditions:
Blocked-Free

Displacement measurement apparatus:
Capacitive sensor MC2930 - 50 µm/V

SG measurement apparatus:
SG75-3 SG22-06012

SG controller gain:
948.6400

Driving frequency (Hz):
10.00 Hz

Max measured displacement:
58.18µm pk-pk for 170V pk-pk

Strain Gauge Gain (mV/µm/V):
34.704E-3

Vcc:
5.0000

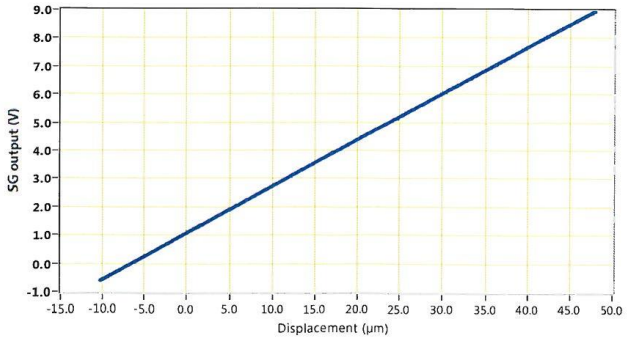

CEDRAT TECHNOLOGIES
Innovation in Mechatronics

Linear Amplifier Factory Verification

LA75A-11050

CH 1

Date of test (DD/MM/YY)
17/05/2016

Test performed by
BBr

Stamp and signature
Quality Control
Certificate of Calibration
18 APR. 2016
CEDRAT TECHNOLOGIES S.A. A.M.A department

Procedure : AQ7701-1 1.3

Output voltage to Square input voltage

Electrical Load: 2.3 µF

Input frequency: 25 Hz

Rise time (10 - 90%): 3,26 ms
Acceptance limits (ms): 3.1 ≤ Tr ≤ 3.45

Fall time (90 - 10%): 3,28 ms
Acceptance limits (ms): 3.1 ≤ Tf ≤ 3.45

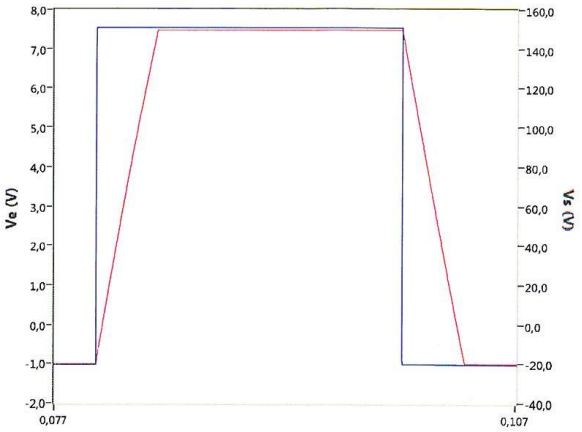

Linearity Output voltage vs. Input voltage

Electrical Load: 2.3 µF

Input frequency: 60 Hz

Gain (Vs/Ve): 19,9

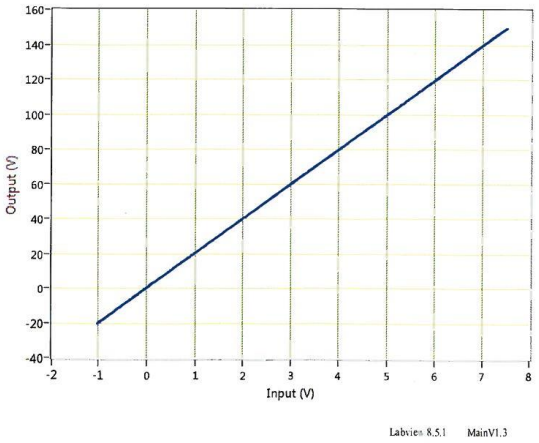

Labview 8.5.1 MainV1.3

CEDRAT TECHNOLOGIES
Innovation in Mechatronics

Linear Amplifier Factory Verification

SG75-12019	Date of test (DD/MM/YY) 18/05/2016	Stamp and signature
CH 1	Test performed by BBr	Procedure: AQ770501 1.6

CEDRAT TECHNOLOGIES S.A. Quality Control Certificate of Calibration 17 MAI 2016

Output sensor voltage vs. Input voltage

Electrical Load: APA40SM 16001

Input frequency: 1,00 Hz

Sensor Type: Strain Gages

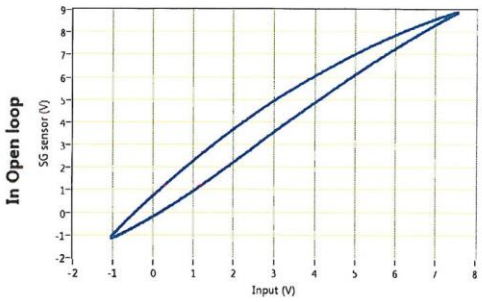

Strain gages Gain (µm/V): 5,79
SG 75 Output voltage vs actuator displacement (In open loop only)

Amplifier Gain (V/V): 958,68
SG 75 Output voltage vs input voltage of strain gages

System Gain (µm/V): 5,92
Output displacement vs input command (In closed loop only)

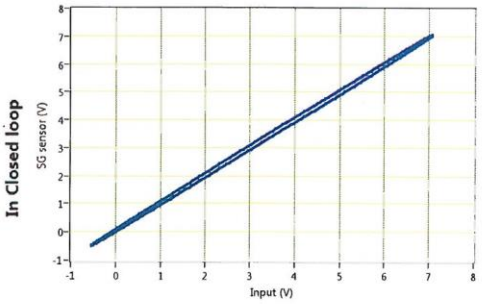

Notes :

Step response in closed loop

Electrical Load: APA40SM 16001

Input frequency: 1,00 Hz

Sensor Type: Strain Gages

Response time 10%-90% :

Rise time (ms): 4,70

Fall time (ms): 5,05

Notes :

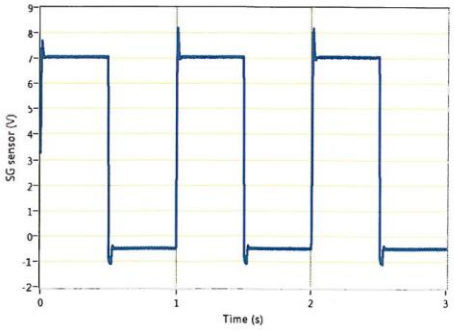

Labview 8.5.1 MainV1.4

A.3. Calibration certificate for DVRT

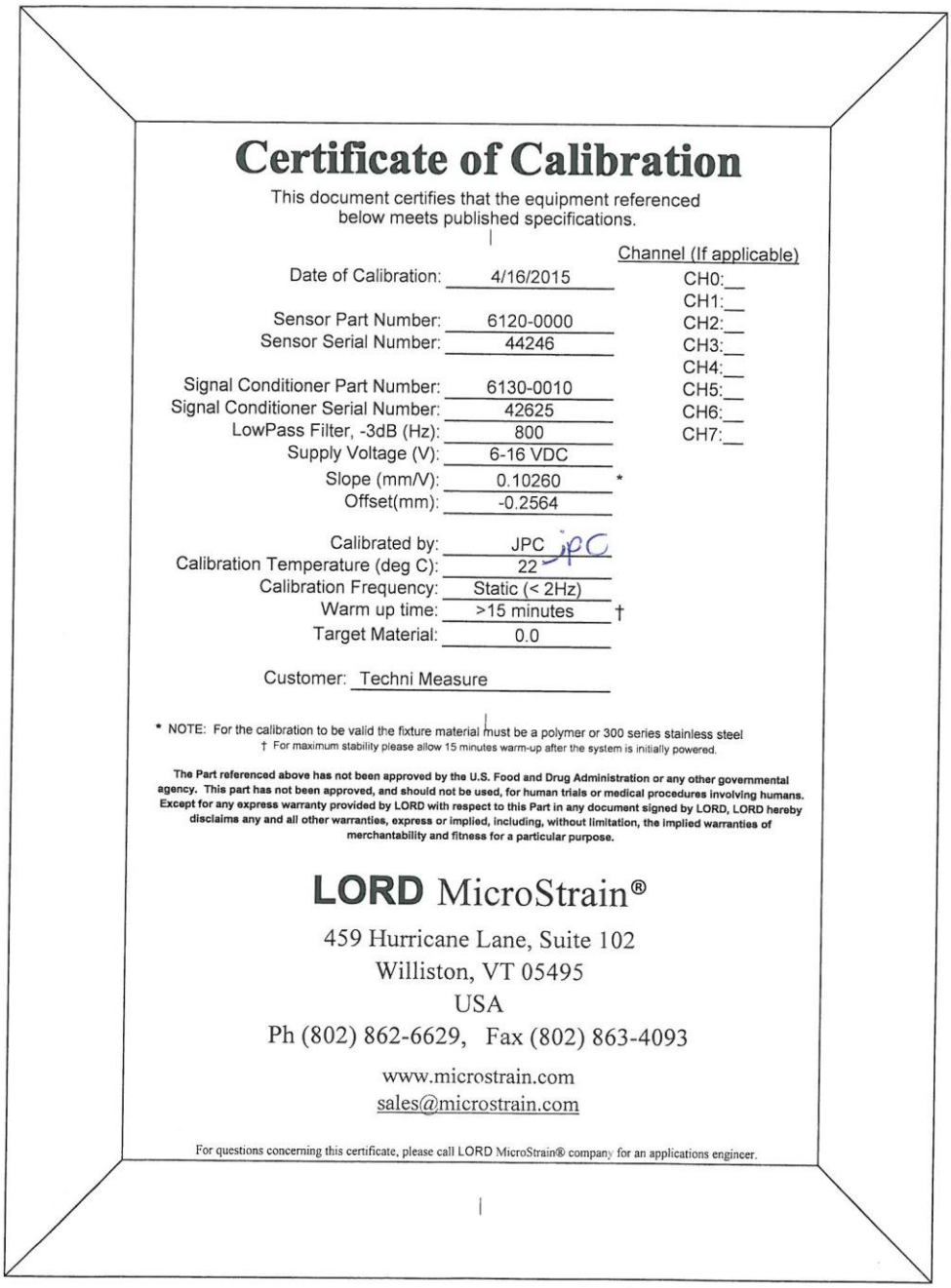

Certificate of Calibration

This document certifies that the equipment referenced below meets published specifications.

		Channel (If applicable)
Date of Calibration:	4/16/2015	CH0:__
		CH1:__
Sensor Part Number:	6120-0000	CH2:__
Sensor Serial Number:	44246	CH3:__
		CH4:__
Signal Conditioner Part Number:	6130-0010	CH5:__
Signal Conditioner Serial Number:	42625	CH6:__
LowPass Filter, -3dB (Hz):	800	CH7:__
Supply Voltage (V):	6-16 VDC	
Slope (mm/V):	0.10260 *	
Offset(mm):	-0.2564	
Calibrated by:	JPC jpc	
Calibration Temperature (deg C):	22	
Calibration Frequency:	Static (< 2Hz)	
Warm up time:	>15 minutes †	
Target Material:	0.0	
Customer:	Techni Measure	

* NOTE: For the calibration to be valid the fixture material must be a polymer or 300 series stainless steel
† For maximum stability please allow 15 minutes warm-up after the system is initially powered.

The Part referenced above has not been approved by the U.S. Food and Drug Administration or any other governmental agency. This part has not been approved, and should not be used, for human trials or medical procedures involving humans. Except for any express warranty provided by LORD with respect to this Part in any document signed by LORD, LORD hereby disclaims any and all other warranties, express or implied, including, without limitation, the implied warranties of merchantability and fitness for a particular purpose.

LORD MicroStrain®
459 Hurricane Lane, Suite 102
Williston, VT 05495
USA
Ph (802) 862-6629, Fax (802) 863-4093
www.microstrain.com
sales@microstrain.com

For questions concerning this certificate, please call LORD MicroStrain® company for an applications engineer.

Displacement Sensor Calibration Report
LORD MicroStrain®

Date: 4/16/2015

Sensor Model: 6120-0000
Sensor Serial Number: 44246

Signal Conditioner Model: 6130-0010
Signal Conditioner Serial Number: 42625

Standard Least Squares Linear Fit

Sensor Output vs. Displacement

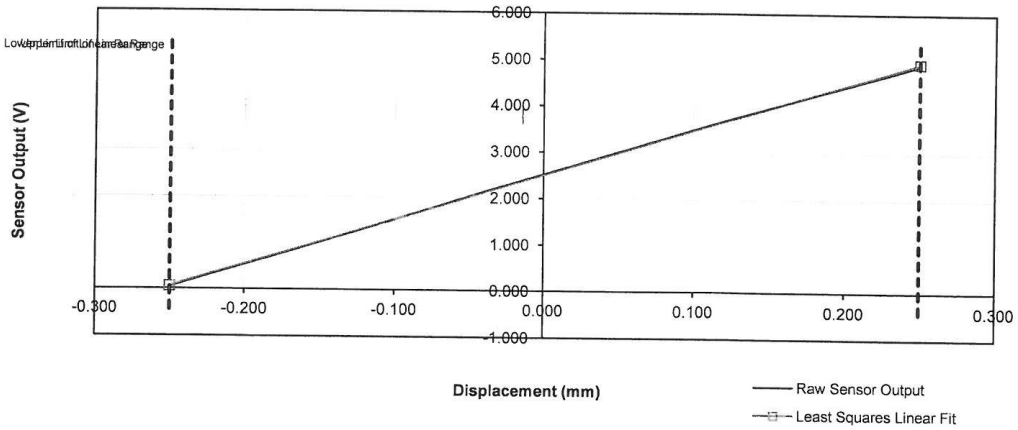

Least Squares Linear Fit Residual Errors vs. Displacement

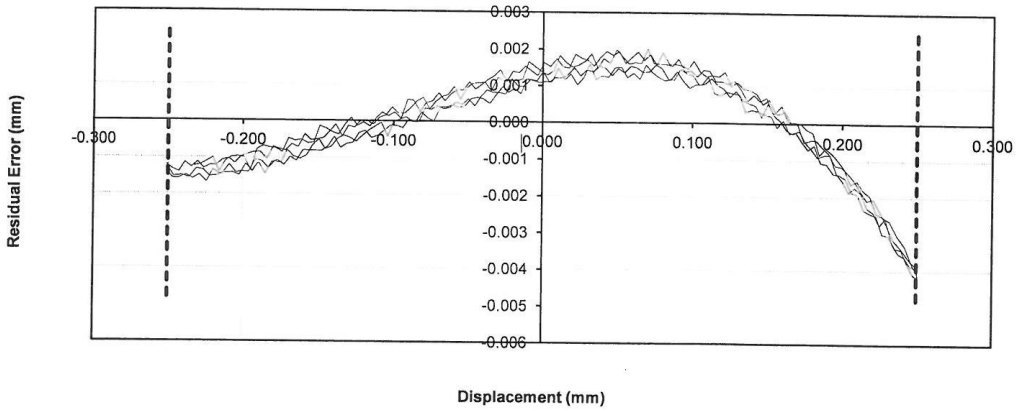

Least Squares Linear Fit Model

$D = M*x + B$

where D = Displacement (mm)
M = Slope (mm/V)
x = Sensor Output (V)
B = Offset (V)

Least Squares Linear Fit Results

Slope (mm/V)	Offset (mm)
0.10260	-0.25641

Residual Errors (within linear range)

Max (%F.S.)	Min (%F.S.)
0.40166	-0.81904

Displacement Sensor Calibration Report
LORD MicroStrain®

Date: 4/16/2015

Sensor Model: 6120-0000
Sensor Serial Number: 44246

Signal Conditioner Model: 6130-0010
Signal Conditioner Serial Number: 42625

Multi-Segment Linear Fit

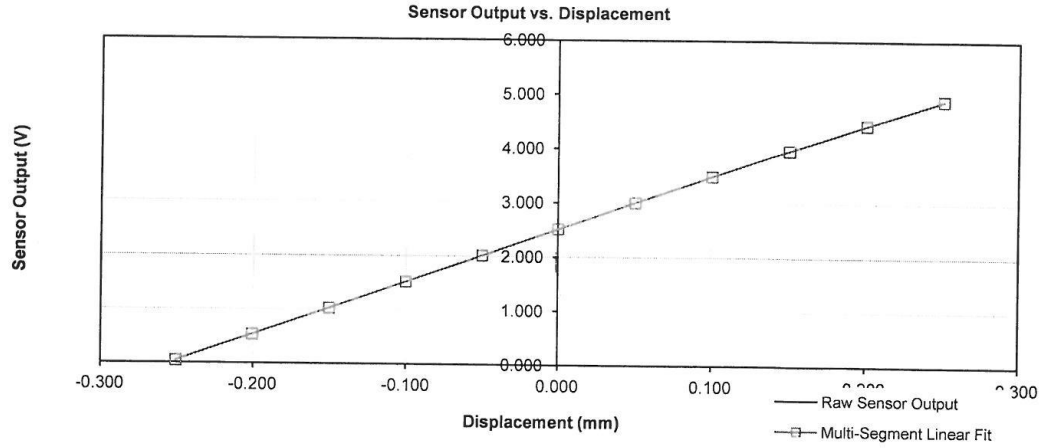

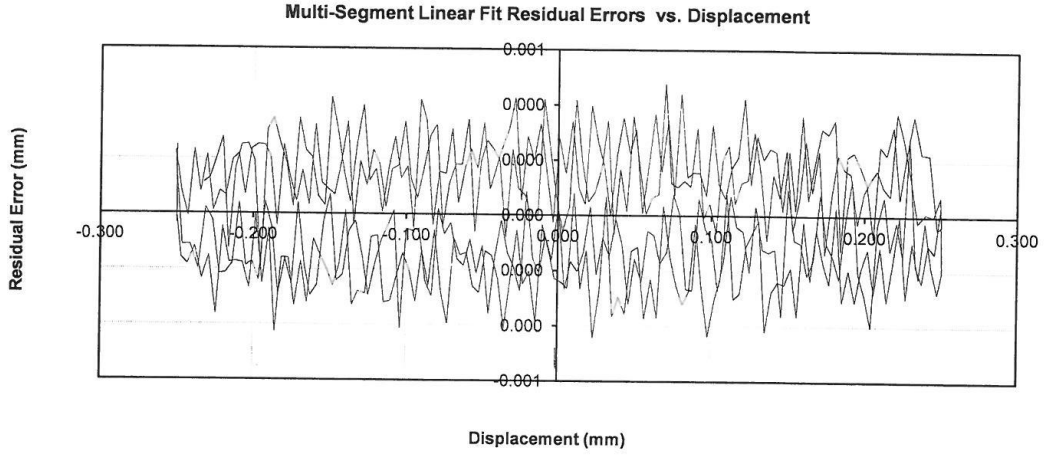

Multi-Segment Linear Fit Model

$$D = M(i)*x + B(i)$$

where D = Displacement (mm)
M(i) = Slope (mm/V)
x = Sensor Output (V)
B(i) = Offset (V)

To select which slope and offset to use, identify index, (i), such that sensor output (in volts) is greater than or equal to X(i) and less than X(i+1). Then use M(i) and B(i) in equation above.

Multi-Segment Linear Fit Results

(i)	X(i) (V)	Slope, M(i) (mm/V)	Offset, B(i) (mm)
0	0.04171	0.10217	-0.25496
1	0.53257	0.10134	-0.25452
2	1.02746	0.10132	-0.25450
3	1.52241	0.10122	-0.25435
4	2.01786	0.10138	-0.25466
5	2.51255	0.10200	-0.25623
6	3.00422	0.10313	-0.25962
7	3.49051	0.10455	-0.26459
8	3.97017	0.10627	-0.27141
9	4.44209	0.10845	-0.28111
10	4.90450		

Displacement Sensor Calibration Report
LORD MicroStrain®

Date: 4/16/2015

Sensor Model: 6120-0000
Sensor Serial Number: 44246

Signal Conditioner Model: 6130-0010
Signal Conditioner Serial Number: 42625

Polynomial Fit

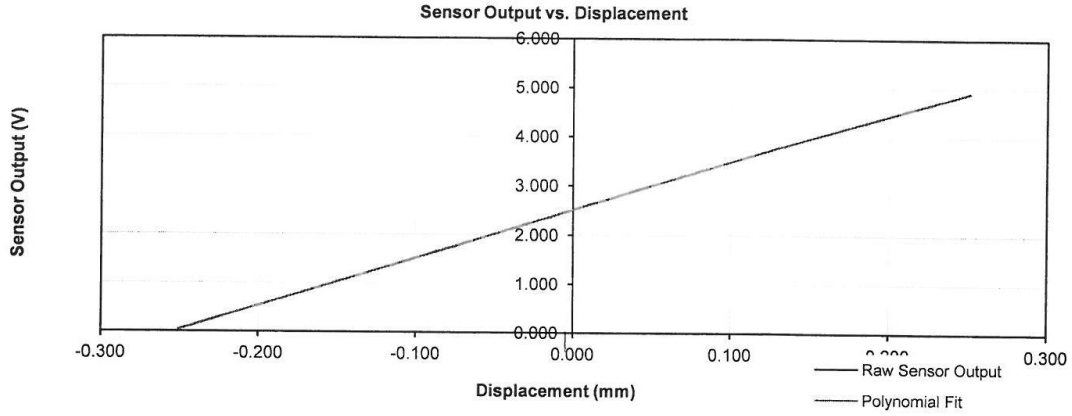

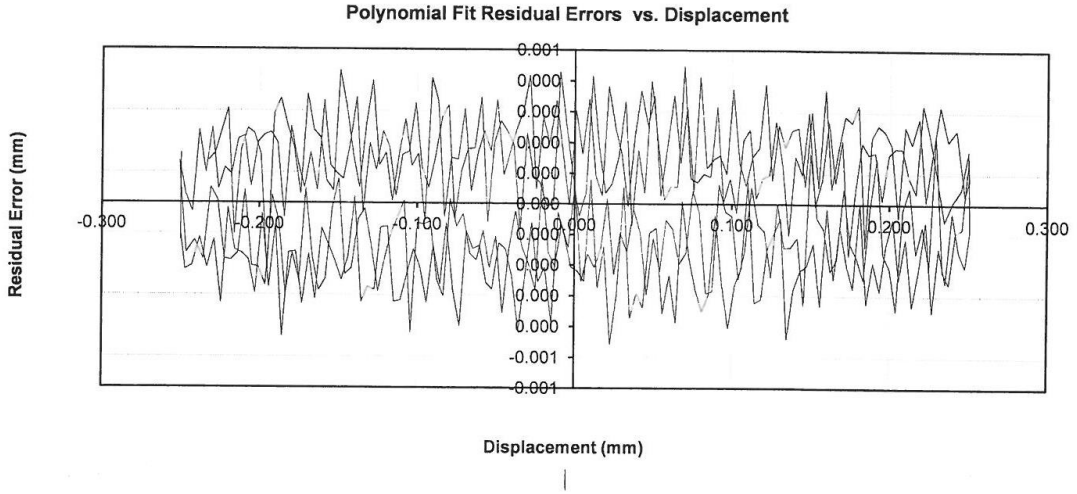

Polynomial Fit Model

$D = A0 + A1*x + A2*x^2 + A3*x^3 + \ldots$

where D = Displacement (mm)
Ai = ith order Polynomial Coefficient
x = Sensor Output (V)

Polynomial Fit Results

Coefficient	Value
A0	-2.55110E-01
A1	1.03629E-01
A2	-3.65864E-03
A3	3.17884E-03
A4	-1.60274E-03
A5	4.48693E-04
A6	-6.26209E-05
A7	3.46283E-06

A.4. Calibration certificate for force sensor

50224

Dytran Instruments, Inc.
21592 Marilla St. Chatsworth, CA 91311 Ph: 818-700-7818 Fax 818-700-7880
www.dytran.com email: info@dytran.com

ACCREDITED

CALIBRATION CERTIFICATE
LIVM DYNAMIC FORCE SENSOR

CUSTOMER:	TECHNI-MEASURE LTD.			TEST REPORT #:	419
PURCHASE ORDER #:	P/4157	SALES ORDER #:	171731	PROCEDURE:	TP-1003
MODEL:	1053V2	SERIAL #:	419	RANGE, F.S. (LbF):	50
NEW UNIT	X	RE-CALIBRATION [1]		AS RECEIVED CODE	AS RETURNED CODE
TEMPERATURE (°C):	24			HUMIDITY (%):	42
SENSITIVITY (mV/LbF) [2]:	102.40	BIAS VOLTAGE (VDC):	8.80	DISCHARGE T.C. (sec):	100
REMARKS: NONE					

TEST EQUIPMENT LIST - CALIBRATION STATION # 11

DII #	MANUFACTURER	MODEL	SERIAL #	DESCRIPTION	CAL DATE	DUE DATE
1439	FLUKE	8808A	1776012	MULTIMETER	11/18/14	11/18/15
1376	NICOLET	310	IAQ9306620	DIGITAL OSCILLOSCOPE	09/24/14	09/24/15
063	MOREHOUSE	500LBF	D-6974	RING DYNAMOMETER	01/22/15	01/22/16

[1] AS RECEIVED / AS RETURNED CODES:
1 = IN TOLERANCE, NO ADJUSTMENTS
2 = IN TOLERANCE, BUT ADJUSTED
3 = OUT OF TOLERANCE < 5%
4 = OUT OF TOLERANCE > 5%
5 = REPAIR REQUIRED
6 = REPAIRED AND CALIBRATED
7 = UNIT NON-REPAIRABLE, RECOMMEND REPLACEMENT
8 = UNIT SERVICEABLE WITH CURRENT CALIBRATION DATA

THIS CALIBRATION IS TRACEABLE TO THE NIST THROUGH TEST REPORT # D6974D2006 PER MIL-STD-45662A, ANSI/NCSL Z540-1-1994, , ISO 1002-1.
ESTIMATED UNCERTAINTY OF CALIBRATION: 0.67%.

CALIBRATION TECHNICIAN: PHAT TRAN (6 CAL) TEST DATE : 04/17/15
RECOMMENDED RECALL DATE : 04/17/16

50224

Dytran Instruments, Inc.
21592 Marilla St. Chatsworth, CA 91311 Ph: 818-700-7818 Fax 818-700-7880
www.dytran.com email: info@dytran.com

ACCREDITED
Calibration Laboratory
CERT #2472.01

CALIBRATION CERTIFICATE
UNITY GAIN CURRENT SOURCE POWER UNIT

CUSTOMER:	*TECHNI-MEASURE LTD.*				**TEST REPORT #:**	*3077*	
PURCHASE ORDER #:	*P/4157*		**SALES ORDER #:**	*171731*	**PROCEDURE:**	*TP4005*	
MODEL:	*4102C*		**SERIAL #:**	*3077*			
BATTERY POWERED	X	**LINE POWERED**		**115VAC**		**230VAC**	
NEW UNIT	X	**RE-CALIBRATION [1]**		**AS RECEIVED CODE**		**AS RETURNED CODE**	
TEMPERATURE (°C):	*24*				**HUMIDITY (%):**	*40*	

CALIBRATION DATA

POWER SUPPLY VOLTAGE (VDC):		**BATTERY VOLTAGE (VDC):**	*18.6*
METER ZERO	X	**METER CALIBRATION**	X

SENSOR DRIVE CURRENT (mA)

CH 1	CH 2	CH 3	CH 4	CH 5	CH 6	CH 7	CH 8
1.60							
CH 9	**CH 10**	**CH 11**	**CH 12**	**CH 13**	**CH 14**	**CH 15**	**CH 16**

AS RECEIVED DATA

GENERAL CONDITION:			
POWER SUPPLY VOLTAGE (VDC):		**BATTERY VOLTAGE (VDC):**	
METER CALIBRATION		**REPLACED BATTERIES**	**YES** / **NO**

SENSOR DRIVE CURRENT (mA)

CH 1	CH 2	CH 3	CH 4	CH 5	CH 6	CH 7	CH 8
CH 9	**CH 10**	**CH 11**	**CH 12**	**CH 13**	**CH 14**	**CH 15**	**CH 16**

NOTES:

TEST EQUIPMENT LIST - CALIBRATION STATION # 6

DII #	MANUFACTURER	MODEL	SERIAL #	DESCRIPTION	CAL DATE	DUE DATE
911	*KENWOOD*	*CS-5230*	*8020007*	*OSCILLOSCOPE*	*09/24/14*	*09/24/15*
285	*FLUKE*	*45*	*7000003*	*DUAL DISPLAY MULTIMETER*	*09/24/14*	*09/24/15*

[1] AS RECEIVED / AS RETURNED CODES:

1 = IN TOLERANCE, NO ADJUSTMENTS
2 = IN TOLERANCE, BUT ADJUSTED
3= OUT OF TOLERANCE
4 = REPAIR RECOMMENDED
5 = REPAIRED AND CALIBRATED
6 = NON-REPAIRABLE, REPLACEMENT RECOMMENDED

THIS CALIBRATION WAS PERFORMED IN ACCORDANCE WITH MIL-STD-45662A, ANSI/NCSL Z540-1-1994, ISO 10012-1
AND IS TRACEABLE TO THE NIST (NATIONAL INSTITUTE OF STANDARDS AND TECHNOLOGY).
THIS CERTIFICATE SHALL NOT BE REPRODUCED EXCEPT IN FULL, WITHOUT THE WRITTEN PERMISSION FROM DYTRAN INSTRUMENTS, INC.

CALIBRATION TECHNICIAN: *DAVID NUTE* 1 CAL

TEST DATE : *04/17/15*

RECOMMENDED RECALL DATE : *04/17/16*

A.5. Operational procedure

1. Insert specimen into the collet and the upper and lower specimen holders. Make sure **NOT** to twist the actuator while opening/closing the collet.
2. Apply the normal load via the dead weight holder. Tighten the bolt on the slip guide to tighten the weights in place.
3. Power on (i) actuator rack (at wall, back of rack and also the 2 switches on the front of the rack), (ii) force sensor (at the wall and on the data conditioning unit) and (iii) DVRT (at the wall) 20 minutes prior to testing.
4. On the PC Desktop, open "HDPM45v16", "Data Acquisition" and "DVRT Locator" VI programs.

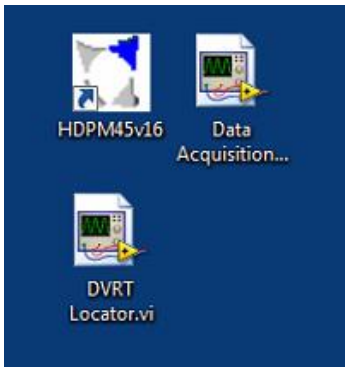

Figure A.1. Programs on PC desktop for control of fretting rig.

5. Using the "DVRT Locator", insert the DVRT in the DVRT holder and slowly push it inwards until the signal is approximately 2.5 V. Stop the program once the signal from the DVRT has been found.
6. On the "HDPM45v16" VI, wait for a signal from the actuator ("**Running**").
7. Choose "External" command.
8. Adjust the voltage amplitude to adjust the stroke amplitude of the actuator (for max stroke use -20 and 150 V).
9. Adjust the PID parameters in the open loop option (P = 1, I = 1000, D = 0).
10. Change to closed loop operation by clicking the "OL/CL" button.

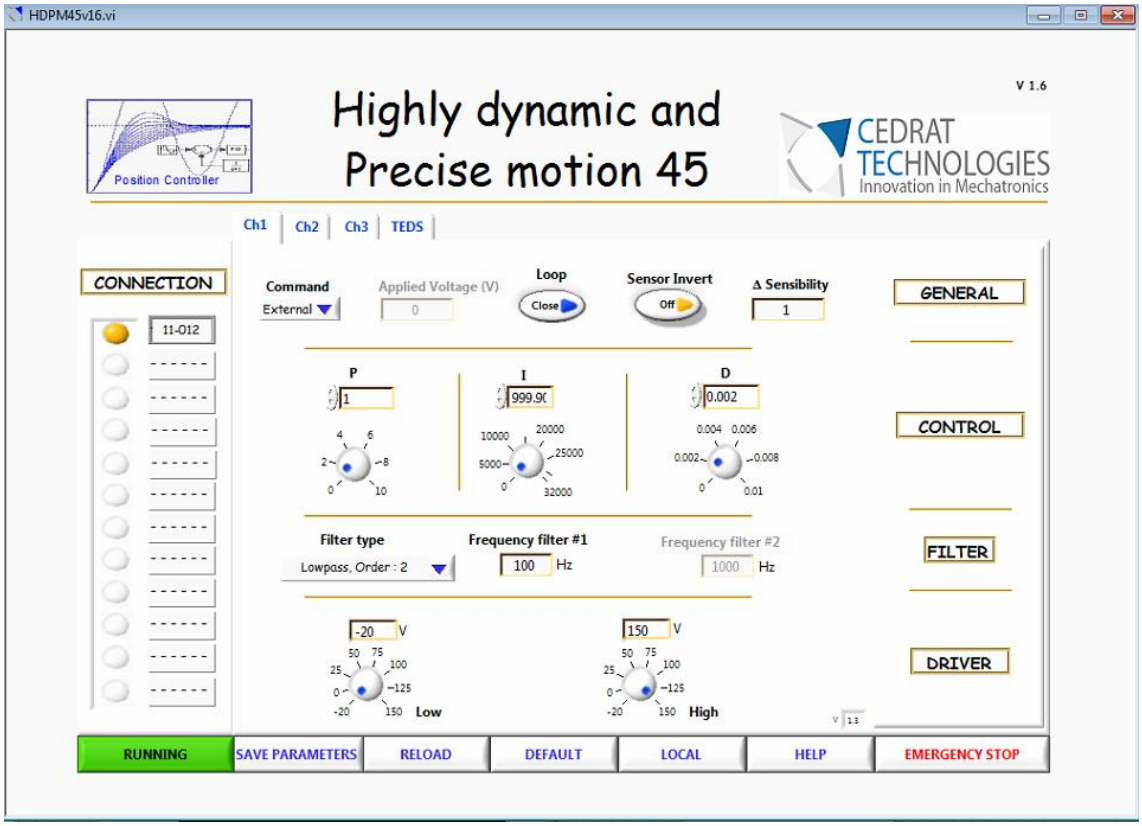

Figure A.2. HDPM45v16 set up for running fretting rig.

11. In the "Data Acquisition" VI choose the voltage amplitude, offset, number of cycles, sampling information and file path. Note that frequency can be calculated using the information on the VI.

12. Click Run.

13. Stop the data logging after desired number of cycles has been reached.

Troubleshooting – see page 29 and 30 of UC45 manual

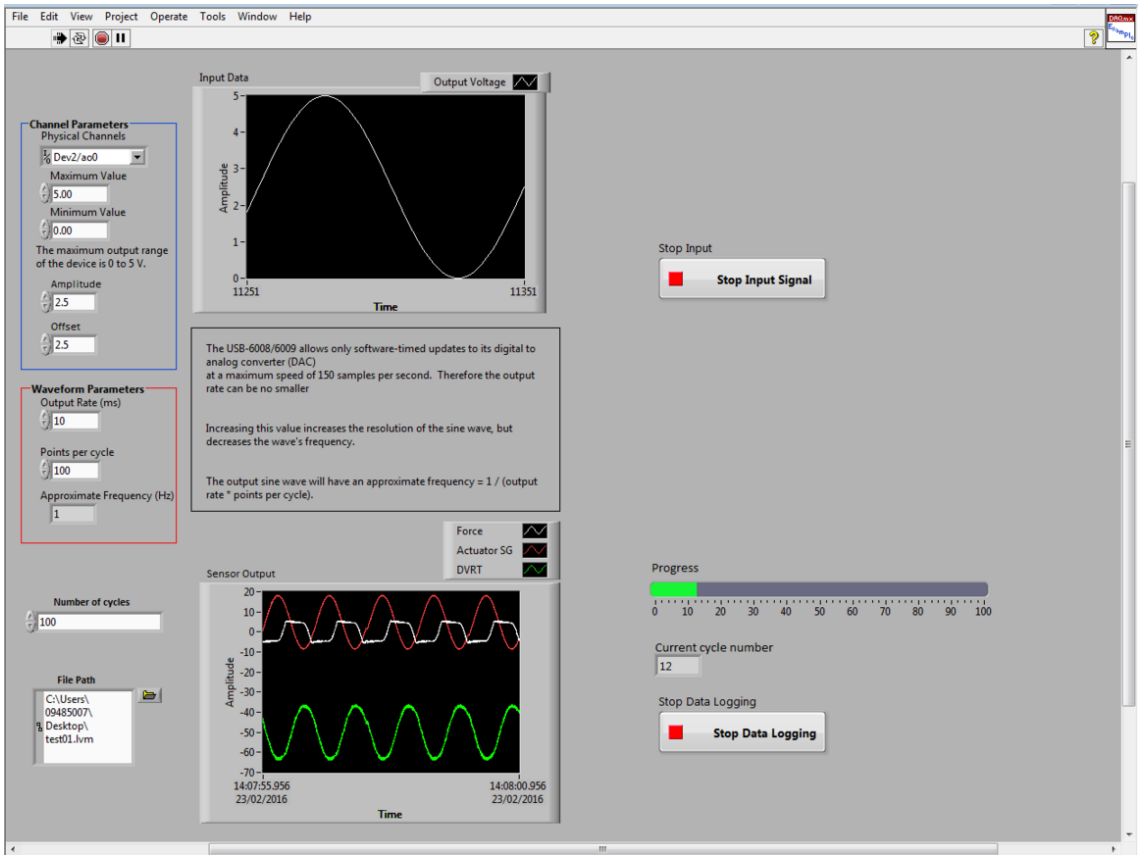

Figure A.3. Data acquisition program for running fretting rig.

Appendix B: Riser dissection procedure

B.1. Overview

In this appendix, the dissection procedure for the pre-service riser section at NUI Galway is outlined. Since the health and safety of technicians is paramount, there is emphases on this throughout the procedure, including safety reminders throughout the procedure section. Photographs of the dissected riser at various stages of the dissection process are also provided.

B.1. Health and Safety

- When performing the riser dissection, personnel must wear correct PPE, including full face visor, safety goggles, a mask, suitable gloves and hearing protection. All clothes must be resistant to sparks.
- Whenever performing cutting operation of metallic material layer, the operator of the cutting grinder must wear a full-face visor, safety goggles, a mask, suitable gloves and hearing protection; also all clothing must be rated for resistance to sparks. The angle grinder **must** be operated using both handles (at 90^{o} to each other) to avoid "kick back".
- Although the pipe to be dissected has not been in use, it may have gone through manufacture safety testing; therefore, there may be pressurised water present between layers.
- Each layer must be restrained using straps as dictated in this report prior to cutting.

- A “buddy” system shall be used, and the “buddy” of the operator shall observe and standby for assistance where and when required.
- Fire extinguishers shall be on standby during all metallic cutting stages.
- Before the start of every new layer cut a hold will be put on cutting to just briefly run over what will be done for the cutting of the next layer to make sure everyone is clear – a bit like a “tool box talk”.

B.2. Procedure

B.2.1. General

Photographs and measurements are to be taken prior to the removal of each layer. Any defects are to be noted and photographed in detail. Also, photographs of layer cross-sections shall be taken. Measurements of layer geometry cross-sections and lay angles will be taken.

Due to the inherent nature of the flexible cross-section and manufacturing, that there is residual energy in the pipe layers that add to the risk of the dissection operation.

It is proposed to dissect section in the middle of a 4m long flexible pipe (see Fig. 2).

Weld end fittings to each end of the pipe, attach a bar to each end fitting. This will be used to rotate the pipe evenly from both ends during the cutting procedure.

The riser is to be placed on sets of rollers and strapped in place using Rachet Straps.

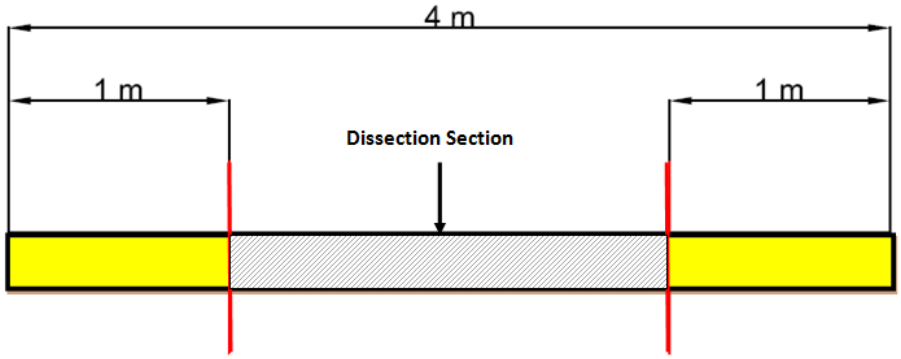

Figure B.1. Proposed dissection area of the pipe.

Mark out the external sheath for the cutting process; transverse lines to mark the ends of the cutting zone and longitudinal lines to mark the rotated. These should be used as a reference with the relative 0, 90, etc. degree markings. These markings shall be transferred down through the layers during the dissection.

B.2.2. External Sheath

Thickness: 7 mm, Material: Polymer

To be cut using a hand-saw or a hack-saw. Make a full circumferential cut at each transverse line followed by one longitudinal cut (two 90^{o} apart if necessary) to remove the external sheath.

B.2.3. High Strength Tape

Thickness: 1.8 mm, Material: Polymer

Remove tape using a knife.

Mark out the cutting zone on the second armour layer; transverse lines to mark the ends of the cutting zone and longitudinal lines to mark the rotated angle.

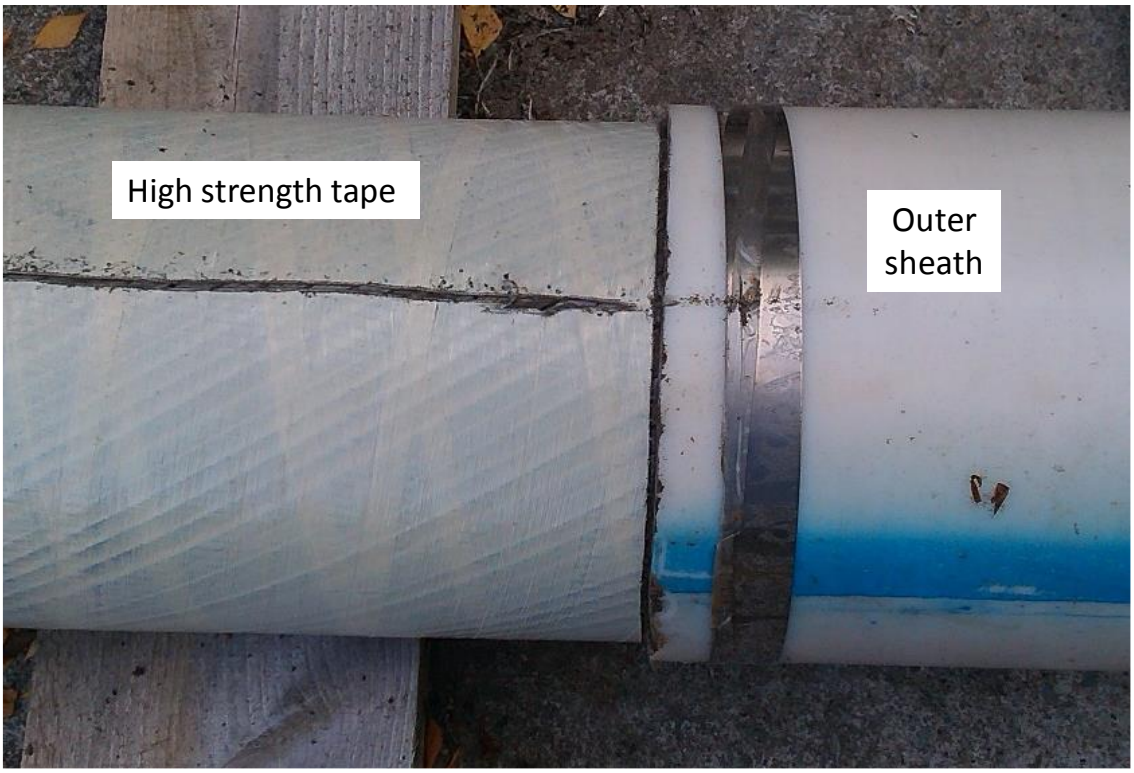

Figure B.1. Stages 1 and 2 of the riser dissection: removal of outer sheath and high strength tape.

B.2.4. Second Armour Layer

Thickness: 4 mm, Material: Metallic

Safety Reminder: Whenever performing cutting operation of metallic material layer, the operator of the cutting grinder must wear a full face visor, safety goggles, a mask, suitable gloves and hearing protection; also all clothing must be rated for resistance to sparks. The angle grinder **must** be operated using both handles (at 90^{o} to each other) to avoid “kick back”.

Hydraulic jacks may need to be used to stop sagging of the pipe along the middle section.

Apply 2-off steel (`BAND-IT` type) straps, one over the outer tensile armour layer, the other over the external sheath, approximately 50 mm in from each end of the exposed sample. Also apply 2-4 rachet straps inside the cut zone approximately equal distances apart.

These straps must be positioned perpendicular to longitudinal axis of the pipe whenever they are applied.

Number each wire either side of an intended cut point, circumferentially, e.g. starting from 0°.

Cut 5 adjacent wires of this layer with the angle grinder, at each end of the exposed/dissection sample. Keep the straps on the outer sheath tight at all times; loosen the straps on the armour layer (rachet straps first followed by steel straps) **slowly** whilst observing any movement / stored energy release. Tape the bundle of 5 wires together for the sake of housekeeping. Apply banding to the cut section of the pipe and continue to remove 5 wires at-a-time in the same way as outlined above.

It may be observed during or after this operation that the pipe twists somewhat, as a torsional imbalance may develop upon removal of one of the two helically wound tensile armour layers.

Hence it should be ensured that the pipe specimen is supported on rollers and free to rotate during the course of the dissection.

This step should be reviewed constantly during the dissection process, and if need be, the ends of the pipe should be strapped down so the pipe does not tip over when the weight of the middle section is removed.

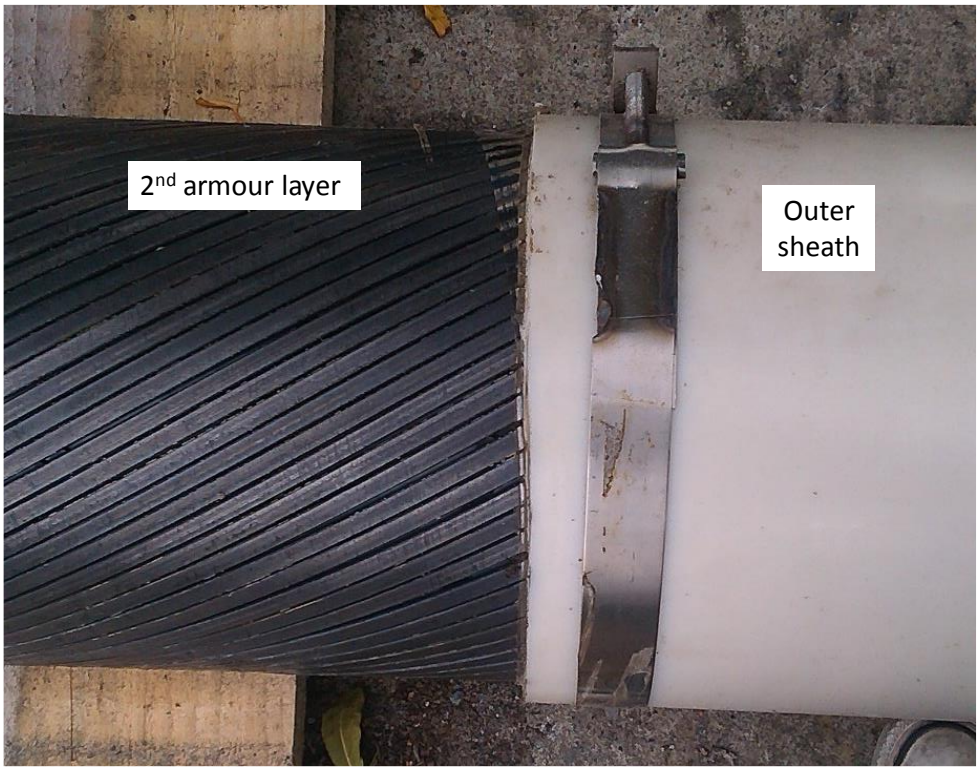

Figure B.2. Prior to stage 3 of the riser dissection, shown is second armour layer.

B.2.5. Anti-Wear Tape

Thickness: 1.5 mm, Material: Polymer

Remove tape using a knife.

Mark out the cutting zone on the first armour layer; transverse lines to mark the ends of the cutting zone and longitudinal lines to mark the rotated angle (as shown in Fig. 3).

B.2.6. First Armour Layer

Thickness: 4 mm, Material: Metallic

Safety Reminder: Whenever performing cutting operation of metallic material layer, the operator of the cutting grinder must wear a full face visor, safety goggles, a mask, suitable gloves and hearing protection; also all clothing must be rated for resistance to sparks. The angle grinder **must** be operated using both handles (at 90^{o} to each other) so as to avoid "kick back".

Apply 2-off steel (`BAND-IT` type) straps, one over the outer tensile armour layer, the other over the external sheath, approximately 50 mm in from each end of the exposed sample. Also apply 2-4 rachet straps inside the cut zone approximately equal distances apart.

These straps must be positioned perpendicular to longitudinal axis of the pipe whenever they are applied.

Number each wire either side of an intended cut point, circumferentially, e.g. starting from 0°.

Cut 5 adjacent wires of this layer with the angle grinder, at each end of the exposed/dissection sample. Keep the straps on the outer sheath tight at all times; loosen the straps on the armour layer (rachet straps first followed by steel straps) **slowly** whilst observing any movement / stored energy release. Tape the bundle of 5 wires together for the sake of housekeeping. Re-tighten the banding and continue to remove 5 wires at-a-time in the same way as outlined above.

It may be observed during or after this operation that the pipe twists somewhat, as a torsional imbalance may develop upon removal of one of the two helically wound

tensile armour layers. Hence it should be ensured that the pipe specimen is supported on rollers and free to rotate during the course of the dissection.

This step should be reviewed constantly during the dissection process, and if need be, the ends of the pipe should be strapped down so the pipe does not tip over when the weight of the middle section is removed.

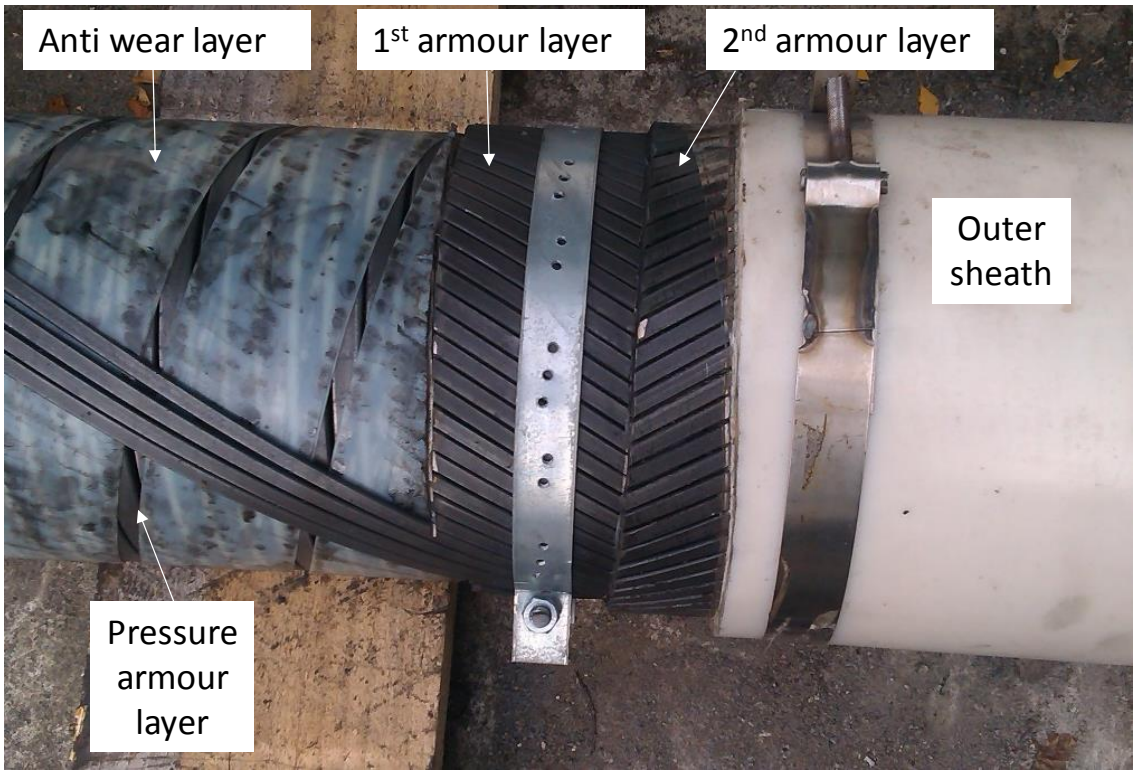

Figure B.3. Stage 5 of the riser dissection: removal of first armour layer.

B.2.7. Anti-Wear Tape

Thickness: 1.5 mm, Material: Polymer

Remove tape using a knife.

Mark out the cutting zone on the pressure armour layer; transverse lines to mark the ends of the cutting zone and longitudinal lines to mark the rotated angle (as shown Fig. 3).

B.2.8. Pressure Armour Zeta Wire

Thickness: 10 mm, Material: Metallic

Apply 2-off steel (`BAND-IT` type) straps at either end of the exposed sample, with each pair of steel bands side-by-side. Take care to ensure that banding is positioned perpendicular to longitudinal axis of the pipe whenever applied.

Apply high tensile strength adhesive tape (duct tape) around the exposed pressure armour layer; in the direction that the pressure armour is wound; leaving a 1m long `tail`/spare of free tape at the end from which the tape application stops.

Apply a further 2-off steel straps at both ends, and on top of the newly applied tape wraps, with each pair of steel straps butted side-by-side but with a 10mm gap between the neighbouring pair of straps (applied at the start). Take care to ensure that banding is positioned perpendicular to the longitudinal axis of the pipe whenever applied.

Also apply rachet straps along between the two cutting lines.

Hydraulic jacks will be used to stop sagging of the pipe in the middle, also to enable the safe removal of the inner section of the pipe. The ends of the pipe should also be strapped down so the pipe does not tip over when the weight of the middle section is removed.

Cut with an angle grinder, following the line, to make a full circumferential cut through the pressure armour layer, pressure sheath and interlocked carcass, at each end of the exposed pipe sample.

Prepare to loosen and remove only one pair of steel straps at each end, i.e. those which are inside of the circumferential cut of the pressure armour layer:

Whilst observing any movement / stored energy release, slowly release the two straps, one at a time, at the end with the tape tail.

Repeat for the other end.

Prepare to remove the tape windings and release the pressure armour in a controlled manner. Holding the end of the tape tail, slowly unwind the tape wraps from a safe distance. The pressure armour layer should begin to release from interlock as the restraint of the tape is removed. If the pressure armour does not release, use a soft, non-metallic hammer to gently tap the exposed interlocked layer until it releases.

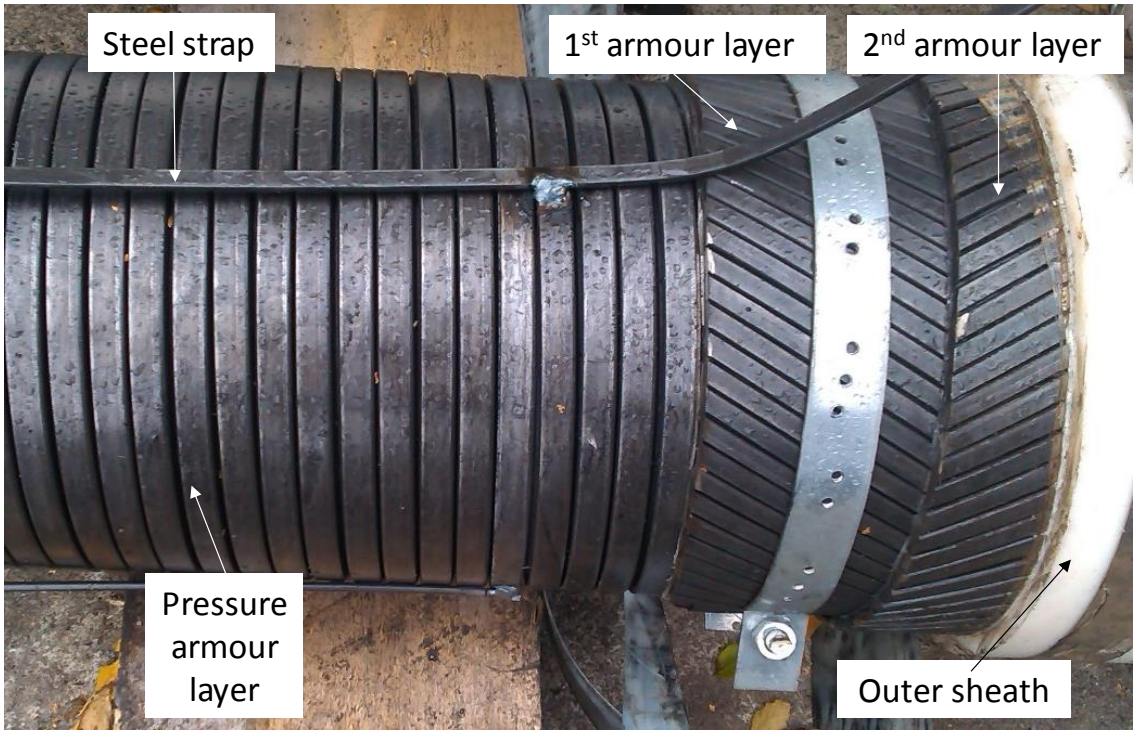

Figure B.4. Prior to stage 7 of the riser dissection, shown is the pressure armour layer.

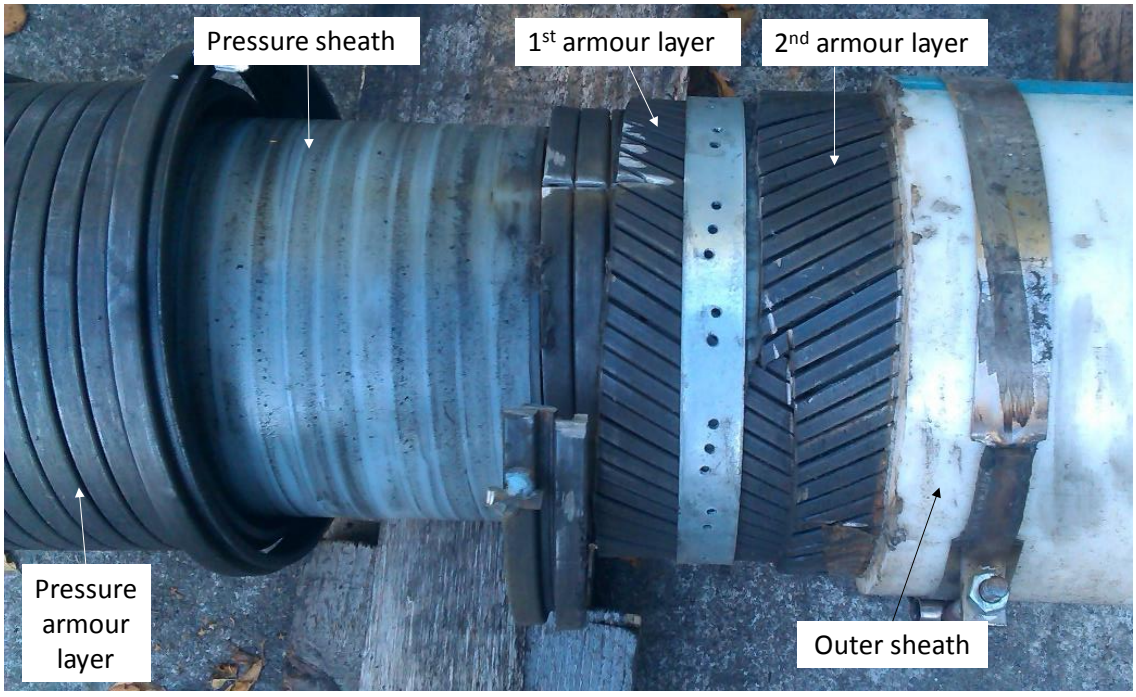

Figure B.5. Stage 7 of the riser dissection: removal of pressure armour layer.

Figure B.6. Pressure armour wire.

Figure B.7. Ex-service riser sections.

Appendix C: Global riser analysis results

C.1. Overview

In this appendix, results from global riser analysis described in Chapter 7 are presented. Global riser curvature envelopes are presented for 6 inch, 9 inch and 11 inch risers for each load case (6). Minimum and maximum nub-groove contact displacements are then presented, based on the minimum and maximum changes in riser curvatures.

C.2. Global riser curvature envelopes

Figures C.1 to C.3 present global riser curvature envelopes are presented for 6 inch, 9 inch and 11 inch risers for six load-cases.

C.3. Local nub-groove contact displacements

Tables C.1 to C.3 present minimum and maximum nub-groove contact displacements are then presented, based on the minimum and maximum changes in riser curvatures.

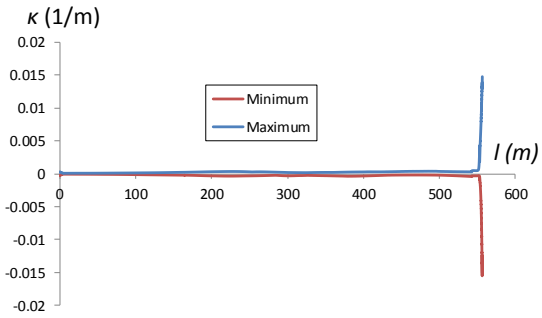

Load case 1

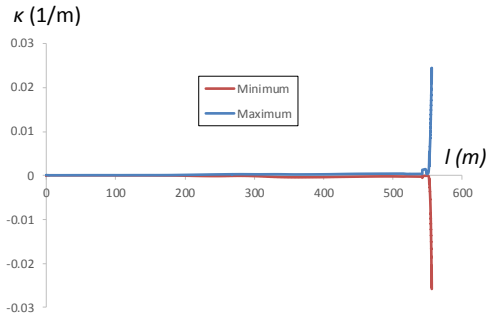

Load case 2

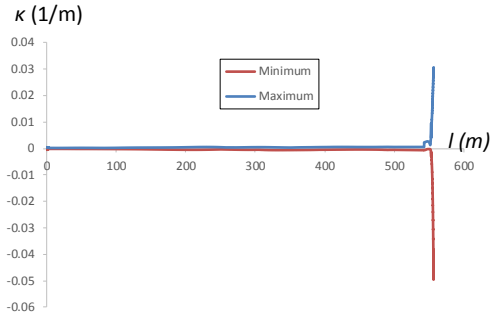

Load case 3

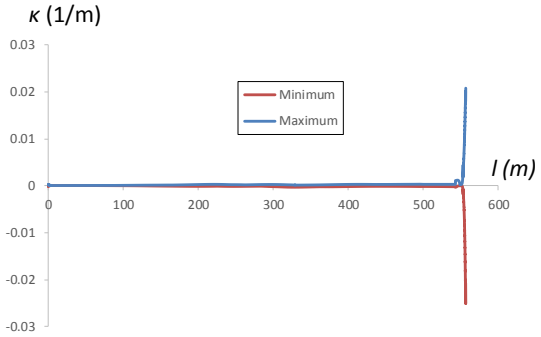

Load case 4

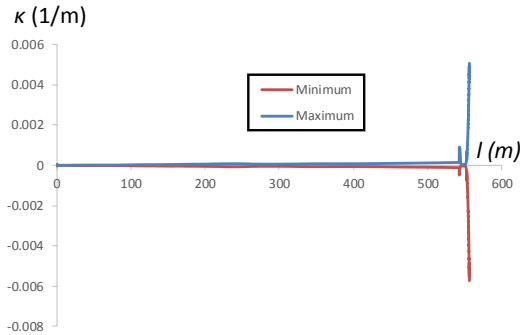

Load case 5

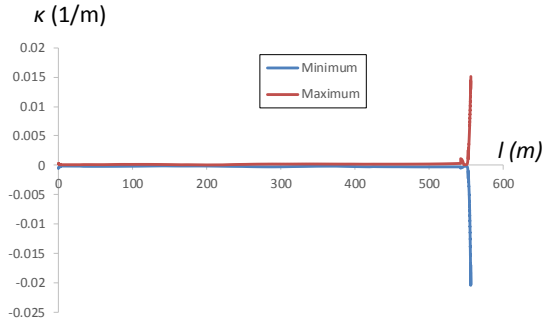

Load case 6

Figure C.1. Riser curvature envelopes for 6 inch.

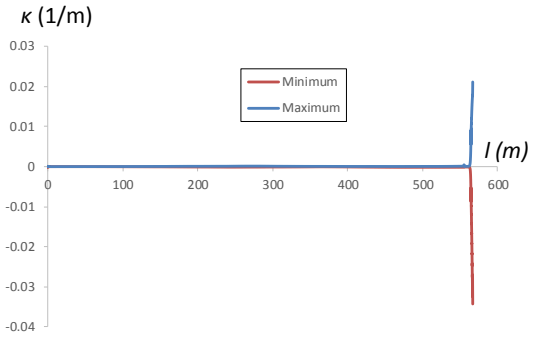

Load case 1

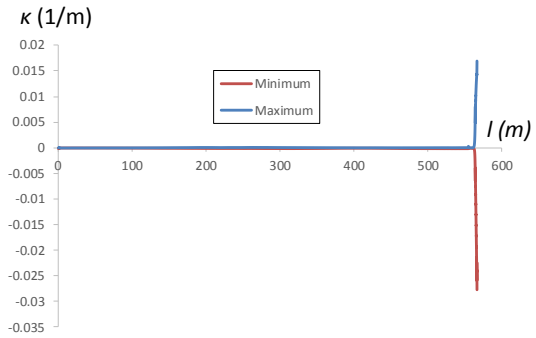

Load case 2

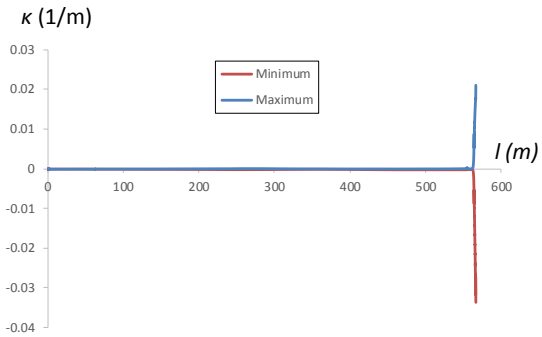

Load case 3

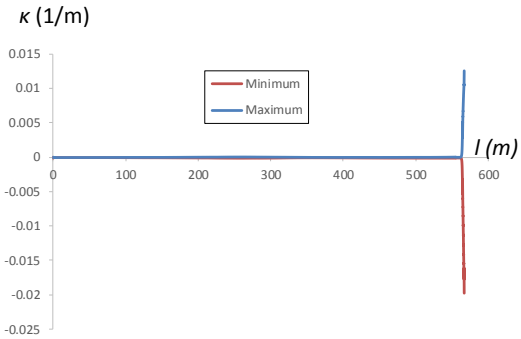

Load case 4

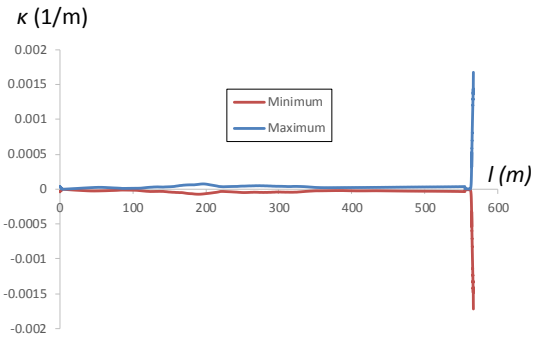

Load case 5

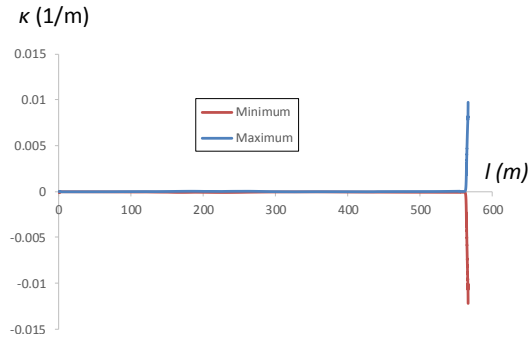

Load case 6

Figure C.2. Riser curvature envelopes for 9 inch.

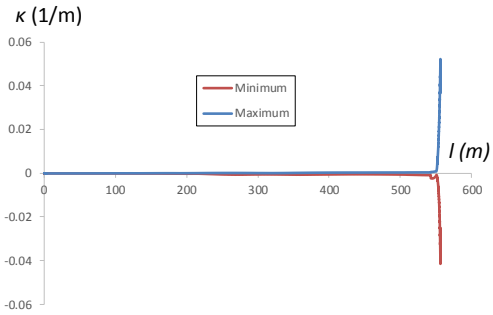

Load case 1

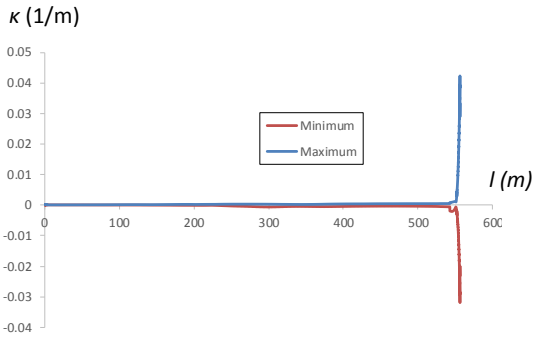

Load case 2

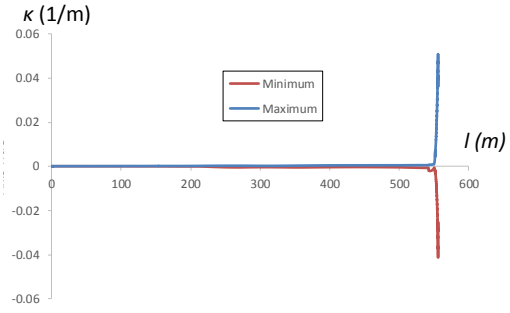

Load case 3

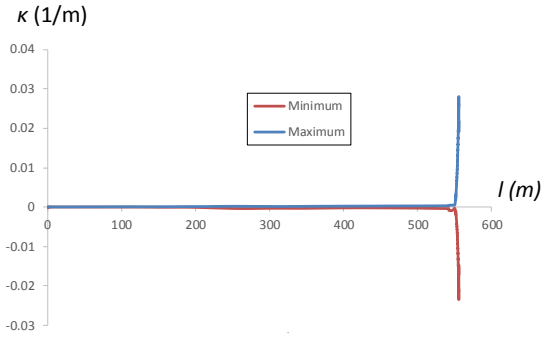

Load case 4

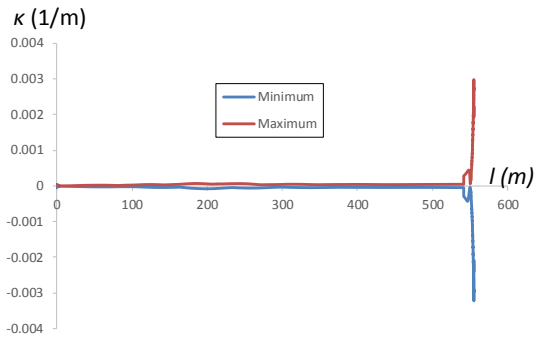

Load case 5

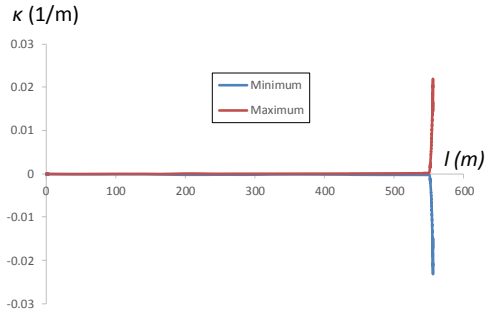

Load case 6

Figure C.3. Riser curvature envelopes for 11 inch.

Table C.1. Maximum and minimum $\Delta\kappa$ values for 6 inch riser and corresponding maximum and minimum nub-groove contact displacements.

Load case	$\Delta\kappa_{min}$ **(1/m)**	$\Delta\kappa_{max}$ **(1/m)**	δ_{min} **(μm)**	δ_{max} **(μm)**
1	1.22×10^{-5}	2.97×10^{-2}	$\sim 4 \times 10^{-3}$	22.8
2	8.79×10^{-6}	5.03×10^{-2}	$\sim 4 \times 10^{-3}$	45.4
3	1.02×10^{-4}	8.01×10^{-2}	$\sim 4 \times 10^{-3}$	78.1
4	2.97×10^{-5}	4.58×10^{-2}	$\sim 4 \times 10^{-3}$	40.5
5	5.49×10^{-6}	1.08×10^{-2}	$\sim 4 \times 10^{-3}$	2.1
6	1.44×10^{-4}	3.55×10^{-2}	$\sim 4 \times 10^{-3}$	29.2

Table C.2. Maximum and minimum $\Delta\kappa$ values for 9 inch riser and corresponding maximum and minimum nub-groove contact displacements.

Load case	$\Delta\kappa_{min}$ **(1/m)**	$\Delta\kappa_{max}$ **(1/m)**	δ_{max} **(μm)**	δ_{max} **(μm)**
1	4.29×10^{-6}	5.56×10^{-2}	$\sim 2 \times 10^{-3}$	83
2	4.94×10^{-6}	4.48×10^{-2}	$\sim 2 \times 10^{-3}$	65.1
3	4.6×10^{-6}	5.48×10^{-2}	$\sim 2 \times 10^{-3}$	81.9
4	3.34×10^{-6}	3.23×10^{-2}	$\sim 2 \times 10^{-3}$	44.6
5	7.08×10^{-6}	3.4×10^{-3}	$\sim 2 \times 10^{-3}$	3.3
6	4×10^{-5}	2.19×10^{-2}	$\sim 2 \times 10^{-3}$	27.2

Table C.3. Maximum and minimum $\Delta\kappa$ values for 11 inch riser and corresponding maximum and minimum nub-groove contact displacements.

Load case	$\Delta\kappa_{min}$ **(1/m)**	$\Delta\kappa_{max}$ **(1/m)**	δ_{max} **(µm)**	δ_{max} **(µm)**
1	1.06×10^{-5}	9.37×10^{-2}	$\sim 4 \times 10^{-4}$	192.1
2	1.06×10^{-5}	9.37×10^{-2}	$\sim 4 \times 10^{-4}$	192.1
3	9.66×10^{-6}	9.21×10^{-2}	$\sim 4 \times 10^{-4}$	188.7
4	9.75×10^{-6}	5.16×10^{-2}	$\sim 4 \times 10^{-4}$	101.8
5	7.8×10^{-6}	6.21×10^{-3}	$\sim 4 \times 10^{-4}$	4.4
6	7.48×10^{-6}	4.51×10^{-2}	$\sim 4 \times 10^{-4}$	87.8

C.2. Global riser axial force envelopes

Figures C.4 to C.6 present global riser axial force envelopes are presented for 6 inch, 9 inch and 11 inch risers for six load-cases.

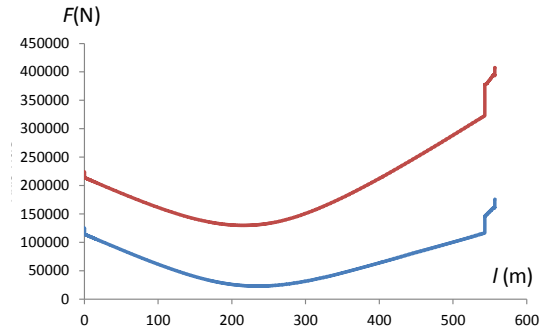

Load case 1

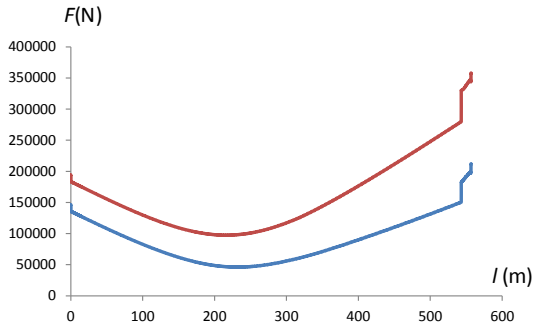

Load case 2

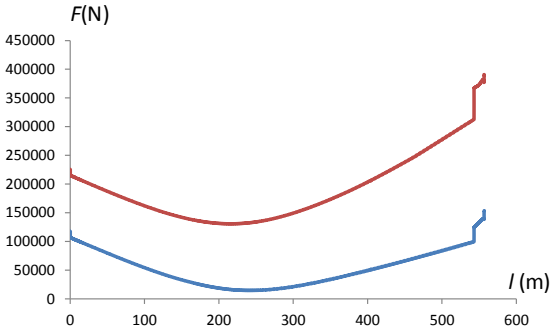

Load case 3

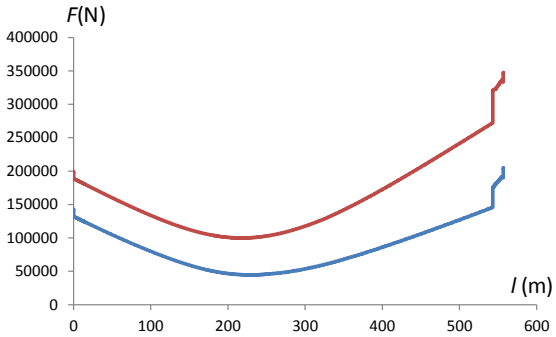

Load case 4

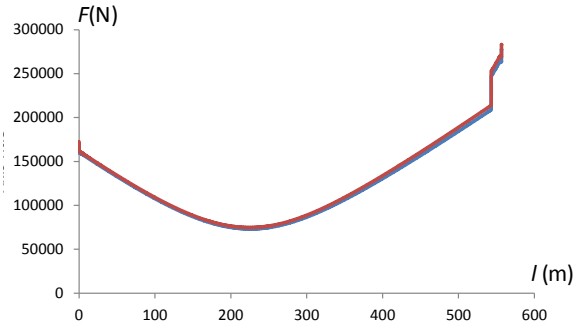

Load case 5

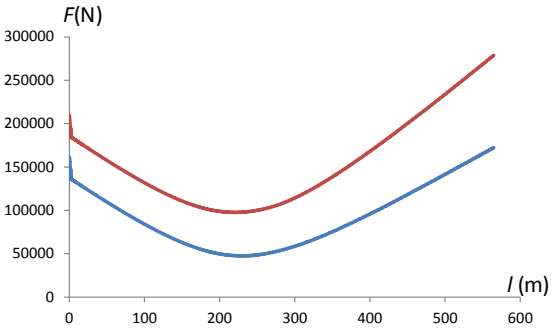

Load case 6

Figure C.4. Riser axial force envelopes for 6 inch.

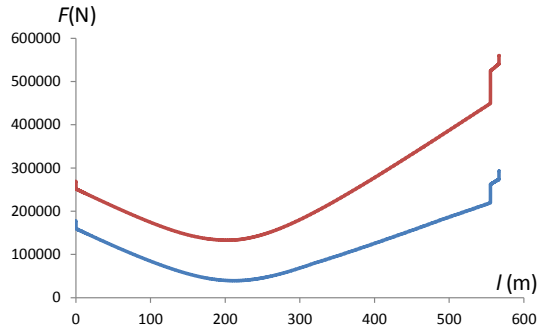

Load case 1

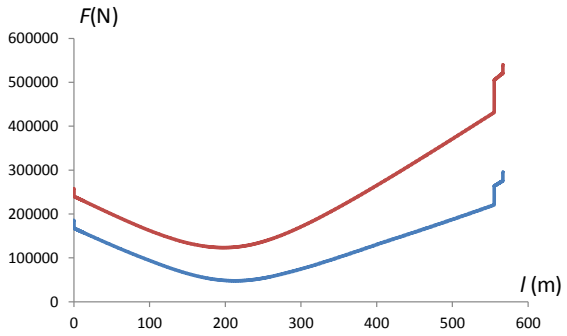

Load case 2

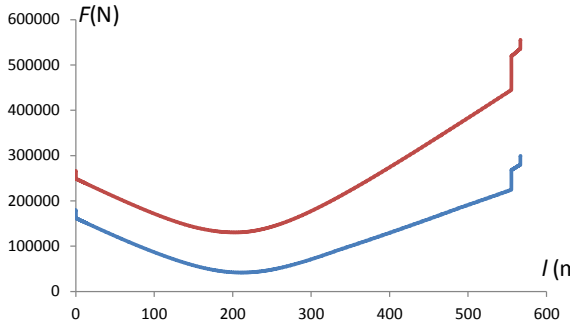

Load case 3

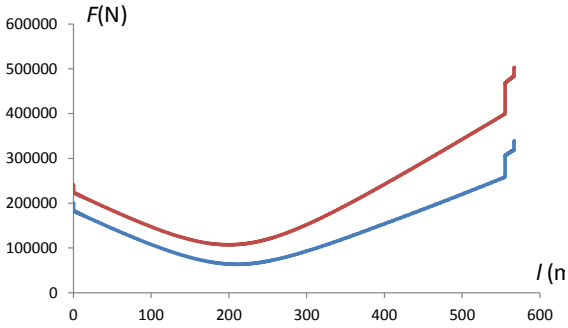

Load case 4

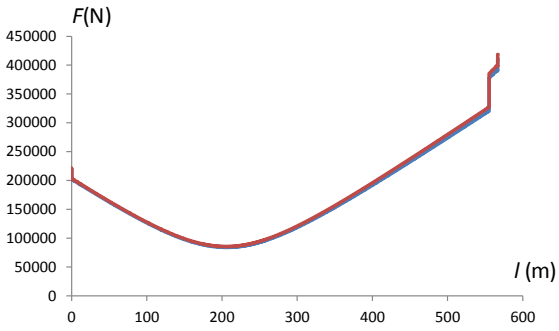

Load case 5

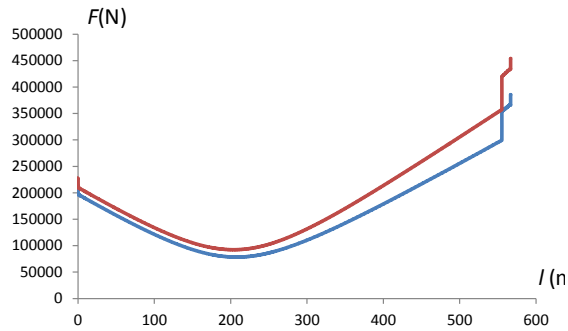

Load case 6

Figure C.5. Riser axial force envelopes for 9 inch.

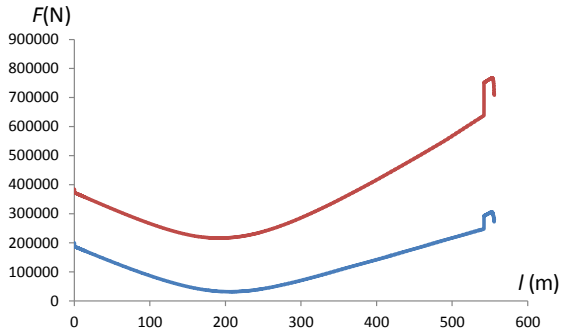

Load case 1

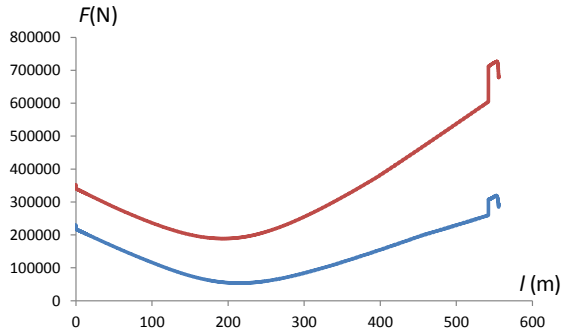

Load case 2

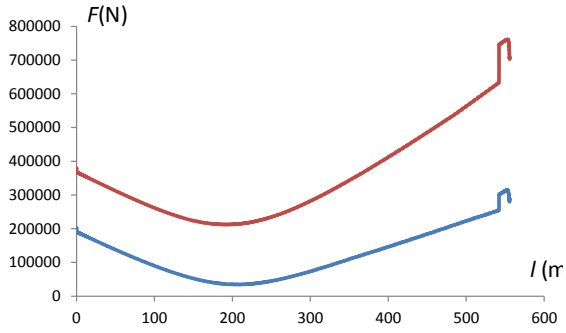

Load case 3

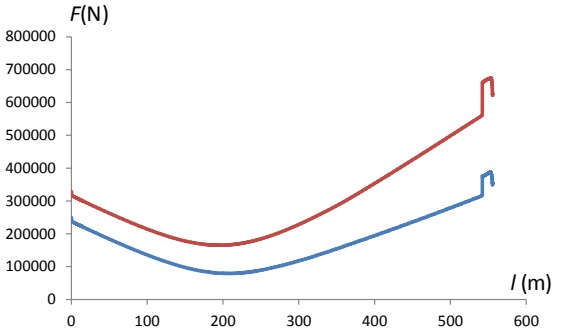

Load case 4

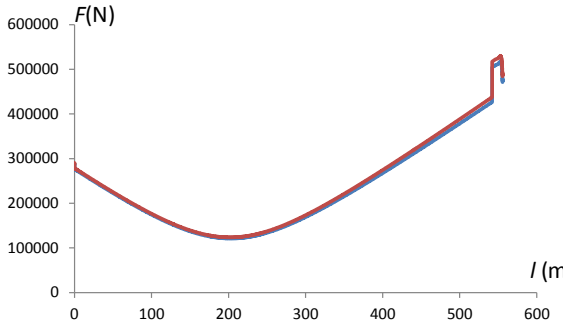

Load case 5

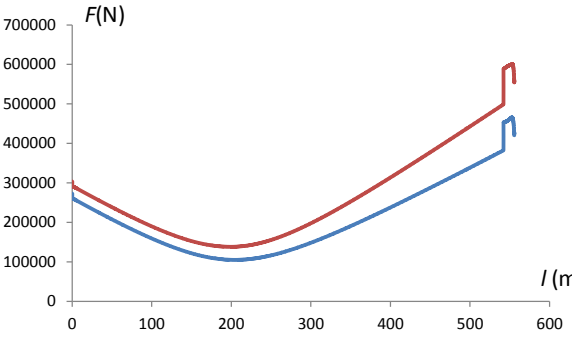

Load case 6

Figure C.6. Riser axial force envelopes for 11 inch.

APPENDIX D: Estimation of stress gradient redistribution due to wear

D.1. Overview

This appendix outlines the methodology used to estimate the Mode I and Mode II, $\Delta\sigma_{xx}$ and $\Delta\sigma_{xy}$ used to predict crack propagation under gross-slip conditions in Chapter 7. Wear induced redistribution of stresses are estimated for the work of Chapter 7 based on observations from finite element wear simulations described in Chapter 6.

D.2. Wear simulation results

Figures D.1 to D.2 show the effect of wear on Mode I and Mode II stress distributions below the contact surface for the fretting geometry described in Chapter 6. As fretting cycles increase, the effect of wear results in stresses below the contact surface reducing.

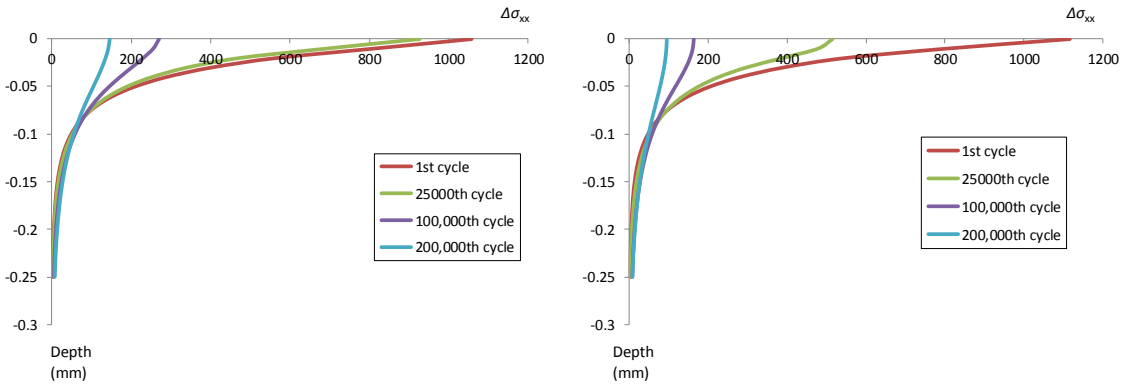

(a) (b)

Figure D.1. Mode I stress distributions Vs depth for wear simulated geometry described in Chapter 6 with applied displacements of (a) 4 μm and (b) 7 μm.

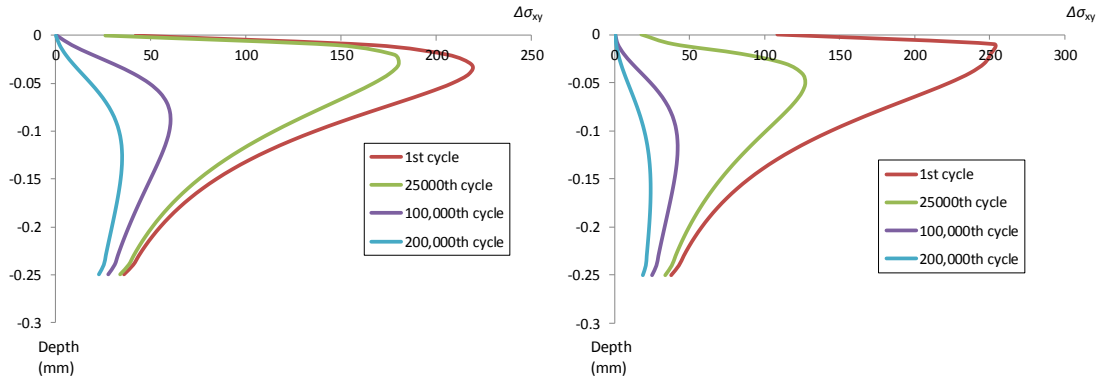

(a) (b)

Figure D.2. Mode II stress distributions Vs depth for wear simulated geometry described in Chapter 6 with applied displacements of (a) 4 μm and (b) 7 μm.

D.3. Estimation of stress distributions

An estimation of the stress distribution (after wear) below the contact surface was required to calculated crack propagation for GS cases in Chapter 7. It was importation not to under-predicted the stresses, as this would lead to an over-prediction of life. Stress estimations were made to fit to the 100,000th cycle stresses shown in Figures D.1 and D.2. Mode I crack propagation stresses were fitted using the following equation:

$$\Delta\sigma_{xx\,est}(z) = 2D_{fret}\Delta\sigma_{xx\,\max}\exp(16z) \tag{D.1}$$

where $\Delta\sigma_{xx\,est}$ is the estimated Mode I crack propagation stress distribution (vs depth below contact surface) for the 100,000th cycle; $\Delta\sigma_{xx\,\max}$ is the maximum $\Delta\sigma_{xx}$ value for 1st; z is the depth below the contact surface.

Figure D.3 shows a comparison between the estimated stress distribution and measured stress distribution (as shown in Figure D.1) for the 100,000th cycle of the wear simulation described in Chapter 6.

Mode I crack propagation stresses were assumed to be constant and found using the following equation:

$$\Delta\sigma_{xy\,est}(z) = 2D_{fret}\Delta\sigma_{xy\,\max} \tag{D.2}$$

where $\Delta\sigma_{xy\,est}$ is the estimated Mode II crack propagation stress distribution (vs depth below contact surface) for the 100,000th cycle and $\Delta\sigma_{xy\,\max}$ is the maximum $\Delta\sigma_{xx}$ value for 1st.

Figure D.4 shows a comparison between the estimated stress distribution and measured stress distribution (as shown in Figure D.2) for the 100,000th cycle of the wear simulation described in Chapter 6.

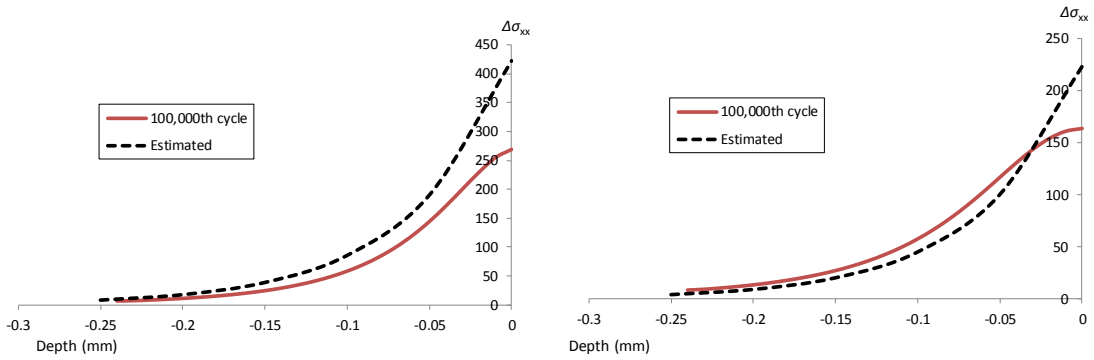

(a) (b)

Figure D.3. Mode I stress distributions Vs depth for wear simulated geometry described in Chapter 6 and estimated distribution for 100,000th cycle and applied displacements of (a) 4 μm and (b) 7 μm.

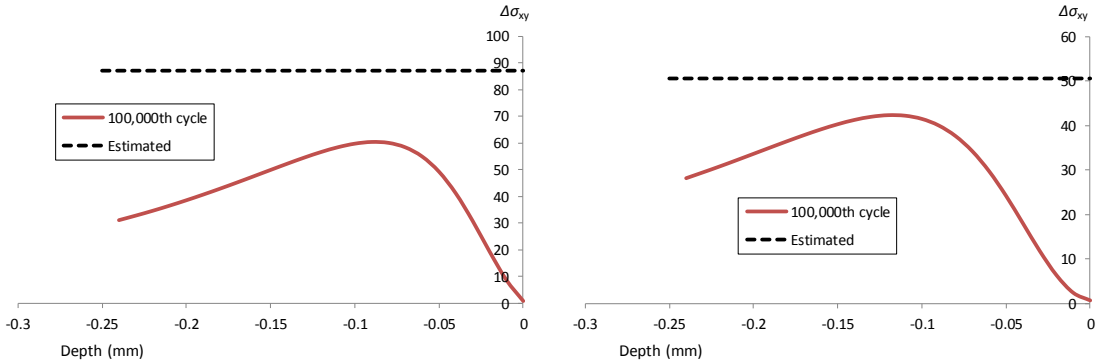

(a) (b)

Figure D.4. Mode II stress distributions Vs depth for wear simulated geometry described in Chapter 6 and estimated distribution for 100,000th cycle and applied displacements of (a) 4 μm and (b) 7 μm.

Bibliography

Aldham, D., Warburton, J., Pendlebury, R.E., 1985. The unlubricated fretting wear of mild steel in air. Wear 106, 177–201. doi:10.1016/0043-1648(85)90109-7

Antler, M., 1982. Fretting of electrical contacts Materials Evaluation Under Fretting Conditions, ASTM International. ASTM International. doi:10.1520/STP29397S

API, 2009. Recomended practices for flexible marine risers, 17J (Journal Article), American Petroleum Industry.

Araújo, J.A., Nowell, D., 2002. The effect of rapidly varying contact stress fields on fretting fatigue. Int. J. Fatigue 24, 763–775. doi:10.1016/S0142-1123(01)00191-8

Araújo, J.A., Nowell, D., Vivacqua, R.C., 2004. The use of multiaxial fatigue models to predict fretting fatigue life of components subjected to different contact stress fields. Fatigue Fract. Eng. Mater. Struct. 27, 967–978. doi:10.1111/j.1460-2695.2004.00820.x

Archard, J., 1953. Contact and rubbing of flate surfaces. J. Appl. Phys. 24, 981–988. doi:10.1063/1.1721448

Archard, J.F., Hirst, W., 1956. The wear of metals under unlubricated conditions. Proc. Roy. Soc. L. A236, 397–410. doi:10.1098/rspa.1956.0144

Ashton, P.J., Harte, A.M., Leen, S.B., 2017. Statistical grain size effects in fretting crack initiation. Tribol. Int. 108, 75–86. doi:10.1016/j.triboint.2016.09.022

ASTM, 2014. Standard terminology relating to fatigue and fracture testing. ASTM Int. doi:10.1520/E1823-13.2

ASTM E 606, 2010. Standard Practice for Strain-Controlled Fatigue Testing, ASTM International. doi:10.1520/E0606-04E01

ASTM International, 2014. ASTM F897-02, Standard test method for measuring fretting corrosion of osteosynthesis plates and screws. doi:10.1520/F0897-02R13.2

ASTM International, 2011. ASTM D7594-11 Standard test method for determining fretting wear resistance of lubricating greases under high Hertzian contact pressure using a high-frequency, linear-oscillation (SVR) test machine. doi:10.1520/D7594-11

ASTM International, 2010. ASTM D4170-10 Standard test method for fretting wear protection by lubricating greases. doi:10.1520/D4170-10

Bailey, J.M., Godfrey, D., Bailey, J.M., 1954. Coefficient of friction and damage to contact area during the early stages of fretting II - steel, iron, iron oxide and glass combinations. Cleveland, Ohio.

Barrett, R.A., O'Donoghue, P.E., Leen, S.B., 2013. An improved unified viscoplastic constitutive model for strain-rate sensitivity in high temperature fatigue. Int. J. Fatigue 48, 192–204. doi:10.1016/j.ijfatigue.2012.11.001

Barril, S., Debaud, N., Mischler, S., Landolt, D., 2002. A tribo-electrochemical apparatus for in vitro investigation of fretting-corrosion of metallic implant materials. Wear 252, 744–754. doi:10.1016/S0043-1648(02)00027-3

Basquin, O.H., 1910. The exponential law of endurance tests, in: Proceedings of the

American Society for Testing and Materials. pp. 625–630.

Berthier, Y., Colombié, C., Vincent, L., Godet, M., 1988. Fretting wear mechanisms and their effects on fretting fatigue. J. Tribol. 110, 517. doi:10.1115/1.3261663

Bhushan, B., Gupta, B.K., 1991. Handbook of tribology: Materials, coatings, and surface treatments, McGraw-Hill, New York, NY (United States).

Bill, R.C., 1983. Fretting wear and fretting fatigue - How are they related? J. Lubr. Technol. 105, 230–238. doi:10.1115/1.3254577

Blau, P., 1998. Glossary of terms. Frict. Lubr. wear Technol. ASM Handb. 18, 1–21.

BPGlobal, 2017. Statistical review of world energy.

Brown, M.W., Miller, K.J., 2006. A theory for fatigue failure under multiaxial stress–strain conditions. Arch. Proc. Inst. Mech. Eng. 1847-1982 (vols 1-196) 187, 745–755. doi:10.1243/PIME_PROC_1973_187_161_02

Budinski, K.G., 1982. Evaluation of Fretting Corrosion by Means of a New Device for the Control of Oscillation Amplitude. Mater. Eval. Under Frett. Cond. 780, 49–67. doi:10.1520/STP29396S

Burke, R.N., Witz, J.A., 1995. Fretting fatigue of flexible pipe pressure armour, in: Proceedings of the Third European Conference on Flexible Pipes, Unbilicals and Marine Cables - Materials Utilisation for Cyclic and Thermal Loading. Bentham Press.

Cattaneo, C., 1938. Sul contatto di due corpi elastici: distribuzione locale degli sforzi. Rend. Accad. Naz. Lincei 27, 342–348.

Ciavarella, M., Hills, D.A., Monno, G., 1998. The influence of rounded edges on

indentation by a flat punch. Proc. Inst. Mech. Eng. Part C J. Mech. Eng. Sci. 212, 319–327. doi:10.1243/0954406981521259

Ciavarella, M., Macina, G., 2003. New results for the fretting-induced stress concentration on Hertzian and flat rounded contacts. Int. J. Mech. Sci. 45, 449–467. doi:10.1016/s0020-7403(03)00061-4

Clarke, T., Jacques, R., Bisognin, A., Camerini, C., Damasceno, S., Strohaecker, T., 2011. Monitoring the structural integrity of a flexible riser during a full-scale fatigue test. Eng. Struct. 33, 1181–1186. doi:10.1016/j.engstruct.2010.12.039

Coffin, L.F., 1954. A study of the effects of cyclic thermal stress on a ductile metal. Trans. Am. Soc. Mech. Eng. 76, 931–950.

Colombié, C., Vincent, L., Godet, M., Berthier, Y., Floquet, A., 1984. Fretting: Load carrying capacity of wear debris. J. Tribol. 106, 194–201. doi:10.1115/1.3260881

Connaire, A., O'Brien, P., Harte, A.M., O'Connor, A., 2015. Advancements in subsea riser analysis using quasi-rotations and the Newton-Raphson method. Int. J. Non-Linear Mech. 70, 47–62. doi:10.1016/j.ijnonlinmec.2014.10.021

Conner, B.P., Nicholas, T., 2006. Using a dovetail fixture to study fretting fatigue and fretting palliatives. J. Eng. Mater. Technol. 128, 133. doi:10.1115/1.2172272

Coulomb, C.A., 1785. Théorie des machines simples, en ayant égard au frottement de leurs parties, et a la roideur des cordages, Memoires de Math. Phys. Acad. Sci. Bachelier, Paris.

Cruzado, A., Leen, S.B., Urchegui, M.A., Gómez, X., 2013. Finite element simulation of fretting wear and fatigue in thin steel wires. Int. J. Fatigue 55, 7–21.

doi:http://dx.doi.org/10.1016/j.ijfatigue.2013.04.025

Cruzado, a., Hartelt, M., Wäsche, R., Urchegui, M. a., Gómez, X., 2010. Fretting wear of thin steel wires. Part 1: Influence of contact pressure. Wear 268, 1409–1416. doi:10.1016/j.wear.2010.02.017

De Pauw, J., De Baets, P., De Waele, W., 2011. Review and classification of fretting fatigue test rigs. Sustain. Constr. Des. 2, 41.

de Sousa, J.R.., de Sousa, F.J.., Siqueira, M.Q. De, Sagrilo, L.V.., Campello, G., Vardaro, E., de Lemos, C.A.., 2012. Fatigue analysis of a 6" flexible pipe with broken tensile armour wires, in: ASME 2012 31st International Conference on Ocean, Offshore and Artic Engineering. Rio de Janeiro, Brazil, pp. 1–13. doi:10.1115/OMAE2012-83532

Del Llano-Vizcaya, L., Rubio-González, C., Mesmacque, G., Cervantes-Hernández, T., 2006. Multiaxial fatigue and failure analysis of helical compression springs. Eng. Fail. Anal. 13, 1303–1313. doi:10.1016/j.engfailanal.2005.10.011

Dimaki, A. V., Dmitriev, A.I., Chai, Y.S., Popov, V.L., 2014. Rapid simulation procedure for fretting wear on the basis of the method of dimensionality reduction. Int. J. Solids Struct. 51, 4215–4220. doi:10.1016/j.ijsolstr.2014.08.003

Ding, J., Bandak, G., Leen, S.B., Williams, E.J., Shipway, P.H., 2009. Experimental characterisation and numerical simulation of contact evolution effect on fretting crack nucleation for Ti-6Al-4V. Tribol. Int. 42, 1651–1662. doi:10.1016/j.triboint.2009.04.040

Ding, J., Houghton, D., Williams, E.J., Leen, S.B., 2011. Simple parameters to predict effect of surface damage on fretting fatigue. Int. J. Fatigue 33, 332–342.

doi:10.1016/j.ijfatigue.2010.09.008

Ding, J., Leen, S.B., McColl, I.R., 2004. The effect of slip regime on fretting wear-induced stress evolution. Int. J. Fatigue 26, 521–531. doi:10.1016/j.ijfatigue.2003.09.001

Ding, J., McColl, I.R., Leen, S.B., 2007a. The application of fretting wear modelling to a spline coupling. Wear 262, 1205–1216. doi:10.1016/j.wear.2006.11.017

Ding, J., McColl, I.R., Leen, S.B., Shipway, P.H., 2007b. A finite element based approach to simulating the effects of debris on fretting wear. Wear 263, 481–491. doi:10.1016/j.wear.2006.12.056

Ding, J., Sum, W.S., Sabesan, R., Leen, S.B., McColl, I.R., Williams, E.J., 2007c. Fretting fatigue predictions in a complex coupling. Int. J. Fatigue 29, 1229–1244. doi:10.1016/j.ijfatigue.2006.10.017

Dini, D., Nowell, D., Dyson, I.N., 2006. The use of notch and short crack approaches to fretting fatigue threshold prediction: Theory and experimental validation. Tribol. Int. 39, 1158–1165. doi:10.1016/j.triboint.2006.02.033

Dobromirski, J., 1992. Variables of fretting process: Are there 50 of them? Stand. Frett. Fatigue Test Methods Equip. doi:10.1520/STP25816S

Doebelin, E.O., 1975. Measurement systems : application and design. Tata McGraw Hill Education Private Limited, New Delhi (India).

Dubourg, M., Lamacq, V., 2000. Stage II crack propagation direction determination under fretting fatigue loading: a new approach in accordance with experimental observations, in: Fretting Fatigue: Current Technology and Practices. ASTM

International, West Conshohocken, PA, pp. 436-436–15. doi:10.1520/STP14746S

Ekberg, A., 2004. Fretting fatigue of railway axles - a review of predictive methods and an outline of a finite element model. IMechE J. Rail Rapid Transit 218, 299–316. doi:10.1243/0954409043125905

El Haddad, M.H., Topper, T.H., Smith, K.N., 1979. Prediction of non propagating cracks. Eng. Fract. Mech. 11, 573–584. doi:10.1016/0013-7944(79)90081-X

Elleuch, K., Fouvry, S., 2002. Wear analysis of A357 aluminium alloy under fretting. Wear 253, 662–672. doi:10.1016/S0043-1648(02)00116-3

El-Sherbiny, M., Salem, F., 1982. Fretting-resistant ion-plated coatings. Mater. Eval. Under Frett. Cond. 780, 125-125–13. doi:10.1520/STP29400S

Fatemi, A., Socie, D.F., 1988. A critical plane approach to multiaxial fatigue damage including out-of-phase loading. Fatigue Fract. Eng. Mater. Struct. 11, 149–165. doi:10.1111/j.1460-2695.1988.tb01169.x

Féret, J.J., Bournazel, C.L., 1987. Calculation of stresses and slip in structural layers of unbonded flexible pipes. J. Offshore Mech. Arct. Eng. 109, 263. doi:10.1115/1.3257019

Fett, T., Munz, D., 1997. Stress intensity factors and weight functions. Computational Mechanics Publications, Southhampton.

Flexcom introductory manual (Unpublished Work), 2014. . Wood Group Kenny.

Forsyth, P.J.E., 1969. The physical basis of metal fatigue, Blackie and Son Ltd. London, 1969.

Fouvry, S., 2001. Shakedown analysis and fretting wear response under gross slip

condition. Wear 251, 1320–1331. doi:10.1016/S0043-1648(01)00767-0

Fouvry, S., Duó, P., Perruchaut, P., 2004. A quantitative approach of Ti-6Al-4V fretting damage: Friction, wear and crack nucleation. Wear 257, 916–929. doi:10.1016/j.wear.2004.05.011

Fouvry, S., Kapsa, P., Vincent, L., 1996. Quantification of fretting damage. Wear 200, 186–205. doi:10.1016/S0043-1648(96)07306-1

Fouvry, S., Kapsa, P., Vincent, L., 1995. Analysis of sliding behaviour for fretting loadings: determination of transition criteria. Wear 185, 35–46. doi:10.1016/0043-1648(94)06582-9

Fouvry, S., Liskiewicz, T., Kapsa, P., Hannel, S., Sauger, E., 2003. An energy description of wear mechanisms and its applications to oscillating sliding contacts. Wear 255, 287–298. doi:10.1016/S0043-1648(03)00117-0

Fouvry, S., Merhej, R., 2013. Introduction of a power law formulation to quantify the contact size effects on friction and wear responses of dry oscillating sliding contacts: Application to a chromium steel interface. Wear 301, 34–46. doi:10.1016/j.wear.2013.01.072

Fouvry, S., Paulin, C., Deyber, S., 2009. Impact of contact size and complex gross-partial slip conditions on Ti-6Al-4V/Ti-6Al-4V fretting wear. Tribol. Int. 42, 461–474. doi:10.1016/j.triboint.2008.08.005

Fridrici, V., Fouvry, S., Kapsa, P., 2001. Effect of shot peening on the fretting wear of Ti–6Al–4V. Wear 250, 642–649. doi:10.1016/S0043-1648(01)00671-8

Giannakopoulos, A.E., Lindley, T.C., Suresh, S., 1998. Aspects of equivalence between

contact mechanics and fracture mechanics: theoretical connections and a life-prediction methodology for fretting-fatigue. Acta Mater. 46, 2955–2968. doi:10.1016/S1359-6454(98)00011-1

Giannakopoulos, A.E., Lindley, T.C., Suresh, S., Chenut, C., 2000. Similarities of stress concentrations in contact at round punches and fatigue at notches: Implications to fretting fatigue crack initiation. Fatigue Fract. Eng. Mater. Struct. 23, 561–571. doi:10.1046/j.1460-2695.2000.00306.x

Glaeser, W.A., 1981. Tribology, the science of combating wear. Battelle, Columbus Division.

Godet, M., 1984. The third-body approach: A mechanical view of wear. Wear 100, 437–452. doi:10.1016/0043-1648(84)90025-5

Goh, C.H., McDowell, D.L., Neu, R.W., 2006. Plasticity in polycrystalline fretting fatigue contacts. J. Mech. Phys. Solids 54, 340–367. doi:10.1016/j.jmps.2005.06.009

Golden, P.J., 2009. Development of a dovetail fretting fatigue fixture for turbine engine materials. Int. J. Fatigue 31, 620–628. doi:10.1016/j.ijfatigue.2008.03.017

Golden, P.J., Calcaterra, J.R., 2006. A fracture mechanics life prediction methodology applied to dovetail fretting. Tribol. Int. 39, 1172–1180. doi:10.1016/j.triboint.2006.02.006

Golden, P.J., Nicholas, T., 2005. The effect of angle on dovetail fretting experiments in Ti-6AI-4V. Fatigue Fract. Eng. Mater. Struct. 28, 1169–1175. doi:10.1111/j.1460-2695.2005.00956.x

Goodman, J., 1899. Mechanics applied to engineering, London: Longmans Green. Longmans, Green.

Goodman, L.E., 1962. Contact stress analysis of nominally loaded rough spheres. Trans. ASME J. Appl. Mech. 29, 515–522. doi:10.1115/1.3640599

Halliday, J.S., 2002. The measurement of frictional forces at vibrating contacts. J. Sci. Instrum. 33, 213–217. doi:10.1088/0950-7671/33/6/303

Halliday, J.S., Hirst, W., 1956. The fretting corrosion of mild steel. Proc. R. Soc. Lond. A. Math. Phys. Sci. 236, 411–425. doi:10.1098/rspa.1956.0145

Harte, A.M., McNamara, J.F., 1993. Modeling porcedured for stress analysis of flexible pipe cross sections. J. Offshore Mech. Artic Eng. 115, 46–51. doi:10.1115/1.2920088

Hassan, S.K., Polyzois, D., Morris, G., 1994. Fatigue behaviour of cold-formed steel sections, in: Proceedings of the Twelfth Internation Specialty Converfernce on Cold-Formed Steel Structures. St. Louis, Missouri, USA, pp. 675–689.

Haverty, K.F., McNamara, J.F., Moran, B., 1982. Finite dynamic motions of articulated offshore loading towers, in: International Conference on Marginal and Deepwater Oilfield Development. Hamburg, Germany.

Haviez, L., Fouvry, S., Toscano, R., Yantio, G., 2015. An energy-based approach to understand the effect of fretting displacement amplitude on grease-lubricated interface. Wear 338–339, 422–429. doi:10.1016/j.wear.2015.07.015

Heredia, S., Fouvry, S., 2010. Introduction of a new sliding regime criterion to quantify partial, mixed and gross slip fretting regimes: Correlation with wear and cracking

processes. Wear 269, 515–524. doi:10.1016/j.wear.2010.05.002

Hertz, H., 1882. Über die Berührung fester elastischer Körper. J. fur die Reine und Angew. Math. 1882, 156–171. doi:10.1515/crll.1882.92.156

Heß, M., 2013. On the reduction method of dimensionality: The exact mapping of axisymmetric contact problems with and without adhesion. Phys. Mesomech. 15, 264–269. doi:10.1134/S1029959912030034

Hills, D.A., Nowell, D., Hills, D.A., 1996. Mechanics of fretting fatigue tests, International Journal of Mechanical Sciences. Kluwer Academic Publishers, Dordrecht/Boston/London. doi:10.1016/0020-7403(87)90117-2

Hills, D.A., Sackfield, A., Paynter, R.J.H., 2009. Simulation of fretting wear in halfplane geometries: Part 1-The solution for long term wear. J. Tribol. 131, 31401. doi:10.1115/1.3118785

Hoffman, J., Dupont, W., Reynolds, B., 2001. A fatigue-life prediction model for metallic tube umbilicals, in: Offshore Technology Conference. doi:10.4043/13203-MS

Houghton, D., Wavish, P.M., Williams, E.J., Leen, S.B., 2009. Multiaxial fretting fatigue testing and prediction for splined couplings. Int. J. Fatigue 31, 1805–1815. doi:10.1016/j.ijfatigue.2008.12.005

Hutchings, L.M., 1992. Triblology: Friction and wear of engineering materials, CRC Press, London. Arnold, London.

Iwabuchi, A., 1991. The role of oxide particles in the fretting wear of mild steel. Wear 151, 301–311. doi:10.1016/0043-1648(91)90257-U

Jacques, R., Clarke, T., Morikawa, S., Strohaecker, T., 2010. Monitoring the structural integrity of a flexible riser during dynamic loading with a combination of non-destructive testing methods. NDT E Int. 43, 501–506. doi:10.1016/j.ndteint.2010.05.005

Jager, J., 2002. New analytical and numerical results for two-dimensional contact profiles. Int. J. Solids Struct. 39, 959–972. doi:New analytical and numerical results for two-dimensional contact profiles

Jin, O., Mall, S., 2004. Effects of slip on fretting behavior: Experiments and analyses. Wear 256, 671–684. doi:10.1016/S0043-1648(03)00510-6

Jin, X., Sun, W., Shipway, P.H., 2016. Derivation of a wear scar geometry-independent coefficient of friction from fretting loops exhibiting non-Coulomb frictional behaviour. Tribol. Int. 102, 561–568. doi:10.1016/j.triboint.2016.06.012

Johnson, K.L., 1985. Contact mechanics. Cambridge University Press. doi:10.1115/1.3261297

Johnson, K.L., 1955. Surface interaction between elastically loaded bodies under tangential forces. Proc. R. Soc. Lond. A. Math. Phys. Sci. 230, 531–548. doi:10.1098/rspa.1955.0149

Kartal, M.E., Mulvihill, D.M., Nowell, D., Hills, D.A., 2011. Determination of the frictional properties of titanium and nickel alloys using the digital image correlation method. Exp. Mech. 51, 359–371. doi:10.1007/s11340-010-9366-y

Kennedy, A.J., 1963. Processes of creep and fatigue in metals. John Wiley & Sons, Incorporated, NJ USA.

Kennedy, P., Peterson, M., Stallings, L., 1982. An evaluation of fretting at small slip amplitudes. Mater. Eval. Under Frett. Cond. 30–48. doi:10.1520/STP29395S

Khotsyanovskii, A.O., 2010. Life prediction of titanium and aluminum alloys under fretting fatigue conditions using various crack propagation criteria. Part 1. Experimental and calculation techniques. Strength Mater. 42, 683–704. doi:10.1007/s11223-010-9256-7

Khrushchov, M.M., Babichev, M.A., 1960. Investigation of wear of metals, Russian Academy of Sciences, Moscow. Izd. Akad. Nauk, SSSR, Moscow.

Kitagawa, H., Takahashi, S., 1976. Applicability of fracture mechanics to very small cracks or the cracks in the early stage, in: Proc 2nd Int. Conf. on Mech. Behavior of Materials. ASM, Metals Park, Ohio., pp. 627–631.

Kusner, D., Poon, C., Hoeppner, D., 1982. A new machine for studying surface damage due to wear and fretting. S.R. Brown Mater. Eval. Under Frett. Cond. 780, 17–29. doi:10.1520/STP29394S

Lane, M., McNamara, J.F., Conroy, J., 1986. Time and frequency domain analysis for marine risers and offshore loading towers, in: International Conference on Marginal and Deepwater Oilfield Development. London, UK.

Lane, M., O'Sullivan, T., Grealish, F., Kavanagh, K., Thompson, H., 2001. Advanced Frequency Domain Analysis Techniques for Steel Catenary Risers, in: Offshore Technology Conference. Houston, Texas, USA, pp. 1–14. doi:10.4043/13017-MS

Lang, D., Kavanagh, W.K., Lane, M., International, M.C.S., Stear, J., Griffin, P., Thompson, H., Petroleum, C., Company, T., 2001. A comparison of spar riser response measurements with results from application of new analysis tools, in:

Offshore Technology Conference. Houston, Texas, USA, pp. 1–8. doi:10.4043/13110-MS

Lang, D.W., Connolly, A., Lane, M., Connaire, A.D., 2005. Advances in Frequency and Time Domain Coupled Analysis for Floating Production and Offloading Systems, in: International Conference on Offshore Mechanics and Arctic Engineering. Halkidiki, Greese. doi:10.1115/OMAE2005-67396

Lang, D.W., Huxtable, J., Roland, L., Lane, M., 2006. Deployment of a Completion Riser Management System Incorporating Advanced on-Board Riser Numerical Analysis – Key Issues and Benefits, in: International Conference on Offshore Mechanics and Arctic Engineering. Hamburg, Germany, pp. 1–9. doi:10.1115/OMAE2006-92425

Lang, D.W., Murphy, K., Lane, M., 2007. Development of a new on-board tool for planning drilling riser operations in high current environments, in: International Conference on Offshore Mechanics and Arctic Engineering. San Diego, California, USA. doi:10.1115/OMAE2007-29252

Lang, D.W., Park, G.T., Lane, M., 2009. Recent developments in drilling riser disconnect and recoil, in: International Conference on Offshore Mechanics and Arctic Engineering. Honolulu, Hawaii, USA, pp. 1–14. doi:10.1115/OMAE2009-79427

Lange, H., Berge, S., 2004. Material selection in the offshore industry (Report), Sintef Material and Chemistry Marintek. MARINTEK, SINTEF Materials and Chemistry.

Lanteigne, J., 1985. Theoretical estimation of the response of helically armored cables

to tension, torsion, and bending. J. Appl. Mech. 52, 423. doi:10.1115/1.3169064

Leen, S.B., Hyde, T.H., McColl, I.R., Williams, E.J., Ratsimba, C.H.H., Williams, E.J., McColl, I.R., 2002. An investigation of the fatigue and fretting performance of a representative aero-engine spline coupling. J. strain Anal. Eng. Des. 37, 565–583. doi:10.1243/030932402320950161

Leen, S.B., McColl, I.R., Ratsimba, C.H.H., Williams, E.J., 2003. Fatigue life prediction for a barrelled spline coupling under torque overload. Proc. Inst. Mech. Eng. Part G J. Aerosp. Eng. 217, 123–142. doi:10.1243/095441003322297234

Lemm, J.D., Warmuth, A.R., Pearson, S.R., Shipway, P.H., 2014. The influence of surface hardness on the fretting wear of steel pairs-Its role in debris retention in the contact. Tribol. Int. 81, 258–266. doi:10.1016/j.triboint.2014.09.003

Leonard, B.D., Sadeghi, F., Shinde, S., Mittelbach, M., 2012. A novel modular fretting wear test rig. Wear 274–275, 313–325. doi:10.1016/j.wear.2011.09.015

Li, S., Kang, Y., Kuang, S., 2014. Effects of microstructure on fatigue crack growth behavior in cold-rolled dual phase steels. Mater. Sci. Eng. A 612, 153–161. doi:10.1016/j.msea.2014.06.002

Li, X., Zuo, Z., Qin, W., 2015. A fretting related damage parameter for fretting fatigue life prediction. Int. J. Fatigue 73, 110–118. doi:10.1016/j.ijfatigue.2014.12.003

Lotveit, S.A., Bjaerum, R., 1994. Second generation analysis tool for flexible pipes, in: Proceedings of the Second European Conference on Flexible Pipes, Umbilicals and Marine Cables-Structural Mechanics and Testing. Bentham, London.

Madge, J.J., Leen, S.B., McColl, I.R., Shipway, P.H., 2007a. Contact-evolution based

prediction of fretting fatigue life: Effect of slip amplitude. Wear 262, 1159–1170. doi:10.1016/j.wear.2006.11.004

Madge, J.J., Leen, S.B., Shipway, P.H., 2008. A combined wear and crack nucleation-propagation methodology for fretting fatigue prediction. Int. J. Fatigue 30, 1509–1528. doi:10.1016/j.ijfatigue.2008.01.002

Madge, J.J., Leen, S.B., Shipway, P.H., 2007b. The critical role of fretting wear in the analysis of fretting fatigue. Wear 263, 542–551. doi:10.1016/j.wear.2006.11.021

Magaziner, R., Jin, O., Mall, S., 2004. Slip regime explanation of observed size effects in fretting. Wear 257, 190–197. doi:10.1016/j.wear.2003.12.005

Malta, E.R., de Arruda Martins, C., Gonçalves, S.H., Neto, A.G., 2013. Finite element modeling of flexible pipes under crushing loads, in: AMSE 2013 32nd International Conference on Ocean, Offshore and Artic Engineering. Nantes, France, pp. 1–9. doi:0.1115/OMAE2013-10307

Manson, S.S., 1965. Fatigue: A complex subject-Some simple approximations - Both ends of the fatigue spectrum are covered in this lecture. On the one hand, the present state of understanding of the mechanism is reviewed and the complexity of the process observed. On the othe. Exp. Mech. 5, 193–226. doi:10.1007/BF02321056

Manson, S.S., 1953. Behaviour of materials under conditions of thermal stress, Heat Transfer Symposium.

Marui, E., Endo, H., Hasegawa, N., Mizuno, H., 1998. Prototype fretting-wear testing machine and some experimental results. Wear 214, 221–230. doi:10.1016/S0043-1648(97)00251-2

Mary, C., Fouvry, S., 2007. Numerical prediction of fretting contact durability using energy wear approach: Optimisation of finite-element model. Wear 263, 444–450. doi:10.1016/j.wear.2007.01.116

McCarthy, O.J., McGarry, J.P., Leen, S.B., 2014. The effect of grain orientation on fretting fatigue plasticity and life prediction. Tribol. Int. 76, 100–115. doi:10.1016/j.triboint.2013.09.023

McCarthy, O.J., McGarry, J.P., Leen, S.B., 2013. Microstructure-sensitive prediction and experimental validation of fretting fatigue. Wear 305, 100–114. doi:10.1016/j.wear.2013.05.012

McColl, I.R., Ding, J., Leen, S.B., 2004. Finite element simulation and experimental validation of fretting wear. Wear 256, 1114–1127. doi:10.1016/j.wear.2003.07.001

McColl, I.R., Waterhouse, R.B., Harris, S.J., Tsujikawa, M., 1995. Lubricated fretting wear of a high-strength eutectoid steel rope wire. Wear 185, 203–212. doi:10.1016/0043-1648(95)06616-0

McNamara, J.F., 1992. Three-dimensional analytical simulation of flexible pipe wall structure. J. Offshore Mech. Arct. Eng. 114, 69–75. doi:10.1115/1.2919961

McNamara, J.F., Lane, M., 1992. 3D frequency domain analysis of offshore structures, in: 9th Conference on Engineering Mechanics. Collece Stateion, TX, USA, pp. 192–195.

McNamara, J.F., Lane, M., 1984. Practical modeling for articulated risers and loading columns. J. Energy Resour. Technol. 106, 444. doi:10.1115/1.3231104

McNamara, J.F., O'Brien, P.J., 1988. Flexible riser technology, in: IBC Conference on

Oil and Gas Production - Recent International Technological Developments. London, UK.

McNamara, J.F., O'Brien, P.J., Gilroy, S.G., 1988. Nonlinear analysis of flexible risers using hybrid finite elements. J. Offshore Mech. Arct. Eng. 110, 197–204. doi:10.1115/1.3257051

Merhej, R., Fouvry, S., 2009. Contact size effect on fretting wear behaviour: Application to an AISI 52100/AISI 52100 interface. Lubr. Sci. 21, 83–102. doi:10.1002/ls.74

Mindlin, R.D., 1949. Compliance of elastic bodies in contact. J. Appl. Mech. 16, 259–268. doi:10.1007/978-1-4613-8865-4_24

Mohd Tobi, A.L., Ding, J., Bandak, G., Leen, S.B., Shipway, P.H., 2009. A study on the interaction between fretting wear and cyclic plasticity for Ti-6Al-4V. Wear 267, 270–282. doi:10.1016/j.wear.2008.12.039

Mohrbacher, H., Celis, J.P., Roos, J.R., 1995. Laboratory testing of displacement and load induced fretting. Tribol. Int. 28, 269–278. doi:10.1016/0301-679X(95)00005-O

Mossakovski, V.I., 1954. The fundamental general problem of the theory of elasticity. PMM 18.

Mossakovskii, V.I., 1963. Compression of elastic bodies under conditions of adhesion (Axisymmetric case). J. Appl. Math. Mech. 27, 630–643. doi:10.1016/0021-8928(63)90150-3

Mugadu, A., Hills, D.A., Limmer, L., 2002a. An asymptotic approach to crack

initiation in fretting fatigue of complete contacts. J. Mech. Phys. Solids 50, 531–547. doi:10.1016/S0022-5096(01)00091-6

Mugadu, A., Hills, D.A., Nowell, D., 2002b. Modifications to a fretting-fatigue testing apparatus based upon an analysis of contact stresses at complete and nearly complete contacts. Wear 252, 475–483. doi:10.1016/S0043-1648(02)00007-8

Mulvihill, D.M., Kartal, M.E., Olver, A. V., Nowell, D., Hills, D.A., 2011. Investigation of non-Coulomb friction behaviour in reciprocating sliding. Wear 271, 802–816. doi:10.1016/j.wear.2011.03.014

Myren, J., 2007. SEAFLEX - Failure modes, inspection, testing and monitoring.

Neto, A.G., 2015. A comparative wet collapse buckling study for the carcass layer of flexible pipes. J. Offshore Mech. Arct. Eng. 134/031701, 1–9. doi:10.1115/1.4005185

Neto, A.G., 2011. Flexible pipes: Influence of the pressure armor in the wet collapse resistance. Omae 136/031401, 1–10. doi:10.1115/OMAE2011-49105

Neto, A.G., Martins, C. de A., Malta, E.R., Tanaka, R.L., Godinho, C.A.F., 2016. Simplified finite element models to study the dry collapse of straight and curved flexible pipes. J. Offshore Mech. Arct. Eng. 138, 21701. doi:10.1115/1.4032156

Neto, A.G., Martins, C.D.A., Pesce, C.P., Meirelles, C.O.C., Malta, E.R., Neto, T.F.B., Godinho, C.A.F., 2013. Prediction of burst in flexible pipes. J. Offshore Mech. Arct. Eng. 135, 11401. doi:10.1115/1.4007046

Neu, R.W., Pape, J., 1998. Methodologies for linking nucleation and propagation approaches for predicting life under fretting fatigue, in: Symposium on Fretting

Fatigue: Current Technology and Practices, Salt Lake City. pp. 369–388. doi:10.1520/STP14742S

Neuber, H., 1958. Theory of notch stresses, Springer. JW Edwards.

Neyman, A., Sikora, J., 2008. Grease effect on fretting wear of mild steel. Ind. Lubr. Tribol. 60, 67–78. doi:10.1108/00368790810858368

Nicholas, T., Hutson, A., John, R., Olson, S., 2003. A fracture mechanics methodology assessment for fretting fatigue. Int. J. Fatigue 25, 1069–1077. doi:10.1016/S0142-1123(03)00115-4

Nishioka, K., Hirakawa, K., 1972. Fundamental investigations of fretting fatigue : Part 6, effects of contact pressure and hardness of materials. Bull. JSME.

Nowell, D., 2010. Simulation of fretting wear in half-plane geometries - Part II: Analysis of the transient wear problem using quadratic programming. J. Tribol. 132, 21402. doi:10.1115/1.4000733

Nowell, D., Dini, D., 2003. Stress gradient effects in fretting fatigue, Tribology International. doi:10.1016/S0301-679X(02)00134-2

O'Brien, P.J., Lane, M., Mcnamara, J.F., 2002. Improvements to the convected co-ordinates method for predicting large deflection extreme riser response, in: International Conference on Offshore Mechanics and Arctic Engineering. Oslo, Norway. doi:10.1115/OMAE2002-28237

O'Brien, P.J., McNamara, J.F., Dunne, F.P.E., 1988. Three-dimensional nonlinear motions of risers and offshore loading towers. J. Offshore Mech. Arct. Eng. 110, 232. doi:10.1115/1.3257056

O'Brien, P.J., McNamara, J.F., Lane, 2003. Three dimensional finite displacements and rotations of flexible beams including non-equal bending stiffnesses, in: International Conference on Offshore Mechanics and Arctic Engineering. Cancun, Mexico. doi:10.1115/OMAE2003-37372

Ohmae, N., Tsukizoe, T., 1974. The effect of slip amplitude in fretting. Wear 27, 281–294. doi:10.1016/0043-1648(74)90114-8

Öqvist, M., 2001. Numerical simulations of mild wear using updated geometry with different step size approaches. Wear 249, 6–11. doi:10.1016/S0043-1648(00)00548-2

Osawa, N., Nakamura, T., Yamamoto, N., Sawamura, J., 2013. Development of a new fatigue testing machine for high frequency fatigue damage assessment 1–5.

Papanikos, P., Meguid, S.A., Stjepanovic, Z., 1998. Three-dimensional nonlinear finite element analysis of dovetail joints in aeroengine discs. Finite Elem. Anal. Des. 29, 173–186. doi:10.1016/S0168-874X(98)00008-0

Pape, J. a., Neu, R.W., 1999. Influence of contact configuration in fretting fatigue testing. Wear 225–229, 1205–1214. doi:10.1016/S0043-1648(98)00398-6

Paris, P.C., Erdogan, F., 1963. A critical analysis of crack propagation laws. J. Basic Eng.(Trans. ASME) 85, 528–534. doi:10.1115/1.3656900

Paulin, C., Fouvry, S., Meunier, C., 2008. Finite element modelling of fretting wear surface evolution: Application to a Ti-6A1-4V contact. Wear 264, 26–36. doi:10.1016/j.wear.2007.01.037

Pearson, S.R., 2013. The effect of nitriding on the fretting wear of a high strength steel

at ambient and elevated temperatures. (Ph.D. Thesis) University of Nottingham.

Perera, S.D.R., Fernando, U.S., Sheldrake, T., Clements, R., 2007. An investigation into fretting behaviour in pressure armor wires of unbonded flexible pipes, in: Volume 3: Pipeline and Riser Technology; CFD and VIV. San Diego, California, USA, pp. 363–370. doi:10.1115/OMAE2007-29393

Popov, V.L., Heß, M., 2014. Methode der dimensionsreduktion in kontakt-mechanik. ZEV rail Glas. Ann. 138, 248–255. doi:10.1007/978-3-642-32673-8

Rajasekaran, R., Nowell, D., 2005. On the finite element analysis of contacting bodies using submodelling. J. Strain Anal. Eng. Des. 40, 95–106. doi:10.1243/030932405X7836

Ramesh, R., Gnanamoorthy, R., 2006. Development of a fretting wear test rig and preliminary studies for understanding the fretting wear properties of steels. Mater. Des. 27, 141–146. doi:10.1016/j.matdes.2004.09.017

Raye, T., 1860. Zur Theorie der Zapfenreibung, Der Civilingenieur.

Ruiz, C., Boddington, P.H.B., Chen, K.C., 1984. An investigation of fatigue and fretting in a dovetail joint. Exp. Mech. 24, 208–217. doi:10.1007/BF02323167

Sabelkin, V., Mall, S., 2005. Investigation into relative slip during fretting fatigue under partial. Fatigue Fract. Eng. Mater. Struct. 28, 809–824. doi:10.1111/j.1460-2695.2005.00918.x

Sævik, S., 2011. Theoretical and experimental studies of stresses in flexible pipes. Comput. Struct. 89, 2273–2291. doi:10.1016/j.compstruc.2011.08.008

Saevik, S., Ye, N., 2009. Armour layer fatigue design challenges for flexible risers in

ultra-deep water depth, in: ASME 2009 28th International Conference on Ocean, Offshore and Arctic Engineering. pp. 1–9. doi:10.1115/OMAE2009-79924

Saufer, E., Fouvry, S., Ponsonnet, L., Kapsa, P., Martine, J.M., Vincent, L., 2000. Tribologically transformed structure in fretting. Wear 245, 39–52.

Shang, D.G., Sun, G.Q., Deng, J., Yan, C.L., 2006. Multiaxial fatigue damage models. Key Eng. Mater. 324–325, 747–750. doi:10.4028/www.scientific.net/KEM.324-325.747

Shima, M., Suetake, H., McColl, I.R., Waterhouse, R.B., Takeuchi, M., 1997. On the behaviour of an oil lubricated fretting contact. Wear 210, 304–310. doi:10.1016/S0043-1648(97)00078-1

Smallwood, R., Pearson, B.R., Brook, P.A., 1988. The influence of dissolved oxygen in seawater on the fretting corrosion of roping steel. Wear 125, 97–106. doi:10.1016/0043-1648(88)90196-2

Smith, K., Watson, P., Topper, T., 1970. Stress- strain function for the fatigue of metals. J Mater 5, 767–778.

Smith, R., Carr, T., Lane, M., 2007. Computational tool for the dynamic analysis of flexible risers incorporating benging hysteresis, in: International Conference on Offshore Mechanics and Arctic Engineering. San Diego, California, USA. doi:10.1115/OMAE2007-29276

Soderberg, C., Sweden, V., 1930. Factor of safety and working stress. Trans. Am. Soc. Test Matls 52, 13–28.

Söderberg, S., Colvin, T., Salama, K., Vingsbo, O., 1986. Ultrasonic fretting wear of a

plain carbon steel. J. Eng. Mater. Technol. 108, 153–158. doi:10.1115/1.3225853

Stephens, R.I. (Ralph I., Fuchs, H.O. (Henry O., 2001. Metal fatigue in engineering. JOHN WILEY SONS, NY. 1980. 472.

Sullivan, M.O., 2009. Meeting the future challenges of flexible pipe technology - advances in industry standards, in: Proceedings of the Offshore Technology Conference (OTC). Houston, Texas, USA, pp. 1–11. doi:10.4043/20027-MS

Sum, W.S., Williams, E.J., Leen, S.B., 2005. Finite element, critical-plane, fatigue life prediction of simple and complex contact configurations. Int. J. Fatigue 27, 403–416. doi:10.1016/j.ijfatigue.2004.08.001

Suresh, S., 1998. Fatigue of materials. Cambridge university press. doi:10.1017/CBO9780511806575

Sweeney, C.A., O'Brien, B., McHugh, P.E., Leen, S.B., 2014. Experimental characterisation for micromechanical modelling of CoCr stent fatigue. Biomaterials 35, 36–48. doi:10.1016/j.biomaterials.2013.09.087

Switek, W., 1984. Early stage crack propagation in fretting fatigue. Mech. Mater. 3, 257–267. doi:10.1016/0167-6636(84)90024-3

Szolwinski, M.P., Farris, T.N., 1996. Mechanics of fretting fatigue crack formation. Wear 198, 93–107. doi:10.1016/0043-1648(96)06937-2

Szolwinski, M.P., Harish, G., McVeigh, P.A., Farris, T.N., 2000. Experimental study of fretting crack nucleation in aerospace alloys with emphasis on life prediction, in: ASTM Special Technical Publication. ASTM International, 100 Barr Harbor Drive, PO Box C700, West Conshohocken, PA 19428-2959, pp. 267–281.

doi:10.1520/STP14735S

Taylor, D., 2001. A mechanistic approach to critical-distance methods in notch fatigue. Fatigue Fract. Eng. Mater. Struct. 24, 215–224. doi:10.1046/j.1460-2695.2001.00401.x

Tomlinson, G.A., 1927. The rusting of steel surfaces in contact. Proc. R. Soc. London. Ser. A, Contain. Pap. a Math. Phys. Character 115, 472–483.

Tomlinson, G.A., Thorpe, P.L., Gough, H.J., 1939. An investigation of the fretting corrosion of closely fitting surfaces. Proc. Inst. Mech. Eng. 1847-1982 141, 223–249. doi:10.1243/PIME_PROC_1939_141_034_02

Uhlig, H.H., Ming Feng, I., Tierney, W.D., 1953. A fundamental investigation of fretting corrosion. Massachusetts Institute of Technology.

Varenberg, M., Halperin, G., Etsion, I., 2002. Different aspects of the role of wear debris in fretting wear. Wear 252, 902–910. doi:10.1016/S0043-1648(02)00044-3

Vidner, J., Leidich, E., 2007. Enhanced Ruiz criterion for the evaluation of crack initiation in contact subjected to fretting fatigue. Int. J. Fatigue 29, 2040–2049. doi:10.1016/j.ijfatigue.2007.02.010

Vingsbo, O., Söderberg, S., 1988. On fretting maps. Wear 126, 131–147. doi:10.1016/0043-1648(88)90134-2

Wang, Z. a., Zhou, Z.R., Chen, G.X., 2011. An investigation of palliation of fretting wear in gross slip regime with grease lubrication. Ind. Lubr. Tribol. 63, 84–89. doi:10.1108/00368791111112207

Warmuth, A.R., Shipway, P.H., Sun, W., 2015. Fretting wear mapping: the influence of

contact geometry and frequency on debris formation and ejection for a steel-on-steel pair. Proc. R. Soc. A Math. Phys. Eng. Sci. 471, 20140291–20140291. doi:10.1098/rspa.2014.0291

Warmuth, A.R., Sun, W., Shipway, P.H., 2016. The roles of contact conformity, temperature and displacement amplitude on the lubricated fretting wear of a steel-on-steel contact. R. Soc. Open Sci. 3. doi:10.1098/rsos.150637

Wavish, P.M., Houghton, D., Ding, J., Leen, S.B., Williams, E.J., McColl, I.R., 2009. A multiaxial fretting fatigue test for spline coupling contact. Fatigue Fract. Eng. Mater. Struct. 32, 325–345. doi:10.1111/j.1460-2695.2009.01334.x

Wittkowsky, B.U., Birch, P.R., Dominguez, J., Suresh, S., 1999. Apparatus for quantitative fretting fatigue testing. Fatigue Fract. Eng. Mater. Struct. 22, 307–320. doi:10.1046/j.1460-2695.1999.00145.x

Witz, J.A., Tan, Z., 1992a. On the flexural structural behaviour of flexible pipes, umbilicals and marine cables. Mar. Struct. 5, 205–227. doi:10.1016/0951-8339(92)90029-O

Witz, J.A., Tan, Z., 1992b. On the axial-torsional structural behaviour of flexible pipes, umbilicals and marine cables. Mar. Struct. 5, 205–227. doi:10.1016/0951-8339(92)90029-O

Wohler, A., 1860. Versuche zur ermittlung der auf die eisenbahnwagenachsen einwirkenden krafte und die widerstandsfahigkeit der wagen-achsen. Zeitschrift für Bauwes. 583–616.

Wöhler, A., 1870. Über die Festigkeitsversuche mit Eisen und Stahl. Auf Anordnung des Ministers für Handel, Gewerbe u. öffentl. Arbeiten, Grafen Itzenblitz,

angestellt. Ernst und Korn, Berlin.

Wöhler, A., 1858. Bericht über die Versuche, welche auf der Königl. Niederschlesisch-Märkischen Eisenbahn mit Apparaten zum Messender Biegung und Verdrehung von Eisen bahnwagenachsen während der Fahrt angestellt wurden. Z. Bauwes. Bd 8, 646.

Wood Group Kenny Ireland Limited, 2014. Flexcom technical maunal version 8.4.

Wright, K., 1952. An investigation of fretting corrosion. Proc. Inst. Mech. Eng. Part B J. Eng. Manuf. 1, 556–574.

Ye, N., Saevik, S., 2001. Multiple axial fatigue of pressure armours in flexible pipes, in: ASME 2011 30th Internaltional Conference on Ocean, Offshore and Artic Engineering. Rotterdam, The Netherlands. doi:10.1115/OMAE2011-50210

Zhang, T., Harrison, N.M., McDonnell, P.F., McHugh, P.E., Leen, S.B., 2014. Micro-macro wear-fatigue of modular hip implant taper-lock coupling. J. Strain Anal. Eng. Des. 49, 2–18. doi:10.1177/0309324713502175

Zhang, T., Harrison, N.M., Mcdonnell, P.F., Mchugh, P.E., Leen, S.B., 2013. A finite element methodology for wear - fatigue analysis for modular hip implants. Tribiology Int. 65, 113–127. doi:10.1016/j.triboint.2013.02.016

Zhang, T., Mchugh, P.E., Leen, S.B., 2011. Computational study on the effect of contact geometry on fretting behaviour. Wear 271, 1462–1480. doi:10.1016/j.wear.2010.11.017

Zhou, Z.., Vincent, L., 1999. Lubrication in fretting—a review. Wear 225, 962–967. doi:10.1016/S0043-1648(99)00038-1

Zhou, Z.R., Kapsa, P., Vincent, L., 1998. Grease lubrication in fretting. J. Tribol. 120, 737–743. doi:10.1115/1.2833773